Fouling during solution polymerization in continuously operated reactors

Von der Fakultät Energie-, Verfahrens- und Biotechnik der Universität Stuttgart zur Erlangung der Würde eines Doktors der Ingenieurwissenschaften (Dr.-Ing.) genehmigte Abhandlung

vorgelegt von
Christian Niklas Zander
geboren in
Frankfurt am Main

Hauptberichter: Prof. Dr.-Ing. Ulrich Nieken
Mitberichter: Prof. Dr. rer. nat. Klaus-Dieter Hungenberg
Prüfungsvorsitzender: Prof. Dr.-Ing. Joachim Groß

Tag der mündlichen Prüfung: 30.06.2021

Institut für Chemische Verfahrenstechnik
der Universität Stuttgart

2021

Danksagung

Diese Dissertation entstand während meiner Zeit als wissenschaftlicher Mitarbeiter am Institut für Chemische Verfahrenstechnik der Universität Stuttgart.

Prof. Ulrich Nieken danke ich für das mir entgegengebrachte Vertrauen und die Freiheit meine Ideen einzubringen und umzusetzen. Dies und die Diskussionen zu wichtigen Punkten meiner Arbeiten haben einen maßgeblichen Beitrag geleistet. Prof. Klaus-Dieter Hungenberg danke ich für die Anfertigung des Zweitgutachtens und insbesondere für die vielen fachlichen Diskussion, die wertvolle Aspekte zu dieser Dissertation beigetragen haben. Dr. Christian Schwede von BASF danke ich für die Unterstützung bei den experimentellen Arbeiten und der Analytik. Gleiches gilt für Dörthe Schiewe und Robert Fettig ohne deren Einsatz der Umfang der experimentellen Arbeiten nicht möglich gewesen wäre. Auch die studentischen Arbeiten von Magnus Gähr, Ernst Jacob-Wendler, Victoria Rembold, Thomas Schall und Lukas Stüdemann haben einen wichtigen Beitrag zum Gelingen dieser Dissertation geleistet. Allen ehemaligen Kollegen am ICVT danke ich für gute Zusammenarbeit in der Werkstatt, im Technikum, in der Verwaltung oder „im zweiten Stock“, aber auch für die vielen Aktivitäten neben der Arbeit. Ich werde die Zeit am ICVT immer in guter Erinnerung behalten.

Nicht zuletzt gilt mein Dank meiner Familie – insbesondere meinen Eltern, deren Unterstützung es mir ermöglicht hat meinen eigenen Weg zu gehen, und meiner Frau Isabel für ihre Unterstützung und Geduld, wenn die Arbeit mich wieder einmal nicht losgelassen hat. Dieser Rückhalt war und ist eine wichtige Stütze für mich.

Für die finanzielle Unterstützung im Rahmen der ENPRO-Initiative danke ich dem Bundesministerium für Wirtschaft und Energie („KoPPonA 2.0“, FKZ 03EN2004F).

Contents

Zusammenfassung

Spezialpolymere werden auf Grund der notwendigen Flexibilität in der Produktion dieser Produktklasse momentan hauptsächlich in diskontinuierlichen Prozessen in Rührkesselreaktoren hergestellt. Milli-strukturierte, kontinuierlich betriebene Reaktoren sind eine vielversprechende Alternative für die Prozessintensivierung, um die Energieeffizienz und die Raum-Zeit-Ausbeute zu erhöhen, die Entwicklungszeit für neue Produkte zu verkürzen und gleichzeitig die Flexibilität zu erhalten. Ein Hindernis für die Übertragung von diskontinuierlichen Prozessen auf diese Art von Reaktorsystem ist die Bildung von Belägen, die aufwachsen und den Reaktor verblocken. Um dieses Hindernis zu überwinden, ist das Verständnis der für die Belagsbildung ursächlichen Mechanismen essenziell.

In dieser Arbeit wird die Belagsbildung während der Polymerisation von N-Vinylpyrrolidon (NVP) in wässriger Lösung sowohl experimentell als auch in Simulationen untersucht, um ein mechanistisches Verständnis des Zusammenspiels der relevanten physikalischen Prozesse zu generieren, den Belagsbildungsmechanismus modellbasiert zu beschreiben und Vorschläge abzuleiten, wie die Bildung von Belägen verhindert oder zumindest verringert werden kann.

Zunächst werden Ergebnisse aus Experimenten in verschiedenen Arten von Rührkessel- und Rohrreaktoren vorgestellt. In all diesen Reaktorsystemen werden Beläge durch ein unlösliches Polymergel gebildet, das stark an metallischen Oberflächen haftet. Das Polymergel entsteht zunächst in Bereichen mit lokal erhöhter Verweilzeit, z. B. in Totzonen von statischen Mischelementen, an Strömungsblechen von Rührkesselreaktoren oder an Wänden von Rohrreaktoren ohne Mischelemente. Einmal gebildete Beläge wachsen durch Reaktion weiter auf und können bis zur Verblockung des Rohrreaktorsystems führen.

Auf Grund der Bildung eines Polymergels müssen Nebenreaktionen, die zu hochmolekularen und verzweigten Polymerketten führen, eine wichtige Rolle bei der Bildung von Ablagerungen spielen. Kinetische Modelle, die diese Nebenreaktionen beinhalten und mikrostrukturelle Eigenschaftsverteilungen beschreiben können, werden vorgestellt und anhand von Experimenten im kontinuierlich gerührten Rührkesselreaktor (CSTR) validiert. Die Ergebnisse bestätigen den vorgeschlagenen Reaktionsmechanismus, bei dem die Bildung und Propagation von terminalen Doppelbindungen zu verzweigten oder vernetzten Polymerketten führt. Obwohl eine Gelierung der Hauptphase nicht auftritt, entstehen Beläge an den Strömungsblechen des Rührkesselreaktors und in anderen schlecht durchmischten Bereichen des Reaktors. Diese Beobachtung unterstreicht die Bedeutung des Strömungsfeldes und des diffusiven Stofftransports für die Bildung von Belägen.

Um das Zusammenspiel von Strömungsfeld, Reaktion und diffusivem Stofftransport zu demonstrieren werden Simulationen mit einem CFD-Solver inklusive einer reduzierten Version des reaktionskinetischen Modells und einem Modell für den diffusiven Stofftransport vorgestellt. Das Stofftransportmodell ist in der Lage, den diffusiven Transport von statistischen Momenten zu beschreiben und daher konsistent mit dem reaktionskinetischen Modell. Simulationen in verschiedenen zweidimensionalen Geometrien bestätigen, dass Bereiche mit lokal erhöhter Verweilzeit zur Bildung von Polymergelen führen, z. B. in der Nähe von Reaktorwänden oder in Totzonen. Auf Grund der unterschiedlichen Verweilzeit entstehen Konzentrationsgradienten zwischen diesen Bereichen und der Hauptphase, wodurch Stofftransport induziert wird. Aufgrund der geringeren Diffusionskoeffizienten im Vergleich zu niedermolekularen Spezies akkumulieren Polymermoleküle in diesen Bereichen und verursachen eine lokale Erhöhung der Viskosität. Die Viskositätsgradienten beeinflussen das Strömungsfeld und führen zur Vergrößerung der Regionen mit erhöhter Verweilzeit. Die Kombination aus erhöhter Verweilzeit, hohem Polymer- und niedrigem Monomergehalt

begünstigt die Bildung von Polymergelen durch Nebenreaktionen.

Zusammen mit der Anhaftung von Makromolekülen an metallischen Oberflächen scheint dies der relevante Mechanismus für die Bildung von Belägen zu sein. Strategien zur Verringerung der Belagsbildung sollten daher auf Oberflächenmodifikationen, die die Adhäsion von Makromolekülen verringern, sowie auf die Beseitigung von Totzonen und Viskositätsgradienten konzentriert werden.

Abstract

Specialty polymers are mostly produced in discontinuous processes in tank reactors due to the need for flexibility in the production of this product class. Milli-structured, continuously operated reactors are promising alternatives for process intensification to increase energy efficiency and space-time-yield, reduce time-to-market for new products and maintain flexibility. A major obstacle for the transfer of batch processes to such reactor systems is the formation of fouling deposits, which grow and block the reactor. To overcome this obstacle, knowledge of the mechanisms of the formation of fouling deposits is essential. In this thesis, fouling during the polymerization of N-Vinylpyrrolidone (NVP) in aqueous solution is studied both experimentally and in simulations to gain insight into the underlying mechanism, find a model-based description of this mechanism and make suggestions how to prevent or at least decrease the formation of fouling deposits.

First, results from experiments in different kinds of tank and tubular reactors are presented. In all these reactor systems, fouling deposits are formed by an insoluble polymer gel, which adheres strongly to metal surfaces. Initially, the polymer gel is formed in regions with increased local residence time, e.g. in dead-water zones of static mixer elements, at baffles of tank reactors or at walls of tubular reactors without mixer elements. Once fouling deposits have been formed, they grow by reaction and lead to clogging of tubular reactors systems.

Since a polymer gel is formed, side reactions that lead to high-molecular and branched polymer chains must play an important role for the formation of deposits. Kinetic models that are based on a recently suggested reaction mechanism and predict microstructural property distribution are presented and validated using continuously stirred tank reactor

(CSTR) experiments. The results confirm the suggested reaction mechanism in which creation and propagation of terminal double bonds lead to branched or crosslinked polymer chains. Although gelation of the bulk phase does not occur, fouling deposits are formed at the baffles of the tank reactor and in other poorly mixed regions of the reactor. This observation emphasizes the importance of the flow pattern and diffusive mass transport for the formation of fouling deposits.

To demonstrate the interplay of the flow pattern, the reaction and diffusive mass transport, simulations using a transient CFD solver including a reduced version of the reaction kinetics model together with a model for diffusive mass transport are presented. The mass transport model is able to describe diffusive transport of statistical moments and is, therefore, consistent with the reaction kinetics model. Simulations in different two-dimensional geometries confirm that regions with increased local residence time lead to the formation of polymer gels. These regions, e.g. regions close to reactor walls or dead-water zones, cause concentration gradients, which induce mass transport between such regions and the bulk phase. Due to their lower diffusion coefficients in comparison to low molecular species, polymer molecules accumulate in these regions, which increases the viscosity locally. Because of the viscosity gradients, the flow pattern is distorted and the size of regions with increased residence time expands. The combination of an increased residence time, high polymer and low monomer contents promotes the formation of polymer gels by side reactions.

Together with the adhesion of macromolecules on metal surfaces, this seems to be the relevant mechanism for the formation of fouling deposits. Therefore, strategies to decrease fouling should focus on surface modifications, which reduce adhesion of macromolecules, as well as the elimination of dead-water zones and viscosity gradients.

List of abbreviations and symbols

Abbreviations

blockMesh	Meshing utility that is included in OpenFOAM®
CFD	Computational fluid dynamics
CODE	Countable ordinardy differential equations
CSTR	Continous stirred tank reactor
DNA	Deoxyribonucleic acid
DFT	Density functional theory
FEP	Fluorinated ethylene propylene polymer
FJC	Freely jointed chain
HPLC	High pressure liquid chromatography
MALS	Multi-angle light scattering
MWD	Molecular weight distribution
NaClO	Sodium hypochlorite
NVP	N-vinylpyrrolidone
PDE	Partial differential equation
PLP-SEC	Pulsed laser polymerization - size exclusion chromatography
PVP	Polyvinylpyrrolidone
RI	Refractive index
SEC	Size exclusion chromatography
snappyHexMesh	Meshing utility that is included in OpenFOAM®

TDB	Terminal double bond
UV	Ultraviolet

Latin letters

$\boldsymbol{A}$	Coefficient matrix in the finite volume method
$A_{0/1/2}$	Model parameters of the TDB reduced moment model
A_{in}	Inlet area
$\boldsymbol{B}$	Maxwell-Stefan diffusion matrix
$\boldsymbol{B}^C$	Maxwell-Stefan diffusion matrix times c
B_2	Model parameter of the TDB reduced moment model
B_{ij}	Elements of the Maxwell-Stefan diffusion matrix
B_{ij}^N	Alternative form of the elements of the Maxwell-Stefan diffusion matrix
B_{ij}^v	Alternative form of the elements of the Maxwell-Stefan diffusion matrix
c^B	Overall concentration of branches
c^{TDB}	Overall concentration of TDBs
c_j	Concentration of species j
C_η	Model parameter of the model for the relative viscosity
C_{r_i}	Relative change of the concentration if species i per time step in the CFD algorithm
$c_{T,in/out}^{sim/exp}$	Simulated/experimental concentration of the tracer species in residence time investigations at the reactor inlet/outlet

Co	Courant number
D	Diffusion coefficient
D'	TDB dispersity
$\boldsymbol{D}^F$	Fickian type diffusion matrix
$\mathfrak{D}_0$	Maxwell-Stefan diffusion coefficient two low molecular species
$\boldsymbol{d}_c$	Distance vector between cell centers in the finite volume method
D_{disp}	Dispersion coefficient
d_i	Inner diameter of the capillary tubular reactor
$\boldsymbol{d}_i$	Driving force for species i in Maxwell-Stefan diffusion model
$\mathfrak{D}_{ij}$	Maxwell-Stefan diffusion coefficient for species i and j
$D^F_{i,j}$	Elements of the Fickian type diffusion matrix
$\mathfrak{D}_P$	Maxwell-Stefan diffusion coefficient low molecular species and polymer species
D_{Taylor}	Taylor dispersion coefficient
D_T	Tracer diffusion coefficient
d_{wind}	Winding diameter of the capillary tubular reactor
D_{Zimm}	Zimm estimate of diffusion coefficient
De	Dean number
$\frac{dn}{d\rho_P}$	Refractive index increment
$E_{in/out}$	Residence time distribution and the reactor inlet/outlet
E_{lam}	Residence time distribution for laminar flow

E_{Taylor}	Residence time distribution in laminar flow with Taylor dispersion
F	Free energy
$\boldsymbol{f}(\boldsymbol{u}, t)$	Right-hand side in the Galerkin FEM method
f_d	Initiator efficiency in the reaction kinetic models
$f_{\Delta t}$	Time step safety factor in the CFD algorithm
$f_{tr,m}$	Ratio of the transfer to monomer and monomer propagation ratios in the reaction kinetic models
g	Branching ratio
g_3	Branching ratio for tri-functional branches
$\boldsymbol{H}$	H-operator in the finite volume method
H^B	Counter species for branches
H^{TDB}	Counter species for TDBs
$\boldsymbol{I}$	Identity matrix
I	Initiator radical
I_0/r^2	Intensity of the incident laser light of a MALS detector corrected for the distance from the detector r
I_2	Undissociated initiator
$i_{in/out}$	Electric current in the conductivity flow cell for residence time measurements and the reactor inlet/outlet
$I_{\Theta_{ls}}$	Intensity of scattered light at angle Θ of a MALS detector (sample)
$I_{\Theta_{ls},S}$	Intensity of scattered light at angle Θ of a MALS detector (pure solvent)
$\boldsymbol{J}(\boldsymbol{u}, t)$	Jacobian in the Galerkin FEM method

$\boldsymbol{J}_j^m$	Diffusive flux of species j in the barycentric frame of reference
$\boldsymbol{J}_j^N$	Diffusive flux of species j in the molar frame of reference
k_B	Boltzmann's constant
k_{cross}	Kinetic rate coefficient of a crosslinking reaction
k_d	Kinetic rate coefficient of the initiator dissociation reaction
K_{LS}	Light scattering detector index
k_p	Kinetic rate coefficient of the monomer propagation reaction
$k_{p,max}$	Maximum value of the kinetic rate coefficient of the monomer propagation reaction
$k_{p,TDB}$	Kinetic rate coefficient of the TDB propagation reaction
k_{RD}	Kinetic rate coefficient for reaction diffusion in the termination reaction
K_{RI}	RI detector constant
k_{SD}	Kinetic rate coefficient for segmental diffusion in the termination reaction
k_t	Kinetic rate coefficient of the termination reaction
$k_{t,c}$	Kinetic rate coefficient of the termination by combination reaction
$k_{t,d}$	Kinetic rate coefficient of the termination by disproportionation reaction
k_{TD}	Kinetic rate coefficient for translational diffusion in the termination reaction
$k_{tr,m}$	Kinetic rate coefficient of the transfer to monomer reaction
$k_{tr,p}$	Kinetic rate coefficient of the transfer to polymer reaction

L	Length
L_c	Cell size in CFD simulations
l_K	Kuhn length
M	Monomer
m	Number of branches
$\dot{m}_F$	Feed mass flow rate
$\overline{M_n}$	Number average molecular weight
$\overline{M_w}$	Weight average molecular weight
$\overline{M_w}^{spline}$	Weight average molecular weight from spline approximation
$\overline{M_z}$	z-average of the molecular weight
MW_i	Molecular weight of species i
N	Number of repeat units
$\boldsymbol{n}$	Normal vector
n	Refractive index
n_0^B	Number of branches per molecule
n_1^B	Number of branches per repeat unit
N_A	Avogadro's number
N_K	Number of Kuhn monomers
$\overline{N_n}$	Number average chain length
N_T^0	Normalization constant for the tracer residence time distribution
$n_{T,in}^{exp/sim}$	Number of injected tracer molecules in experiments/simulations

$\overline{N_w}$	Weight average chain length
$\overline{N_z}$	z-average of the chain length
P	Polymer
p	Pressure
$p_{0/1/2}(n)$	Number of TDBs in chains of length n
$P_{n,i,k}$	Concentration of polymer chains with zero radical centers, n repeat units i TDBs and k branches
$P(s, j_1, \dots, j_N)$ $= P_{s,j_1,\dots,j_N}$	Concentration distribution of chain length s and additional properties $j_1, \dots, j_N$
$p_{SEC}(s)$	SEC distribution of chain lengths
Pe_{Taylor}	Peclet number in a reactor with laminar flow and Taylor dispersion
$p_w(s)$	Distribution of chain lengths in term of weight fractions
R	Size of molecule or particle (no index) / ideal gas constant
$\boldsymbol{R}(\phi^t)$	Right-hand side in the finite volume method
$R(\Theta_{ls})$	Rayleigh ratio
R_c	Contour length of a polymer chain
$\boldsymbol{R}_{cm}$	Position vector of the center of mass of a polymer chain
R_e	End-to-end distance of a polymer chain
$\boldsymbol{R}_e$	End-to-end vector of a polymer chain
$\langle \boldsymbol{R}_e \rangle$	Ensemble average of the end-to-end vector of linear polymers
$\langle R_g^2 \rangle$	Ensemble average of the squared radius of gyration

$\overline{\langle R_g^2 \rangle_z}$	Ensemble average of the z-average of the squared radius of gyration
$\boldsymbol{r}_i$	Bond vector between Kuhn monomers
r_j^{total}	Overall reactor rate of all reaction that affect the concentration of species j
$R_{n,i,k}$	Concentration of polymer chains with one radical center, n repeat units i TDBs and k branches
R_{reac}	Reactor radius
$\boldsymbol{R}_s$	Position vector of the with index s of a polymer chain
Re	Reynoldsnumber
S	Solvent
S_c	Surface of control volume V_c
$\boldsymbol{S}_f$	Face area vector of face f in the finite volume method
s_{max}	Maximum chain length in Galerkin FEM solver
S_{RI}	RI detector signal
T	temperature
t	Time
$\boldsymbol{u}(t)$	State vector in the Galerkin FEM method
V	Volume
$\boldsymbol{v}$	General velocity vector
v	Magnitude of a velocity vector
V^{elu}	Elution volume
$\boldsymbol{v}^m$	Barycentric velocity vector

$\boldsymbol{v}^N$	Molar velocity vector
V_c	Control volume / finite volume
$\boldsymbol{v}_i$	Overall velocity of species i
$\boldsymbol{v}_i^N$	Diffusion velocity of species i relative to molar average velocity $\boldsymbol{v}^N$
V_j	Volume that is occupied by species j
v_K	Excluded volume of a Kuhn monomer
V_{MALS}	Sample volume of MALS detector
w_j	Weight fraction of species j
x_j	Molar fraction of species j

Greek letters

Γ	Source term in the finite volume method
γ_i	Activity coefficient
ϵ_{mixer}	Empty volume mixer
ζ	Friction coefficient
η	Shear viscosity
Θ_{ls}	Scattering angle of light scattering detector
κ_S	Safety factor in Galerking finite element solver
$\lambda^{k,l}$	k–th chain length moment and l–th TDB moment of polymers with one radical center
Λ_i^k	k–th chain length moment (pseudo-) TDB (i) distribution of polymers with one radical center

λ_k^P	k-th chain length moment of the distribution P
λ_{ls}	Laser wave length of MALS detector
$\mu^{k,l}$	k–th chain length moment and l–th TDB moment of polymers with no radical center
M_i^k	k–th chain length moment (pseudo-) TDB (i) distribution of polymers with no radical center
μ_j	Chemical potential of species j
ρ	Overall mass density
ρ_j	Mass density of species j
ρ_s	Mass density of polymers with chain length s
$\boldsymbol{\tau}$	Viscous stress tensor
τ	Average residence time
$\tilde{\tau}$	Estimated average residence time
ν	Zimm growth law exponent
ϕ	Arbitrary scalar state variable
Φ_n^l	l–th TDB moment (pseudo-) chain length (n) distribution of polymers with one radical center
$\Psi_n^{l,o}$	l–th TDB moment (pseudo-) chain length n distribution of polymers with no radical center

Indices (high and low)

0	Reference state or inlet/initial condition
av	Average

br	Branched
$classes$	TDB classes model
f	Face value in CFD simulations
gs	Good solvent
in	Inlet
lin	Linear
loc	Local
M	Monomer
$mixer$	Static mixer-like geometry
out	Outlet
P	Polymer
PF	Plug Flow
$reac$	Reactor
rel	relative
S	Solvent
T	Tracer
Θ	Theta condition
x	x-direction
y	y-direction

1 Introduction

Fouling is the undesired deposition of material on solid surfaces, which alters their properties and influences the function of the associated apparatus [1], [2]. Important examples are fouling in heat exchangers or on membranes, which cause significant economic costs due to reduced heat transfer or permeability and increased pressure drop [3]. The origin of fouling deposits strongly depends on the process that is conducted in the apparatus. Typical reasons are crystallization, accumulation of solid particles or growth of bio organisms [2], [3]. Another important factor in chemical reactors, are side reactions that lead to the formation of insoluble byproducts, which accumulate on the reactor surfaces. This is especially important in small scale micro- or milli-reactor systems with a large volume-specific surface area [4]. Such reactors are in the focus for process intensification for specialty and fine chemicals, e.g. certain polymer products, which are mostly produced in batch and semibatch processes today [5]. The formation of fouling impedes the transfer from discontinuously operated reactors to continuously operated small scale reactor systems [5], [6], which was the motivation to systematically investigate fouling during polymerization reactions in this thesis. The goal of this theses is to generate deeper knowledge of the underlying processes that cause fouling and find a model-based description of the latter to support the development of reactor systems and process variants with decreased fouling susceptibility. In this chapter, an overview of studies on fouling during polymerization reactions will be given in Section 1.1. Their results will then be summarized in Section 1.2 and the scope of this thesis will be set.

1.1 Literature review on fouling in polymerization reactors

Many studies on fouling in polymerization reactors have been conducted for heterogeneous systems, e.g. suspension and emulsion polymerization [7]–[15], while fouling during polymerization in (initially) homogeneous phase, e.g. in solution or bulk [5], [16]–[19], has been investigated less often. Fouling is mostly described as a problem that occurs during process development and is circumvented somehow, e.g. by changing feed concentrations [5]. Only a few authors have tackled the problem of fouling in polymerization reactors systematically [9], [11], [14], [17], [19].

For heterogeneous systems two main mechanism have been proposed as the source of fouling deposits [7], [10]: the adsorption of polymer particles and agglomerates of the latter, which are formed in the bulk phase, on surfaces and the adsorption of monomers and radicals that polymerize in a layer at the surface. Therefore, the stability of the emulsion plays a crucial role and temperature, the concentration of electrolytes and emulsifier as well as the solid content influence fouling [8], [13]. Very low as well as very high impeller speeds in tank reactors have also been reported to increase fouling due to Brownian [8] or shear induced coagulation [12], [15] respectively. From detailed investigations of the flow pattern in the reactor system, it was suggested that deposits most likely occur in regions with slow fluid velocities [10]. Another important factor are the properties of reactor surfaces. While repulsive potentials between polymer particles and the reactor surface have shown to decrease the amount of fouling deposits [10], attractive interactions as well as higher surface roughness may increase fouling significantly [10], [11]. Especially in emulsion polymerization, polymers and macroradicals that are produced in the continuous phase may adsorb on reactor surfaces and initiate the formation of deposits [10]. Of course, this phenomenon is even more important for the formation of fouling deposits in solution polymerization. In [5], the polymerization of acrylic acid in aqueous solution in static mixer

heat-exchanger reactors was investigated and polymer gel deposits were observed. The authors suggested that the combination of different processes, including side reactions, which lead to crosslinked polymers, together with non-ideal mixing in dead-water zones and adsorption of polymers on reactor surfaces is the reason for the formation of fouling deposits. Especially, recipes that lead to high-molecular polymer chains were found to produce fouling deposits. Similar observations were reported for the polymerization of N-Vinylpyrrolidone (NVP) in aqueous solution in [6]. A systematic investigation of the influence of surface properties on the formation of deposits in the polymerization of NVP in aqueous solution [17] underlined the importance of the surface energy of reactor walls: hydrophobic surfaces reduce the formation of fouling layers in aqueous solution significantly, while no significant influence of the microscopic surface roughness was reported. It must be noted, though, that the experiments in [17] were carried out in batch operation and the fouling layers, which were dried on the surface, could be dissolved again. In [5], the formation of gel like deposits was only reported to occur in continuous operation mode for high molecular systems and not in batch mode. The importance of the flow pattern for the formation of fouling deposits in initially homogeneous systems was highlighted in a study on tubular reactors for the production of polyethylene, which suggests that the formation of a highly viscous boundary layer is characteristic for systems in which fouling occurs [19], [20]. Similar results have been reported for the polymerization in solution [6], [16], [21]. Especially in [6], in which residence time measurements in a tubular reactor during the polymerization of NVP in aqueous solution suggested that a wall layer is formed during the reaction. The micro-mixing efficiency for mixing of the educts has been suggested as another factor, which influences the formation of fouling deposits in [6]. This observation is contradictory to [5] in which improved mixing by including micro-mixers did not lead to any effect on the formation of fouling deposits. In low-density polyethylene

production a phase separation due to temperature gradients in the reactor was also reported as an important part in the fouling mechanism [22].

Based on these observations different strategies to reduce fouling in polymerization reactors have been suggested. Popular examples are pulsed flow [23], using hydrophobic surfaces [24], [25] or adding anti-fouling agents, which inhibit polymerization on reactor walls [9].

1.2 Scope of this thesis

From the observations that have been described in the preceding section, three main factors that influence the formation of fouling deposits in solution polymerization and are closely connected can be identified as illustrated in Figure 1.

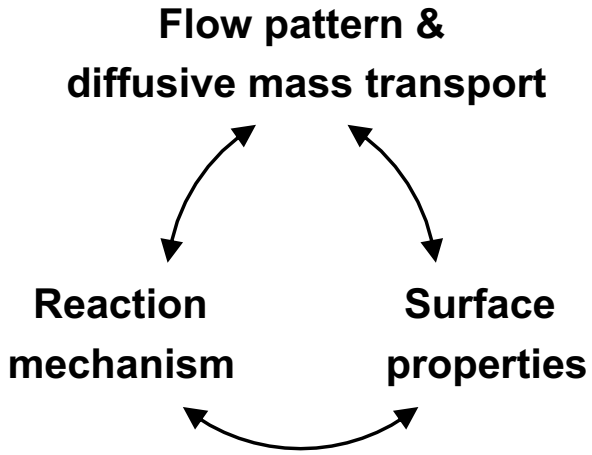

Figure 1. Main factors that influence fouling in polymerization reactors for solution polymerization.

Reactions that lead to high-molecular, branched or crosslinked polymer chains may cause the formation of an insoluble polymer gel [26]. The rates of these reactions strongly depend on the composition of the reaction mixture and local mixing, which is determined by the flow pattern and diffusive mass transport in the reactor system. For example, dead-water

zones or boundary layers increase the local residence time and cause mixing of products with fresh reaction mixture. The adsorption of polymer molecules on surfaces is essential for the formation of deposits, which is enhanced by attractive interaction between the polymer and the wall material. Adsorbed chains may still take part in side reactions, which causes the deposit layer to grow in the course of the reaction.

In this thesis, the mechanism of the formation of fouling deposits will be examined in detail using the example of the homo-polymerization of NVP in solution. As mentioned before, this system has shown to be susceptible to fouling in continuously operated reactors and is of industrial interest. In Chapter 2, the theoretical background and methods that are used in following chapters will be introduced. In Chapter 3, experimental observations with emphasize on fouling in different reactor systems will be presented and compared to the observations in literature that have been described in this chapter. From these observations, a hypothesis on the fouling mechanism during the polymerization of NVP will be made. This hypothesis will be tested in the following chapters in which the interplay of the main influencing factors that have been identified in Chapter 3 will be discussed using different simulation and modeling strategies. The focus of Chapter 4 is on the reaction mechanism of the polymerization of NVP and new reaction kinetic models will be presented. In Chapter 5, the interplay of the flow pattern, diffusive mass transport and the reaction mechanism will be discussed using CFD simulations. Finally, the results will be concluded in Chapter 6 and approaches to prevent fouling and suggestions for future work will be given.

2 Theoretical background and methods

In this chapter, the theoretical background of different methods that are used in this thesis will be outlined and the methods themselves will be described with emphasize on the aspects that are relevant for following chapters. The goal is not to give a comprehensive overview, but to provide the reader with a basic understanding of these methods. In Section 2.1 and Section 2.2, important characteristics of polymers in solution as well as analytical methods for their characterization will be discussed. In Section 2.3, modelling and solution strategies for reaction kinetics of polyreactions will be outlined and the finite volume method, which has been used for CFD simulations, will be summarized in Section 2.4.

2.1 Characteristics and physical properties of polymers in solution

Polymer systems do not consist of molecules that have the same chemical structure but are characterized by discrete microstructural property distributions, which determine the macroscopic properties. The most important one is the distribution of molecular weights or chain lengths $P(s)$, which gives the concentration of chains with s repeat units. Since molar concentrations of different species are involved, this distribution – usually referred to as the concentration or frequency distribution – can be obtained from a kinetic simulation of a polymer system. Other representations of the same distribution in terms of the weight of polymer chains [27]

$$p_w(s) = sP(s)MW_M \tag{1}$$

with the molecular weight of a repeat unit MW_M in case of homo-polymerization, which is considered in this thesis, may be convenient. Especially, if a comparison to experimental results is desired, the so-called SEC distribution

$$p_{SEC}(s) = s^2P(s)(MW_M)^2 \tag{2}$$

allows a comparison of simulations to results from size exclusion chromatography (SEC) measurements [27]. Of course, not only the chain length but other microstructural properties as for example the distribution of branches or end groups influence the macroscopic properties of the product and a multi-dimensional distribution $P(s, j_1, \dots, j_N)$ with the additional properties $j_1, \dots, j_N$ would have to be considered in general. The complexity of the problem increases significantly and usually some kind of averaging is used to reduce the amount of information. An important method to do so is the method of moments, which will be outlined in the next section for the case in which s is the only structural property of interest.

2.1.1 Molecular weight averages

The key to average properties of polymer systems are the statistical moments of the discrete property distribution $P(s)$

$$\lambda_k^P = \sum_{s=1}^{\infty} s^k P(s) \tag{3}$$

with the k-th moment λ_k^P of the distribution $P(s)$. The zeroth moment is the overall molar concentration of polymers of population P and the first moment is the overall molar concentration of repeat units that are polymerized in population P. Higher moments do

not have an intuitive physical interpretation but are used to define other average quantities. Important examples are the molecular weight averages

$$\overline{M_n} = \frac{\lambda_1^P}{\lambda_0^P} MW_M = \overline{N_n} MW_M \ , \tag{4}$$

$$\overline{M_w} = \frac{\lambda_2^P}{\lambda_1^P} MW_M = \overline{N_w} MW_M \ , \tag{5}$$

$$\overline{M_z} = \frac{\lambda_3^P}{\lambda_2^P} MW_M = \overline{M_z} MW_M \ . \tag{6}$$

$\overline{N_n}$ is the molar fraction weighted average of repeat units in chains of population P and $\overline{M_n}$ the corresponding molecular weight average. $\overline{N_w}$ and $\overline{M_w}$ are averages that are weighted with mass fractions and $\overline{N_z}$ and $\overline{M_z}$ are the so-called z-averages. These definitions may of course also be applied on moments of other properties as will be done in following sections.

2.1.2 Radius of gyration

A common quantity to measure the size of polymer molecules is the radius of gyration R_g, which is defined by [28]

$$\langle R_g^2 \rangle = \frac{1}{N} \left\langle \sum_s^N (\boldsymbol{R}_s - \boldsymbol{R}_{cm})^2 \right\rangle \tag{7}$$

with the number of repeat units N in the polymer chain. $\boldsymbol{R}_s$ is the position vector of repeat unit s and $\boldsymbol{R}_{cm}$ is the position vector of the center of mass (cm) of the polymer chain. These vectors are illustrated in Figure 2. Brackets denote ensemble averages over all possible configurations.

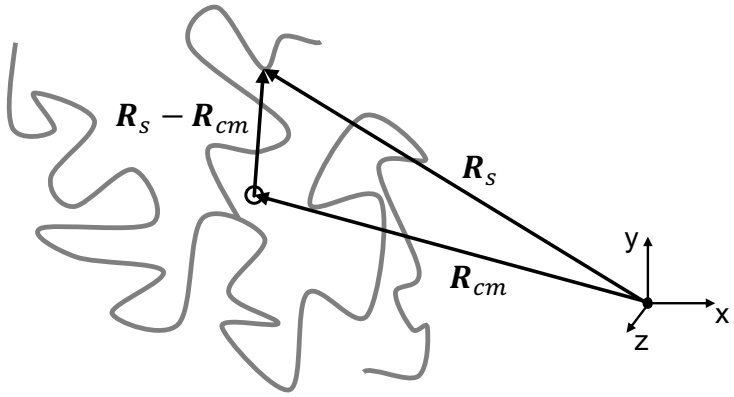

Figure 2. Illustration of the vectors that are used for the calculation of the radius of gyration R_g (based on [28]). Gray lines symbolize the polymer chain, the unfilled circle symbolizes the center of mass (cm).

This definition applies to linear as well as to branched polymer chains. The radius of gyration is related to N by a power law [28]

$$R_g = \sqrt{\langle R_g^2 \rangle} \sim N^{\nu} \tag{8}$$

for polymers in dilute solutions. The exponent ν may take different values depending on the solvent and molecular architecture. For linear chains in a good solvent, values of $\nu = 0.6$ and $\nu = 0.5$ for chains in theta (Θ) solvents[1] are the theoretical values [28]. Since a branched polymer chain with N repeat units will be more compact than a linear chain with N repeat units, the branched chain has a lower radius of gyration. This fact can be used to characterize the degree of branching. Zimm and Stockmayer defined the branching ratio [29]

[1]In theta (Θ) solvents, attractive and repulsive interactions between monomers cancel each other out and the chain behaves ideally [28].

$$g = \frac{\langle R_g^2 \rangle_{br}}{\langle R_g^2 \rangle_{lin}} \tag{9}$$

in which the index *br* and *lin* denote the squared radius of gyration of a branched and a linear chain with the same number of repeat units N. For chains with trifunctional (index 3, e.g. Figure 2) branches, they related g to the number of branches m by

$$g_3 = \left[\left(1 + \frac{m}{7}\right)^{\frac{1}{2}} + \frac{4m}{9\pi} \right]^{-\frac{1}{2}}. \tag{10}$$

The radius of gyration and method of Zimm and Stockmayer will be used in Section 4.3.3 to characterize branching experimentally using size exclusion chromatography (SEC). The combination of these methods will be explained in Section 2.2.2 in more detail.

2.1.3 Coarse-grained models for polymers in solution

Many properties of polymers can be described on a coarse-grained level without considering the large number of degrees of freedom on the atomistic level explicitly, e.g. positions of atoms or repeat units as well as torsion angles etc. An important theoretical concept is the freely jointed chain (FJC), which consists of so-called Kuhn monomers and has a backbone or contour length

$$R_c = N_K l_K \tag{11}$$

with the number of Kuhn monomers N_K and the Kuhn length l_K. Beyond the Kuhn length, the movement of chemical monomers is uncorrelated, and the FJC behaves as a flexible chain with freely rotating bonds. The behavior of many real polymer systems can be described by an equivalent FJC with the Kuhn length depending on the local stiffness and the chemical structure of the real polymer [28]. Typical values for Kuhn lengths range from ~10 Å for flexible vinyl polymers [28] to ~500 Å for a more rigid double-stranded

DNA molecule [30]. Based on this concept, models for transport properties, e.g. the diffusion coefficient of polymer chains, can be can developed. The ideas behind such models will be outlined in the following and the Zimm model, which will be used in Chapter 5 will be explained.

Neglecting any interactions between Kuhn monomers, the free energy of an ideal, linear FJC [28]

$$F(N_K, \boldsymbol{R}_e) = \frac{3}{2} kT \frac{\boldsymbol{R}_e^2}{N_K l_K^2} + F(N_K, \mathbf{0}) \tag{12}$$

depends on the number of Kuhn monomers and their configuration that is characterized by the end-to-end vector $\boldsymbol{R}_e$. In Equation (12), k is the Boltzmann constant and T is the temperature. The first term is the entropic contribution due to the elongation of the chain and the latter is a reference value for the equilibrium end-to-end distance $\langle \boldsymbol{R}_e \rangle = \mathbf{0}$. The definition of the free energy in Equation (12) neglects any interaction between different Kuhn monomers in the polymer chain, which is only valid for Θ–conditions in which repulsive and attractive interactions cancel each other out. Another important concept is that of a good solvent in which the polymer chain is swollen in solvent and repulsive interaction due to excluded volume effects must be considered. In this case the free energy can be estimated by the Flory theory as [28]

$$F(N_K, R_e) \approx kT \left(v_K \frac{N_K^2}{R_e^3} + \frac{R_e^2}{N_K l_K^2} \right) \tag{13}$$

with $R_e = |\boldsymbol{R}_e|$ and v_K is the excluded volume of a Kuhn monomer. The equilibrium size of the molecule in this approximation minimizes the free energy and can be found to be

$$R_{e,gs} \approx v_K^{1/5} l_K^{2/5} N_K^{3/5} \ . \tag{14}$$

For Θ–conditions, i.e. for an ideal FJC, the root mean squared end-to-end distance is simply [28]

$$R_{e,\Theta} = l_K N_K^{1/2} \ . \tag{15}$$

For linear polymer chains $R_e \sim R_g$, which leads to the scaling laws in Section 2.1.2. For linear polymer chains, the polymer size R may be defined either by the root mean squared end-to-end radius or radius of gyration.

If a polymer molecule or particle of size R moves in a solvent with the viscosity η_S, the surrounding solvent molecules exert a drag force, which is characterized by the friction coefficient [28]

$$\zeta \sim \eta_S R \ . \tag{16}$$

Inserting Equation (16) into the Einstein relation [31] gives an estimate for the diffusion coefficient

$$D \sim \frac{kT}{\eta_S R} \tag{17}$$

of the particle and can be combined with an appropriate scaling law for the particle size to obtain an estimate for the polymer diffusion coefficient. Using Equation (14) yields the Zimm model for the diffusion coefficient of unentangled polymers in dilute solution [28]

$$D_{Zimm} \sim \frac{kT}{\eta_S N^{\nu}} \ . \tag{18}$$

with $\nu = 0.6$. The Zimm model and the Einstein relation will be used in Chapter 5 to get a rough estimate of the effect of viscosity and chain length on diffusion coefficients.

2.2 Size exclusion chromatography (SEC)

Size exclusion chromatography (SEC) is one of the most common techniques to obtain information on the molecular weight distribution (MWD) of polymers experimentally. A diluted sample of the polymer probe is injected into a stream of the so-called eluent and transported to a chromatographic separation system consisting of one or more separation columns. The packed bed columns are filled with a swollen polymer gel with pores of different sizes in which the macromolecules in the sample may or may not enter by diffusion depending on their size. By proper choice of the eluent's composition and the addition of salt, any effective attractive interaction of the sample and column material can be eliminated, and the separation mechanism is purely by size [32]. Large molecules with high molecular weight will elute first, while the smallest molecules can enter all pores and elute last. Thus, a classification of the sample is achieved, if the pore distribution of the column bed covers the full range of hydrodynamic volumes that are contained in the sample. To characterize the polymers in each chromatographic slice, the eluent stream passes different concentration and molar mass sensitive detectors from which's data the MWD can be constructed. If absolute MWDs and branching analysis are desired, a combination of a concentration sensitive detector and a multi-angle light scattering (MALS) detector is the setup of choice [32], which will be outlined subsequently.

As concentration sensitive detectors, systems that measure the refractive index (RI) or ultraviolet (UV) light adsorption are usually employed. Since many polymer systems are not UV active, most SEC systems are equipped with an RI detector which's output signal is

$$S_{RI} = K_{RI} \frac{dn}{d\rho_P} \rho_P \ . \tag{19}$$

In Equation (19), $dn/d\rho_P$ is the change of the refractive index with increasing polymer mass concentration ρ_P[2] and K_{RI} is the detector constant, which must be calibrated. If the system is properly calibrated and the refractive index increment $dn/d\rho_P$ is known, the mass concentration ρ_P in each chromatographic slice can be measured via the RI detector. If standards with known molecular weight of the system of interest exist, a calibration curve can be generated from measurements of standard samples, and the real or absolute MWD can be obtained. If this is not the case, only information relative to the calibration standards is accessible and a molar mass sensitive detector needs to be integrated into the system to measure the absolute MWD.

The most general way to obtain absolute MWDs is to use static light scattering detectors in combination with concentration sensitive detectors. A laser beam with a specific wavelength λ_{ls} passes through the flow cell of the light scattering detector in which the sample is injected. The laser light is scattered at the macromolecules or particles and its intensity at different angles is detected and averaged over time. If the size of the polymer is smaller than $\sim \frac{\lambda_{ls}}{20}$ the polymer behaves as a point scatterer and no angular dependence of the scattered light intensity can be observed [32]. The scattering intensity is characterized by the so-called Rayleigh ratio [32]

[2] In SEC literature c is used for the mass concentration of the sample. Here, ρ_P has been used to avoid conflict with die molar density in later chapters.

$$R(\Theta_{ls}) = \frac{(I_{\Theta_{ls}} - I_{\Theta_{ls},S})r^2}{I_0 V_{MALS}} \,. \tag{20}$$

$I_{\Theta_{ls}}$ and $I_{\Theta_{ls},S}$ are the intensities of the light that is scattered at angle Θ_{ls} of the MALS detector for the sample and the pure solvent respectively. I_0/r^2 is the intensity of the incident laser light corrected for the distance from the detector r [28] and V_{MALS} is the volume of the sample. For dilute, polydisperse samples and small scattering angles [32]

$$\lim_{\rho_P \to 0} R(\Theta_{ls}) = K_{LS} \sum_s \rho_{P(s)} \, MW_{P(s)} \tag{21}$$

with the optical constant of the detector

$$K_{LS} = \frac{4\pi n^2}{{\lambda_{ls}}^4 N_A} \left(\frac{dn}{d\rho_P}\right)^2 . \tag{22}$$

In Equation (21) and Equation (22), n is the refractive index of the eluent, λ_{ls} is the laser wave length, N_A is the Avogadro number, $\rho_{P(s)}$ is the mass concentrations of polymers with chain length s and $MW_{P(s)}$ their molecular weight. Since $dn/d\rho_P$ enters to the power of 2, very precise knowledge of the latter is necessary to obtain accurate results. Since

$$\sum_s \rho_{P(s)} \, MW_{P(s)} = \rho \overline{M_w} \,, \tag{23}$$

the weight average molecular weight $\overline{M_w}$ average is obtained by static light scattering in case of a polydisperse sample [28]. Since the separation on SEC columns is not ideal, this also applies to each chromatographic slice in SEC measurements.

In case of an isotropic scatterer, $\overline{M_w}$ can be obtained directly by rearranging Equation (21) to

$$\lim_{\rho_P \to 0} \frac{K_{LS} \rho_P}{R(\Theta_{ls})} = \frac{1}{\overline{M_w}} \,. \tag{24}$$

If the molecule is larger than $\sim \frac{\lambda_{ls}}{20}$, multiple scattering centers exist and interference of the scattered light leads to an angular dependence and, therefore, anisotropic scattering. The angular dependence can be approximated by a form factor leading to [28]

$$\lim_{\rho_P \to 0} \frac{K_{LS}\ \rho_P}{R(\Theta_{ls})} = \frac{1}{\overline{M_w}} \left(1 + 16\pi^2 \frac{\overline{\langle R_g^2 \rangle_z}}{\lambda_{ls}^2} \sin\left(\frac{\Theta_{ls}}{2}\right)^2 \right) \tag{25}$$

in which $\overline{\langle R_g^2 \rangle_z}$ is the z-average of the squared radius of gyration. By collecting data from different scattering angles, $\overline{M_w}$ can be obtained by plotting Equation (25) against $\sin\left(\frac{\Theta_{ls}}{2}\right)^2$ and extrapolation to zero angle and $\overline{\langle R_g^2 \rangle_z}$ can be obtained from the angular dependence. This procedure is referred to as the Zimm plot or method [28], [32] and a polynomial fit – usually linear for small to medium sized particles – is used. For polydisperse samples with broad MWDs and larger molecules, linearity of the angular dependence is not always true. Since the Zimm method tends to overestimate the slope especially for systems in which branching occurs, plotting

$$\lim_{\rho_P \to 0} \left(\frac{K \left(\frac{dn}{d\rho_P}\right)^2 \rho_P}{R(\Theta_{ls})} \right)^{0.5} = \left(\frac{1}{\overline{M_w}} \left(1 + 16\pi^2 \frac{\overline{\langle R_g^2 \rangle_z}}{{\lambda_{ls}}^2} \sin\left(\frac{\Theta_{ls}}{2}\right)^2 \right) \right)^{0.5} \tag{26}$$

should be preferred in this case [32]. This procedure is referred to as the Berry method and gives better results over a broad range of molecular weights. Because of the angular dependence, a multi-angle detector is necessary to obtain $\overline{M_w}$ of samples with large molecules accurately, while single angle detectors are sufficient in the case of isotropic scatterers.

2.2.1 Molecular weight distributions and averages from SEC data

By employing concentration and molar mass sensitive detectors, the mass concentration ρ_P and the weight average molecular weight $\overline{M_w}$ can be measured as a function of time or more commonly as a function of eluent volume V^{elu} that has eluted from the SEC system. Of course, such elugrams depend on the SEC setup and for comparison the data needs to be converted into a form that is independent of the separation system [28].

First, the weight fraction w in every chromatographic slice V_i^{elu} is determined by renormalizing $\rho_P(V_i^{elu})$ to

$$w(V_i^{elu}) = \frac{\rho_P(V_i^{elu})}{\sum_i \rho_P(V_i^{elu})} \ , \tag{27}$$

which can be converted to a function of molecular weight $w(MW_i)$ or $w(logMW_i)$ using the calibration curve $MW(V_i^{elu})$ or its logarithmic version $logMW(V_i^{elu})$. Usually the logarithmic version is used, and the collected data is represented by a polynomial. The two distributions are related by

$$w(logMW_i) = -w(V_i^{elu}) \ \frac{dV_i^{elu}}{dlogMW_i} \tag{28}$$

in which a correction for the nonlinearity of $logMW(V_i^{elu})$ has been performed. The negative sign comes from the fact that the molecular weight decreases with increasing eluted volume [28]. $w(logMW_i)$ is proportional to p_{SEC} defined in section 2.1.1 [27].

The molecular weight averages can be determined directly from the measured concentrations $\rho_P(V_i^{elu}) = \rho_{P,i}$ and $MW(V_i^{elu}) = MW_i$ by

$$\overline{M_n} = \frac{\sum_i \rho_{P,i}}{\sum_i {\rho_{P,i}}/{MW_i}}, \tag{29}$$

$$\overline{M_w} = \frac{\sum_i \rho_{P,i} MW_i}{\sum_i \rho_{P,i}}, \tag{30}$$

$$\overline{M_z} = \frac{\sum_i \rho_{P,i} {MW_i}^2}{\sum_i \rho_{P,i} MW_i}. \tag{31}$$

It should be noted, that MW_i is the molecular weight that is determined by a molecular weight sensitive detector, which is actually the weight average molecular weight $\overline{M_w}$ for each chromatographic slice in case of non-ideal separation in the SEC system or dispersion in the detector systems. Thus, $\overline{M_w}$ is the most reliable average value that can be obtained from SEC measurements, while $\overline{M_n}$ and $\overline{M_z}$ can only be determined correctly by Equation (29) and (31) in case of monodispersity in every eluted volume [28]. All three averages are equivalent to the averages defined in Section 2.1.1 through statistical moments. The weight average molecular weight $\overline{M_w}$ and SEC distribution $w(logMW_i)$ from experiments in tank reactors will be compared to results from simulations in Section 4.3.

2.2.2 Identification of structural changes from SEC data

Since branched molecules have a smaller hydrodynamic volume compared to linear molecules because of their more compact structure, they will elute later from an SEC system due to the classification by size. If molecular weight sensitive detectors are used, this can be identified qualitatively by a shift in the measured calibration curve $logMW(V_i^{elu})$ compared to a linear or less branched reference sample of the same polymer. The effect is illustrated for different samples in Figure 3.

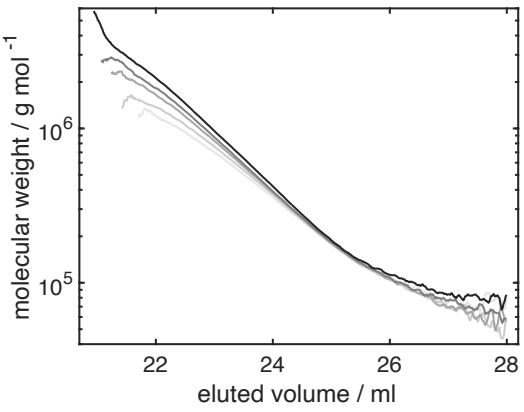

Figure 3. Measured calibration curve of different samples. Branching increases from light gray to black.

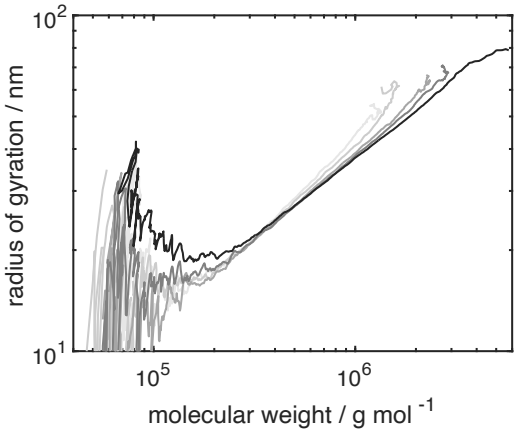

Figure 4. Conformation plot of different samples. Branching increases from light gray to black.

Using a MALS detector, the z-average of the radius auf gyration $\overline{\langle R_g^2 \rangle_z}$ can be obtained in addition to the weight average molecular $\overline{M_w}$ for every chromatographic slice leaving the SEC system as described before. Assuming monodisperse polymers systems in each chromatographic slice, these averages are the actual values of the polymer leaving the system at every eluted volume. As described in Section 2.1.2 the radius of gyration is related to the molecular weight through a power law of the form

$$R_g \sim MW^{\nu} \ . \tag{32}$$

If branched chains are present, a polymer with the same molecular weight as a corresponding linear chain will have a lower radius of gyration, which is a measure for the molecule's size. The growth law exponent of Equation (32) and, therefore, the slope in a double-logarithmic plot will decrease as shown in Figure 4. This offers another possibility to characterize topological changes experimentally and, if data for linear chains is available, the theory of Zimm and Stockmayer allows to estimate of the number of branches per

molecule from Equation (9) and Equation (10) as described in Section 2.1.2. This method will be used in Section 4.3.3 to characterize structural changes.

2.3 Kinetic modelling and simulation of polyreactions

As already mentioned, polymer systems are usually characterized by their microstructural property distribution $P(s, j_1, \ldots, j_N, t)$ with the time t as an independent continuous variable and the discrete property coordinates s and $j_1, \ldots, j_N$. The time evolution of such systems is described by a system of countable ordinary differential equations (CODE) [27]

$$\frac{dP_{s,j_1,\ldots,j_N}}{dt} = f(P_{s,j_1,\ldots,j_N}) \tag{33}$$

in which $P_{s,j_1,\ldots,j_N}$ is the common notation for $P(s, j_1, \ldots, j_N, t)$ taking the discrete property coordinates as indices and implying the time dependence. The right-hand side of Equation (33) contains source terms for reaction rates and transport terms depending on the reactor system and spatial dimension of the problem. Due to its dependence on discrete property variables, the system shows similarities to a discretized partial differential equation (PDE) but has a nearly full Jacobian, if reactions rates depend on all other property indices – which is mostly the case.

Generally, the discrete property coordinates may take values from 1 to ∞. In most problems, the properties $j_1, \ldots, j_N$ characterize, for example, the number of branches or the number of double bonds per molecule and usually range up to moderate values about 10^2. The chain length, which is characterized by the number of repeat units s, on the other hand, may range up to maximum values of order $s_{\max} \approx 10^8$. Thus, the CODE may become very large and sophisticated methods are needed to solve for the time evolution of $P_{s,j_1,\ldots,j_N}$. An overview of different methods, which have been proposed and applied in literature, is given in [27]. Here, only the two methods that are used in this thesis will be

presented. The finite element Galerkin method as implemented in PREDICI®, which can be used to solve for the evolution of property distributions at a reasonable computational effort, and the method of moments as a tool to reduce the computational effort of models, if average property information is sufficient, will be outlined in the next sections.

2.3.1 Method of moments

By using statistical moments as defined in Section 2.1.1, a much simpler system of equations can be derived. The cost is a loss of information, but the numerical effort can be reduced significantly. This is especially important, if the model is to be used in parameter estimations or CFD simulations. By applying the moment operator on Equation (33) a set of differential equations

$$\sum_{s}^{\infty} s^k \frac{dP_s}{dt} = \frac{d\lambda_k^P}{dt} = f(\lambda_0^P, \lambda_1^P, \dots, \lambda_k^P, \dots) \tag{34}$$

for the moments λ_k^P can be derived. Only a one-dimensional property distribution in a system with only one type of polymer population has been considered for simplicity, but the method can be applied on multiple property dimensions and populations. If the right-hand side depends on moments up to the k-th, a closed set of equations can be derived. This is only the case for a so-called linear polymerization in which reaction rates do not depend on a property index [26]. If reactions as for example crosslinking

$$R_r + P_s \xrightarrow{s \cdot k_{cross}} R_{r+s} \ , \tag{35}$$

which is proportional to the number of repeat units, are relevant, the system of equations cannot be closed since higher moments appear on the right-hand site of Equation (34):

$$\sum_{s}^{\infty} s^k \frac{dP_s}{dt} = \frac{d\lambda_k^P}{dt} += -\sum_{s}^{\infty} s^k \, sk_{cross} P_s \sum_{r}^{\infty} R_r = -k_{cross} \lambda_{k+1}^P \lambda_0^R. \tag{36}$$

As indicated by the += sign, only the additional part to the right-hand side of the differential equation for λ_k^P has been considered to demonstrate the idea. The latter case has been termed non-linear polymerization since the reaction rate is proportional to a property index [26]. Since the (k+1)-th moment appears, a closure relation that relates

$$\lambda_{k+1}^P = f(\lambda_0^P, \lambda_1^P, \ldots, \lambda_k^P) \tag{37}$$

is necessary. To derive such a relation, assumptions have to be made and the solution of the time evolution of the moments cannot be exact anymore, contrary to the case of a linear polymerization. Different closure relations have been suggested in literature and should be chosen depending on the reaction mechanism of the polymerization system [26]. The applicability of the closure relation should be validated carefully.

For a linear polymerization system, only moments up to the highest moment that is needed to calculate characteristic quantities have to be considered – for example the second moment of the chain length s, if the weight average molecular weight $\overline{M_w}$ is of interest. In case of a non-linear polymerization, the highest moment considered in the model must be chosen such that a closure relation can be found that does not significantly influence the results for the moments of interest [33].

2.3.2 Hp-Galerkin finite elements

If detailed information on the shape of $P_{s,j_1,\ldots,j_N}$ is desired, the CODE in Equation (33) has to be solved for all chain lengths and other property coordinates, which is infeasible for most realistic problems. Therefore, strategies to reduce the computational effort are necessary. An efficient method to do so is the Galerkin finite element method, which is

implemented in the commercially available software package PREDICI®. A general overview of the ideas behind the algorithm is given in [27] and more detailed information can be found in [34], [35]. Here, only a brief overview will be given to illustrate the idea behind the solution algorithm for a distribution P_s with one discrete property dimension.

The numerical effort is reduced by approximating the discrete distribution P_s piecewise by polynomials of order p on intervals h and limiting the chain length s to [35]

$$s_{max} = \frac{\lambda_1^P}{\lambda_0^P} + \kappa_S \sqrt{\frac{\lambda_2^P}{\lambda_0^P} + \left(\frac{\lambda_1^P}{\lambda_0^P}\right)^2} \tag{38}$$

based on the moments λ_k^P of P_s with the safety factor κ_S, which is chosen by the user. Starting from a state $\boldsymbol{u}(t)$, which includes all concentrations of low molecular species and polymers P_s and has been defined initially or originates from the previous time step, the initial grid for the approximation of P_s is coarsened by merging intervals and reducing the order of polynomials. Additionally, a new maximum chain length $s_{\max}$ as well as an appropriate time step size Δt are chosen. Based on these modifications an estimate of

$$\boldsymbol{u}(t + \Delta t) = \boldsymbol{u}(t) + \Delta \boldsymbol{u}_1 + \Delta \boldsymbol{u}_2 \ . \tag{39}$$

is calculated using the linear implicit Euler method with error correction (MEC) [27]. The increment $\Delta \boldsymbol{u}_1$ is calculated from the linear implicit Euler step

$$(\boldsymbol{I} - \Delta t \boldsymbol{J}(\boldsymbol{u}, t)) \Delta \boldsymbol{u}_1 = \Delta t \boldsymbol{f}(\boldsymbol{u}, t) \tag{40}$$

in which $\boldsymbol{f}(\boldsymbol{u}, t)$ is the right-hand side of Equation (33), $\boldsymbol{J}(\boldsymbol{u}, t)$ its Jacobian and $\boldsymbol{I}$ the identity matrix. The error correction $\Delta \boldsymbol{u}_2$ is calculated from

$$(\boldsymbol{I} - \Delta t \boldsymbol{J}(\boldsymbol{u}, t))\Delta \boldsymbol{u}_2 = -\frac{\Delta t}{2}\boldsymbol{J}(\boldsymbol{u}, t)\Delta \boldsymbol{u}_1. \tag{41}$$

Afterwards, the error of the discretization is estimated by comparing the results using different refinement levels of the approximation the discrete distribution P_s. If the error is above a tolerance level, the grid has to be refined further and a new estimate is calculated until the requirement is met. The objective of this procedure is to find an approximation of P_s that fulfills the error requirements while using the least number of intervals and the lowest order of polynomials possible. Since the numerical effort increases with the number of intervals and order of polynomials, this amounts to maximizing the accuracy of the representation specific to the computational effort [35]. The time step size is controlled using the error correction Δu_2 included in the MEC method.

Theoretically, an algorithm for more than one discrete property coordinate is possible but extremely complex and, therefore, not implemented in commercially available simulation packages. If systems with multi-dimensional property distributions are of interest, methods to transform the original problem into a series of one-dimensional problems are needed.

2.3.3 Model reduction using classes and pseudo distributions

The straightforward way is to solve for one dimension directly, e.g. the chain length, and define different populations – so-called classes – for the other discrete property coordinates, e.g. $P_{s,0}$ for all polymer chains without any branches, $P_{s,1}$ for polymer chains carrying one branch and so on for a two-dimensional distribution $P_{s,b}$ in which b characterizes the number of branches. A widely used application is to collect polymers with an active center, e.g. a radical center in a radical polymerization, in one class called the living species R and to define a second class called the dead species P for all polymers without an active center. Further classes can be defined if multiple radical centers need to be considered or

other property coordinates are of interest. An advantage of the classes approach is that a multi-dimensional distribution can be constructed from the concentration distributions of different classes. The downsides are that the numerical effort increases with every additional distribution used in the model and that a cutoff value must be defined for every property index that is considered as a class. Therefore, this approach should only be used if reasonable cutoff values are not too high, usually < 10 [35].

If this is not the case, another approach is to use so-called pseudo distributions [33], [36]. The pseudo distributions are defined as the moments of all discrete property coordinates except one – usually the chain length – which is solved for explicitly. Reconsidering the example from the previous paragraph,

$$\Phi_s^k = \sum_{b=0}^{\infty} b^k P_{s,b} \tag{42}$$

is k-th branching moment for chains of length s. The zeroth moment

$$\Phi_s^0 = P_s \tag{43}$$

is the concentration distribution and the first moment Φ_s^1 can be understood as a chain length distributed counter and gives the concentration of branches in chains of length s. Higher moments do not have an intuitive physical interpretation. The number of distributions in this kind of model is usually lower compared to the classes model that has been described before, since only the zeroth, first and second moments need to be considered in typical applications [33], [36]. If the system is non-linear in the second property coordinate b, a closure problem exists as discussed in Section 2.3.1 and an estimate for a higher moment of this property must be found by a suitable closure relation.

As long as suitable closure relations can be found, pseudo distribution models are preferable, since for many applications a large number of classes, e.g. >10, would have to be

used [33]. Both methods will be used in Chapter 4 to derive and validate reaction kinetics models for the polymerization of NVP.

2.4 Computational fluid dynamics simulation of reactive systems

The transport of physical properties such as linear momentum or densities of different species can be described by partial differential equations [37], [38]. For example, the transport equation of a scalar property ϕ, which may be the mass fraction of a diluted tracer component, is [39]

$$\frac{\partial}{\partial t}\rho\phi + \nabla \cdot \rho \boldsymbol{v}\phi - \nabla \cdot \rho D \nabla \phi = \Gamma(\phi). \tag{44}$$

The first term on the left-hand side describes the accumulation of ϕ per unit volume, the second and third terms describe convective transport with the velocity $\boldsymbol{v}$ and diffusive transport due to gradients of ϕ respectively. ρ is the overall mass density. Fick's law for diffusive transport of the diluted species with the diffusion coefficient D has been assumed [37] and the term on the right-hand side is a volumetric source term due to chemical reactions, for example.

2.4.1 The finite volume method

To solve this type equation numerically, a discretization procedure must be applied to transform the partial differential equation into a system of ordinary differential equations. For fluid dynamics problems, a popular method is to decompose the solution domain into discrete control volumes also referred to as cells, which are connected by flat surfaces, and to integrate Equation (44) over the cell volume V_c leading to

$$\int_{V_c} \frac{\partial}{\partial t} \rho\phi \, dV + \int_{V_c} \nabla \cdot \rho \boldsymbol{v} \phi \, dV - \int_{V_c} \nabla \cdot \rho D \nabla \phi \, dV = \int_{V_c} \Gamma(\phi) \, dV \ . \tag{45}$$

By applying the Gaussian theorem, Equation (45) can be rewritten as

$$\frac{\partial}{\partial t} \int_{V_c} \rho\phi \, dV + \oint_{S_c} \rho v \phi \cdot \boldsymbol{n} \, dS_c - \oint_{S_c} \rho D \nabla \phi \cdot \boldsymbol{n} \, dS_c = \int_{V_c} \Gamma(\phi) \, dV \tag{46}$$

with the infinitesimal surface element dS_c and the outward pointing normal vector $\boldsymbol{n}$ on the surface S_c of V_c. Since S_c consists of flat elements, the so-called faces f, surface integrals can be replaced by summation over the dot products of the value of the integrant at the face f and the face area vector $\boldsymbol{S}_f$. $\boldsymbol{S}_f$ has the direction of the normal vector $\boldsymbol{n}$ and the magnitude of the face area. Therefore, Equation (46) can be rewritten as

$$\left(\frac{\partial \rho\phi}{\partial t}\right)_{V_c} V_c + \sum_f \boldsymbol{S}_f \cdot (\rho \boldsymbol{v} \phi)_f - \sum_f \boldsymbol{S}_f \cdot (\rho D \nabla \phi)_f = (\Gamma(\phi))_{V_c} V_c \ . \tag{47}$$

The index V_c denotes average values in the control volume and the index f denotes average values at the faces. In the implementation used in this thesis, all variables are stored at the geometric center of V_c, which is referred to as a co-located grid. Thus, the face values must be determined by interpolation from the cell center values of neighboring cells. [39], [40]

The transport terms for convection and diffusion are usually rewritten as

$$\left(\frac{\partial \rho\phi}{\partial t}\right)_{V_c} V_c + \sum_f \boldsymbol{S}_f \cdot (\rho \boldsymbol{v})_f (\phi)_f - \sum_f (\rho D)_f \boldsymbol{S}_f \cdot (\nabla \phi)_f = (\Gamma(\phi))_{V_c} V_c \ . \tag{48}$$

$\boldsymbol{S}_f \cdot (\rho \boldsymbol{v})_f$ is called the face flux, which is evaluated while solving the incompressible momentum equation [40]. The face value $(\phi)_f$ can be obtained from linear interpolation between neighboring cell centers, which is called central differencing, and may lead to oscil-

lations of the solution in convection dominated problems [39]. A simple and stable approach to prevent this problem is to use the value of the upwind cell but comes at the cost of reduced accuracy. This method is only first order accurate and causes so-called numerical diffusion, which smears out the solution due to the truncation error [40]. Therefore, the centered scheme is usually combined with a flux limiter that reduces oscillations of the solution [39].

The diffusion term requires the evaluation of the gradient $(\nabla\phi)_f$ at the face f. If the mesh is orthogonal, i.e. the distance vector $\boldsymbol{d}_c$ between neighboring cell centers c_1 and c_2 and the face normal vector $\boldsymbol{n}$ are collinear,

$$\boldsymbol{S}_f \cdot (\nabla\phi)_f = |\boldsymbol{S}_f| \frac{(\phi_{c_1} - \phi_{c_2})}{|\boldsymbol{d}_c|} \tag{49}$$

can be evaluated using the values of ϕ at the cell centers c_1 and c_2. On non-orthogonal meshes, a correction has to be applied additionally. [40]

At faces that are part of a physical domain boundary, either the face value $(\phi)_f$ or the fluxes on f can be specified directly. The first approach is the implementation of a Dirichlet boundary condition, the second that of a Neumann boundary condition. Other types of boundary conditions may, of course, also be applied. [39], [40]

If the transient solution is of interest, Equation (48) needs to be integrated in time additionally, which gives

$$\begin{aligned} \int_t^{t+\Delta t} \left[\left(\frac{\partial \rho\phi}{\partial t} \right)_{V_c} V_c + \sum_f \boldsymbol{S}_f \cdot (\rho \boldsymbol{v}\phi)_f - \sum_f \boldsymbol{S}_f \cdot (\rho D \nabla\phi)_f \right] dt \\ = \int_t^{t+\Delta t} \left[(\Gamma(\phi))_{V_c} V_c \right] dt \end{aligned} \tag{50}$$

and can be rewritten as

$$\frac{(\rho\phi)_{V_c}{}^{t+\Delta t} - (\rho\phi)_{V_c}{}^{t}}{\Delta t} V_c + \sum_f \boldsymbol{S}_f \cdot (\rho \boldsymbol{v} \phi)_f^{t+\Delta t} - \sum_f \boldsymbol{S}_f \cdot (\rho D \nabla \phi)_f^{t+\Delta t} = \Gamma(\phi^{t+\Delta t}) V_c \tag{51}$$

by applying a simple finite difference approximation for the temporal derivative. In Equation (51) a choice of which time level is to be used for all other terms than the transient had to be made. Using the value at the new time level, as has been done here, is called the implicit or backward Euler method. This method is unconditionally stable but only first order accurate in time and, therefore, produces numerical diffusion, too [39]. Second order accuracy can be achieved by approximating the temporal derivative as [40]

$$\frac{\partial \rho\phi}{\partial t} = \frac{3\rho\phi(t+\Delta t) - 4\rho\phi(t) + \rho\phi(t-\Delta t)}{2\Delta t} , \tag{52}$$

for example. The latter method was applied in this thesis, but the simpler Euler method will be used as an example in this section due to the more compact form.

So far, no special attention has been paid to the treatment of the source term. If the source does not depend on ϕ, Equation (51) can simply be rearranged to

$$\frac{(\rho\phi)_{V_c}{}^{t+\Delta t}}{\Delta t} + \frac{1}{V_c} \sum_f \boldsymbol{S}_f \cdot (\rho \boldsymbol{v} \phi)_f^{t+\Delta t} - \frac{1}{V_c} \sum_f \boldsymbol{S}_f \cdot (\rho D \nabla \phi)_f^{t+\Delta t} = \frac{(\rho\phi)_{V_c}{}^{t}}{\Delta t} + \Gamma , \tag{53}$$

which leads to the system of linear equations

$$\boldsymbol{A} \phi^{t+\Delta t} = \boldsymbol{R}(\phi^t) . \tag{54}$$

The right-hand side $\boldsymbol{R}$ contains all constant terms and terms with information from the old time step. The coefficients of the matrix $\boldsymbol{A}$ result from terms, which include the values of $\phi^{t+\Delta t}$ at the new time step. Since the equation for each cell only involves the values of the neighboring cells, the system is sparse and can be solved efficiently using iterative solvers, as long as the matrix $\boldsymbol{A}$ is diagonal dominant to ensure convergence [39]. Care

must be taken, if source terms depend on ϕ and, especially, if the source terms are non-linear [40], e.g. when chemical reactions are included. To improve convergence in such situations, source terms are usually linearized as [39]

$$\Gamma(\phi) \approx \Gamma(\phi^*) + \left(\frac{\partial \Gamma}{\partial \phi}\right)^* (\phi - \phi^*) \tag{55}$$

with the value at the previous iteration ϕ^*. While terms involving only ϕ^* are treated explicitly and added to the right-hand side $\boldsymbol{R}$ of Equation (54), the term involving ϕ is handled differently depending on the sign of $\Gamma(\phi)$. Sinks have a negative sign and, consequently, a positive contribution to the main diagonal of the matrix $\boldsymbol{A}$, which improves its diagonal dominance and, therefore, the convergence behavior of iterative solvers. Vice versa, implicit treatment of sources would have a negative effect on convergence, which is why the latter are usually treated explicitly and added to the right-hand side $\boldsymbol{R}$.

2.4.2 Solution of the isothermal, incompressible Navier-Stokes equations

The goal of a computational fluid dynamics simulation is usually to calculate the velocity field in the specified geometry and possibly also the transport of other properties, e.g. the concentration of a tracer species as in the previous section. To obtain the velocity field, the linear momentum balance

$$\frac{\partial \rho \boldsymbol{v}}{\partial t} + \nabla \cdot \rho \boldsymbol{v}\boldsymbol{v} + \nabla \cdot \boldsymbol{\tau} = -\nabla p \tag{56}$$

and the mass balance

$$\frac{\partial \rho}{\partial t} + \nabla \cdot \rho \boldsymbol{v} = 0 \tag{57}$$

must be solved together to ensure the conservation of mass. In Equation (56), $\boldsymbol{\tau}$ is the viscous stress tensor, p is the pressure and effects from gravity have been neglected. For incompressible fluids with constant density, Equation (57) reduces to [37]

$$\nabla \cdot \boldsymbol{v} = 0 \tag{58}$$

and the momentum balance for Newtonian fluids can be written as [37]

$$\frac{\partial \rho \boldsymbol{v}}{\partial t} + \nabla \cdot \rho \boldsymbol{v}\boldsymbol{v} + \eta \nabla^2 \boldsymbol{v} = -\nabla p \ . \tag{59}$$

Equation (58) and Equation (59) are usually referred to as the incompressible Navier-Stokes equations for isothermal systems.

Equation (58) poses a constraint on the solution of the momentum balance Equation (59). To solve this problem, a so-called pressure Poisson equation is constructed and solved instead of Equation (58). The latter can be derived from a semi-discretized form of the momentum balance [40] and is usually solved sequentially with Equation (59) in a predictor-corrector scheme. This procedure is called PISO algorithm and was used in this thesis. More details on the algorithm and the solution strategy are given in Section A.2.4 of the appendix and Section 5.1.2.

3 Phenomenology of fouling during aqueous phase polymerization of N-vinylpyrrolidone

In this chapter, the fouling behavior during the aqueous phase polymerization of N-vinylpyrrolidone (NVP) in tank and tubular reactor systems will be discussed and compared to observations in literature. The purpose of this chapter is not to give a comprehensive, quantitative experimental analysis of fouling in this polymerization system but to corroborate the effect of the influencing factors that have been summarized in Section 1.2 and to motivate the detailed analysis of different phenomena in the following chapters.

There are only a few studies in literature that focus on fouling during polymerization of NVP. In [17], the formation of fouling layers was studied in tank reactors but only in batch operation mode. The fouling layers that occurred under these conditions were dried and characterized but could be dissolved in water again. These layers were most pronounced on metal or other hydrophilic surfaces, while low energy surfaces such as PTFE decreased the layer formation. In [6], the formation of fouling deposits, which could not be dissolved in water, in continuously operated reactors was reported. The focus was on static mixer heat exchanger reactors with different mixer geometry modifications. It was found that fouling deposits occurred initially in characteristic regions of mixer elements where the fluid velocity is low. The importance of side reactions under the reaction conditions in these dead-water zones was highlighted. Since these regions exist in all geometrical variations of static mixer elements that were studied in [6], the fouling behavior was similar for all of them. Additionally, experiments in tubular reactors were carried out to study the

effect of the laminar flow pattern. Residence time measurements during the reaction suggested that a wall layer is formed and influences the flow pattern. The results in [17] and [6] are in agreement with observations during a copolymerization of acrylic acid [5]. In [5], insoluble polymer gel deposits were observed in static mixer reactors but not in a batch reactor. A combination of side reactions, non-ideal mixing in dead-water zones and adsorption on surfaces was suggested to cause the formation of fouling deposits.

The experiments that will be presented in this chapter were conducted using the equipment from [6], which was adapted for the purposes of this thesis. In Section 3.1, results from static mixer heat exchanger reactors will be presented with emphasize on surface modifications, aging of the mixer element surfaces and the position of mixer elements in the reactor. Results of fouling in tank reactors in continuous and batch operation mode will be presented in Section 3.2 and the formation of wall layers and fouling deposits in tubular reactors without mixer elements will be discussed in Section 3.3. Finally, the results will be summarized and a hypothesis on the mechanism of the formation of fouling deposits in the polymerization of NVP will be formulated in Section 3.4.

The recipe in Table 1 was identified previously and leads to the formation of fouling deposits in different reactor system in [6]. This recipe will be used throughout this thesis as the basis for parameter variations.

3.1 Tubular reactors with static mixer elements

Since the formation of fouling deposits in milli-structured, continuously operated reactors was the original motivation for this thesis, the fouling behavior in such reactor systems will be discussed first. The same static mixer heat exchanger reactor system with different kinds of mixer elements as in [6] was used for these studies.

Table 1. Parameters for the reference case. This setup was used, if not stated otherwise. Throughout this thesis, the monomer M is NVP, the initiator I_2 is V-50 and the solvent S is water. Details on the chemicals that have been used are summarized in Section A.3.1 of the appendix.

Feed / Initial concentration	
Monomer weight fraction – w_M^0	0.2
Initiator weight fraction – $w_{I_2}^0$	0.0002
Solvent weight fraction – w_S^0	$1 - w_M^0 - w_{I_2}^0$
Reaction temperature – T_{reac} / °C	85
Average residence time / superficial velocity	As specified in text.

3.1.1 Experimental setup

The flow sheet of the experimental setup is given in Figure 5 and will be described briefly. More detailed information on the equipment and experimental procedures can be found in Section A.3 of the appendix. Four storage containers B1 to B4 were prepared with degassed monomer, solvent and an initiator solution as specified in Figure 5 and Table 2. The feed streams were pumped using the HPLC piston pumps P1 to P4 and controlled using Coriolis mass flow meters and PI controllers. The mass flow rates are given in Table 2 for the reference conditions in Table 1 and a superficial velocity of 6 mm s^{-1}. The feed streams of P1 and P2 as well as those of P3 and P4 were premixed using 1/16" HPLC T-connectors and these premixed streams were mixed in a 1:1 mass flux ratio in another 1/16" HPLC T-connector to ensure a good micro-mixing quality. For experiments with different superficial velocities, all feed streams were scaled equally. To mimic a batch experiment, pure water was pumped from the storage container B3 instead of the initiator solution initially and the three-way valve V3 was switched to B4 to start the experiment.

Table 2. Mass fluxes and composition for the reference case conditions and a superficial velocity of 6 mm s^{-1} in the Fluitec Contiplant reactor.

Feed pump	Mass flux / g min^{-1}	Weight fractions (NVP / water / initiator)
P1	6.2	1 / 0 / 0
P2	9.3	0 / 1 / 0
P3	9.3	0 / 1 / 0
P4	6.2	0 / 0.999 / 0.001

The reactor system consists of four Fluitec Contiplant reactors with an internal diameter of 12.3 mm and a length 500 mm. Different static mixer elements were inserted, which will be described in the following sections. The reactor system was heated using a water circuit including the circulation pump P5 and a coiled pipe heat exchanger, which was placed in the oil bath thermostat T3. A circulation flux between 7 l min^{-1} and 8 l min^{-1} and an oil bath temperature of 100 °C were chosen to achieve a temperature of the heating medium of 85 °C at the reactor inlet. These parameters lead to a temperature drop in the water circuit in the reactor of around 1 °C due to heat loss.

3.1.2 Fouling in static mixer reactors

Figure 6 illustrates the typical evolution of the pressure drop in the reactor system, if fouling occurs. After an initial increase due to the increase in viscosity that is caused by the reaction, the reactor can be operated at an almost constant pressure drop for a couple of hours. After five to six hours of operation, the pressure drop starts to increase and becomes more and more volatile. Even after a flushing cycle with water and an increased superficial velocity of 24 mm s^{-1} after around 8 h, the pressure drop does not return to its original value.

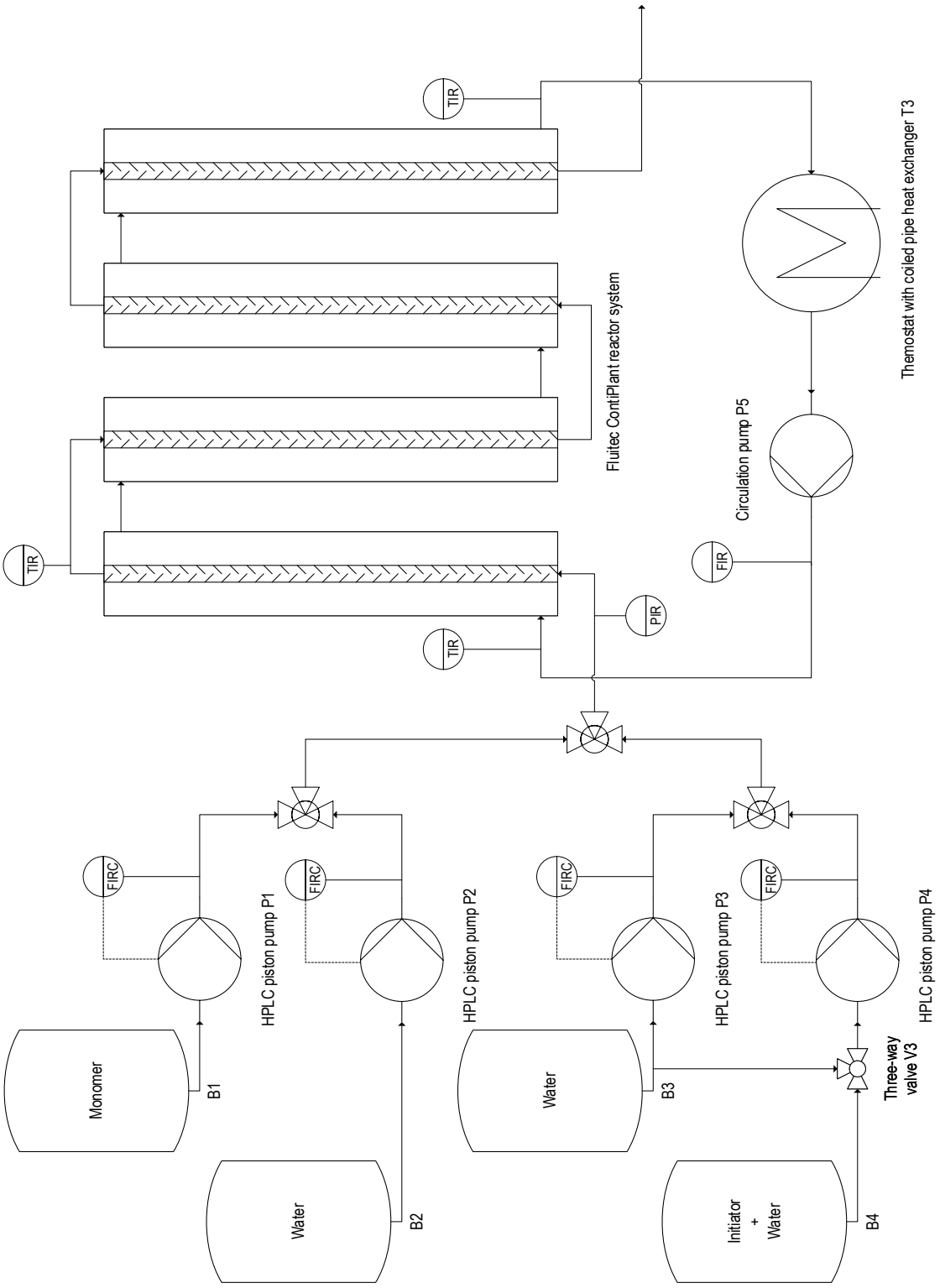

Figure 5. Simplified flow sheet of the setup for experiments in the Fluitec Contiplant reactor system. Details on the equipment and experimental procedures can be found in Section A.3 of the appendix.

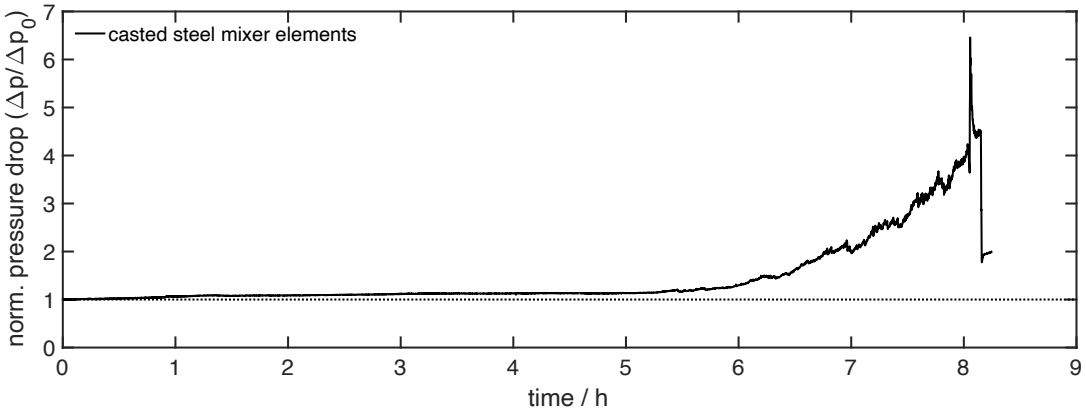

Figure 6. Normalized entry pressure evolution in an experiment using the setup described in Section 3.1.1 with strong fouling. The experiment was conducted as described in the text and Table 1 with a superficial velocity of 6 mm s^{-1}. $\Delta p_0 = \Delta p(0\ \text{h})$.

The reason for this observation is the accumulation of an insoluble polymer gel, which adheres to the casted steel mixer elements and blocks the empty volume in the reactor. Typical examples of mixer elements from experiments using the reference conditions in Table 1 with a superficial velocity of 6 mm s^{-1} are shown in Figure 7 and Figure 8. The mixer element in Figure 7 was taken from an experiment that was stopped after around 5.5 h and demonstrates the initial states of fouling on static mixer elements. Although the surface is covered by polymer gel, regions with stronger accumulation exist, which seem to be mostly on the backside in the direction of flow. These regions had already been identified and proposed to be the origin of polymer gel fouling in [6] and are characterized by a low fluid velocity. In Figure 8, a mixer element after 7-8 h of operation is shown. The polymer gel accumulated further and blocked most of the empty volume in the reactor. Polymer gel that was removed from these mixer elements had a solid content of 24-28 wt.-%, which is higher than expected from the feed concentrations. By placing the dismounted mixer elements in water over night, the accumulated gel could be swollen further to a final solid content of only 5 wt.-%.

Figure 7. Initial states (5.5 h of operation) of PVP gel fouling on a casted steel static mixer element. The experiment was conducted as described in the text and Table 1 with a superficial velocity of 6 mm s^{-1}. The direction of flow is from right to left.

Figure 8. PVP gel fouling on a casted steel static mixer element. The experiment was conducted as described in the text and Table 1 with a superficial velocity of 6 mm s^{-1}.

Different mixer element geometries of the Fluitec CSE/X series were used but all of them showed strong fouling after several experiments and no significant difference could be observed. Most of the surfaces were covered with polymer gel, which adhered strongly and had to be removed by water jet cleaning. Interestingly, fouling increased with the number uses. While only small amounts of polymer gel accumulated in the very first experimental run with factory-fresh mixer elements, the amounts increased to the state that is shown in Figure 7 and Figure 8 in further experiments. These observations suggest that besides the flow pattern, surface properties must play an important role for the accumulation of polymer gel and that aging of polymer gel deposits may also be part of the fouling mechanism. These two effects were studied experimentally and will be discussed in more detail in the next sections.

3.1.2.1 Influence of surface modifications

Since the adhesion of macromolecules seems to be an important part of the fouling mechanism, experiments with different surface modifications were carried out. A hydrophobic coating on mixer elements as well as reduced surface roughness by slide grinding were tested.

As a hydrophobic coating, a 30 µm layer of fluorinated ethylene propylene copolymer (FEP) and additives was applied to casted steel mixer elements[3]. Since the initial states of the mixer elements had already been identified to influence the amount of polymer gel accumulation, the coated mixer elements were used several times. Figure 9 shows a comparison of the pressure drop evolution using coated and uncoated mixer elements. The former had been in use for the fifth time, while the latter had been used even more often. The experiment with coated mixer elements showed a similar increase of the pressure drop

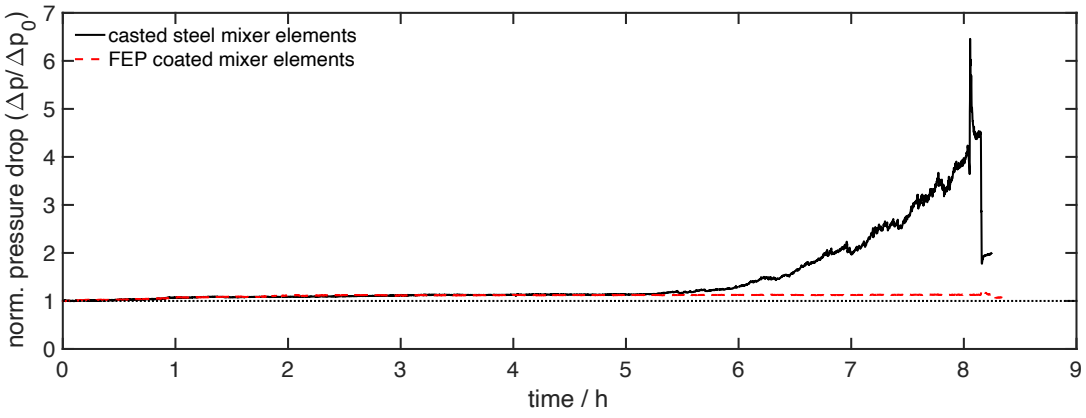

Figure 9. Comparison of the normalized entry pressure evolution in experiments using the setup described in Section 3.1.1 without (see Figure 8) and with hydrophobic coating (see Figure 10). The experiments were conducted as described in the text and Table 1 with a superficial velocity of 6 mm s^{-1}. $\Delta p_0 = \Delta p(0\ \mathrm{h})$.

[3]by courtesy of Fluitec mixing + reaction solution AG

in the beginning of the experiment but a stationary state was reached. After a short flushing cycle with water after around 8.2 h, the pressure drop almost returned back to its original value.

A mixer element from the experiment described above is shown in Figure 10. Only a small amount if fouling deposits was observed in regions close to the metal reactor walls. These fouling deposits could easily be removed by rinsing with water.

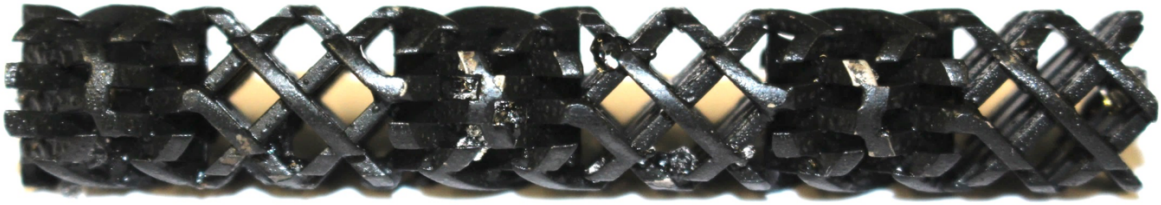

Figure 10. Reduced fouling due to hydrophobic coatings (FEP + additives, 30µm) on casted steel static mixer element. The experiment was conducted as described in the text and Table 1 with a superficial velocity of 6 mm s^{-1}.

Another type of surface modification, which might influence the fouling behavior, is the reduction of the microscopic surface roughness. The effect of such modification on PVP gel fouling was tested using mixer elements with surfaces that had been polished by slide grinding. After repeated use, the mixer elements showed strong polymer gel fouling depos-

Figure 11. PVP gel fouling on a static mixer element with reduced surface roughness by slide grinding. The experiment was conducted as described in the text and Table 1 with a superficial velocity of 6 mm s^{-1}.

its and no significant difference to the regular casted steel mixer elements could be observed. An example of a mixer element with a reduced surface roughness after its fourth use is illustrated in Figure 11. The experiments were carried out with the reference case procedure described before.

3.1.2.2 Aging of metallic surfaces and influence cleaning strategies

As already mentioned, the amount of PVP fouling deposits increased with the number of uses of mixer elements with metallic surfaces. This observation suggests that, although the mixer elements were apparently clean after mechanical cleaning with a water jet, a change of the surface properties must have happened. Since PVP forms a complex with iodine [41], PVP residues on surfaces can be detected by dyeing the mixer elements with an iodine solution and rinsing off the excessive solution. Doing so revealed that the surface of the mixer elements was still covered with a thin layer of PVP, which was indicated by the yellow-brown color of the PVP-iodine complex. This layer may have grown up again under reaction conditions. Since water jet cleaning cannot remove this residue, different ways to degrade the layer were tested.

Sodium hypochlorite solutions (NaClO) are widely used in membrane production to degrade and remove PVP, which is added in the precipitation process, from the product [42]. Investigations on PVP degradation with NaClO suggest that the underlying mechanism is the formation of hydroxy radicals, which degrade the polymer [42], [43]. A comparison of mixer elements that were treated with NaClO solutions (12 % Cl_2) to ones that were cleaned mechanically using a water jet is given in Figure 12 and Figure 13. Both mixer elements had been used in the same experiment and showed fouling deposits. The mixer element in Figure 12 was cleaned with a water jet and then dyed with iodine solution to detect residual PVP on its surface. It can easily be seen that the surface was still covered with polymer and a repeated experiment with this mixer element led to heavy fouling

deposits again. Figure 13 shows the behavior of a mixer element that was cleaned chemically using NaClO solution. After dyeing with iodine solution no coloring and, therefore, no PVP residue could be observed. After using this mixer element in the same repeated experiment as the mixer element from Figure 12, only minor fouling deposit were visible, similar to those on factory-fresh mixer elements.

Figure 12. Effect of mechanical cleaning with water jet on PVP gel fouling on a casted steel static mixer element. Left: casted steel static mixer element after several experiments as described in the text and Table 1 with a superficial velocity of 6 mm s^{-1} with water jet cleaning in between. Middle: same mixer element after mechanical cleaning with water jet and dyeing with iodine solution. Right: mechanically cleaned mixer element after repetition of the experiment.

Figure 13. Effect of cleaning with NaClO solution on PVP gel fouling on a casted steel static mixer element. Left: casted steel static mixer element after several experiments as described in the text and Table 1 with a superficial velocity of 6 mm s^{-1} with water jet cleaning in between. Middle: same mixer element after treatment with NaClO solution and dyeing with iodine solution. Right: chemically cleaned mixer element after repetition of the experiment.

Thermal degradation of PVP residue on the mixer elements surfaces at 600 °C in the oven led to similar results, although the degradation products remained on the surface in form of a black residue as shown in Figure 14.

Figure 14. Effect of thermal cleaning at 600 °C on PVP gel fouling on a static mixer element. The casted steel static mixer element was subject to strong fouling in several experiments as described in the text and Table 1 with a superficial velocity of 6 mm s^{-1} with water jet cleaning in between (similar to Figure 12). The picture shows the same mixer element after thermal treatment in an oven and repetition of the experiment.

Figure 15. Dyeing (iodine solution) of a casted steel static mixer element with hydrophobic coating after an experiment as described in the text and Table 1 with a superficial velocity of 6 mm s^{-1} with subsequent water jet cleaning.

Figure 16. Dyeing (iodine solution) of a casted steel static mixer element with reduced surface roughness through slide grinding after an experiment as described in the text and Table 1 with a superficial velocity of 6 mm s^{-1} with subsequent water jet cleaning.

Dyeing tests with FEP coated and slide grinded mixer elements after water jet cleaning revealed that the metallic surface of the latter was still covered with PVP while the hydrophobic surface of the coated mixer element showed no indication of residual PVP. Only

some regions where the coating was spalled showed the yellow-brown color of the PVP-iodine complex. The results are illustrated in Figure 15 and Figure 16.

3.1.2.3 Dependence of fouling on the position of mixer elements in the reactor

The experiments in the previous sections were carried out with a superficial velocity of 6 mm s^{-1}, which leads to a monomer conversion of around 50 % at the outlet of the fourth Contiplant reactor. To investigate the influence of local monomer conversion on the onset of fouling, the superficial velocity was decreased to only 1 mm s^{-1} in another series of experiments to achieve full conversion in the reactor system. The expected monomer conversion profile for a plug flow reactor with the same average residence time of 2050 s is shown in Figure 17 together with experimental results after the first, third and fourth Contiplant reactor. As shown in Figure 18, the sampling procedure at different positions has a strong

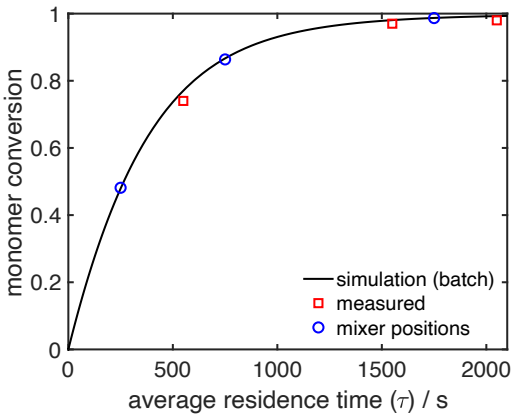

Figure 17. Monomer conversion using the setup described in Section 3.1.1 and a simulation using the kinetic model form Section 4.2.4. The experiments were conducted as described in the text and Table 1 with a superficial velocity of 1 mm s^{-1}. Blue circles indicate the theoretical value of monomer conversion in a plug flow reactor at the positions of mixer elements that are illustrated in Figure 19.

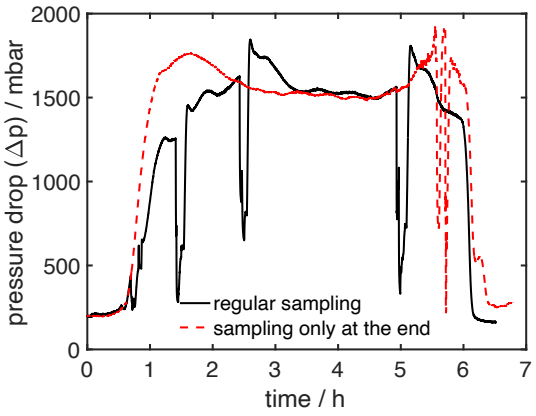

Figure 18. Pressure drop in the reactor using the setup described in Section 3.1.1. The experiments were conducted as described in the text and Table 1 with a superficial velocity of 1 mm s^{-1}.

impact on the pressure profile, since opening the sampling valves close to the reactor entry caused the pressure to drop. Therefore, only one sample at the end of the experiment was taken in the second experimental run. The experiments were stopped after 5.5 h to capture the fouling behaviour in the early stages, and the reactor was flushed with water at 1 mm s^{-1} to prevent deposits from spreading in the reactor due to the flushing procedure. As illustrated in Figure 18, the pressure drop increased drastically after around one residence time due to the increased viscosity and reaches a plateau. A slight increase from the latter was observed in the second run after around 5 h, shortly before the experiment was stopped by flushing with water. After flushing with water for around one hour, the pressure drop decreased to a value close to the original value after the first run and remained at a slightly increased level in the second run.

The fouling behaviour at different positions, which are also marked with blue circles in the monomer profile in Figure 17, is illustrated in Figure 19. Only mixer elements from the second run are shown, but the amount of fouling deposits was similar in the first run.

Figure 19. Influence of the position in the reactor on the formation of fouling deposits using stainless steel static mixer element after 5.5 h of operation using the experimental conditions described in the text and Table 1 with a superficial velocity of 1 mm s^{-1}. The mixer elements had been cleaned with a water jet before the experiment. Left to right: middle of the first Contiplant® reactor (~250 s average residence time), middle of the second Contiplant® reactor (~750 s average residence time), middle of the fourth Contiplant® reactor (~1750 s average residence time).

Fouling is most pronounced close to the reactor inlet where monomer conversion is low. In the fourth reactor where monomer conversion is close to unity, barely any fouling deposits are visible.

3.2 Tank reactors

Tank reactors were used for kinetic studies in continuous and batch operation, which will be discussed in Chapter 4. In this section, the formation of fouling deposits in such reactor systems will be discussed.

3.2.1 Experimental setup

The experimental setup is shown in Figure 20. A brief description will be given in this section and more detailed information on the equipment and experimental procedures can be found in Section A.3 of the appendix. Monomer and initiator solutions were pumped from the storage containers B1 and B2 using the HPLC piston pumps P1 and P2. The storage containers were degassed before the experiments and put under argon atmosphere to prevent oxygen from entering. The mass flow rates were controlled using Coriolis mass flow meters and PI controllers. In Table 3, the mass flow rates for the reference case conditions as well as the composition in the storage containers for a CSTR experiment with a typical average residence time are summarized. To change the average residence

Table 3. Mass fluxes and composition for the reference case conditions and a hydrodynamic residence time of around 2.25 h in the CSTR reactor.

Feed pump	Mass flux / g min^{-1}	Weight fractions (NVP / water / initiator)
P1	2.36	0.4 / 0.6 / 0
P2	2.36	0 / 0.9996 / 0.0004

time, both feed streams were scaled equally, and the concentrations in the storage containers were modified to change the feed composition. The feed streams were mixed in the high-pressure mixing tee M1 in a 1:1 ratio. To ensure the correct concentrations at the start of the experiment, the purge valve V1 was installed. The reactor was filled with water initially and the reactive solution was pumped into a separate waste container. The experiment was started by switching the position of V1. For operation in batch mode, the reactor was filled will monomer and solvent and an initiator solution was injected using a syringe to start the experiment. Additionally, a reflux cooler was installed for batch experiments and the gaseous atmosphere was flushed with argon to prevent oxygen from entering. In CSTR operation mode no gaseous atmosphere was present since the reactor outlet is at the top of the reactor.

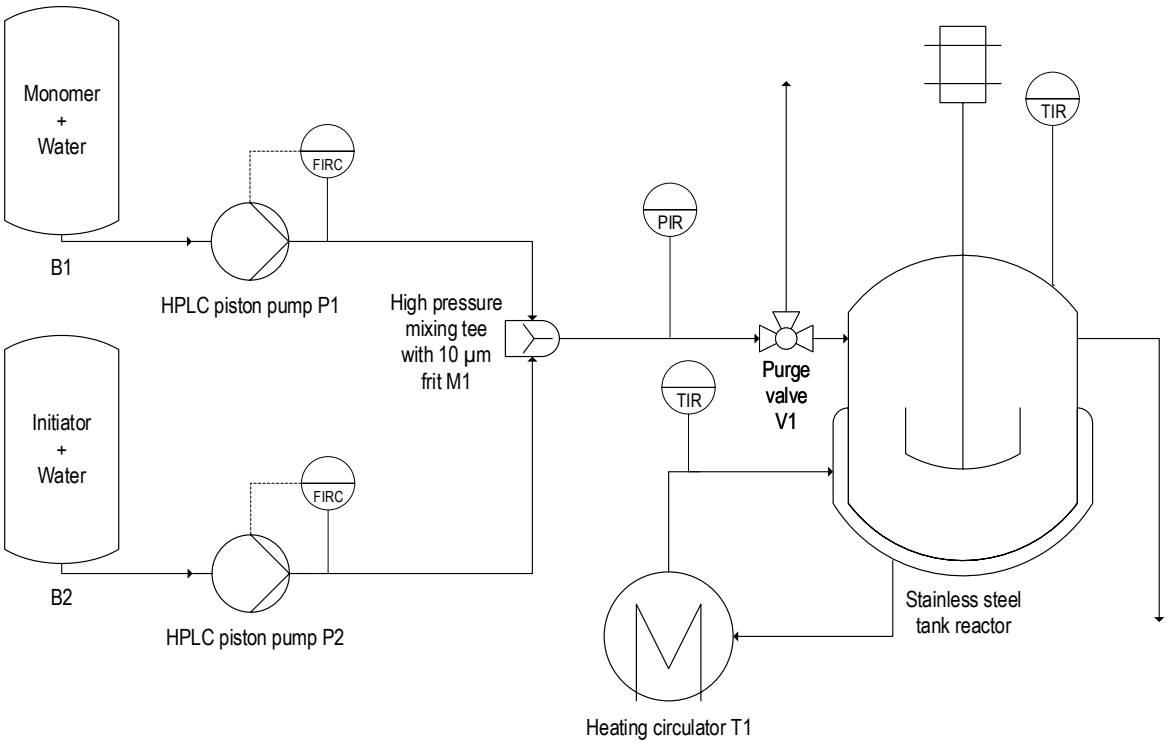

Figure 20. Simplified flow sheet of the setup for tank reactor experiments. Details on the equipment and experimental procedures can be found in Section A.3 of the appendix.

The Juchheim stainless steel tank reactor with 650 ml internal volume was thermostated using the heating circulator T1 and water as heating medium. The plate stirrer was operated at 250 rpm.

3.2.2 Fouling in tank reactors

In Figure 21 and Figure 22 the fouling behavior in a batch experiment, which took 1.5 h, and in CSTR operation mode with an average residence of 4.5 h, which took 56 h, is illustrated. The difference in the amount auf fouling deposit is remarkable. While there were heavy deposits after the CSTR experiment, there were no significant deposits on surfaces that were in contact with the liquid phase after the batch experiment. Only at interface with gaseous atmosphere, which is not present in CSTR operation, some high-molecular material was observed but could be dissolved again.

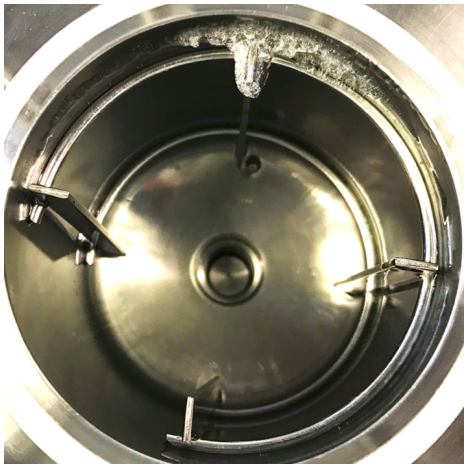

Figure 21. Fouling in the vessel of a tank reactor operated in batch mode after an experiment as described in the text and Table 1. No insoluble fouling deposits were observed. The experiment took 1.5 h.

Figure 22. Fouling in the vessel of a tank reactor operated in continuous mode with a hydrodynamic residence time of 4.5 h after an experiment as described in the text and Table 1. Heavy fouling deposits were observed on metal surfaces in contact with liquid. The experiment took 56 h.

Another important factor is the solid content in the reactor. Figure 23 and Figure 24 show the fouling deposits after CSTR experiments with an average residence time of 2.25 h and a monomer content in the feed of $w_M^0 = 0.2$ and $w_M^0 = 0.1$ respectively. The experiments were run for 29 h and the stationary conversion was just below 90 % for both experiments. After the experiment with a higher polymer content, much more fouling deposits could be observed.

Although fouling deposits occurred in characteristic regions of CSTRs, e.g. at the baffles, no gelation of the bulk phase was observed in any of the experiments. As for static mixer reactors, these critical regions are characterized by low fluid velocities, which highlights the importance of such regions for the formation of fouling deposits.

Figure 23. Fouling in the vessel of a tank reactor operated in continuous mode with a hydrodynamic residence time of 2.25 h after an experiment as described in the text and Table 1. The experiment took 29 h.

Figure 24. Fouling in the vessel of a tank reactor operated in continuous mode with a hydrodynamic residence time of 2.25 h after an experiment as described in the text and Table 1 but the feed concentration of monomer was decreased to $w_M^0 = 0.1$. The experiment took 29 h.

3.3 Capillary tubular reactors without mixer elements

Tubular reactors have a simple internal geometry and, consequently, a well-known flow pattern and residence time distribution. Therefore, this reactor type is a convenient candidate to study the effect of the flow pattern and diffusive mass transport on the formation of fouling deposits in detail. In this section, experimental evidence on fouling in tubular reactors und the formation of wall layers will be presented.

3.3.1 Experimental setup

The experimental setup from Section 3.2.1 was adapted. Again, additional information on the equipment and experimental procedures can be found in Section A.3 of the appendix. The dosing system is mostly the same as for CSTR experiments, but a dynamic mixing chamber was added to improve the mixing quality due to the low mass flow rates. As for the CSTR experiments, the reactor was filled with water initially and the experiment was started by switching the position of the three-way valve V1. Before entering the reactor, the process stream passes a HPLC switching valve including a sample loop, which was used to inject 1 M aqueous NaCl solution as a flow tracer. If the valve is in the green position in Figure 25, the process medium enters the reactor directly and the sample loop can be filled manually using a syringe. By switching the position of the valve, the tracer

Table 4. Mass fluxes and composition for the reference case conditions and a superficial velocity of 12 mm s^{-1} in the capillary tubular reactor.

Feed pump	Mass flux / g min^{-1}	Weight fractions (NVP / water / initiator)
P1	0.875	0.4 / 0.6 / 0
P2	0.875	0 / 0.9996 / 0.0004

solution in the sample loop was flushed into the reactor system. The reactor is a tubular reactor, which was placed in an oil bath which's temperature was controlled by the heating circulator T2. The inner diameter of the reactor is $d_i = 1.76$ mm and its length is 3 m. The mass fluxes in Table 4 and the reactor winding diameter $d_{wind} \approx 300$ mm were chosen to achieve laminar flow with an average velocity of $v_{av} \approx 12$ mm s^{-1} and a maximum Dean number at the inlet

$$De_{in} = \frac{\rho d_i v_{av}}{\eta}\sqrt{\frac{d_i}{d_{wind}}} = Re_{in}\sqrt{\frac{d_i}{d_{wind}}} \approx 21\sqrt{\frac{d_i}{d_{wind}}} \approx 1.6 \tag{60}$$

at the inlet to prevent secondary flow in the radial direction [44]. A density of $\rho = 1000$ kg m^{-3} and $\eta = 10^{-3}$ Pa s were assumed in Equation (60). Since the viscosity increases much stronger than the density, the Dean number decreases along the reactor axis.

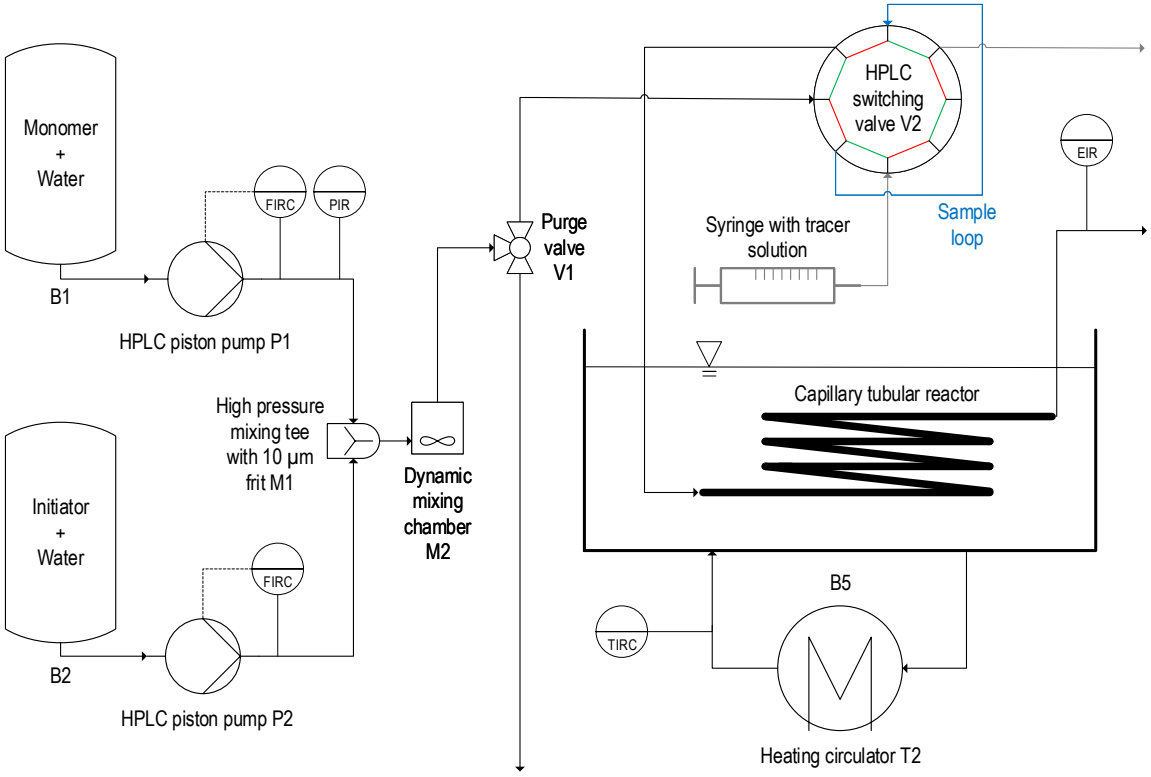

Figure 25. Simplified flow sheet of the setup for experiments using the capillary tubular reactor. Details on the equipment and experimental procedures can be found in Section A.3 of the appendix.

The mass fluxes in Table 4 lead to a hydrodynamic residence time of only 250 s, which corresponds to a monomer conversion of around 30 %. These conditions were chosen to characterize the fouling behavior shortly after the reactor inlet, since this position was identified to be crucial in the experiments described in Section 3.1.2.3. A conductivity flow cell at the reactor outlet was installed to measure the current at 12 V alternating voltage using the setup described in [6] to detect the tracer.

3.3.2 Residence time distributions and fouling in capillary tubular reactors without mixer elements

The idealized input signal during the first 1.5 h of the first experimental run under the conditions described in the preceding section are shown in Figure 26. Of course, the input signal at the reactor inlet is not an ideal Dirac delta function because the sample loop as well as the piping that connects the HPLC switching valve and the reactor inlet have a finite length and the flow pattern is not an ideal plug flow. Since only a qualitative comparison of the evolution of the residence time distribution was desired, this effect was

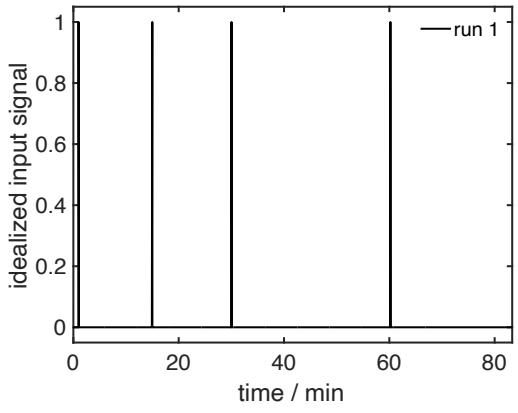

Figure 26. Idealized input signal in the first 1.5 h of the first experimental run of experiment in the capillary tubular reactor as described in Section 3.3.1.

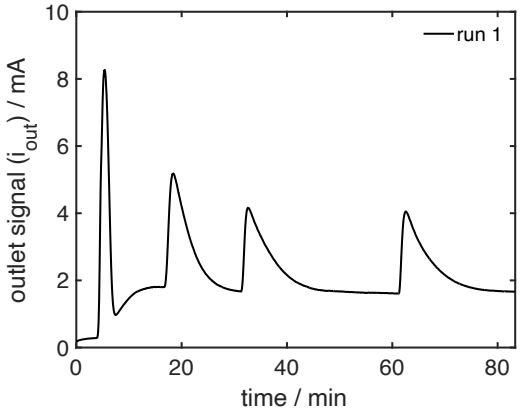

Figure 27. Tracer output signal i_{out} that corresponds to the idealized inlet signal in Figure 26.

neglected. No deconvolution of the input and output signals was done, and the measured output signal will be discussed instead of the residence time distribution. A discussion of the form of the measured input signal is given in Section A.3.3 of the appendix.

The measured output signal that corresponds to the injection times that are marked by the idealized input signals in Figure 26 is shown in Figure 27. Shortly after the start of the experiment, the baseline current increases, which indicates the break-through of the reactive process medium. The latter has a higher conductivity, which is caused by the dissolved initiator.

Figure 28 shows the response signals after different injection times during the first experimental run and a reference signal, which was measured before the reaction in pure water. As described in Section A.3.3 of the appendix, a baseline correction was done for better

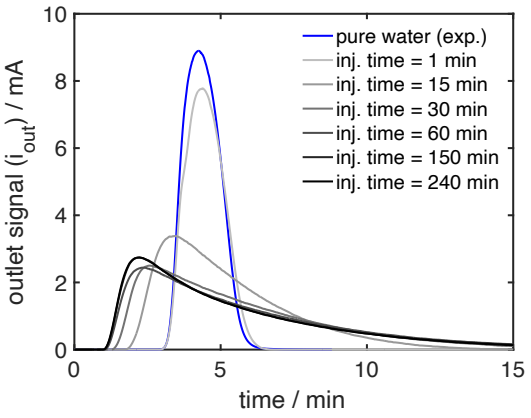

Figure 28. Evolution of the output signals of the capillary tubular reactor during the first experimental run as described in Section 3.3.1. The origin of the time axis corresponds to the switching time of the HPLC switching valve. The time of injection is counted from the time at which monomer and initiator were dosed. Signals at 150 min and 240 min are indistinguishable, and the reference signal was measured in pure water before the reaction.

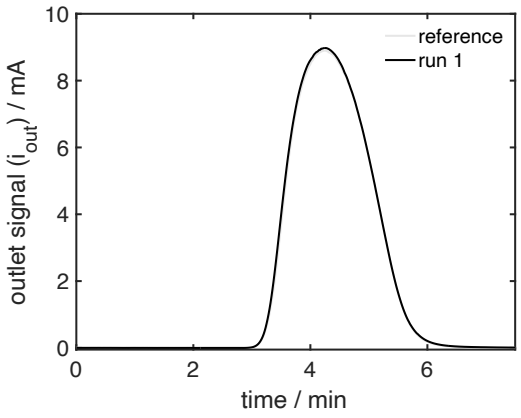

Figure 29. Comparison of the absolute tracer output signal of the capillary tubular reactor in pure water before the first experimental run (reference) and after the flushing procedure after the first experimental run as described in Section 3.3.1. The signals are indistinguishable.

comparison. The reference signal shows more similarity with a Gaussian function than with the residence distribution of a laminar velocity profile, which is attributed to radial diffusion of the tracer and will be discussed in Section 5.2.3 in detail. With increasing operation time, the tracer breaks through faster and the signal becomes more tailed. The experiment was stopped after 7 h of operation by flushing the reactor with pure water for 1 h at 12 mm s^{-1} and, additionally, for around 5 min at a velocity of approximately 500 mm s^{-1}. After this procedure, the measured response signal in pure water returned to its original reference state in the first experimental run as shown in Figure 29.

The experiment was repeated three times and the response signals in pure water after the flushing procedure after each experiment are shown in Figure 30. The response signal in pure water returned to its original state only after the first run and transformed more and more to a shape that is similar to the one during the reaction in the first run with a factory fresh reactor.

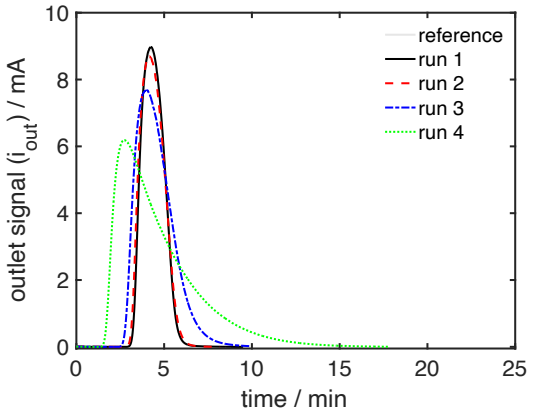

Figure 30. Comparison of the tracer output signal of the capillary tubular reactor in pure water before the first experimental run (reference) and after the flushing procedure with water after repeated experimental runs 1 to 4 as described in Section 3.3.1. The reference and the signal after run 1 are indistinguishable.

The reason for this behavior can be understood from the evolution of the pressure drop in Figure 31. During the first experimental run, the pressure drop profile was smooth but already showed a slight drift. After the flushing procedure, it almost returned to its original

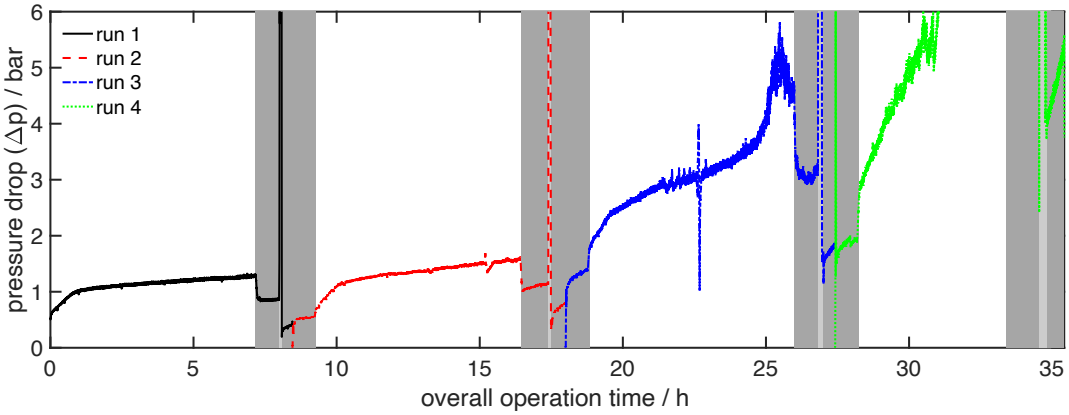

Figure 31. Evolution of the pressure drop in the capillary tubular reactor in the repeated experimental runs 1 to 4 as described in Section 3.3.1 including all flushing procedures. Dark gray background indicates flushing with water at 12 mm s^{-1} and light gray background corresponds to flushing with the maximum flowrate that lead to a pressure drop of 50 bar.

value. The drift increased during the repeated experiments and, from the second run onward, the pressure drop became volatile and did not return to its original value even after flushing with an increased velocity. The maximum flow rate during the flushing procedure even had to be decreased to stay below the pressure drop limit of the experimental setup, which is 50 bar. As discussed in Section 3.1.2, a volatile increase of the pressure

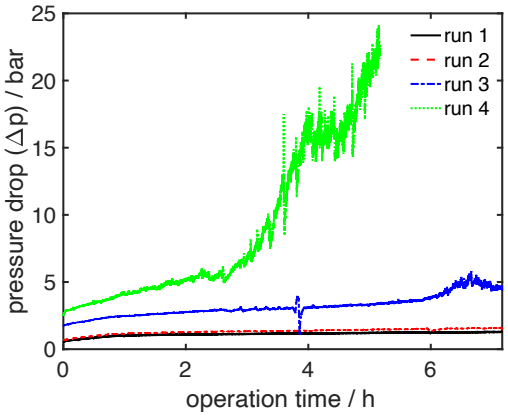

Figure 32. Evolution of the pressure drop in the capillary tubular reactor during the repeated experimental runs 1 to 4 as described in Section 3.3.1. The origin of the time axis corresponds to the time at which monomer and initiator were dosed.

drop is a strong indicator for the formation of polymer gel fouling deposits. Indeed, polymer gel particles were observed in the effluent process stream in the third and fourth experimental runs and, especially, during the flushing procedure.
For comparison, the increase of the pressure drop during the reaction is shown in Figure 32 in a different presentation. The initial pressure drop increased in all repeated runs.

3.4 Concluding remarks

During the polymerization of NVP in aqueous solution, fouling deposits are formed by an insoluble polymer gel, which accumulates in the reactor and reaches higher solid contents than expected from the feed concentrations. The effect is especially important in reactor systems with broad residence time distributions, e.g. in CSTRs or different kinds of tubular reactors in which dead-water zones or wall layers can lead to locally increased residence times. In tank reactors that are operated in batch mode, highly viscous material is formed at the gas-liquid interface but can be dissolved in water again. The results are in agreement with [5] where no fouling deposits were reported for solution polymerization in batch mode, while continuous operation over 8 h in static mixer heat exchanger reactors lead to heavy fouling deposits. Fouling layers from batch experiments, which were reported in [17], could be dissolved as well. Since an insoluble gel is formed only in continuously operated reactor systems with broad residence time distributions, side reactions between macromolecules must be an important part of the reaction mechanism as was already stated in [6].
In static mixer reactors, fouling deposits are found in dead-water zones close to the reactor inlet, initially. Dead-water zones were also reported to be relevant for the formation of fouling deposits in [5] and [6]. Since the feed streams were mixed at room temperature using static and dynamic mixers, which were designed for low flow rates, it is unlikely that the micro-mixing efficiency is the reason for the formation of fouling deposits close to the

inlet. This is consistent with the observation that including micro-mixers did not lead to reduced fouling in [5]. Residence time measurements in a capillary reactor demonstrate that radial diffusion due to concentration gradients plays an important role. Such gradients are caused by different residence times in radial direction due to the flow pattern, e.g. low fluid velocities in wall regions or dead-water regions compared to the main flow. These gradients are most pronounced where the monomer concentration in the bulk is still high, i.e. close to the reactor inlet. Diffusive mass transport in non-ideally mixed regions may also be the reason for the formation of fouling deposits at the baffles of CSTRs, which were also described in [10], and wall layers in laminar flow, which were reported in [6], [16], [19], [21]. Therefore, it is more likely that concentration gradients in the radial direction are the reason for the formation of fouling deposits close to the reactor inlet.

Another important factor are the surface properties of the reactor. As demonstrated for static mixer elements in Section 3.1.2.1, polymer residue remains on metal surfaces and can only be eliminated by degradation. This thin polymer layer can grow up again, which is the reason that fouling increases in repeated experiments with mechanical cleaning in between. Low energy surfaces as for example FEP coating can prevent the adhesion of polymers on the surfaces. The effectiveness of such modifications was also suggested in [5] and [17].

The observations that have been described in this section are in agreement with reports on fouling in literature and lead to the following hypothesis on the mechanism of the formation of fouling deposits during the polymerization of NVP. Regions with locally increased residence time, e.g. dead-water zones, in continuously operated reactors lead to concentration gradients, which induce mass transport and cause mixing of unreacted monomer and initiator with the polymer product. These regions are characterized by low monomer and high polymer concentrations, which fosters the importance of side reactions

between macromolecules and leads to the formation of an insoluble polymer gel. The polymer gel adheres to metal surfaces and grows up by reactions with polymers and monomers to finally block the reactor.

In the following chapters, this hypothesis will be tested and substantiated by reaction kinetic and CFD simulations and a comparison to the experimental results that have been presented in this chapter will be done.

4 Side reactions and long-chain branching[4]

The observation that fouling deposits are formed by an insoluble polymer gel suggests that reactions, which produce high molecular and highly branched polymer chains, are relevant in the reaction mechanism. Therefore, kinetic models that capture all relevant reactions are one important cornerstone to understand the origin of fouling deposits and to predict the formation of polymer gels and their microstructure.

Several publications on the reaction mechanism and kinetics of the polymerization of NVP in various solvents exist. The propagation rate coefficients in aqueous and organic solution [45], [46] as well as the termination rate coefficient in aqueous solution [47] have been studied extensively using pulsed laser polymerization-size exclusion chromatography (PLP-SEC). While termination by combination seems to be the relevant mechanism in aqueous solution, transfer reactions to the solvent dominate the termination in organic solution [41]. Besides transfer to solvent molecules, transfer to monomer was also proposed to take part in the reaction mechanism in [48]. Some confusion exists about transfer mechanisms that are relevant for long chain branching during the polymerization in aqueous solution. Since broad, high molecular tails were observed in the MWD in batch and semi-batch experiments, transfer to polymer was assumed to be part of the reaction mechanism in [48]. Recently, another mechanism was suggested in which creation of terminal double

[4] Large parts of this chapter have been published in [63] under the terms of the Creative Commons Attribution License (CC BY 4.0) prior to this thesis. Minor changes to the text have been made to fit the contents into the context of this thesis and some additional paragraphs and sections have been added.

bonds (TDBs) by transfer to monomer and subsequent propagation of TDBs is the reason for long chain branching [49]. The suggestion was motivated by calculations from density functional theory (DFT) and validated by batch experiments.

The goal of this chapter is to systematically develop kinetic models, which can be used to get detailed microstructural property information, e.g. on chain length or TDBs, but may also be applied in parameter estimations or CFD simulations in which the computational effort needs to be low. Since these objectives are contradictory, multiple models with different levels of detail need to be developed and the informational content must be transferred consistently between these levels. For this purpose, two modeling approaches, the classes [33], [50] and the pseudo distribution approach [27], [33], [36], [51], will be applied to handle the multi-dimensional property distributions that result from the reaction mechanism described in [49]. The detailed information gained from simulations using these models will be condensed and used to develop much simpler models with significantly lower computational effort. To refine the kinetic coefficients from [49] and to test the predictive capability of the models, simulation results will be compared with experimental results for monomer conversion, molecular weight averages and MWD from CSTR experiments. Details on the experimental setups and analytical methods can be found in Section 3.2.1 and Section A.3 of the appendix.

4.1 Reaction mechanism of the polymerization of NVP

The reaction scheme that is assumed in this thesis was identified and discussed in detail in [49]. Initiation, propagation with monomer M and termination are the main reactions in the radical polymerization of NVP in aqueous solution and lead to linear polymer chains. Only termination by combination is assumed, since this is considered to be the relevant termination mechanism for mono-substituted vinyl-monomers [26]. The two side

reactions, transfer to monomer, which initiates a new polymer radical carrying a TDB, as illustrated in Figure 33 and the propagation of TDBs as illustrated in Figure 34 may lead to branched or crosslinked polymer chains. Since termination by combination is assumed, chains with more than one TDB are created as illustrated in Figure 35.

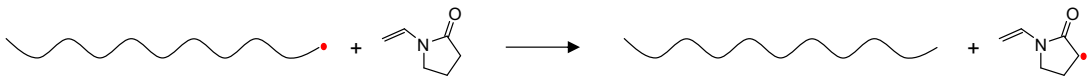

Figure 33. Reaction scheme of the transfer to monomer reaction. The radical center (red) is transferred to a monomer molecule by H-abstraction. Adapted and simplified from [49].

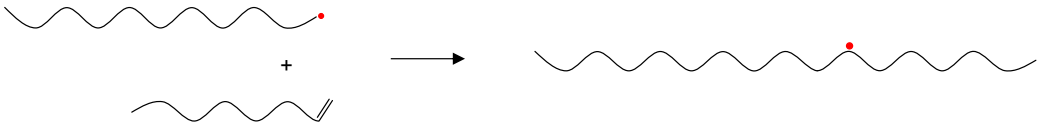

Figure 34. Terminal double bond (TDB) propagation reaction for a polymer chain carrying only one TDB. A mid chain radical is created and causes long chain branching. Adapted and simplified from [49].

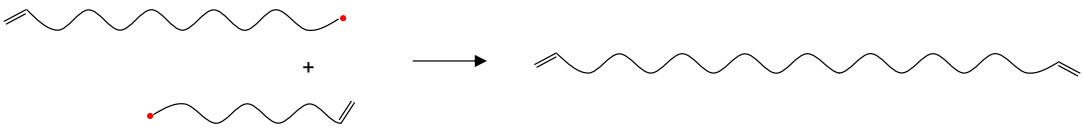

Figure 35. Creation of polymer chain with more than one TDB by the termination by combination reaction. Adapted and simplified from [49].

The polymer population $P_{n,i,k}$ is characterized by three property coordinates: the chain length n, the number of TDBs i and the number of branches k. It should be noticed, that the property dimensions i and k are linked – but not directly. TDBs are produced by

transfer to monomer and consumed by the TDB propagation reaction. The number of branching points, on the other hand, increases only, if TDBs are consumed, not when they are produced. Thus, the simulation of the evolution of a three-dimensional property distribution would be necessary to describe the system in full detail. In principal, if reactions between polymer radicals that carry TDBs were included in the model, the number of radical centers per molecule would have to be considered as a fourth property coordinate. Since the complexity of the model would increase even further, this will not be considered in this thesis and the model will be restricted to species with either zero or one radical center as in [49]. These species will be referred to as the dead species P and living species R respectively.

The full set of reactions that was proposed to be relevant in the radical polymerization of NVP in aqueous solution in [49] is shown in Table 5 for the three-dimensional system. Since the rate of the TDB propagation reaction is proportional to the number of TDBs, the reaction scheme is non-linear in the TDB property coordinate.

Table 5. Full set of reactions for the polymerization of NVP in aqueous solution. The definition of rate coefficients and species is given in the text.

Initiation	$I_2 \overset{k_d}{\rightarrow} 2f_d I \quad / \quad I + M \overset{k_p}{\rightarrow} R_{1,0,0}$
Propagation	$R_{n,i,k} + M \overset{k_p}{\rightarrow} R_{n+1,i,k}$
Termination by combination	$R_{n,i,k} + R_{m,j,l} \overset{k_{t,c}}{\rightarrow} P_{n+m,i+j,k+l}$
Transfer to monomer	$R_{n,i,k} + M \overset{k_{tr,m}}{\longrightarrow} P_{n,i,k} + R_{1,1,0}$
Propagation of TDBs	$R_{n,i,k} + P_{m,j,l} \overset{j \cdot k_{p,TDB}}{\longrightarrow} R_{n+m,i+j-1,k+l+1}$

Most of the rate coefficients in Table 5 are taken from literature. The propagation rate coefficient can be calculated from [45]

$$\frac{k_p}{k_{p,\max}} = 0.36 + 0.64 \exp(-9.2\ w_M) - 0.31\ w_M \tag{61}$$

with

$$k_{p,\max} \Big/ \text{l mol}^{-1}\ \text{s}^{-1} = 2.57 \cdot 10^7 \exp\left(-\frac{17.6\ \text{kJ mol}^{-1}}{RT}\right) \tag{62}$$

and the weight fraction of NVP w_M. As in [48], the transfer to monomer rate coefficient was assumed to be proportional to the monomer propagation rate coefficient with a ratio of $k_{tr,m}/k_p = f_{tr,m} = 6 \cdot 10^{-4}$. The termination rate coefficient depends on the monomer weight fraction w_M in the low conversion regime in which segmental diffusion (SD) is the rate determining mechanism. With increasing polymer content, the viscosity increases and translational diffusion (TD) limits the termination rate until at very high polymer contents reaction diffusion (RD) determines the termination rate. Based on these mechanisms, a correlation for the termination rate coefficient of the form

$$k_t \Big/ \text{l mol}^{-1}\ \text{s}^{-1} = \left(\frac{1}{k_{SD}} + \frac{\eta_{rel}}{k_{TD}}\right)^{-1} + k_{RD} \tag{63}$$

has been proposed [47] with the rate coefficients k_{SD}, k_{TD} and k_{RD} for each mechanism respectively and the relative bulk viscosity η_{rel}, which is related to the viscosity at zero conversion. The rate coefficients and a correlation for η_{rel} at 40 °C and 2000 bar were determined by single laser pulse experiments in combination with k_p data from literature to be [47]

$$k_{SD}\Big/_{\text{l mol}^{-1}\ \text{s}^{-1}} = 4.87 \cdot 10^7 \exp(-\tfrac{w_M}{0.29}) + 5.67 \cdot 10^6\ , \tag{64}$$

$$k_{TD} = 31\ k_{SD}, \quad \eta_{rel} = \exp(14.75\ w_P) \tag{65}$$

with the polymer weight fraction w_P and

$$k_{RD} = 140\ w_M\ k_p\ . \tag{66}$$

The effect of pressure p on diffusion can be corrected by

$$k_{SD}(p) = k_{SD}(2000\ \text{bar}) \exp\left(-5.61 \cdot 10^{-4}\ \left(\frac{p}{\text{bar}} - 2000\right)\right)\ . \tag{67}$$

Reaction diffusion does not play a significant role for the conditions under investigation in this thesis but was implemented for completeness. The temperature dependence of the termination rate coefficient is usually low, and so, the correlation discussed above was used without any correction as was done in [48].

For the decomposition rate coefficient of initiator I_2 to the initiator radical species I, the correlation

$$k_d\Big/_{\text{s}^{-1}} = 9.17\ 10^{14} \exp\Big(-\tfrac{1.24 \cdot 10^2\ \text{kJ mol}^{-1}}{RT}\Big). \tag{68}$$

taken from the supplier [48] was used. The TDB propagation rate coefficient $k_{p,TDB}$ as well as the initiator efficiency f_d were estimated using experimental data.

4.2 Model development

A reference case will be used throughout the model development to test different models against each other. The reaction conditions and kinetic parameters are typical for the

polymerization of NVP in aqueous solution in an isothermal CSTR and are summarized in Table 6. The average residence time

$$\tau = \frac{V_{reac} \cdot \rho_S}{\dot{m}_F} \tag{69}$$

with the reactor volume V_{reac} and the mass feed rate $\dot{m}_F$ is around 1 h. The pure component mass densities of the solvent and monomer at 85 °C were assumed to be $\rho_S = 959$ kg m^{-3} and $\rho_M = 989$ kg m^{-3} respectively [48].

Table 6. Parameters for the reference case. This setup was used for all simulations, if not stated otherwise. The value of $k_{p,TDB}$ has been chosen arbitrarily.

Kinetic coefficients	
k_d, k_t, k_p	Equation (61) to Equation (68)
$k_{tr,m}/k_p = f_{tr,m}$	$6 \cdot 10^{-4}$ [48]
$k_{p,TDB}$ / l mol^{-1} s^{-1}	2500
f_d	0.7 [48]
Feed	
Monomer weight fraction w_M^0	0.2
Initiator weight fraction $w_{I_2}^0$	0.0002
Solvent weight fraction w_S^0	$1 - w_M^0 - w_{I_2}^0$
Feed rate $\dot{m}_F$ / g min^{-1}	10.38
Initial conditions in reactor	
Solvent weight fraction w_S^0	1
Reactor temperature T_{reac} / °C	85
Reactor volume V_{reac} / ml	650

4.2.1 Modelling strategies for multi-dimensional property distributions

Commercially available Galerkin-FEM solvers such as the one implemented in PREDICI® are usually capable of solving problems with one discrete property dimension. Generally, an extension to more than one dimension would be possible, but the increased numerical effort makes this practically infeasible [35]. To simulate systems with multi-dimensional property distribution as described in the Section 4.1, the problem has to be transformed into a series of one-dimensional problems.

The straightforward way is to solve for one property dimension directly, e.g. the chain length, and define different populations – so-called classes – for the other discrete property dimensions [50], e.g. $R_{n,1,0}$ for living polymer chains carrying one TDB and zero branches, $R_{n,2,1}$ for living polymer chains carrying two TDBs and one branch and so on for the present example. The reaction scheme can be derived by assigning numbers to the second and third property indices in Table 5, for example

$$R_{n,1,0} + R_{m,2,1} \overset{k_{t,c}}{\rightarrow} P_{n+m,3,1} \ . \tag{70}$$

Other properties, e.g. the number of radical centers per chain, may be used as well. As already mentioned, polymer chains with multiple radical centers are not considered here, but the dead species P and living species R can be considered classes with one or zero radical centers respectively. The advantage of the classes approach is that a multi-dimensional property distribution can be reconstructed from the concentration distributions of different classes. Since only a finite number of property classes can be considered, a cut-off class must be defined in which all classes for property indices that are higher than the cut-off value are collected. Reconsidering the example in Equation (70), a cut-off value of 10 for the number of TDBs and the number of branches would lead to

$$R_{n,6,7} + R_{m,8,9} \overset{k_{t,c}}{\rightarrow} P_{n+m,10,10} \ . \tag{71}$$

Of course, the computational effort increases with every additional property class, and so, this approach should only be used, if suitable cut-off values are not too high, typically lower than 10 [35].

If this is not the case, another approach using so-called pseudo distributions may be used [36]. These pseudo distributions are defined as the moments of all discrete property coordinates except one – usually the chain length – that is solved for explicitly. For example,

$$\Psi_n^{l,o} = \sum_{k=0}^{\infty} k^o \sum_{i=0}^{\infty} i^l P_{n,i,k} \tag{72}$$

is the l–th TDB and o–th branching moment for chains of length n. Taking the zeroth moments of all other property coordinates gives the distribution of chain lengths

$$\Psi_n^{0,0} = P_n \ , \tag{73}$$

which is widely used in one-dimensional models. The first moments can be understood as chain length distributed counters for this property. For the system considered here, $\Psi_n^{1,0}$ and $\Psi_n^{0,1}$ give the concentration of TDBs and branches in chains of length n respectively. If the system is non-linear in one of the property coordinates, a closure problem exists as discussed in Section 2.3.1 and an estimate for a higher moment of this property must be found by a suitable closure relation. In this case, using higher moments of this property is a necessity to minimize the effect of the closure relation on lower moments, while, otherwise, higher moments may be used to gain additional, averaged information.

As long as suitable closure relations can be found, moment models should be preferred, since a large number of classes, would have to be used for many applications [33], [35]. For example, the number of TDBs may take very large values for some process conditions in the present case. Therefore, pseudo distribution models will either be derived or models from literature will be adapted for the polymerization of NVP. For validation purposes, a comparison to an equivalent model using property classes for the number of TDBs for the reference case will be made. A model with classes up to 10 TDBs is applicable in this case as will be seen in Section 4.2.2 and Section 4.2.3. This model will be referred to as the TDB classes model.

The three-dimensional balance equations corresponding to the reaction system in Table 5 are given in [33] and will not be repeated here in full length. As an example, the contribution of the TDB propagation reaction is

$$\begin{aligned}\frac{dR_{n,i,k}}{dt} \mathrel{+}= & -k_{p,TDB} R_{n,i,k} \sum_{m=1}^{\infty}\sum_{j=0}^{\infty}\sum_{l=0}^{\infty} jP_{m,j,l} \\ & + k_{p,TDB} \sum_{m=1}^{n-1}\sum_{j=0}^{i+1}\sum_{l=0}^{k} jP_{m,j,l} R_{n-m,i-j+1,k+l-1}\end{aligned} \tag{74}$$

and

$$\frac{dP_{n,i,k}}{dt} \mathrel{+}= -k_{p,TDB} iP_{n,i,k} \sum_{m=1}^{\infty}\sum_{j=0}^{\infty}\sum_{l=0}^{\infty} R_{m,j,l} \tag{75}$$

for the living and the dead species respectively. Since the number of branches does not appear in any reaction rate and, therefore, has no direct feedback on the reaction kinetics, the property index may simply be dropped as long as no information on the distribution of branches is desired [33]. Therefore, the two-dimensional reaction system in Table 7 will be used as the basis of the model development in this thesis. Since the chain

length distribution is usually desired because it is experimentally accessible and determines the macroscopic properties of the product, models that give the full chain length distribution will be derived first in Section 4.2.2. As will be seen, closure relations are needed in these models due to the non-linearity in the TDB propagation reaction. In Section 4.2.3, a model that does not need any closure relation and, therefore, contains exactly the same average information as the original two-dimensional model will be presented. Based on the model in Section 4.2.3, a model with zero property dimensions, which can be applied in CFD simulations or parameter estimations, will be introduced in Section 4.2.4. An overview of the kinetic models that were developed is given in Table 8. An illustration of the modeling workflow and a summary of the microstructural polymer properties that can be extracted from the models are given in Section A.1.1 of the appendix.

Table 7. Set of the two-dimensional reactions as basis of the model development.

Initiation	$I_2 \overset{k_d}{\rightarrow} 2f_d I \quad / \quad I + M \overset{k_p}{\rightarrow} R_{1,0}$
Propagation	$R_{n,i} + M \overset{k_p}{\rightarrow} R_{n+1,i}$
Termination by combination	$R_{n,i} + R_{m,j} \overset{k_{t,c}}{\rightarrow} P_{n+m,i+j}$
Transfer to monomer	$R_{n,i} + M \overset{k_{tr,m}}{\longrightarrow} P_{n,i} + R_{1,1}$
Propagation of TDBs	$R_{n,i} + P_{m,j} \overset{j \cdot k_{p,TDB}}{\longrightarrow} R_{n+m,i+j-1}$

Table 8. Overview of all models used in this thesis.

Short name of model	Sections	Distributions	Definition
TDB classes	4.2.2, 4.2.3	$R_{n,i=(0,1,...i_{\max})}$	chain length (n) distribution/class with i TDBs of polymers with one radical center
		$P_{n,i=(0,1,...i_{\max})}$	chain length (n) distribution/class with i TDBs of polymers with no radical center
TDB moment	4.2.2	$\sum_{i=0}^{\infty} i^l R_{n,i} = \Phi_n^l$	l–th TDB moment (pseudo-) chain length (n) distribution of polymers with one radical center
		$\sum_{i=0}^{\infty} i^l P_{n,i} = \Psi_n^l$	l–th TDB moment (pseudo-) chain length (n) distribution of polymers with no radical center
TDB reduced moment	4.2.2.1	$\sum_{i=0}^{\infty} R_{n,i} = R_n$	zeroth TDB moment chain length (n) distribution of polymers with one radical center
		$\sum_{i=0}^{\infty} P_{n,i} = P_n$	zeroth TDB moment chain length (n) distribution of polymers with no radical center

TDB distribution	4.2.3	$\sum_{n=1}^{\infty} n^k R_{n,i} = \Lambda_i^k$	k–th chain length moment (pseudo-) TDB (i) distribution of polymers with one radical center
		$\sum_{n=1}^{\infty} n^k P_{n,i} = M_i^k$	k–th chain length moment (pseudo-) TDB (i) distribution of polymers with no radical center
TDB double moment	4.2.4	$\sum_{i=0}^{\infty} i^l \sum_{n=1}^{\infty} n^k R_{n,i} = \lambda^{k,l}$	k–th chain length moment and l–th TDB moment of polymers with one radical center
		$\sum_{i=0}^{\infty} i^l \sum_{n=1}^{\infty} n^k P_{n,i} = \mu^{k,l}$	k–th chain length moment and l–th TDB moment of polymers with no radical center

4.2.2 Chain length as the only discrete property coordinate

If the distribution of polymer chain lengths is of interest, which is mostly the case, a one-dimensional model in the chain length property coordinate is desirable. The number of TDBs as a discrete property coordinate can be eliminated by applying the moment operator on this coordinate leading to the pseudo distributions

$$\sum_{i=0}^{\infty} i^l R_{n,i} = \Phi_n^l \tag{76}$$

for the l-th TDB moment on living polymer chains with n repeat units and

$$\sum_{i=0}^{\infty} i^l P_{n,i} = \Psi_n^l \tag{77}$$

as the equivalent for dead polymer chains. The nomenclature as in [33] has been used for easier comparison. A detailed derivation of the model is given in [33] as well and will not be repeated here but the most important properties will be highlighted.

As mentioned before, creation and propagation of TDBs are considered to be important side reactions leading to broad chain length distributions and chains with very high molecular weights. The corresponding reaction rate is proportional to the number of TDBs incorporated in the chain that is involved in the propagation reaction and the set of equations of the moments of i can, therefore, not be closed as illustrated for the zeroth TDB moments:

$$\frac{\partial \Phi_n^0}{\partial t} += -k_{p.TDB} \Phi_n^0 \sum_m \Psi_m^1 + k_{p,TDB} \sum_m \Psi_{n-m}^1 \Phi_m^0 \ , \tag{78}$$

$$\frac{\partial \Psi_n^0}{\partial t} += -k_{p,TDB} \Psi_n^1 \sum_m \Phi_m^0 \ . \tag{79}$$

It was shown in [33] that, if equations up to the second TDB moment are solved, simple closure relations like

$$\Psi_n^3 = D' \frac{\Psi_n^2 \Psi_n^2}{\Psi_n^1} \tag{80}$$

for the third TDB moment are sufficient. D' is a dispersity and is assumed to be constant for all chain lengths and all times. In this section $D' = 1.15$ will be used, which was estimated using the steady state value

$$D' \approx \frac{\mu_{classes}^{0,3}\mu_{classes}^{0,1}}{\mu_{classes}^{0,2}\mu_{classes}^{0,2}} \tag{81}$$

with

$$\mu_{classes}^{0,l} = \sum_{i}^{i_{max}} \sum_{n}^{\infty} i^l P_{n,i} \tag{82}$$

of the TDB classes model for the reference case.

If the reaction mechanism allows for a maximum of one TDB per chain – which is the case, if only termination by disproportionation takes place and creation of TDBs through this reaction is ignored – then all TDB moments higher than $l = 1$ are the same since

$$\sum_{i=0}^{1} i^l P_{n,i} = 0^l \cdot P_{n,0} + 1^l \cdot P_{n,1}. \tag{83}$$

No closure relation is necessary and only equations for the zeroth and first TDB moments need to be solved. This is not the case for the polymerization of NVP in aqueous solution but will serve as a reference for the development of further models. Of course, the TDB classes model using only two classes for one or zero TDBs must be equivalent to the TDB moment model in this case [33].

Information that can be extracted from the TDB moment model are, for example, the average number of TDBs per chain of length n

$$p(n) = \frac{\Psi_n^1}{\Psi_n^0} \tag{84}$$

as well as the corresponding ratio of the integrals over all chain lengths

$$\frac{c^{TDB}}{\lambda_0^P} = \frac{\sum_n \Psi_n^1}{\sum_n \Psi_n^0}\,, \tag{85}$$

which is the average number of TDBs per molecule.

As a first example, a system with a maximum of one TDB per chain is studied in which the TDB moment model and the TDB classes model are equivalent. This can be achieved by switching off termination by combination and using the disproportionation reaction without creation of TDBs instead. As can be understood from Figure 36 and Figure 37, the TDB classes and the TDB moment model give the same results. The average distribution of TDBs shown in Figure 36 and Figure 37 is constant over all chain lengths and its value decreases with lower values of the ratio of the transfer to monomer to propagation

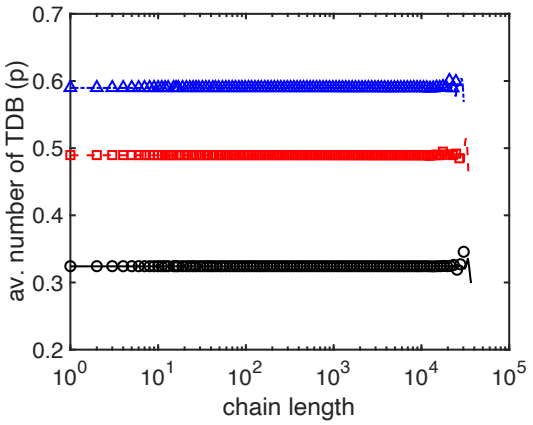

Figure 36. Effect of the variation of the ratio of transfer to monomer to propagation $f_{tr,m}$ on the average number of TDBs $p(n)$ as a function of chain length using the TDB moment model for the case of a maximum of one TDB per molecule and the reference case: lines – TDB moment model, symbols – TDB classes; black – $f_{tr,m} = 3 \cdot 10^{-4}$, red – $f_{tr,m} = 6 \cdot 10^{-4}$, blue – $f_{tr,m} = 9 \cdot 10^{-4}$.

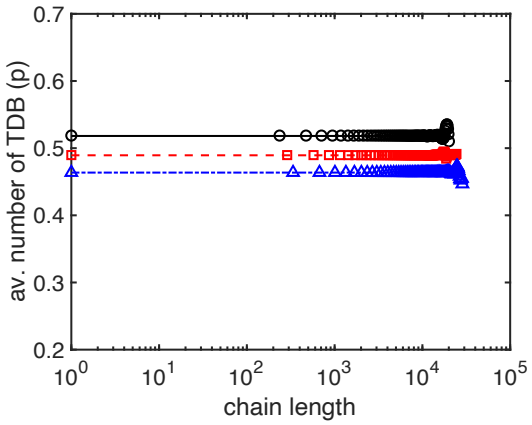

Figure 37. Effect of the variation of $k_{p,TDB}$ on the average number of TDBs $p(n)$ as a function of chain length using the TDB moment model for the case of a maximum of one TDB per molecule and the reference case: lines – TDB moment model, symbols – TDB classes;
black – $k_{p,TDB} = 1250$ l mol^{-1} s^{-1},
red – $k_{p,TDB} = 2500$ l mol^{-1} s^{-1},
blue – $k_{p,TDB} = 3750$ l mol^{-1} s^{-1}.

rate $f_{tr,m}$ and higher values for TDB propagation coefficient $k_{p,TDB}$ due to the lower production and higher consumption rate of TDBs respectively. As mentioned before, this model cannot be used for the polymerization of NVP in aqueous solution due to the different termination mechanism, but it will serve as a reference for the model development in Section 4.2.2.1.

The more relevant case for the polymerization of NVP is one in which termination by combination takes place and, thus, more than one TDB per chain may exist. As shown in Figure 38, the number of TDBs increases approximately linear with the chain length intersecting at a value between 0 and 1 at $n = 1$. The average number of TDBs per molecule c^{TDB}/λ_0^P illustrated in Figure 39 increases steeply in the beginning of simulation and decreases at higher monomer conversion, which corresponds to higher polymer contents when TDBs are consumed at a higher rate in the TDB propagation reaction. Figure 40 and Figure 41 show the stationary chain length distribution and the evolution of monomer conversion. A comparison to the TDB classes model with classes for 0 to a maximum of

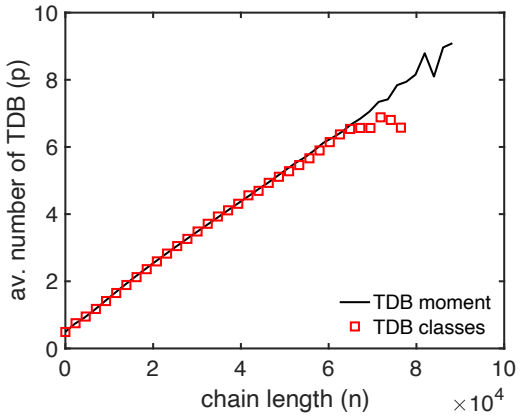

Figure 38. Comparison of the average number of TDBs $p(n)$ as a function of chain length for the TDB moment ($D' = 1.15$) and classes model for the case of more than one TDB per chain and the reference case.

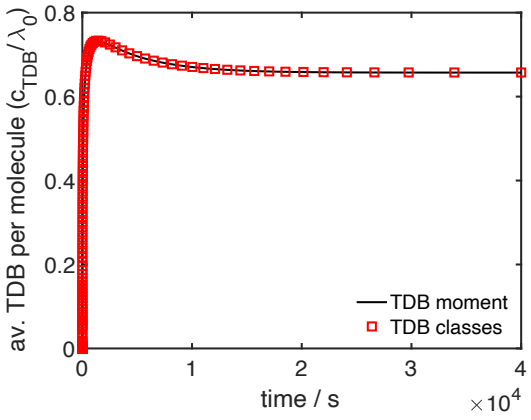

Figure 39. Comparison of the evolution of the average number of TDB per molecule c^{TDB}/λ_0^P for the TDB moment ($D' = 1.15$) and classes model for the case of more than one TDB per chain and the reference case.

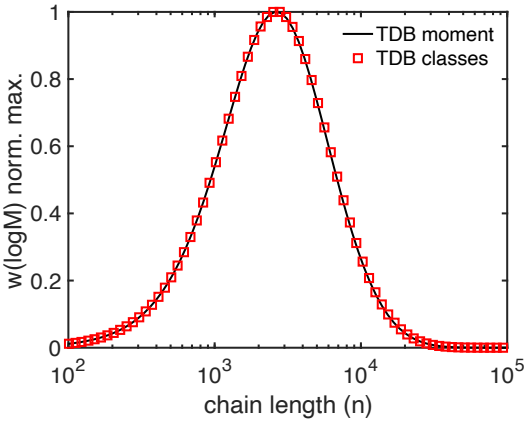

Figure 40. Comparison of the normalized GPC distribution for the TDB moment ($D' = 1.15$) and classes model for the case of more than one TDB per chain and the reference case.

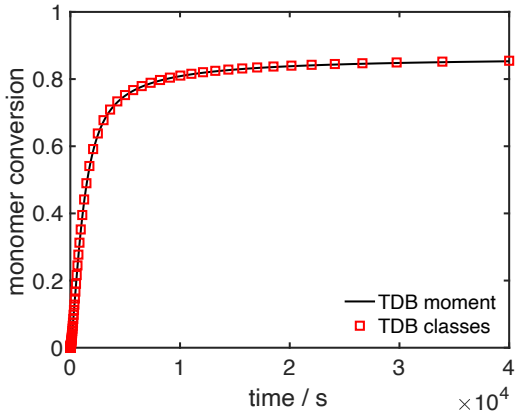

Figure 41. Comparison of the evolution of monomer conversion for the TDB moment ($D' = 1.15$) and classes model for the case of more than one TDB per chain and the reference case.

10 TDBs per chain was made, demonstrating the validity of the implementation of both models and their applicability for the reference case.

As shown in Figure 42, the average number of TDBs per molecule c^{TDB}/λ_0^P strongly depends on the ratio of transfer to monomer to propagation $f_{tr,m}$ and, therefore, the production rate of TDBs. After a maximum at around 50 % monomer conversion, the average number of TDBs per molecule c^{TDB}/λ_0^P decreases to its stationary value, which also depends on the TDB consumption rate as shown in Figure 43.

As shown in Figure 44 and Figure 45, the slope of the average number of TDBs $p(n)$ as a function of chain length is strongly affected by the ratio of transfer to monomer to propagation $f_{tr,m}$ while changes of the TDB propagation rate coefficient $k_{p,TDB}$ only have a minor effect under the reference case conditions.

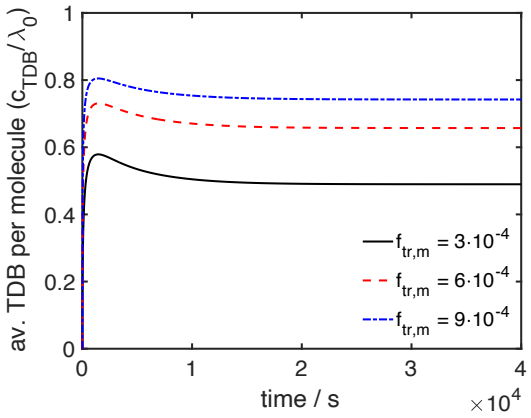

Figure 42. Effect of the variation of the ratio of transfer to monomer to propagation $f_{tr,m}$ on the evolution of the average number of TDB per molecule c^{TDB}/λ_0^P using the TDB moment model ($D' = 1.15$) for the case of more than one TDB per chain and the reference case.

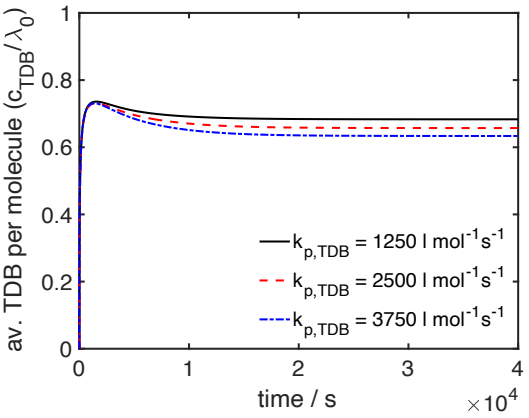

Figure 43. Effect of the variation of the TDB propagation rate coefficient $k_{p,TDB}$ on evolution of the average number of TDB per molecule c^{TDB}/λ_0^P using the TDB moment model ($D' = 1.15$) for the case of more than one TDB per chain and the reference case.

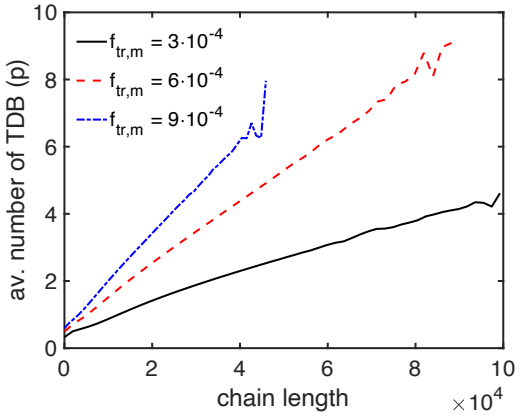

Figure 44. Effect of the variation of the ratio of transfer to monomer to propagation $f_{tr,m}$ on the average number of TDBs $p(n)$ as a function of chain length using the TDB moment model ($D' = 1.15$) for the case of more than one TDB per chain and the reference case.

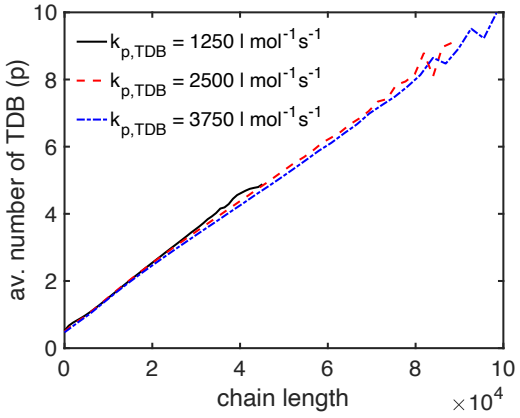

Figure 45. Effect of the variation of TDB propagation rate coefficient $k_{p,TDB}$ on the average number of TDBs $p(n)$ as a function of chain length using the TDB moment model ($D' = 1.15$) for the case of more than one TDB per chain and the reference case.

The conditions of the reference case can be considered mild as will be seen in later sections and the closure relation for the TDB moment model as well as the cutoff at a maximum 10 TDBs per chain do not seem to affect the results under these conditions. Nevertheless, the computational effort for the simulations presented here was already too large to apply these models for practical purposes, e.g. parameter estimation or process design. Models with lower computational effort are desirable.

4.2.2.1 Reduction of model complexity by simple correlations for the chain length-dependence of the concentration of TDBs

The simplest possible model contains only two distributions – one for the living and one for the dead polymer species – as defined in Equation (73). As outlined in Section 4.2.1 and Section 4.2.2, closure relations are necessary, if the moment approach is used on the number of TDB property coordinate because of the non-linearity of the TDB propagation rate. For the case that only the evolution of the zeroth TDB moments Ψ_n^0 and Φ_n^0 is calculated, an estimate for the first TDB moment Ψ_n^1 is necessary. The contribution of the reaction rates for TDB propagation can be rewritten as

$$\begin{aligned}\frac{\partial \Phi_n^0}{\partial t} \mathrel{+}= & -k_{p,TDB}\Phi_n^0 \sum_m \Psi_m^1 + k_{p,TDB} \sum_m \Psi_{n-m}^1 \Phi_m^0 \\ = & -k_{p,TDB}\Phi_n^0 \sum_m \frac{\Psi_m^1}{\Psi_m^0}\Psi_m^0 + k_{p,TDB} \sum_m \frac{\Psi_{n-m}^1}{\Psi_{n-m}^0}\Psi_{n-m}^0 \Phi_m^0 \ ,\end{aligned} \tag{86}$$

$$\frac{\partial \Psi_n^0}{\partial t} \mathrel{+}= -k_{p,TDB}\Psi_n^1 \sum_m \Phi_m^0 = -k_{p,TDB}\frac{\Psi_n^1}{\Psi_n^0}\Psi_n^0 \sum_m \Phi_m^0 \ , \tag{87}$$

which can be recast into the reaction scheme

$$\Phi_n^0 + \Psi_m^0 \xrightarrow{k_{p,TDB} \cdot \frac{\Psi_m^1}{\Psi_m^0}} \Phi_{n+m}^0 \ . \tag{88}$$

The ratio $\Psi_m^1/\Psi_m^0 = p(m)$ is the probability of finding a TDB in a dead chain of length m, which has been defined previously and can generally be calculated from higher moment models. As suggested by the results shown in Figure 36 and Figure 38 before, $p(n)$ may be approximated by different linear relationships in n depending on the termination mechanism:

$$\frac{\Psi_n^1}{\Psi_n^0} \approx p_0(n) = A_0 \ , \tag{89}$$

$$\frac{\Psi_n^1}{\Psi_n^0} \approx p_1(n) = A_1 \cdot n, \tag{90}$$

$$\frac{\Psi_n^1}{\Psi_n^0} \approx p_2(n) = A_2 \cdot n + B_2 \ . \tag{91}$$

The first approximation with index 0 assumes a constant distribution of TDBs over all chain lengths and can only be valid for the case of a maximum of one TDB per molecule. If the overall concentration of TDBs in all chains

$$c^{TDB} = \sum_{n=1}^{\infty} \Psi_n^1 = \lambda_0^{\Psi^1} \tag{92}$$

is known, A_0 is determined by

$$c^{TDB} = \sum_{n=1}^{\infty} \Psi_n^1 = A_0 \sum_{n=1}^{\infty} \Psi_n^0 = A_0 \cdot \lambda_0^P \ , \tag{93}$$

and, therefore,

$$p_0(n) = A_0 = \frac{c^{TDB}}{\lambda_0^P} \,. \tag{94}$$

The other two models may be applied for the case of more than one TDB per chain. The coefficient of the second model with index 1 can be determined by

$$c^{TDB} = \sum_{n=1}^{\infty} \Psi_n^1 = A_1 \sum_{n=1}^{\infty} n \cdot \Psi_n^0 = A_1 \cdot \lambda_1^P \tag{95}$$

and, therefore,

$$p_1(n) = n \cdot \frac{c^{TDB}}{\lambda_1^P} \tag{96}$$

and for the last model with index 2 one of the coefficients may be determined by

$$c^{TDB} = \sum_{n=1}^{\infty} \Psi_n^1 = A_2 \sum_{n=1}^{\infty} n \cdot \Psi_n^0 + B_2 \sum_{n=1}^{\infty} \Psi_n^0 = A_2 \cdot \lambda_1^P + B_2 \cdot \lambda_0^P. \tag{97}$$

If B_2 is determined, then

$$p_2(n) = A_2 \cdot n + \frac{c^{TDB}}{\lambda_0^P} - A_2 \cdot \frac{\lambda_1^P}{\lambda_0^P} = A_2 \cdot (n - \overline{N_n}) + \frac{c^{TDB}}{\lambda_0^P} \,. \tag{98}$$

with the number average chain length $\overline{N_n}$ of dead polymer chains. The models including $p_0(n)$ and $p_1(n)$ are actually equivalent to the models discussed in [49] except that all dead and living species are collected in one distribution respectively. In [49], it was found that the approximation $p_0(n)$ cannot represent experimental data of the polymerization of NVP. This is in agreement with the previous discussion that the approximation $p_0(n)$ is equivalent to the assumption of a constant distribution of TDBs over all chain lengths, which is not true for the polymerization of NVP due to the termination mechanism. Approximations similar to $p_1(n)$ and $p_2(n)$ were also suggested in [52] and [53] for the TDB

propagation rate in the polymerization of ethylene based on arguments using the reaction mechanism. The models described in [49] and [52] include an estimate of the concentration of TDB c^{TDB} from a balance of a massless counter species [27] H^{TDB}

$$\frac{dH^{TDB}}{dt} = f_{tr,M} k_p M \sum_{m=1}^{\infty} R_m - \sum_{n=1}^{\infty} k_{p,TDB} \left(p(n) P_n \sum_{m=1}^{\infty} R_m \right) \tag{99}$$

that is produced and consumed with the same rates at which TDBs are produced or consumed. By introducing this counter species, c^{TDB} can be calculated without explicit knowledge of the distribution Ψ_n^1 as

$$c^{TDB} = \sum_{n=1}^{\infty} \Psi_n^1 = H^{TDB} \ . \tag{100}$$

Besides a counter for the concentration of TDBs, all reactions leading to branches in the polymer backbone structure may be quantified by another counter species $c^B = H^B$ that allows the calculation of the average number of branches per molecule

$$n_0^B = \frac{c^B}{\lambda_0^P} \tag{101}$$

or per repeat unit

$$n_1^B = \frac{c^B}{\lambda_1^P} \ . \tag{102}$$

The full set of reactions for this model, which will be referred to as the TDB reduced moment model, is given in Table 9 using the common notation $\Psi_n^0 = P_n$ and $\Phi_n^0 = R_n$. For completeness, Figure 46 and Figure 47 show a comparison of the TDB moment model for the case of a maximum of one TDB per chain and the TDB reduced moment model using $p_0(n)$. The results are in agreement. Compared to the TDB moment or TDB classes model, only two distributions are needed, which reduces the computational effort for the

simulation of such systems. As discussed, this model should not be used for the polymerization of NVP and will, therefore, be excluded from the following discussion.

Table 9. Full set of reactions for the reduced model including counter species.

Reaction type	Reaction scheme
Initiation	$I_2 \overset{k_d}{\rightarrow} 2I^* \quad / \quad I^* + M \overset{k_p}{\rightarrow} R_1$
Propagation	$R_n + M \overset{k_p}{\rightarrow} R_{n+1}$
Termination by disproportionation	$R_n + R_m \overset{k_{t,d}}{\rightarrow} P_n + P_m$
Termination by combination	$R_n + R_m \overset{k_{t,c}}{\rightarrow} P_{n+m}$
Transfer to monomer	$R_n + M \xrightarrow{k_{tr,m}} P_n + R_1 + H^{TDB}$
Propagation of TDBs	$R_n + P_m \xrightarrow{p(m)\cdot k_{p,TDB}} R_{n+m} + H^B - H^{TDB}$

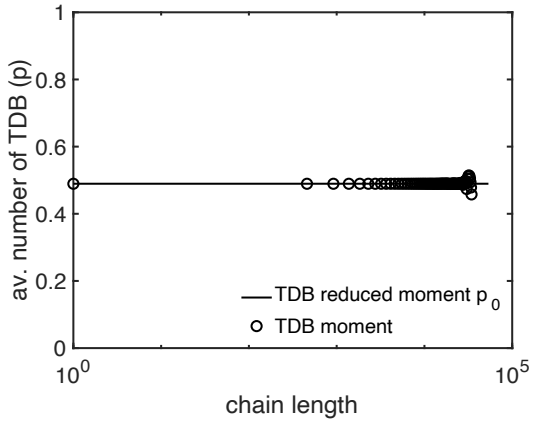

Figure 46. Comparison of the steady state average number of TDBs $p(n)$ as a function of chain length for the TDB moment and reduced model for the case of a maximum of one TDB per chain and the reference case.

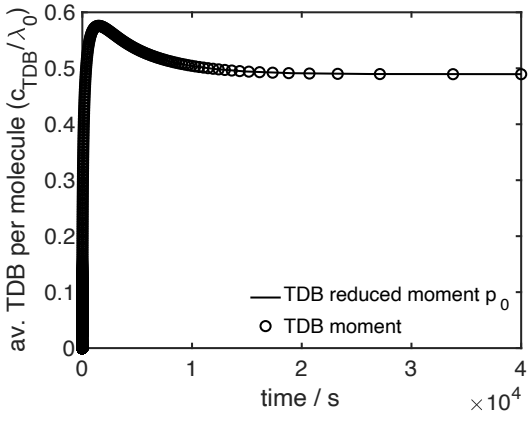

Figure 47. Comparison of the evolution of the average number of TDB per molecule c^{TDB}/λ_0^P for the TDB moment and reduced model for the case of a maximum of one TDB per chain and the reference case.

Since both $p_1(n)$ and $p_2(n)$ account for the chain length dependence of number of TDBs, they are candidates as models for Ψ_n^1/Ψ_n^0 in case of termination by combination. The additional parameter A_2 in Equation (98) may be fixed by extracting the slope of a linear fit to the data from the TDB moment model presented in Figure 38. From Figure 48 and Figure 49, it can easily be seen that $p_2(n)$ gives a more realistic approximation of $\Psi_n^1 = \Psi_n^0 \cdot p(n)$ than $p_1(n)$. While the approximation of Ψ_n^1 that is calculated from simulations using $p_2(n)$ is in reasonable agreement with the moment model, applying $p_1(n)$ results in a completely different form of the distribution. The reactivity of short chains is strongly underestimated, while that for long chains is overestimated. In consequence, the weight average molecular weight $\overline{M_w}$ shown in Figure 51 is in very good agreement with the TDB moment model, if $p_2(n)$ is used, while it diverges, if $p_1(n)$ is applied.

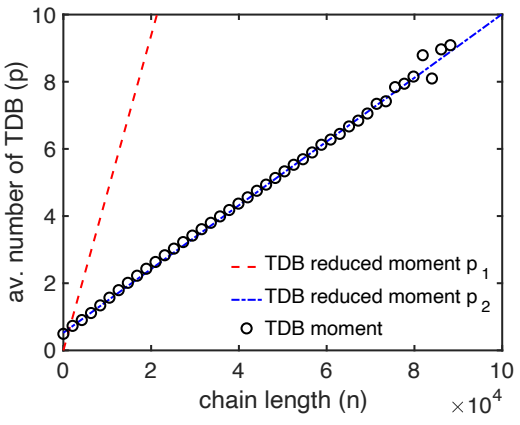

Figure 48. Comparison of the steady state average number of TDBs $p(n)$ as a function of chain length for the TDB moment ($D' = 1.15$) and reduced models using p_1 and p_2 ($A_2 = 9.49 \cdot 10^{-5}$) for the case of more than one TDB per chain and the reference case.

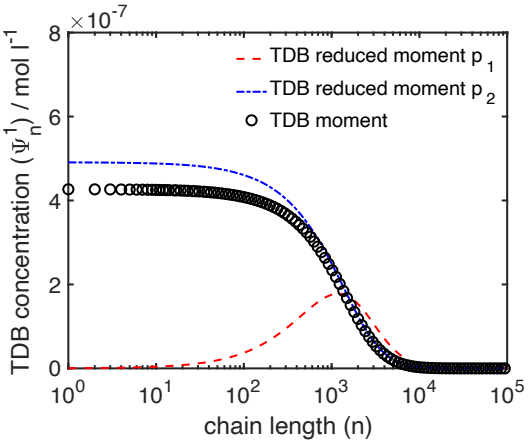

Figure 49. Comparison of the steady state TDB concentration distribution Ψ_n^1 as a function of chain length for the TDB moment ($D' = 1.15$) and reduced models using p_1 and p_2 ($A_2 = 9.49 \cdot 10^{-5}$) for the case of more than one TDB per chain and the reference case.

Interestingly, the overall average number of TDBs per molecule illustrated in Figure 50 as well as the number average molecular weight $\overline{M_n}$ shown in Figure 51 are in very good agreement with the TDB moment model for both approximations. The reason for this

behavior is that the coefficients of $p_1(n)$ and $p_2(n)$ were fixed using the same integral value c^{TDB} in Equation (95) and Equation (97). Therefore, the overall concentration of TDBs as well as overall polymer concentration, i.e. the zeroth chain length moment, are the same for both approximations. Since the TDB propagation reaction does not influence the overall concentration of polymerized monomer units in chains R and P, the number average molecular weight $\overline{M_n}$ is not affected by the choice of $p(n)$ either. A more detailed discussion can be found in Section A.1.2 of the appendix.

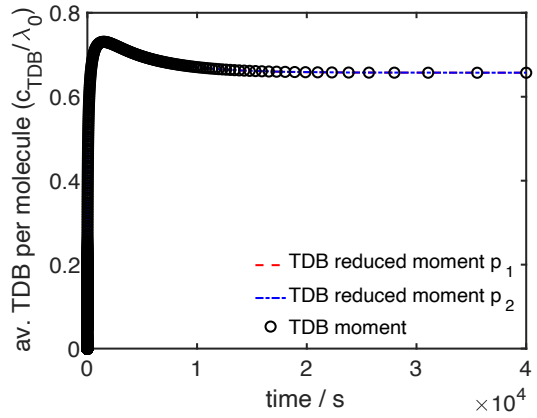

Figure 50. Comparison of the evolution of the average number of TDB per molecule c^{TDB}/λ_0^P for the TDB moment ($D' = 1.15$) and reduced models using p_1 and p_2 ($A_2 = 9.49 \cdot 10^{-5}$) for the reference case. Red and blue lines are indistinguishable by eye.

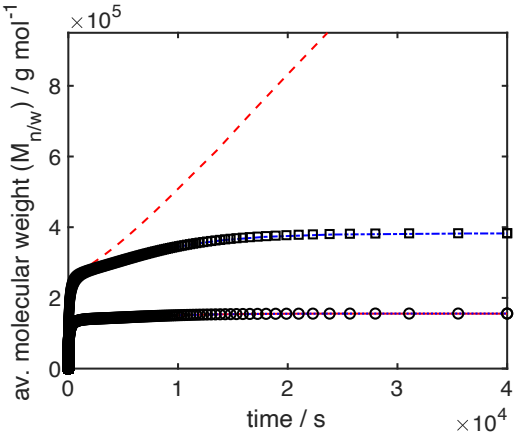

Figure 51. Comparison of the evolution of the molecular weight averages for the TDB moment ($D' = 1.15$) and reduced models using p_1 and p_2 ($A_2 = 9.49 \cdot 10^{-5}$) for the reference case: red – TDB reduced moment model using p_1; blue – TDB reduced moment model using p_2; symbols – TDB moment model; solid, dotted, circles – $\overline{M_n}$; dashed, dashed-dotted, squares – $\overline{M_w}$.

As observed in [49] and confirmed by theoretical arguments in this thesis, the approximation $p_0(n)$ should not be used for the polymerization of NVP. The approximation $p_1(n)$ cannot represent the results from the TDB moment model adequately, and, therefore, $p_2(n)$ should be preferred although one more parameter needs to be fixed. The

latter may be estimated from simulations using the TDB moment model as discussed in this section. The estimation of the parameter A_2 will be revisited in Section 4.2.4.1.

4.2.3 Number of terminal double bonds as the only discrete property coordinate

The moment models introduced in Section 4.2.2 suffer from the drawback that the systems of equations cannot be closed because the reaction mechanism is non-linear in the discrete property coordinate i, the number of TDBs. The average information of these models can, therefore, not be exactly the same as that of the two-dimensional original model, since additional assumptions in form of the closure relations Equation (80) or Equation (98) must be introduced. For the polymerization of NVP this problem can be circumvented by using the moment approach on the other discrete property coordinate, the chain length n, since no reaction rate is proportional to this property coordinate. The corresponding pseudo distributions are

$$\sum_{n=1}^{\infty} n^k R_{n,i} = \Lambda_i^k \tag{103}$$

for the k-th chain length moment on living polymer chains carrying i TDBs and

$$\sum_{n=1}^{\infty} n^k P_{n,i} = M_i^k \tag{104}$$

as the equivalent for dead polymer chains. For the zeroth chain length moments Λ_i^0 and M_i^0, the closed set of equations is

$$\frac{d\Lambda_i^0}{dt} += -k_{t,c}\Lambda_i^0 \sum_{j=0}^{\infty}\Lambda_j^0 - k_{tr,m}M\Lambda_i^0 - k_{p,TDB}\left(\Lambda_i^0\sum_{j=0}^{\infty}jM_j^0 - \sum_{j=0}^{i+1}jM_j^0\Lambda_{i-j+1}^0\right), \quad (105)$$

$$\frac{dM_i^0}{dt} += \frac{1}{2}k_{t,c}\sum_{j=0}^{i}\Lambda_j^0\Lambda_{i-j}^0 + k_{tr,m}M\Lambda_i^0 - k_{p,TDB}iM_i^0\sum_{j=0}^{\infty}\Lambda_j^0. \quad (106)$$

Since this model gives the chain length averaged distribution of TDBs, it will be referred to as the TDB distribution model. If only the distribution of TDBs is of interest, only the equations for the zeroth moments Λ_i^0 and M_i^0 need to be solved. Of course, higher moments offer additional information as for example the molecular weight averages

$$\overline{M_n} = \frac{\sum_{i=0}M_i^1}{\sum_{i=0}M_i^0}\cdot MW_M, \quad (107)$$

$$\overline{M_w} = \frac{\sum_{i=0}M_i^2}{\sum_{i=0}M_i^1}\cdot MW_M. \quad (108)$$

The full set of equations of the TDB distribution model up to the second chain length moments Λ_i^2 and M_i^2 as well as a formulation in terms of reaction modules for the implementation in PREDICI® are given in Section A.1.4 and Section A.1.5 of the appendix respectively. The average number of TDBs per molecule c^{TDB}/λ_0^P defined in Equation (85) can be extracted as

$$\frac{c^{TDB}}{\lambda_0^P} = \frac{\sum_{i=0}iM_i^0}{\sum_{i=0}M_i^0}\ , \quad (109)$$

but is not illustrated again. To demonstrate the information gained from this model, simulations using the reference case were performed and compared to simulations using the TDB classes model to validate the derivation and implementation. Figure 52 shows the concentration distribution as a function of TDB. With increasing number of TDBs, the concentration decreases rapidly by orders of magnitude. Despite their low concentration,

these chains have a high reactivity because of the large number of TDBs they carry and may act as precursors for an insoluble gel phase. A maximum of 10 TDBs per chain is a reasonable cut off for the TDB classes model for the reference case as confirmed by the molecular weight averages shown in Figure 53. It is interesting to note that the concentration of chains with 10 TDB calculated from the TDB classes model is slightly higher than that calculated from the TDB distribution model. The reason is simply that all molecules with more TDBs than the cut-off are collected in the cut-off distribution, which is in this case 10 TDB.

Although applicable for the reference case, the TDB classes model is computationally very expensive. The TDB distribution model, on the other hand, can be applied for all process parameters that were tested at a low computational cost, which is suitable for parameter estimations or large simulation studies. Additionally, it can be applied in cases in which

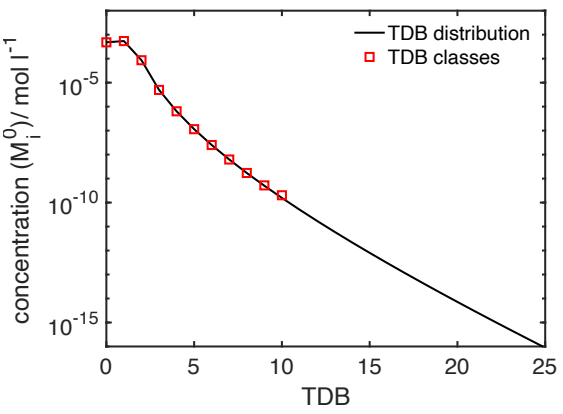

Figure 52. Comparison of the concentration distribution M_i^0 as a function of TDBs for the TDB distribution and classes models for the case of more than one TDB per chain and the reference case.

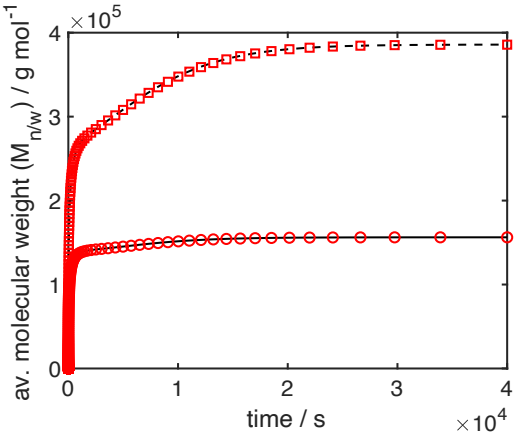

Figure 53. Comparison of the evolution of the molecular weight averages for the TDB distribution and classes models for the case of more than one TDB per chain and the reference case: black solid – number average molecular weight $\overline{M_n}$, TDB classes model; red circles – $\overline{M_n}$, TDB distribution model; black dashed – weight average molecular weight $\overline{M_w}$, TDB classes model; red squares – $\overline{M_w}$, TDB distribution model.

the concentration of polymers with more than 10 TDBs is relevant and is, therefore, a more versatile benchmark and will be used as such subsequently.

As can be understood from Figure 54 and Figure 55, the concentration of chains with a large number of TDBs increases both with the TDB propagation rate coefficient $k_{p,TDB}$ and the ratio of the transfer to monomer reaction rate coefficient to the propagation rate coefficient $f_{tr,m}$. Since the former is a combination reaction, the number of TDBs is additive and the concentration of chains with many TDB increases while the concentration of chains with a low number of TDBs decreases slightly. Of course, the fact that TDBs are consumed by the reaction dampens this effect. The transfer to monomer reaction increases the frequency and the overall concentration of TDBs on the polymer backbone and the distribution is shifted to higher concentrations for all except for chains with zero TDBs. If the transfer to monomer rate is high enough, more chains with one than with zero TDB exist in the stationary state. In the reference case over 56% of chains carry at least one TDB and over 8% carry at least two TDB.

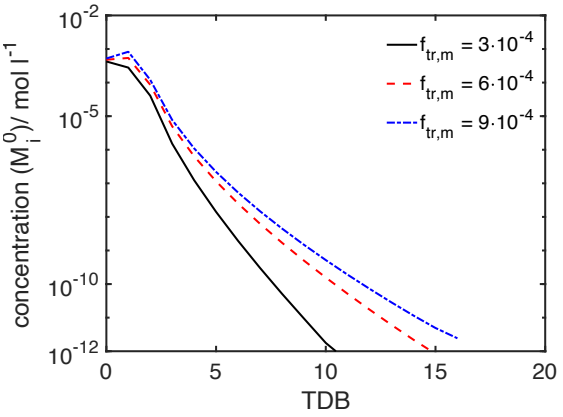

Figure 54. Effect of the variation of the ration of transfer to monomer to propagation $f_{tr,m}$ on the concentration distribution as a function of TDBs for the TDB distribution model for the case of more than one TDB per chain and the reference case.

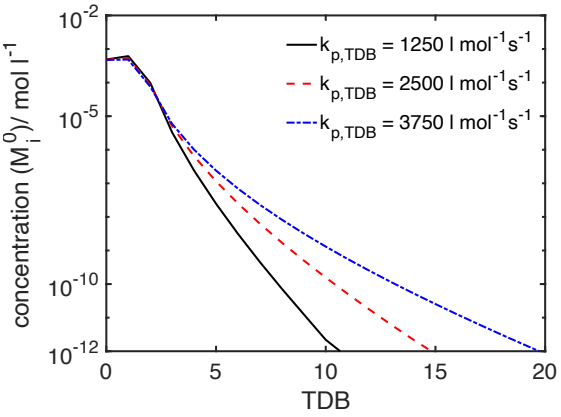

Figure 55. Effect of the variation of the TDB propagation rate coefficient $k_{p,TDB}$ on the concentration distribution as a function of TDBs for the TDB distribution model for the case of more than one TDB per chain and the reference case.

4.2.4 A moment model on all discrete property coordinates

For some applications, as for example the implementation in CFD codes or parameter estimations, models with zero property dimensions, i.e. moments taken on all property dimensions, are desirable because of the reduction of the computational effort. For the TDB reduced moment model, this is possible, but the redefined closure relation for the first TDB moment, Equation (98), introduces an additional parameter A_2 into the model, which has to be estimated. This moment model is given in Section A.1.3 of the appendix for completeness but was not used for any simulations in this thesis.

It is more desirable to derive a zero-dimensional model based on the TDB distribution model from Section 4.2.3, since no additional assumption has to be made in its derivation and the average information is exactly the same as that of the original two-dimensional model. The quantities of interest are the double moments

$$\sum_{i=0}^{\infty} i^l \sum_{n=1}^{\infty} n^k R_{n,i} = \sum_{i=0}^{\infty} i^l \, \Lambda_i^k = \lambda^{k,l} \tag{110}$$

and

$$\sum_{i=0}^{\infty} i^l \sum_{n=1}^{\infty} n^k P_{n,i} = \sum_{i=0}^{\infty} i^l \, M_i^k = \mu^{k,l} \tag{111}$$

where $\lambda^{k,l}$ and $\mu^{k,l}$ are the $k-$th moment on the chain length and the $l-$th moment on the number on TDB for living and dead chains respectively. This model will be referred to as the TDB double moment model. The resulting set of ODEs is quite lengthy and the full model is given in Section A.1.6 of the appendix. As can be seen from

$$\begin{aligned}\frac{d\lambda^{2,2}}{dt} = {} & k_p M(2\lambda^{1,2} + \lambda^{0,2}) - k_{t,c}\lambda^{2,2}\lambda^{0,0} - k_{tr,m}M(\lambda^{2,2} - \lambda^{0,0}) \\ & + k_{p,TDB}(2\lambda^{2,1}\mu^{0,2} - 2\lambda^{2,1}\mu^{0,1} + \lambda^{2,0}\mu^{0,3} - 2\lambda^{2,0}\mu^{0,2} + \lambda^{2,0}\mu^{0,1} \\ & + 2(\lambda^{1,2}\mu^{1,1} + 2\lambda^{1,1}\mu^{1,2} - 2\lambda^{1,1}\mu^{1,1} + \lambda^{1,0}\mu^{1,3} - 2\lambda^{1,0}\mu^{1,2} \\ & + \lambda^{1,0}\mu^{1,1}) + \lambda^{0,2}\mu^{2,1} + 2\lambda^{0,1}\mu^{2,2} - 2\lambda^{0,1}\mu^{2,1} + \lambda^{0,0}\mu^{2,3} \\ & - 2\lambda^{0,0}\mu^{2,2} + \lambda^{0,0}\mu^{2,1}) \ ,\end{aligned} \tag{112}$$

and

$$\begin{aligned}\frac{d\mu^{2,2}}{dt} = {} & k_{t,c}(\lambda^{2,0}\lambda^{0,2} + 2\lambda^{2,1}\lambda^{0,1} + \lambda^{2,2}\lambda^{0,0} + \lambda^{1,0}\lambda^{1,2} + 2\lambda^{1,1}\lambda^{1,1} + \lambda^{1,2}\lambda^{1,0}) \\ & + k_{tr,m}M\lambda^{2,2} - k_{p,TDB}\lambda^{0,0}\mu^{2,3} \ ,\end{aligned} \tag{113}$$

closure relations are necessary due to the TDB propagation reaction. The moments $\mu^{k,3}$ with $k = 1,2,3$ are the moments

$$\mu^{k,3} = \sum_{i=0}^{\infty} i^3 \, M_i^k \ , \tag{114}$$

which can generally be calculated from the TDB distribution model. It is convenient to define a closure relation similar to Equation (80) as

$$D'_k = \frac{\mu^{k,3}\mu^{k,1}}{\mu^{k,2}\mu^{k,2}} \tag{115}$$

and to specify D'_k. Three closure relations are needed in total, which does not sound very promising, but actually does not turn out to be a limitation for the system considered here. Figure 56 shows the dispersity defined in Equation (115) for $k = 2$ calculated from the TDB distribution model over a wide range of values for the TDB propagation rate coefficient $k_{p,TDB}$. As illustrated in Figure 56, $D'_{k=2}$ varies in a range between 1 and 2. This range was used to study the sensitivity of the TDB double moment model against D'_k using a very high TDB propagation rate of $k_{p,TDB} = 6250\,\mathrm{l\,mol^{-1}\,s^{-1}}$. To do so all D'_k

were set equal for $k = 0,1,2$. The results are shown in Figure 57 for $k = 2$ where the effect is most significant. No additional insight can be gained from the results from $k = 0$ and $k = 1$ which are not shown here. The second TDB moment $\mu^{2,2}$ is affected by the closure relation, which is not surprising, since $\mu^{2,3}$ directly affects the dynamics of the second chain length moments as can be understood from Equation (112). The effect on lower moments decreases and is barely visible in the dynamics of zeroth TDB moments, which are needed to calculate molecular weight averages, the most important average characteristics of the system for comparison with experiments. Since the latter do not seem to be affected by the choice of D'_k its value will be set to 1 for all k subsequently.

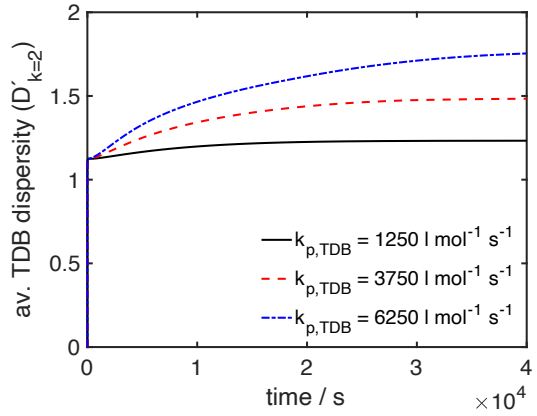

Figure 56. Effect of the variation of $k_{p,TDB}$ on the evolution of the average dispersity $D'_{k=2}$ for the TDB distribution model for the case of more than one TDB per chain and the reference case. The variation for $k = 1,2$ is even smaller.

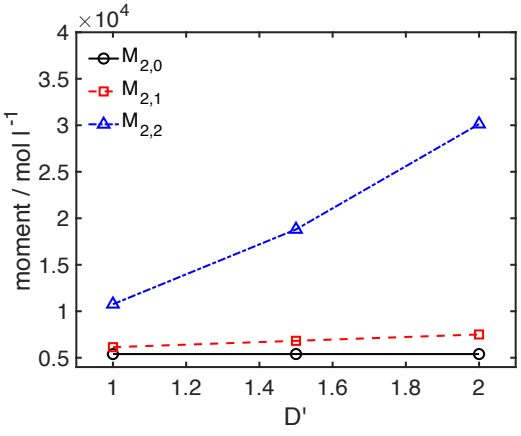

Figure 57. Effect of the closure relation on the steady state value of $\mu^{2,2}$ using the average dispersity $D'_{k=2}$ for the TDB double model for the case of more than one TDB per chain and the reference case. The variation for $k = 1,2$ is even smaller.

To verify this assumption simulations with two different values for the propagation rate coefficient were carried out. The results in Figure 58 and Figure 59 show a very good agreement between the TDB distribution model without any assumption and TDB double moment model assuming $D'_{k=\{0,1,2\}} = 1$. It should be emphasized that simulations with TDB propagation reaction rate coefficients as high as $k_{p,TDB} = 6250\,\mathrm{l\,mol^{-1}\,s^{-1}}$ are

infeasible using the TDB moment or TDB classes models due to computational time and memory limitations.

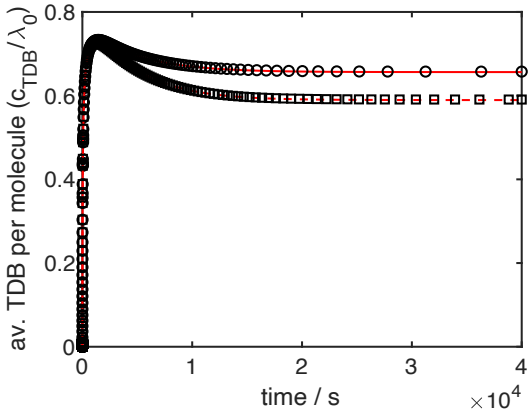

Figure 58. Comparison of the evolution of the average number of TDB per molecule c^{TDB}/λ_0^P for the TDB distribution and TDB double moment ($D'_{k=\{0,1,2\}} = 1$) models for the case of more than one TDB per chain for the reference case but different $k_{p,TDB}$: symbols – TDB distribution model; lines – TDB double moment model; solid, circles – $k_{p,TDB} = 2500$ l mol^{-1} s^{-1}; squares, dashed – $k_{p,TDB} = 6250$ l mol^{-1} s^{-1}.

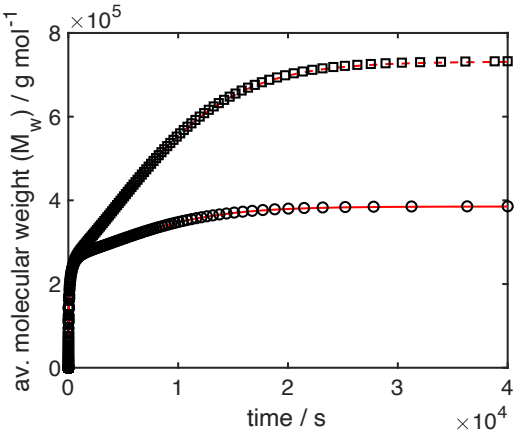

Figure 59. Comparison of the evolution of the weight average molecular weight $\overline{M_w}$ for the TDB distribution and TDB double moment ($D'_{k=\{0,1,2\}} = 1$) models for the case of more than one TDB per chain for the reference case but different $k_{p,TDB}$: symbols – TDB distribution model; lines – TDB double moment model; solid, circles – $k_{p,TDB} = 2500$ l mol^{-1} s^{-1}; squares, dashed – $k_{p,TDB} = 6250$ l mol^{-1} s^{-1}.

4.2.4.1 Comparison to the TDB reduced moment models

Finally, a comparison between the TDB double moment model and the TDB reduced moment model will be made to check the validity of the approximation $p_2(n)$ over a wider range of parameters and demonstrate another way of fixing the parameter A_2. As can be understood from Figure 60, the results using the parameter $A_2 = 9.49 \cdot 10^{-5}$, which was estimated as described in Section 4.2.2.1, are generally in good agreement with the results from the TDB double moment model using the reference case but different values of the TDB propagation rate coefficient $k_{p,TDB}$. For longer residence times and higher

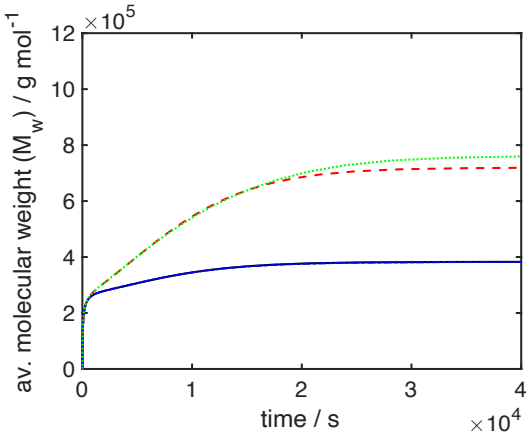

Figure 60. Comparison of the evolution of the weight average molecular weight $\overline{M_w}$ for the TDB reduced moment model with p_2 ($A_2 = 9.49 \cdot 10^{-5}$) and TDB double moment model ($D'_{k=\{0,1,2\}} = 1$) for the case of more than one TDB per chain and for the parameters of the reference case but different $k_{p,TDB}$: black solid – TDB double moment model, $k_{p,TDB}$ = 2500 l mol^{-1} s^{-1}; blue dashed-dotted – TDB reduced moment model, $k_{p,TDB}$ = 2500 l mol^{-1} s^{-1}; red dashed – TDB double moment model, $k_{p,TDB}$ = 6250 l mol^{-1} s^{-1}; green dotted – TDB reduced moment model, $k_{p,TDB}$ = 6250 l mol^{-1} s^{-1}. The black and blue lines are indistinguishable by eye.

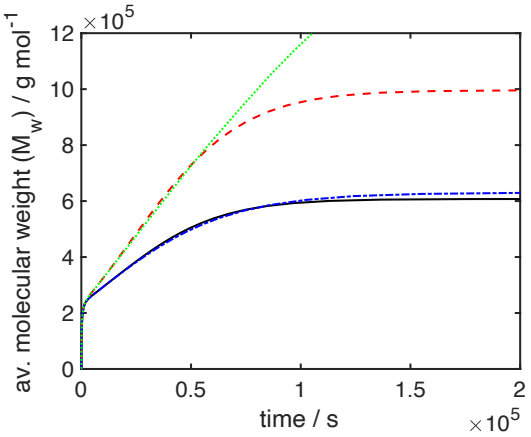

Figure 61. Comparison of the evolution of the weight average molecular weight $\overline{M_w}$ for the TDB reduced moment model with p_2 ($A_2 = 9.49 \cdot 10^{-5}$) and TDB double moment model ($D'_{k=\{0,1,2\}} = 1$) for the case of more than one TDB per chain and for the parameters of the reference case but average residence time changed to 4.5 h and different $k_{p,TDB}$: black solid – TDB double moment model, $k_{p,TDB}$ = 2500 l mol^{-1} s^{-1}; blue dashed-dotted – TDB reduced moment model, $k_{p,TDB}$ = 2500 l mol^{-1} s^{-1}; red dashed – TDB double moment model, $k_{p,TDB}$ = 3750 l mol^{-1} s^{-1}; green dotted – TDB reduced moment model, $k_{p,TDB}$ = 3750 l mol^{-1} s^{-1}.

values of $k_{p,TDB}$, on the other hand, the results deviate significantly as shown in Figure 61.

Comparing the TDB propagation contribution to the evolution of the first chain length moment $\lambda_1^P = \sum_n nP_n$ of the TDB reduced moment model

$$\frac{d\lambda_1^P}{dt} \mathrel{+}= -k_{p,TDB}\lambda_0^R \left(A_2\lambda_2^P - A_2\frac{\lambda_1^P}{\lambda_0^P}\lambda_1^P + \frac{c^{TDB}}{\lambda_0^P}\lambda_1^P \right) \tag{116}$$

and the equivalent double moment $\mu^{1,0} = \lambda_1^P$

$$\frac{d\mu^{1,0}}{dt} += -k_{p,TDB}\lambda^{0,0}\mu^{1,1} \ , \tag{117}$$

a definition of

$$A_2 = \frac{\mu^{1,1}\mu^{0,0} - \mu^{1,0}\mu^{0,1}}{\mu^{2,0}\mu^{0,0} - \mu^{1,0}\mu^{1,0}} \tag{118}$$

can be derived. Note, that the concentration of TDB $c^{TDB} = \mu^{0,1}$. As can be understood from Figure 62 and Figure 63, the transfer to monomer rate coefficient has a strong impact on the stationary value of A_2, while the effect of a variation of the TDB propagation rate coefficient $k_{p,TDB}$ is less pronounced, if all other parameters are those of the reference case. Since A_2 characterizes the slope of $p(n)$, this is consistent with the results of the TDB moment model presented in Figure 44 and Figure 45. For the reference case, the predicted stationary value $A_2 = 9.48 \cdot 10^{-5}$ is very similar to the one that was extracted from the TDB moment model.

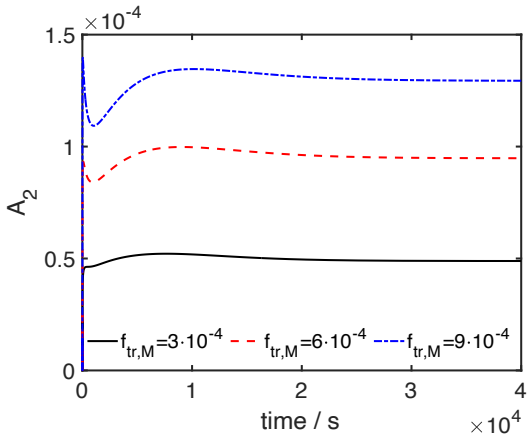

Figure 62. Comparison of the evolution of the parameter A_2 calculated from the TDB double moment model ($D'_{k=\{0,1,2\}} = 1$) for the case of more than one TDB per chain and the parameters of the reference case but different values of the transfer to monomer rate coefficient.

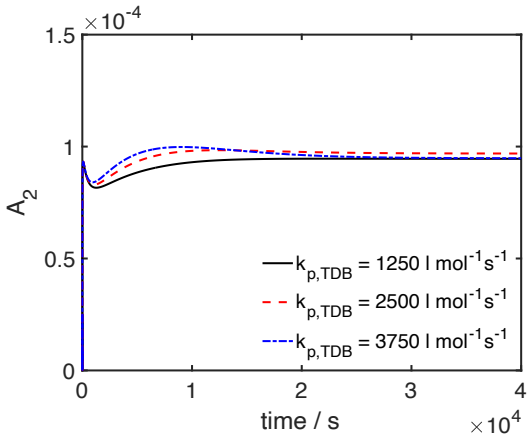

Figure 63. Comparison of the evolution of the parameter A_2 calculated from the TDB double moment model ($D'_{k=\{0,1,2\}} = 1$) for the case of more than one TDB per chain and the parameters of the reference case but different values of the TDB propagation rate coefficient.

For longer residence times the effect of $k_{p,TDB}$ on A_2 is more pronounced as shown in Figure 64. As shown in Figure 65, using the calculated stationary value from the TDB double moment model in the correlation $p_2(n)$ of the TDB reduced moment model gives very good agreement of the stationary values of the weight average molecular weight $\overline{M_w}$. The initial increase is underestimated, since the value of A_2 decreases as TDBs are consumed.

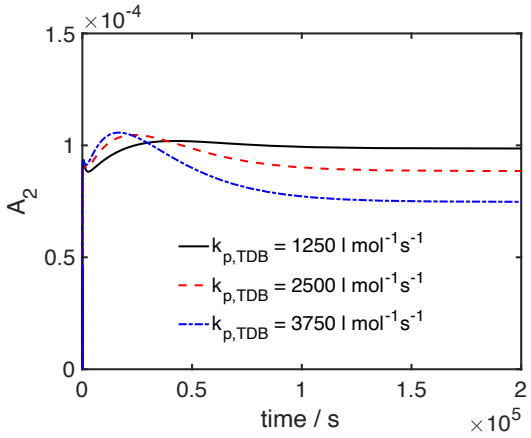

Figure 64. Comparison of the evolution of the parameter A_2 calculated from the TDB double moment model ($D'_{k=\{0,1,2\}} = 1$) for the case of more than one TDB per chain and the parameters of the reference case with the residence time changed to 4.5 h and different values of the TDB propagation rate coefficient.

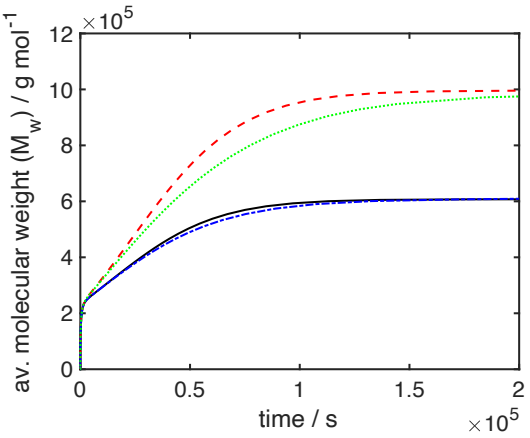

Figure 65. Comparison of the evolution of the weight average molecular weight $\overline{M_w}$ for the TDB reduced moment model with p_2 (A_2 final value from Figure 64) and TDB double moment model ($D'_{k=\{0,1,2\}} = 1$) for the case of more than one TDB per chain and for the parameters of the reference case but average residence time changed to 4.5 h and different $k_{p,TDB}$: see footnote for legend[5].

[5] Legend of Figure 65: black solid – TDB double moment model, $k_{p,TDB} = 2500$ l mol^{-1} s^{-1}, $A_2 = 8.85 \cdot 10^{-5}$; blue dashed-dotted – TDB reduced moment model, $k_{p,TDB} = 2500$ l mol^{-1} s^{-1}, $A_2 = 8.85 \cdot 10^{-5}$; red dashed – TDB double moment model, $k_{p,TDB} = 3750$ l mol^{-1} s^{-1}, $A_2 = 7.48 \cdot 10^{-5}$; green dotted – TDB reduced moment model, $k_{p,TDB} = 3750$ l mol^{-1} s^{-1}, $A_2 = 7.48 \cdot 10^{-5}$.

4.3 Comparison to experimental results

The models proposed in the preceding sections were validated against each other and capture the reaction mechanism, which was described in Section 4.1, correctly. To prove that the assumptions on the reaction mechanism are correct and to estimate the rate coefficient of the TDB propagation reaction, experiments in batch and CSTR reactors were conducted.

The details of the experimental setups, analytical conditions and preparation of chemicals that were used in these experiments are described in detail in Section 3.2.1 and in Section A.3 of the appendix. For a comparison to results from simulations, the monomer conversion was measured offline using HPLC and absolute molecular weight averages and distributions as well as radii of gyration were acquired using SEC with MALS and RI detectors. Molecular weight average data was used to estimate the rate coefficient of the TDB propagation reaction and will be presented in Section 4.3.1. A comparison to MWDs and branching will be done subsequently in Section 4.3.2 and Section 4.3.3. The kinetic coefficients and process parameters for CSTR experiments and simulations that will be used in this section are summarized in Table 10.

4.3.1 Molecular weight averages and parameter estimation

The weight average molecular weight $\overline{M_w}$ and the monomer conversion for CSTR experiments with different residence times and monomer weight fraction in the feed w_M^0 are illustrated in Figure 66 to Figure 69. $\overline{M_w}$ of samples taken at different times during the experiment show an increase in $\overline{M_w}$, which depends strongly on the hydrodynamic residence time and the polymer content in the reactor. This behavior indicates that side

Table 10. Parameters for comparison of simulations to experiments. The average residence time was defined merely to identify the cases and rounded to quarter hours.

Kinetic coefficients	
k_d, k_t, k_p	Equation (61) to (68)
$k_{tr,m}/k_p$	$6 \cdot 10^{-4}$ [48]
$k_{p,TDB}$ / l mol^{-1} s^{-1}	3300
f_d	0.6
Feed	
Monomer weight fraction w_M^0	0.2 or 0.1
Initiator weight fraction $w_{I_2}^0$	0.0002
Solvent weight fraction w_S^0	$1 - w_M^0 - w_{I_2}^0$
Overall feed rate $\dot{m}_F$ / g min^{-1}	14.16, 4.728 or 2.364
Initial conditions in reactor	
Solvent weight fraction $w_{H_2O}^0$	1
Reactor temperature T_R / °C	85
Reactor volume V_R / ml	650
Average residence time τ / h	~ 0.75, 2.25 or 4.5

reactions involving dead polymer chains play an important role in the reaction mechanism. Simulations using the TDB distribution model are in agreement using $k_{p,TDB} = 3300$ l mol^{-1} s^{-1}.

Since the TDB distribution model has a closed set of equations, no additional parameter or closure relation had to be specified. For computational reasons $k_{p,TDB}$ was estimated using the TDB double moment model but the results of both models are indistinguishable.

The steady state $\overline{M_w}$ and monomer conversion are summarized in Table 11 and Table 12. From Table 11, it can be seen that the steady state value of $\overline{M_w}$ is underestimated for low residence times and overestimated for high residence times. The reason for this observation may be that TDB propagation rate coefficient $k_{p,TDB}$ was assumed to be constant. It is possible, that the coefficient decreases with higher polymer content and, consequently, higher viscosity.

Table 11. Comparison of steady state weight average molecular $\overline{M_w}$ weight data from experiments and model predictions. The parameters are listed in Table 10.

Average residence time / h	Monomer weight fraction in feed w_M^0	Steady state $\overline{M_w}$ / 10^3 g mol^{-1}		
		TDB distribution model	TDB reduced moment model	experiment
0.75	0.2	424	424	524
2.25	0.2	591	592	601
4.5	0.2	870	857	805
2.25	0.1	321	318	313

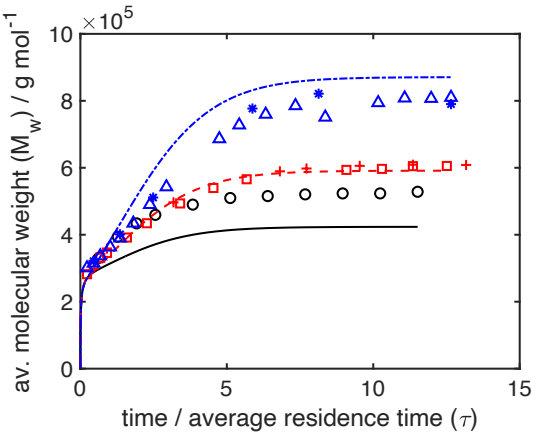

Figure 66. Comparison of the evolution of the weight average molecular weight $\overline{M_w}$ from experiments (markers) and simulations using the TDB distribution model (lines) for CSTR experiments with different average residence times: black circles, black solid line – 0.75 h; red squares and crosses, red dashed line – 2.25 h; blue triangles and stars, blue dashed dotted line – 4.5 h. Different symbols denote repeated experiments.

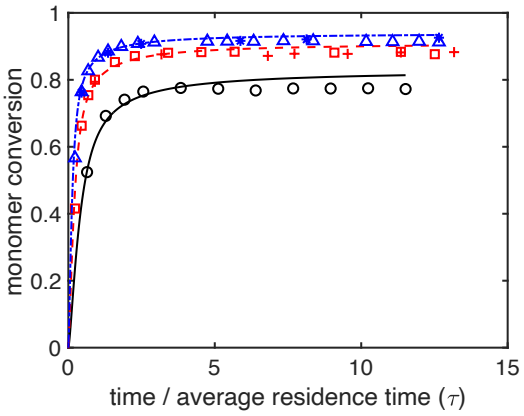

Figure 67. Comparison of the evolution of the monomer conversion from experiments (markers) and simulations using the TDB distribution model (lines) for CSTR experiments with different average residence times: black circles, black solid line – 0.75 h; red squares and crosses, red dashed line – 2.25 h; blue triangles and stars, blue dashed dotted line – 4.5 h. Different symbols denote repeated experiments.

Table 12. Comparison of steady state monomer conversion data from experiments and model predictions. Model predictions are the same for all models. The steady state values from simulations are all slightly higher than the experimental values, but the early stage monomer conversion can be captured best using the parameters listed in Table 10.

Average residence time / h	Monomer weight fraction in feed w_M^0	Steady state monomer conversion	
		models	experiment
0.75	0.2	0.81	0.77
2.25	0.2	0.9	0.88
4.5	0.2	0.93	0.91
2.25	0.1	0.89	0.88

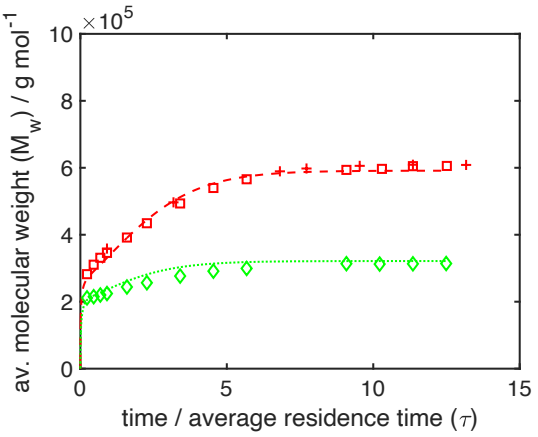

Figure 68. Comparison of the evolution of the weight average molecular weight $\overline{M_w}$ from experiments (markers) and simulations using the TDB distribution model (lines) for CSTR experiments with different monomer weight fractions in the feed w_M^0: red squares and crosses, red dashed line – 20 wt.-% green diamonds, green dotted line – 10 wt.-% Different symbols denote repeated experiments.

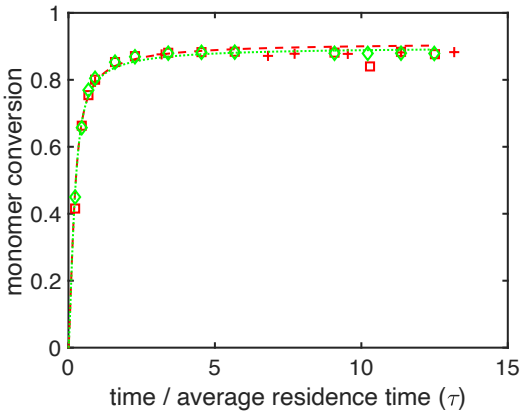

Figure 69. Comparison of the evolution of the monomer conversion from experiments (markers) and simulations using the TDB distribution model (lines) for CSTR experiments with different monomer weight fractions in the feed w_M^0: red squares and crosses, red dashed line – 20 wt.-%; green diamonds, green dotted line – 10 wt.-%. Different symbols denote repeated experiments.

Generally, the results from simulations using the TDB distribution model are in agreement with experimental results presented in this section and support the validity of the reaction mechanism proposed in [49]. Since transfer to polymer has also been proposed as a possible side reaction in literature, simulations using the latter reaction instead of propagation of TDB were performed as an additional validation. The results presented in Figure 70 clearly show that models, which only include transfer to polymer cannot represent the experimental data.

All of the experimental conditions that have been discussed in this section lead to steady state monomer conversion and MWDs. No gelation of the bulk phase occurred, which is in agreement with simulation results. As shown in Figure 71 and Figure 72, simulations using the TDB double moment model predict gelation only for very high average residence

times, which cannot be validated using the experimental equipment that was employed for this thesis. Nevertheless, fouling deposits occurred at the baffles of the tank reactor and in other poorly mixed regions as described in Section 3.2.2.

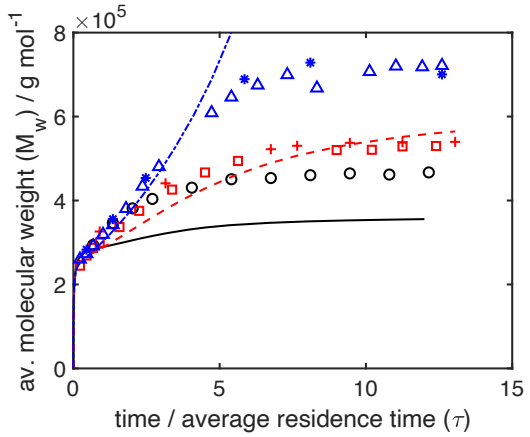

Figure 70. Comparison of the evolution of the weight average molecular weight $\overline{M_w}$ from experiments (markers) and simulations using the TDB reduced moment model (lines) with transfer to polymer instead of TDB propagation ($k_{tr,p} = 1.75$ l mol^{-1} s^{-1}) for CSTR experiments with different hydrodynamic residence times: black, solid – 0.75 h; red, dashed – 2.25 h; blue, dashed dotted – 4.5 h. Different symbols denote different experiments.

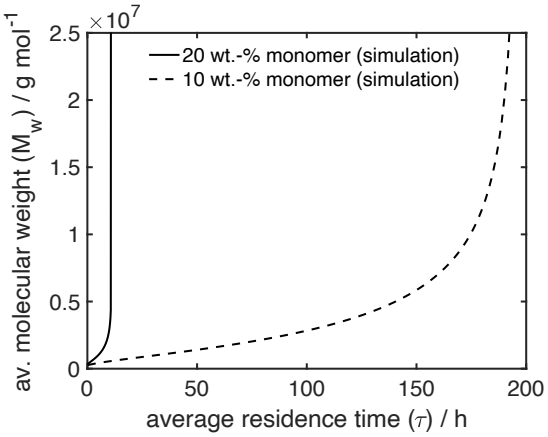

Figure 71. Dependence of the steady state weight average molecular weights $\overline{M_w}$ from simulations using the TDB double moment model on the average residence time (Equation (69)) for different monomer weight fractions in the feed w_M^0.

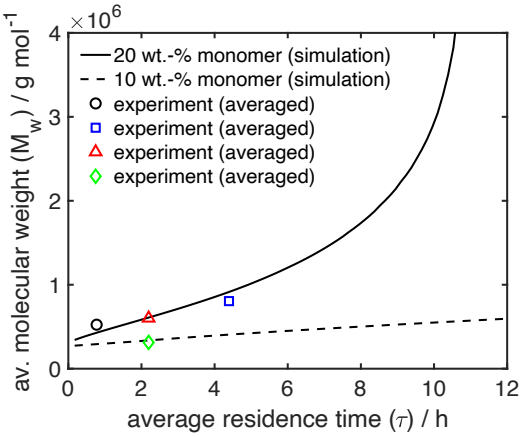

Figure 72. Magnification of Figure 71 and comparison to experiments for different average residence times (Equation (69)) and monomer weight fractions in the feed w_M^0. The experimental values are averaged steady state values of the experiments from Table 11.

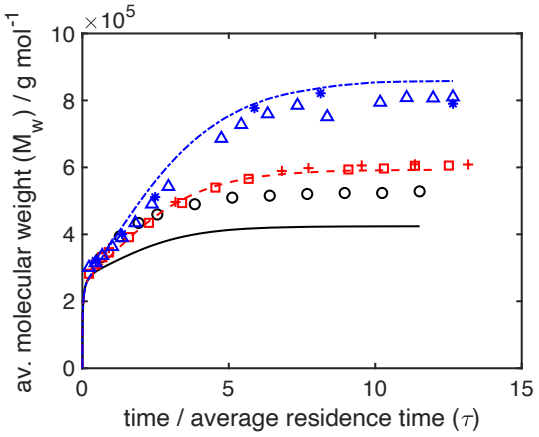

Figure 73. Comparison of the evolution of the weight average molecular weight $\overline{M_w}$ from experiments (markers) and simulations using the TDB reduced moment model (lines) with p_2 for CSTR experiments with different average residence times: black squares, black solid line – 0.75 h ($A_2 = 9.3 \cdot 10^{-5}$) ; red squares and crosses, red dashed line – 2.25 h ($A_2 = 9.05 \cdot 10^{-5}$); blue triangles and stars, blue dashed dotted line – 4.5 h ($A_2 = 8.1 \cdot 10^{-5}$) . Different symbols denote repeated experiments.

4.3.2 Steady state molecular weight distributions

Since full chain length distributions are often of interest, a model capable of calculating the latter is desirable and, therefore, a comparison to simulations using the TDB reduced moment model was made. The stationary value of A_2 calculated from the TDB double moment as described in Section 4.2.4.1 was chosen for these simulations. The results for the weight average molecular weight $\overline{M_w}$ are also in agreement with experimental results as shown in Figure 73. Differences to the results of the TDB distribution model are attributed to the assumption of a constant value for A_2 for each simulation.

The advantage of the TDB reduced moment model is that the full MWD is available. A comparison of the latter for the steady state GPC distributions of the CSTR experiments are shown in Figure 74 to Figure 77 and match the experimental results very well.

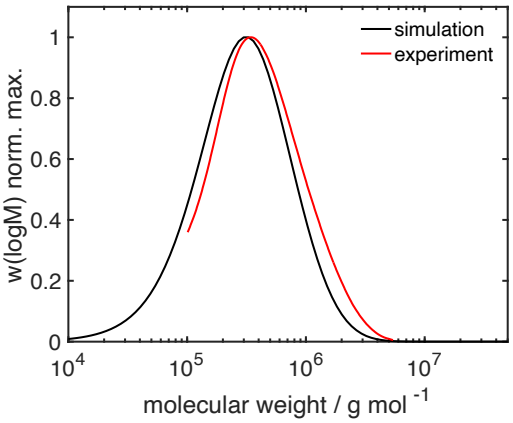

Figure 74. Comparison of the steady state normalized GPC distribution from experiment and simulation using the TDB reduced moment model with p_2 ($A_2 = 9.49 \cdot 10^{-5}$) for a CSTR experiments with a hydrodynamic residence time of 0.75h and a monomer weight fraction w_M^0 of 20 wt.-% in the feed.

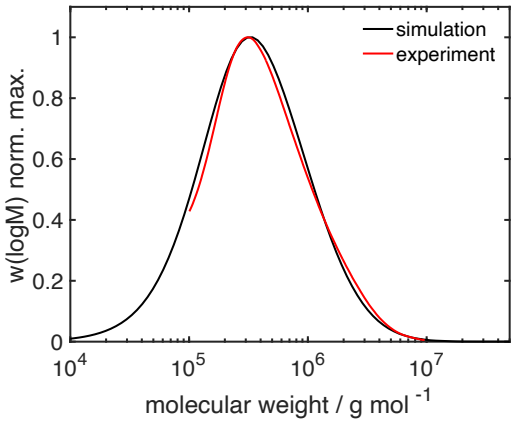

Figure 75. Comparison of the steady state normalized GPC distribution from experiment and simulation using the TDB reduced moment model with p_2 ($A_2 = 9.49 \cdot 10^{-5}$) for a CSTR experiments with a hydrodynamic residence time of 2.25h and a monomer weight fraction w_M^0 of 20 wt.-% in the feed.

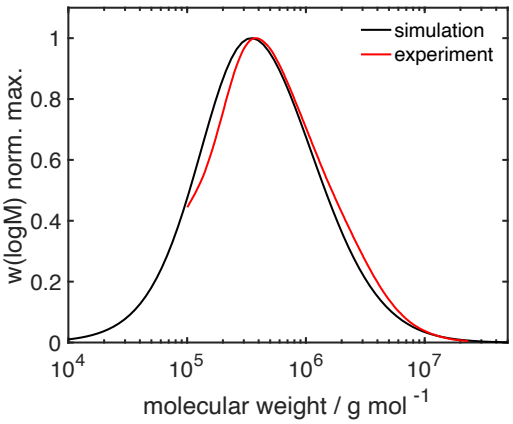

Figure 76. Comparison of the steady state normalized GPC distribution from experiment and simulation using the TDB reduced moment model with p_2 ($A_2 = 9.49 \cdot 10^{-5}$) for a CSTR experiments with a hydrodynamic residence time of 4.5h and a monomer weight fraction w_M^0 of 20 wt.-% in the feed.

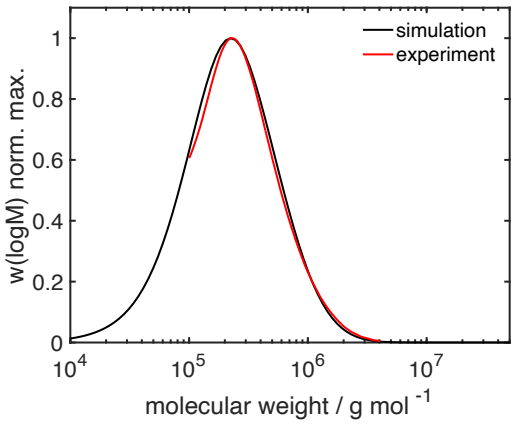

Figure 77. Comparison of the steady state normalized GPC distribution from experiment and simulation using the TDB reduced moment model with p_2 ($A_2 = 9.49 \cdot 10^{-5}$) for a CSTR experiments with a hydrodynamic residence time of 2.25h and a monomer weight fraction w_M^0 of 10 wt.-% in the feed.

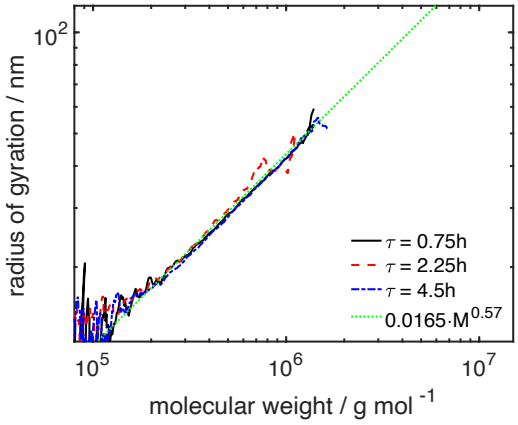

Figure 78. Comparison of the conformation plots from CSTR experiments with different hydrodynamic residence times at early reaction times with polymer contents around 5 w-%. The green dotted line is a power law fit, which is assumed as a linear reference.

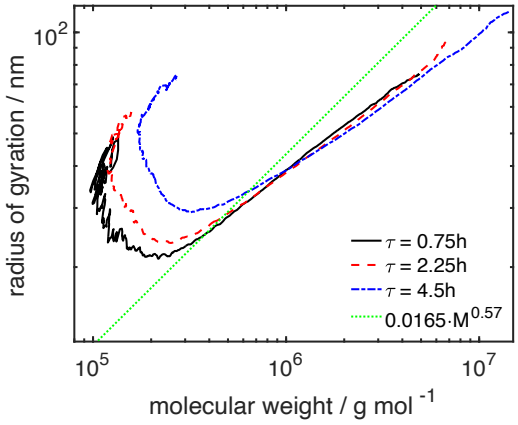

Figure 79. Comparison of the conformation plots from the steady state of CSTR experiments with different hydrodynamic residence corresponding to the distributions in Figure 74 to Figure 76. The green dotted line is the same as in Figure 78.

4.3.3 Characterization of structural changes using the conformational plot

If the increase in the weight average molecular weight $\overline{M_w}$ and the broadening the GPC distributions is caused by the propagation of TDBs, the conformation of high-molecular chains must also change due to branching. The latter can be characterized by changes of the radius of gyration of molecules with the same molecular weight as described in Section 2.2.2.

Conformation plots of samples from CSTR experiments are illustrated in Figure 78 and Figure 79. At early operation times the plots coincide for all three residence times and approach a power law with an exponent of 0.57. Therefore, the molecular structure should be the same for all three samples and the power law will be taken as a linear reference sample in the following. Figure 79 shows the conformation plots corresponding to the steady state. The slopes of these plots in the double logarithmic graph decrease

with longer hydrodynamic residence times indicating structural changes of the molecules by branching. The apparent increase of the radius of gyration at low molecular weights is an intrinsic artefact of the SEC separation of branched molecules referred to as anchoring [32] and is discussed in Section A.3.4 of the appendix.

Assuming trifunctional branches and a linear reference sample as discussed before, the number of branches per molecule can be estimated as described in Section 2.1.2. Details on the application of the method can also be found in Section A.3.4 of the appendix. As expected and illustrated in Figure 80, the number of branches per thousand repeat units increases with longer hydrodynamic residence times since more TDBs are consumed. The results from simulations illustrated in Table 13 show a similar trend although only chain length averaged information is available through counter species from the models presented here.

The experimental results on branching presented here should be interpreted only qualitatively, since a power law function had to be taken as linear reference sample. Due to the non-ideal separation of branched samples in the low molecular regime, a linear extrapolation had to be used, which introduces additional errors. Nevertheless, the branching density does not seem to be high and the experimental results suggest that molecules with a molecular weight below ~4 10^3 g mol^{-1} are mostly linear. This is in agreement with studies on insoluble PVP, which suggest that the number of chemical crosslinks is small and that physical crosslinks form the polymer gel [41].

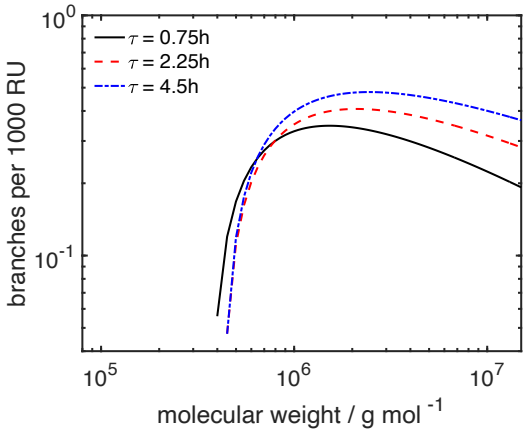

Figure 80. Comparison of the estimated number of branches per 1000 repeat units (RU) as a function of molecular weight from the steady state of CSTR experiments with different hydrodynamic residence.

Table 13. Average number of branches per 1000 repeat units calculated from the TDB distribution model.

Average residence time / h	Average number of branches per 1000 repeat units ($1000 \cdot n_1^B$, see Equation (102)) from simulations
0.75	0.115
2.25	0.208
4.5	0.265

4.4 Concluding remarks

In this chapter, different models based on a reaction mechanism including the formation of TDBs by transfer to monomer and their propagation as side reactions were derived and predictions from simulations were compared to experiments. The evolution of monomer conversion and molecular weight data can be represented well. These results support the assumption that broad MWDs are caused by propagation of TDB and not by

a transfer to polymer reaction, which was also proposed in [48].

The TDB classes model offers the most detailed information and even a two-dimensional distribution could be reconstructed from simulations using this model. The downside is the very high computational effort, which restricts the application of this model to validation purposes under mild reaction conditions. The TDB moment model derived in [33] reduces the computational effort and may be applied over a wider range of parameters but it is still too computationally expensive for process design or parameter estimations. Therefore, if the full MWD is required the TDB reduced moment model derived in Section 4.2.2.1 is recommended, although the additional parameter A_2 needs to be introduced. The TDB distribution model, which was introduced in Section 4.2.3, offers average information without any assumption and works well over a wide range of parameters with moderate computational effort. The latter can be reduced even further by using the TDB double moment model from Section 4.2.4, which requires closure relations but is not affected by their choice significantly. As discussed in Section 4.2.4.1, the parameter A_2, which is required for closure relation $p_2(n)$ for the TDB reduced moment model, can be calculated from this model as well. The value does not remain constant during the reaction but using the stationary value gives very good agreement of the stationary weight average molecular weight averages $\overline{M_w}$ in CSTR experiments. Thus, the suggested workflow for parameter estimations is to fix the ratio of transfer to monomer and propagation $f_{tr,m}$ and the TDB propagation rate coefficient $k_{p,TDB}$ using the TDB distribution or TDB double moment model and estimate A_2 for the TDB reduced moment model subsequently from these models, if the full MWD is desired. An illustration of the modeling workflow and a summary of the microstructural polymer properties that can be extracted from the models are given in Section A.1.1 of the appendix.

As discussed in Section 4.3.1, no gelation of the bulk phase was observed in any of the

experiments but fouling deposits occurred on the baffles of the tank reactor. This observation emphasizes the importance of dead-water zones and diffusion for the formation of fouling deposits. Polymer material, which accumulates in such regions is still highly reactive, due to the large number of TDBs as was seen from the simulation results in this chapter. This is especially important, if polymer chains are immobilized on surfaces and is a possible explanation for the increase in fouling in repeated experiments.

5 Flow pattern and diffusive mass transport

The experimental results in Section 3.2.2 and Chapter 4 suggest that dead-water zones in the reactor lead to the formation of fouling deposits, even if the process conditions do not lead to gelation of the bulk phase. The locally increased residence time in such regions may increase the importance of side reactions and cause concentration gradients, which induce diffusive mass transport. Additionally, viscosity gradients can alter the flow pattern and, thereby, increase the extend of dead-water zones.

Such behavior has been reported for polymerization in tubular reactors in which a highly viscous boundary layer is formed, for example [6], [16], [19], [21], [54]. In static mixer reactors, dead-water zones and non-ideal mixing were also proposed to be an important factor for the formation of fouling deposits in [5], [6]. Similar suggestions were made for regions of low flow rate at the baffles of tank reactors in [10].

The focus of this chapter will be on the interplay of different transport phenomena, which are induced by the flow pattern in different reactor geometries, and the reaction mechanism that has been discussed in Chapter 4. First, the balance equations including all relevant transport phenomena will be discussed in Section 5.1 and special features of systems that contain polymers will be highlighted in Section 5.1.1. In Section 5.2, the influence of diffusive mass transport and viscosity gradients on the formation of stagnant regions will be discussed using the example of a tubular reactor. The influence of the reactor geometry will be demonstrated subsequently using a geometry that resembles a static mixer reactor in Section 5.3.

5.1 Balance equations for isothermal multi-component systems

The barycentric velocity $\boldsymbol{v}^m$ in isothermal, single-phase systems can be calculated from the momentum balance equation

$$\frac{\partial \rho \boldsymbol{v}^m}{\partial t} + \nabla \cdot \rho \boldsymbol{v}^m \boldsymbol{v}^m + \nabla \cdot \boldsymbol{\tau} = -\nabla p \tag{119}$$

in which ρ is the mass density, $\boldsymbol{\tau}$ is the viscous stress tensor and p is the pressure. The effect of the gravitational field has been neglected. Additionally, the mass balance

$$\frac{\partial \rho}{\partial t} + \nabla \cdot \rho \boldsymbol{v}^m = 0 \tag{120}$$

must be fulfilled to ensure the conservation of mass. For incompressible fluids with a constant density, Equation (120) reduces to [37]

$$\nabla \cdot \boldsymbol{v}^m = 0 \tag{121}$$

and can be used as a constraint in a pressure correction scheme to obtain a pressure field, which ensures that the barycentric velocity field has the specified divergence. In this case, the pressure p is a mechanical variable and not the pressure in a thermodynamic sense, which can be obtained from an equation of state [38]. The constitutive relation for the viscous stress tensor in 3D is [55]

$$\boldsymbol{\tau} = \eta \left[(\nabla \boldsymbol{v}^m + \nabla^T \boldsymbol{v}^m) - \frac{2}{3} \nabla \cdot \boldsymbol{v}^m \right] \tag{122}$$

with the shear viscosity η, which may be a function of composition in case of a multi-component fluid. The contribution from dilatational effects has been neglected and Newtonian behavior has been assumed.

For multicomponent systems, the balance equations for different species need to be considered as well to account for changes in the composition. These equations can either be written in terms of the mass densities ρ_j of species j

$$\frac{\partial \rho_j}{\partial t} + \nabla \cdot \boldsymbol{v}^m \rho_j + \nabla \cdot \boldsymbol{J}_j^m = MW_j r_j^{total} \tag{123}$$

or molar densities c_j

$$\frac{\partial c_j}{\partial t} + \nabla \cdot \boldsymbol{v}^N c_j + \nabla \cdot \boldsymbol{J}_j^N = r_j^{total} \tag{124}$$

in which r_j^{total} is a source term including all reaction rates that influence the concentration of species j and MW_j is the molecular weight of species j. The diffusive flux $\boldsymbol{J}_j^m$ is defined relative to the barycentric velocity

$$\boldsymbol{v}^m = \sum_j w_j \boldsymbol{v}_j \ , \tag{125}$$

while $\boldsymbol{J}_j^N$ is defined relative to the molar average velocity

$$\boldsymbol{v}^N = \sum_j x_j \boldsymbol{v}_j \ . \tag{126}$$

In Equation (125) and Equation (126), w_j and x_j are the weight and molar fraction of species j in the mixture and the average velocities are related by [37]

$$\boldsymbol{v}^N = \boldsymbol{v}^m - \frac{1}{\rho} \sum_j MW_j \boldsymbol{J}_j^N \ . \tag{127}$$

In the following, the upper index m indicates the barycentric reference frame and the upper index N indicates for molar reference frame. Since polymer systems can be modeled efficiently in terms of statistical moments of molar concentration distributions, the component balances in form of Equation (124) were chosen in this thesis. Equation (124) can

be transformed to the barycentric reference frame by inserting Equation (127) to ensure compatibility with the barycentric velocity that is calculated from the momentum balance Equation (119).

In multicomponent systems the overall density ρ depends on the molecular composition of the mixture and is not necessarily constant, if diffusive transport or chemical reactions take place. Generally, this dependence can be described by an equation of state. Another possibility, which is convenient for the implementation in CFD solvers for incompressible fluids, is the definition of a constraint in terms of volume fractions

$$\sum_j \frac{V_j}{V} = 1 \tag{128}$$

with the volume V_j that species j occupies in the overall volume V and the sum is over all species in the system. Assuming that the fluid can be approximated as an ideal mixture, excess volumina can be neglected and Equation (128) can be rewritten as [55]

$$\sum_j \frac{\rho_j}{\rho_j^0} = 1 \tag{129}$$

with the pure component density ρ_j^0 of species j, which is assumed to be constant for isothermal, incompressible fluids. By taking the temporal derivative

$$\sum_j \frac{\partial}{\partial t}\frac{\rho_j}{\rho_j^0} = 0 = \sum_j \frac{MW_j}{\rho_j^0}\frac{\partial c_j}{\partial t} \tag{130}$$

and inserting Equation (124) and Equation (127)

$$0 = \sum_j \frac{MW_j}{\rho_j^0}\left(-\nabla\cdot\left(\boldsymbol{v}^m - \frac{1}{\rho}\sum_i MW_i\boldsymbol{J}_i^N\right)c_j - \nabla\cdot\boldsymbol{J}_j^N + r_j^{total}\right), \tag{131}$$

the divergence of the barycentric velocity can be calculated to be

$$\nabla \cdot \boldsymbol{v}^m = \nabla \cdot \sum_j MW_j \boldsymbol{J}_j^N \frac{\rho_j^0 - \rho}{\rho \rho_j^0} + \sum_j \frac{MW_j}{\rho_j^0} r_j^{total} \ . \tag{132}$$

As can be seen from Equation (132), the latter can only be equal to zero if $\rho_j^0 = \rho = \text{const.}$ [55]. In incompressible fluids with a concentration dependent density, changes in the composition due to diffusion or reactions lead to an expansion or contraction of the fluid [56] and, therefore, a non-zero divergence of the barycentric velocity field.

So far, the diffusive fluxes $\boldsymbol{J}_j^N$ have not been defined. For isothermal, multicomponent mixtures, these fluxes can be calculated from the Maxwell-Stefan equations

$$\boldsymbol{d}_i = -\frac{1}{RT} \nabla \mu_i = \sum_{j=1}^{N} \frac{x_j \boldsymbol{v}_i - x_j \boldsymbol{v}_j}{\mathfrak{D}_{ij}} \tag{133}$$

in which $\boldsymbol{d}_i$ is the driving force for species i, R is the universal gas constant, T is the temperature, μ_i is the chemical potential of species i, x_i its molar fraction, $\boldsymbol{v}_i$ its overall transport velocity and $\mathfrak{D}_{ij}$ the Maxwell-Stefan diffusion coefficient for species i and j. In the isothermal case

$$\nabla \mu_i = \nabla \left(\mu_i^0 + RT \cdot ln(x_i \gamma_i) \right) = RT \frac{1}{x_i} \sum_{j=1}^{N} \left(\delta_{ij} + x_i \frac{\partial ln(\gamma_i)}{\partial x_j} \right) \cdot \nabla x_j \tag{134}$$

in which μ_i^0 is the chemical potential at a reference state and γ_i is the activity coefficient for species i. In case of an ideal mixture with $\gamma_i = 1 = \text{const.}$ the driving force becomes

$$-\frac{1}{RT} \nabla \mu_i = -\frac{1}{x_i} \nabla x_i \ . \tag{135}$$

By fixing the reference frame to the molar average velocity $\boldsymbol{v}^N$, a set of equations for the fluxes $\boldsymbol{J}_j^N$ up to species $J-1$

$$-c\nabla x_i = -\nabla c_i + \frac{c_i}{c}\nabla c = \sum_{j=1}^{J-1} B_{ij} \cdot \boldsymbol{J}_j^N \tag{136}$$

with the overall molar concentration c and

$$B_{ij} = \frac{c_i}{c}\left(\frac{1}{\mathfrak{D}_{iJ}} - \frac{1}{\mathfrak{D}_{ij}} + \delta_{ij}\sum_{k=1}^{J}\frac{c_k}{c_j}\frac{1}{\mathfrak{D}_{jk}}\right) \tag{137}$$

can be derived. See Section A.2.3 in the appendix for a detailed discussion. A form that is explicit in the fluxes $\boldsymbol{J}_j^N$ is convenient for the implementation in CFD codes and can be achieved by inverting the matrix $\boldsymbol{B}$ that contains the elements B_{ij} as

$$\boldsymbol{J}_j^N = \sum_{i=1}^{J-1} -(\boldsymbol{B}^{-1})_{ji} \cdot \left(\nabla c_i - c_i \frac{1}{\mathrm{c}}\nabla c\right) = \sum_{i=1}^{J-1} -(\boldsymbol{D}^F)_{ji} \cdot \left(\nabla c_i - c_i \frac{1}{\mathrm{c}}\nabla c\right) \tag{138}$$

with the matrix $\boldsymbol{D}^F = \boldsymbol{B}^{-1}$, which's elements are Fickian type diffusion coefficients. Since the fluxes $\boldsymbol{J}_j^N$ are defined relative to the molar average velocity $\boldsymbol{v}^N$,

$$\boldsymbol{J}_J^N = -\sum_{j=1}^{J-1} \boldsymbol{J}_j^N \tag{139}$$

must hold by definition.

Usually, only $J-1$ balance equations are solved in a J component mixture and the concentration of the J-th component is calculated from a constraint, e.g. Equation (129) as

$$c_J = \frac{\rho_J^0}{MW_J} - \sum_{j=1}^{J-1}\frac{MW_j}{MW_J}\frac{\rho_J^0}{\rho_j^0}c_j \tag{140}$$

and the total mass density ρ can be calculated from

$$\rho = \sum_j c_j MW_j \ . \tag{141}$$

5.1.1 Special features of systems containing polymers

If systems that contain polymers are of interest, the property distributions of the polymer species are usually treated using the method of moments to keep the computational effort at a feasible level. Therefore, balance equations for statistical moments of polymer property distributions appear besides the component balances for low molecular species and reaction rates as well as diffusive fluxes for these moments need to be specified as constitutive relations. The reaction rates have already been derived in Chapter 4 and are the same as for a tank reactor. A relation for diffusive fluxes of polymer moments was derived in [57] under the assumption that the Maxwell-Stefan diffusion coefficients for polymers of all chain lengths s and r $\mathfrak{D}_{P_s P_r} \to 0$. The result is a definition of the fluxes of the k-th chain length moment $\lambda_k^P = \sum_n n^k P_n$ of the polymer population P that is linked of the flux of the zeroth chain length moment λ_0^P

$$\boldsymbol{J}_{\lambda_k^P}^N = \frac{\lambda_k^P}{\lambda_0^P} \boldsymbol{J}_P^N \tag{142}$$

with

$$\boldsymbol{J}_{\lambda_0^P}^N = \boldsymbol{J}_P^N \ . \tag{143}$$

Therefore, in terms of the Stefan-Maxwell equations, each polymer population is treated as a species, e.g. P.

The approach can be generalized to multi-dimensional property distributions and is discussed in full detail in Section A.2.3 of the appendix. The result is a modification of Equation (142) as

$$\boldsymbol{J}_{\mu^{k,l}}^N = \frac{\mu^{k,l}}{\mu^{0,0}} \boldsymbol{J}_P^N \tag{144}$$

with

$$\boldsymbol{J}^N_{\mu^{0,0}} = \boldsymbol{J}^N_P \tag{145}$$

in which the double moments $\mu^{k,l}$ may be those that have been defined in Section 4.2.4, for example.

Another important detail needs to be considered in the divergence constraint. For systems that contain polymers, the temporal derivative of the partial mass density ρ_P of a polymer population must be considered, which is

$$\frac{\partial \rho_P}{\partial t} = MW_M \frac{\partial \lambda_1^P}{\partial t} = MW_M \left(-\nabla \cdot \lambda_1^P \boldsymbol{v}^N - \nabla \cdot \frac{\lambda_1^P}{\lambda_0^P} \boldsymbol{J}^N_{\lambda_0^P} + r^{total}_{\lambda_1^P} \right). \tag{146}$$

Therefore, the reaction rates that affect the concentration of the first polymer chain length moment λ_1^P and the molecular weight of a repeat unit MW_M have to be considered in Equation (130) rather than the polymer concentration, which is characterized by the zeroth polymer chain length moment λ_0^P, and the number average molecular weight $\overline{M_n}$. If the reaction rates for λ_0^P in combination with $\overline{M_n}$ were used, the contribution of the reaction rates to the divergence would not vanish in case of equal pure component mass densities. If multi-dimensional property distributions are of interest, the first moment of the chain length property coordinate and the zeroth moments of all other property coordinates should be used.

5.1.2 Model equations for the system of interest

The model equations that will be used in the rest of this chapter are the momentum balance equation (119), which is solved in a pressure correction scheme together with the divergence constraint Equation (132) and the molar balance equations

$$\frac{\partial c_j}{\partial t} = -\nabla \cdot \left(\boldsymbol{v}^m - \frac{1}{\rho} \sum_i MW_i \boldsymbol{J}_i^N \right) c_j - \nabla \cdot \boldsymbol{J}_j^N + r_j^{total} \ . \tag{147}$$

The latter are solved for those polymer moments that are relevant for the kinetic model and all low molecular species except the solvent S, which's concentration is calculated from Equation (140). Details on the solution strategy for the system of equations and the numerical setup can be found in Section A.2.4 of the appendix.

The reaction rates were calculated using the TDB double moment model from Section 4.2.4 and the viscosity is assumed to be a function of polymer weight fraction [47]

$$\frac{\eta}{\eta_0} = \eta_{rel} = \exp(C_\eta w_P) \tag{148}$$

with $C_\eta = 14.75$, but no dependence on the shear rate, i.e. a Newtonian fluid, is assumed. η_0 is the solution viscosity for $w_P = 0$. Equation (148) is also included in the correlation for the termination rate coefficient of the kinetic model and has been chosen for consistency. The viscosity of a polymer system also depends on the chain length of polymer chains, which is not considered here. Diffusive fluxes are not considered for radical species with a very short lifetime and low concentrations and the Maxwell-Stefan equations are reduced to a system of three equations for the undissociated initiator I_2, the monomer M, and the polymer population P, if the solvent S is treated as the J-th species. Assuming $\mathfrak{D}_{i,j} = \mathfrak{D}_0$, if i and j are both low molecular species, and $\mathfrak{D}_{i,P} = \mathfrak{D}_P$, if j is a polymer species, the non-zero entries of the Fickian type diffusion matrix $\boldsymbol{D}^F$ are

$$D^F_{I_2,I_2} = D^F_{M,M} = \frac{c\mathfrak{D}_0\mathfrak{D}_P}{(c_{I_2} + c_M + c_{LM})\mathfrak{D}_P + c_P\mathfrak{D}_0}\,, \tag{149}$$

$$D^F_{P,P} = \frac{c\mathfrak{D}_P}{c_P + c_{LM} + c_{I_2} + c_M} \tag{150}$$

$$D^F_{M,P} = \frac{c_M(\mathfrak{D}_0 - \mathfrak{D}_P)}{c\mathfrak{D}_0\mathfrak{D}_P} \cdot D^F_{M,M} \cdot D^F_{P,P} \tag{151}$$

$$D^F_{I_2,P} = \frac{c_{I_2}(\mathfrak{D}_0 - \mathfrak{D}_P)}{c\mathfrak{D}_0\mathfrak{D}_P} \cdot D^F_{I_2,I_2} \cdot D^F_{P,P} \tag{152}$$

and the diffusive fluxes are

$$\boldsymbol{J}^N_{I_2} = -D^F_{I_2,I_2} \cdot \left(\nabla c_{I_2} - c_{I_2}\frac{1}{c}\nabla c\right) - D^F_{I_2,P} \cdot \left(\nabla \mu^{0,0} - \mu^{0,0}\frac{1}{c}\nabla c\right), \tag{153}$$

$$\boldsymbol{J}^N_{M} = -D^F_{M,M} \cdot \left(\nabla c_{M} - c_{M}\frac{1}{c}\nabla c\right) - D^F_{M,P} \cdot \left(\nabla \mu^{0,0} - \mu^{0,0}\frac{1}{c}\nabla c\right), \tag{154}$$

$$\boldsymbol{J}^N_{\mu^{0,0}} = -D^F_{P,P} \cdot \left(\nabla \mu^{0,0} - \mu^{0,0}\frac{1}{c}\nabla c\right), \tag{155}$$

$$\boldsymbol{J}^N_{\mu^{k,l}} = \frac{\mu^{k,l}}{\mu^{0,0}}\boldsymbol{J}^N_{\mu_{0,0}}\,, \tag{156}$$

$$\boldsymbol{J}^N_S = -\boldsymbol{J}^N_{I_2} - \boldsymbol{J}^N_M - \boldsymbol{J}^N_{\mu_{0,0}}\,. \tag{157}$$

A detailed derivation is given in Section A.2.3 of the appendix. Motivated by the Stokes-Einstein relation, all Maxwell-Stefan diffusion coefficients were scaled by η_{rel}

$$\mathfrak{D}_{0/P} = \frac{\mathfrak{D}^0_{0/P}}{\eta_{rel}} \tag{158}$$

with the reference Maxwell-Stefan diffusion coefficient $\mathfrak{D}^0_{0/P}$ for $w_P \to 0$ to include the effect of decreasing diffusion coefficients with increasing solution viscosity. This type of scaling is also included in correlation for the termination rate coefficient to model the

effect of translational diffusion as described in Section 4.1 [47], [58].

Diffusion coefficients depend not only on concentrations, but also on the polymer chain length. An estimate for the ratio

$$\frac{\mathfrak{D}_P}{\mathfrak{D}_0} = \left(\frac{\mu^{1,0}}{\mu^{0,0}}\right)^{-0.6} \tag{159}$$

with the number average chain length $\mu^{1,0}/\mu^{0,0}$is motivated by the Zimm theory, although, this approximation can only be rough, since the latter has been formulated for monodisperse, linear polymers in diluted solution. Nothing has been depicted about entanglements or structural changes of the polymer back-bone, but the effect of different polymer chain lengths should be captured at least qualitatively. The ratio of the Maxwell-Stefan diffusion coefficients of polymer and low molecular species $\mathfrak{D}_P/\mathfrak{D}_0$ calculated from Equation (159) for several average chain lengths is given in Table 14. For typical polymers, values between

Table 14. Estimation of the ratio of the Maxwell-Stefan diffusion coefficients of polymer and low molecular species $\mathfrak{D}_P/\mathfrak{D}_0$ for different average chain lengths $\mu^{1,0}/\mu^{0,0}$ from Equation (159).

$\mu^{1,0}/\mu^{0,0}$	$\mathfrak{D}_P/\mathfrak{D}_0$
10^1	0.25
$4.6 \cdot 10^1$	0.10
10^2	0.063
10^3	0.016
$1.3 \cdot 10^3$	0.014
$2.15 \cdot 10^3$	0.010
10^4	0.0040

10^{-1} and 10^{-2} should be appropriate. A constant value was chosen throughout all simulations and varied in parameter studies to demonstrate the effect of different polymer diffusion coefficients.

As in previous sections, a reference set of parameters was defined and is summarized in Table 15. This set of parameters will be used throughout this chapter, if not stated otherwise.

Table 15. Reference set of parameters for the model defined in Section 5.1.2. These values were used if not stated otherwise. Due to the lack of data, the pure component density of all solid species was set to the value of PVP (see material safety data sheet). The molecular weight of dissociated initiator MW_I was set to 0.5 MW_{I_2}, production of nitrogen was ignored.

Parameter	Reference value
η_0	10^{-3} Pas
C_η	14.75
$\mathfrak{D}_0^0$	10^{-9} m^2 s^{-1}
$\mathfrak{D}_P/\mathfrak{D}_0$	0.1
ρ_M^0	989.72 kg m^{-3} [48]
ρ_S^0	958.57 kg m^{-3} [48]
ρ_j^0 (all other)	1200 kg m^{-3}
MW_M	111.4 g mol^{-1}
MW_{I_2}	271.2 g mol^{-1}
MW_I	135.6 g mol^{-1}
MW_S	18 g mol^{-1}
Kinetic model	TDB double moment model (see Table 10)

5.2 Tubular reactors without mixer elements

As a first system to study the effect of different transport phenomena on the polymerization in continuously operated reactors, a tubular reactor was considered because of its geometric simplicity. The focus will be on the influence of transport coefficients for mass and momentum, which are expected to have the strongest impact on deposit formation. Other effects as for example density changes are discussed in Section A.2.5 of the appendix for a simplified system but seem to be of minor importance.

To reduce the computational effort, a two-dimensional, symmetric substitute system was studied as illustrated in Figure 81. The mesh was refined linearly by a factor of 5 in y-direction to achieve a higher resolution at the wall where formation of deposits was expected. As a reference geometry, a channel with a length L_x of 250 mm and a width of 2 mm was defined and will be used in the following sections, if not specified otherwise. The same holds for the hexahedral mesh, which consists of 1500 cells in x and 50 cells in y direction up to the symmetry axis at the length L_y of 1 mm.

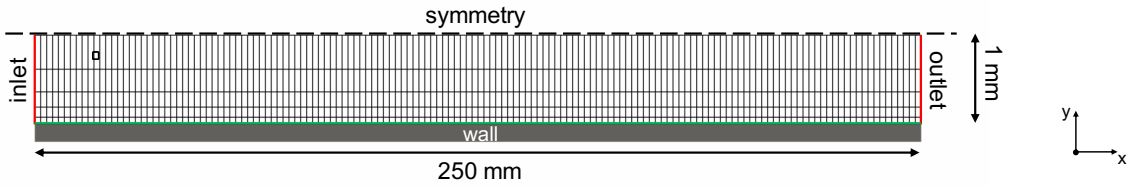

Figure 81. Geometry for the two-dimensional channel flow cases: The axis perpendicular to the wall (y-axis) is scaled by a factor of 25 and the mesh is coarsened for visualization purposes. Details on the case setup are given in Section 5.2. The green line represents the line on which data for spacial profiles in the next sections has been gathered.

The boundary conditions are common for a channel flow case. Besides the wall and symmetry boundary conditions illustrated in Figure 81, uniform Dirichlet boundary conditions for all concentrations and the barycentric velocity at the inlet patch as well as zero gradient Neumann boundary conditions at the outlet patch were specified. For the pressure p, a

zero gradient Neumann boundary condition was specified at the inlet patch and a uniform, zero value Dirichlet boundary condition at the outlet patch. Plug flow solutions were used as initial conditions for all concentration profiles and the initial velocity and pressure field were set to zero inside the simulation domain. The reference conditions from Table 15, the inlet concentrations in Table 16 and the inlet velocity $|\boldsymbol{v}_{in}| = 1$ mm s^{-1} were used.

Table 16. Inlet concentrations for the two-dimensional channel flow cases. These values were used, if not stated otherwise.

Component i	Inlet concentration c_i / mol l^{-1}	Inlet weight fraction w_i
I_2	$7.113 \cdot 10^{-4}$	$2 \cdot 10^{-4}$
M	1.734	0.2
S	Equation (140)	$1 - w_M - w_{I_2}$
All other	0	0

5.2.1 Formation of highly viscous wall layers

The reference conditions described in Section 5.2 lead to a Reynolds number of

$$Re_{in} = \frac{\rho |\boldsymbol{v}_{in}| 2L_y}{\eta} \approx 2 \tag{160}$$

at the inlet and, therefore, a laminar velocity profile develops after around 2 mm as shown in Figure 82. Since the advective or barycentric velocity $\boldsymbol{v}^m$ is lower in regions closer to the wall, the local residence time is higher in these regions and the polymer content increases not only along the reactor central axis but also towards the reactor walls. The viscosity increases with the polymer content as specified by Equation (148) and causes the velocity profile to lace in, which increases the local residence over an even wider region as illustrated in Figure 83.

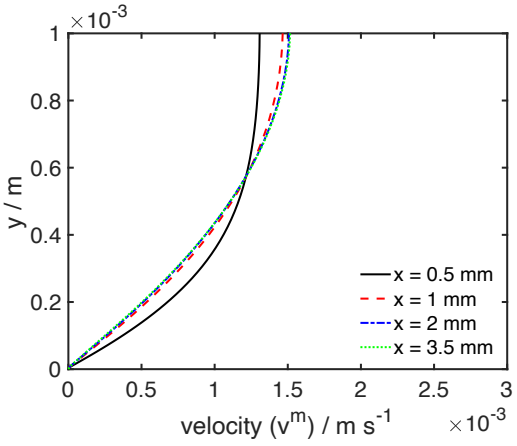

Figure 82. Barycentric velocity profiles in y direction at different positions close to the reactor inlet of the geometry shown in Figure 81 after 3600 s. All other parameters are those of the reference conditions described in Section 5.1 to Section 5.2.

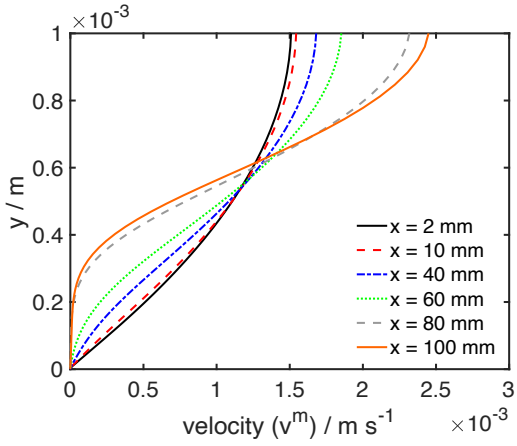

Figure 83. Barycentric velocity profiles in y direction at different positions further away from the reactor inlet of the geometry shown in Figure 81 after 3600 s. All other parameters are those of the reference conditions described in Section 5.1 to Section 5.2.

This situation leads to the formation of a highly viscous wall layer with a very high polymer content and monomer weight fractions w_M close to zero as shown in Figure 84. Due to the large concentration gradients between the wall layer and the bulk region, diffusive transport of monomer perpendicular to the reactor walls into the wall layer increases as indicated by the inverse of the modified Peclet number field for monomer transport

$$(Pe_{mod,M})^{-1} = \frac{|\boldsymbol{v}_M^N|}{|\boldsymbol{v}^m|} \tag{161}$$

with the diffusive transport velocity of monomer

$$\boldsymbol{v}_M^N = \frac{\boldsymbol{J}_M^N}{c_M} \tag{162}$$

also shown in Figure 84. Since the Maxwell-Stefan diffusion coefficients involving transport of polymer $\mathfrak{D}_P$ were specified to be an order of magnitude lower than $\mathfrak{D}_0$ for low molecular species, monomers that are polymerized in the wall layer accumulate. The polymer weight

fraction w_P in this region even exceeds 0.2, which would be the final concentration in a plug flow reactor using the same initial conditions.

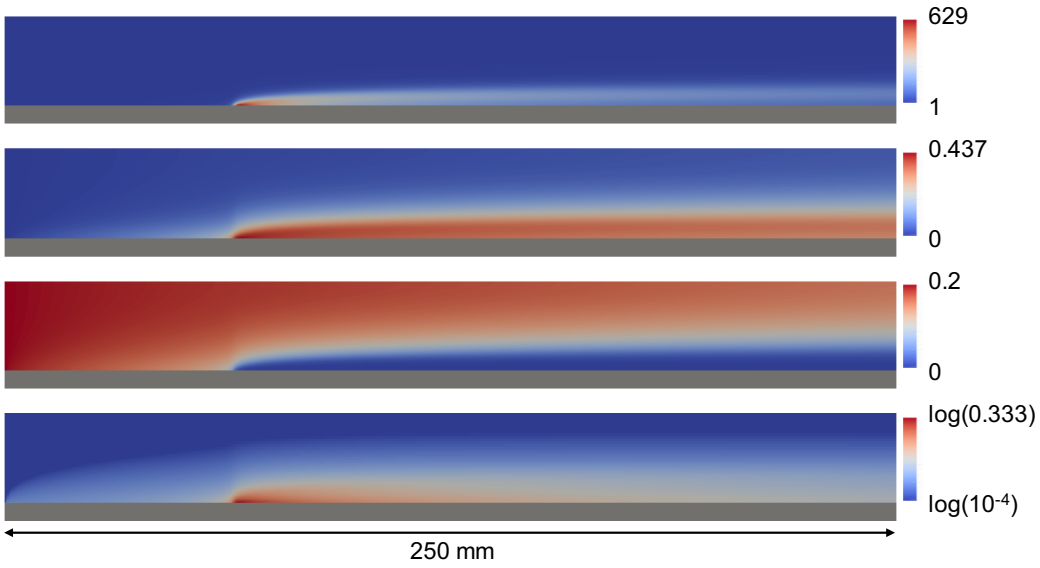

Figure 84. Relative viscosity η_{rel} field, polymer weight fraction w_P field, monomer weight fraction w_M field and inverse modified Peclet number $(Pe_{mod,M})^{-1}$ field (top to bottom) in the geometry shown in Figure 81 after 3600 s. All other parameters are those of the reference conditions described in Section 5.1 to Section 5.2.

High polymer contents together with an increased local residence time foster the importance of side reactions. The evolution of the polymer weight fraction w_P and weight average molecular weight $\overline{M_w}$ profiles at the wall are shown in Figure 85 and Figure 86. As expected, the polymer weight fraction w_P increases most drastically in the critical region where the layer develops and $(Pe_{mod,M})^{-1}$ has the highest value. The increase in the weight average molecular weight $\overline{M_w}$ is also most pronounced in this region and even accelerates, indicating gelation.

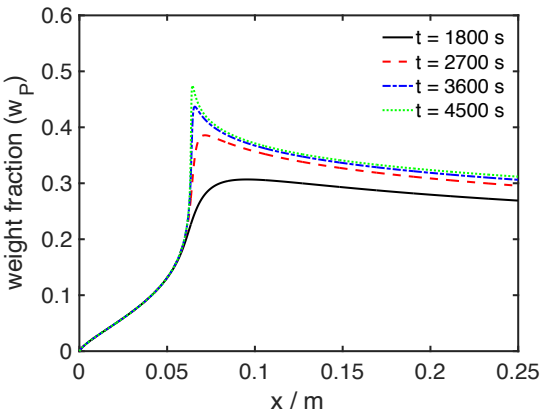

Figure 85. Polymer weight fraction w_P profiles in x-direction at different times in the geometry shown in Figure 81 at the wall (green line in Figure 81). All other parameters are those of the reference conditions described in Section 5.1 to Section 5.2.

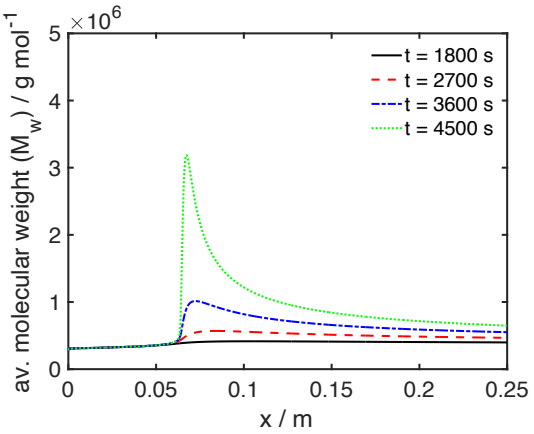

Figure 86. Weight average molecular weight $\overline{M_w}$ fraction profiles in x-direction at different times in the geometry shown in Figure 81 at the wall (green line in Figure 81). All other parameters are those of the reference conditions described in Section 5.1 to Section 5.2.

The viscous wall layer creates conditions under which the TDB propagation reaction leads to gelation locally at the wall, although no gelation in the bulk phase in the middle of the channel is observed. Although, this side reaction causes the formation of polymer gel, its effect on the formation of the wall layer is small, as illustrated by a simulation in which the TDB propagation reaction has been switched off by setting the corresponding reaction rate coefficient $k_{p,TDB} = 0\,\mathrm{l\,mol^{-1}\,s^{-1}}$. The polymer weight fraction fields w_P are shown in Figure 87. The TDB propagation reaction affects the formation of the viscous wall layer only slightly, since it mostly influences the evolution of the second polymer chain length moment $\mu^{2,0}$, which is manifested in the increasing weight average molecular weight $\overline{M_w}$. The formation of the viscous wall layer, on the other hand, depends on the polymer weight fraction w_P and, therefore, the concentration of polymerized repeat units, which is characterized by the first chain length moment $\mu^{1,0}$. The latter is not directly affected by the TDB propagation reaction as discussed in Section A.1.2. but the concentration of polymer molecules $\mu^{0,0}$ reduces, which changes the driving force for diffusive transport of polymer.

It should be remembered that the dependence of the solution viscosity on the chain length is not included in the model for the relative viscosity η_{rel} in this thesis. If this were considered in the model, the effect of the side reaction on the formation of the viscous wall layer might be more pronounced.

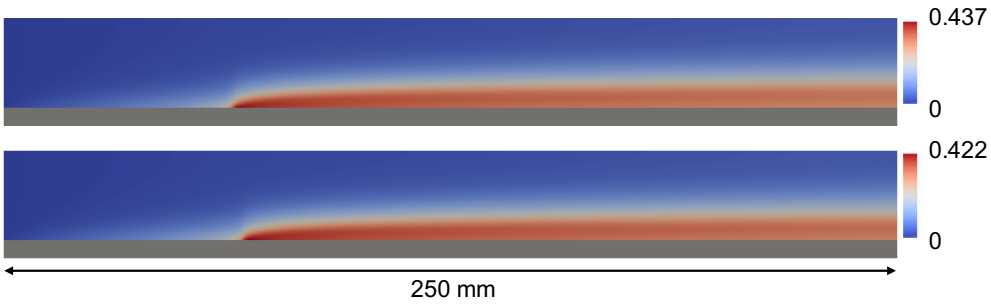

Figure 87. Polymer weight fraction w_P fields with $k_{p,TDB} = 3300\,\mathrm{l\,mol^{-1}\,s^{-1}}$ (top) and $k_{p,TDB} = 0\,\mathrm{l\,mol^{-1}\,s^{-1}}$ (bottom) in the geometry shown in Figure 81 after 3600 s. All other parameters are those of the reference conditions described in Section 5.1 to Section 5.2.

As shown in Figure 88, the formation of the wall layer affects the weight average molecular weight $\overline{M_w}$ even without the branching reaction due to different monomer and radical concentrations inside the layer, which determine the kinetic chain length

$$\nu_{kin} = \frac{k_p\ M}{k_p f_{trm} M + k_t \lambda^{0,0}}\ . \tag{163}$$

An overview of the concentration fields of different species is given in Section A.2.6 of the appendix. Although the kinetic chain length ν_{kin} decreases inside the layer, the formation of high-molecular polymer chains increases due to the branching reaction as illustrated in Figure 89 and finally causes gelation. Without the branching reaction, a stationary state can be reached as shown in Figure 90 and Figure 91. This is an important observation and emphasizes the importance of diffusive mass transport and the increase in viscosity for the formation of the viscous wall layer and, in the end, for the formation of insoluble polymer

gel deposits. Therefore, the effect transport phenomena will be discussed in more detail in the following section by variation of transport coefficients and the inlet velocity.

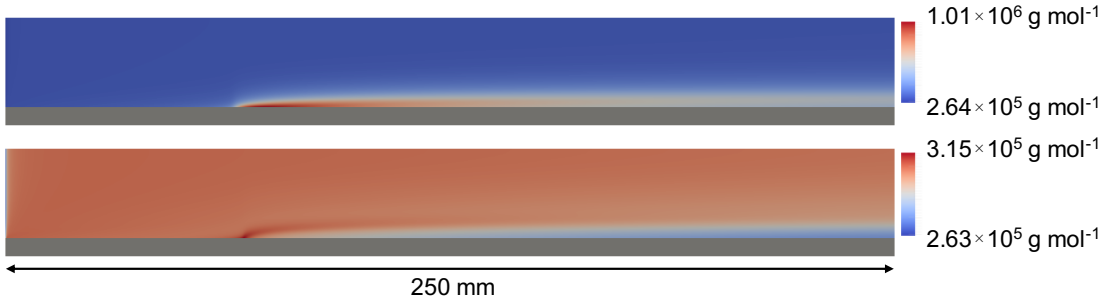

Figure 88. Weight average molecular weight $\overline{M_w}$ fraction fields with $k_{p,TDB} = 3300\,\mathrm{l\,mol^{-1}\,s^{-1}}$ (top) and $k_{p,TDB} = 0\,\mathrm{l\,mol^{-1}\,s^{-1}}$ (bottom) in the geometry shown in Figure 81 after 3600 s. All other parameters are those of the reference conditions described in Section 5.1 to Section 5.2.

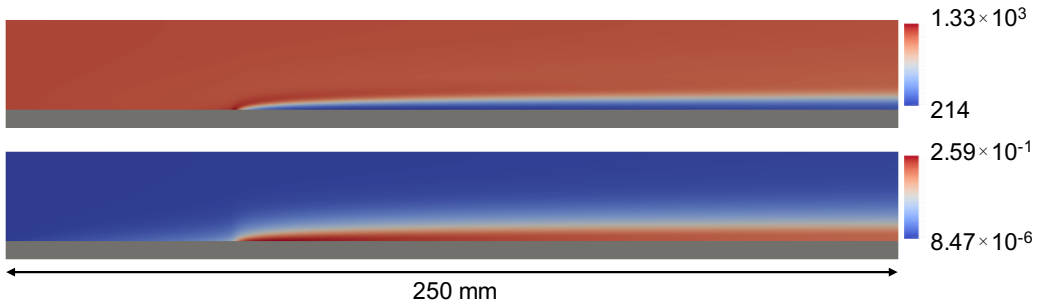

Figure 89. Kinetic chain length (top) and branches per 1000 repeat units (bottom) field in the geometry shown in Figure 81 after 3600 s. All other parameters are those of the reference conditions described in Section 5.1 to Section 5.2.

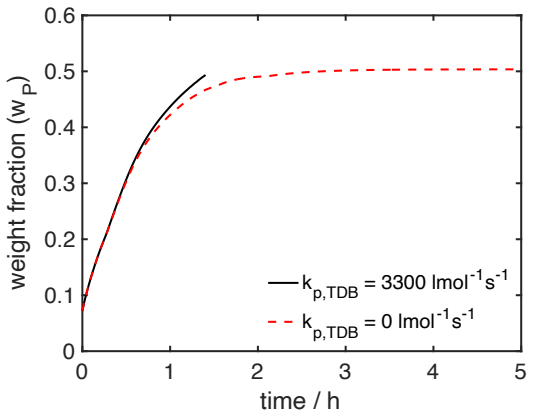

Figure 90. Evolution of the maximum value of the polymer weight fraction w_P in the geometry shown in Figure 81 for different values of the TDB propagation reaction coefficient. All other parameters are those of the reference conditions described in Section 5.1 to Section 5.2.

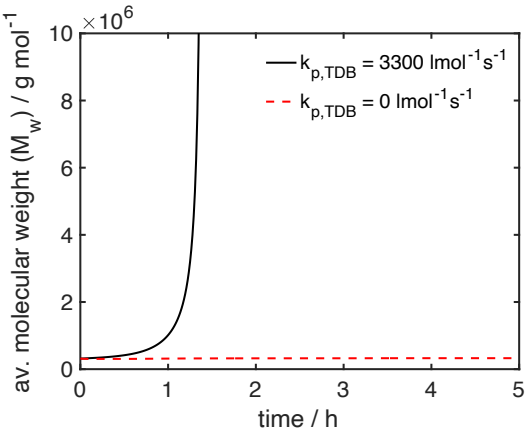

Figure 91. Evolution of the maximum value of the weight average molecular weight $\overline{M_w}$ in the geometry shown in Figure 81 for different values of the TDB propagation reaction coefficient. All other parameters are those of the reference conditions described in Section 5.1 to Section 5.2.

5.2.2 Influence of transport properties and inlet velocity on wall layer formation

An important process parameter, which can easily be controlled in an isothermally operated tubular reactor, is the inlet velocity. As shown in Figure 92 and Figure 93, the position of the peaks of the polymer weight fraction w_P and weight average molecular weight $\overline{M_w}$ profiles are proportional to the inlet velocity. The effect becomes even clearer by plotting the profiles over the corresponding plug flow residence time

$$\tau_{PF}(x) = \frac{x}{|\boldsymbol{v}_{in}|} \tag{164}$$

with the position x along the reactor length coordinate as illustrated in Figure 94 for a wider range of inlet velocities. The timescale for gelation shown in Figure 95 does not depend on the inlet velocity.

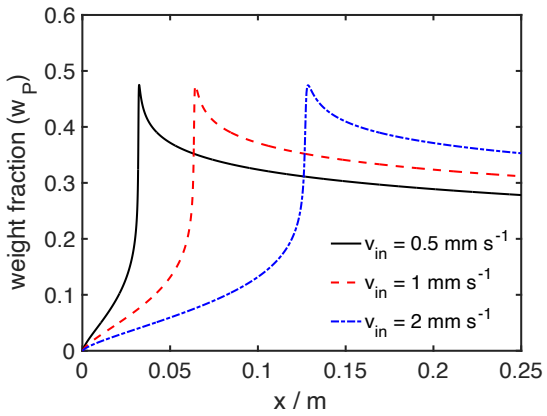

Figure 92. Polymer weight fraction w_P profiles in x-direction in the geometry shown in Figure 81 at the wall (green line in Figure 81) after 4500 s for different inlet velocities. All other parameters are those of the reference conditions described in Section 5.1 to Section 5.2.

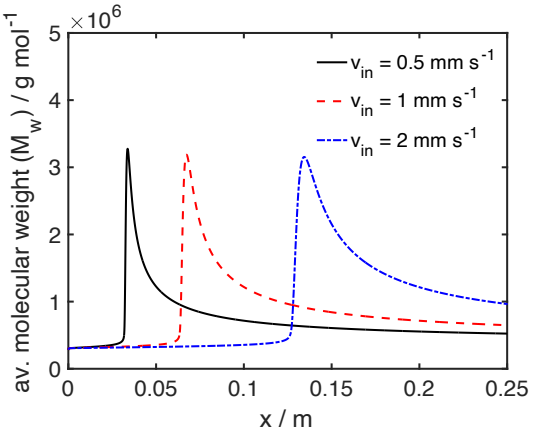

Figure 93. Weight average molecular weight $\overline{M_w}$ profiles in x-direction in the geometry shown in Figure 81 at the wall (green line in Figure 81) after 4500 s for different inlet velocities. All other parameters are those of the reference conditions described in Section 5.1 to Section 5.2.

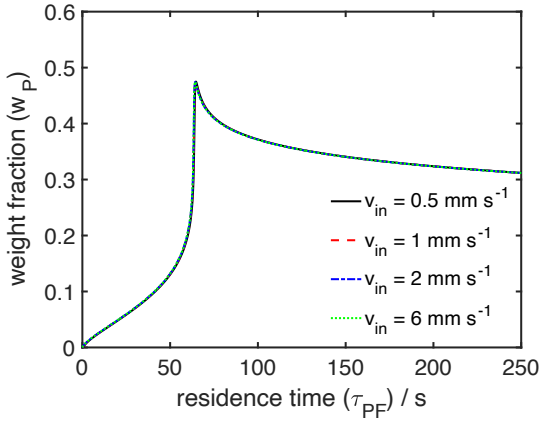

Figure 94. Polymer weight fraction w_P profiles in x-direction in the geometry shown in Figure 81 at the wall after 4500 s for different inlet velocities plotted over the plug flow residence time τ_{PF}. All other parameters are those of the reference conditions described in Section 5.1 to Section 5.2.

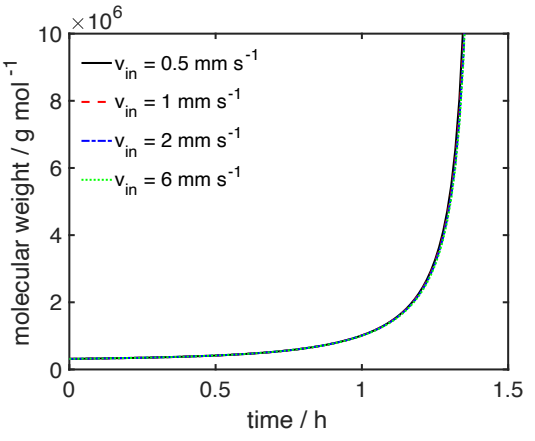

Figure 95. Evolution of the maximum value of the weight average molecular weight $\overline{M_w}$ in the geometry shown in Figure 81 for different inlet velocities. All other parameters are those of the reference conditions described in Section 5.1 to Section 5.2.

Different transport coefficients for monomer and polymer transport have been suggested as an important factor for the strong increase of the polymer weight fraction w_P in the wall layer in Section 5.2.1. Therefore, the ratio of the Maxwell-Stefan transport coefficients for polymers and low molecular species $\mathfrak{D}_P/\mathfrak{D}_0$ is expected to have a strong influence on the layer formation and gelation and was varied, while keeping the reference value $\mathfrak{D}_0^0$ constant. With increasing $\mathfrak{D}_P/\mathfrak{D}_0$, the peak position of the polymer weight fraction w_P and weight average molecular weight $\overline{M_w}$ moves further away from the inlet in x-direction as shown in Figure 96 and Figure 97.

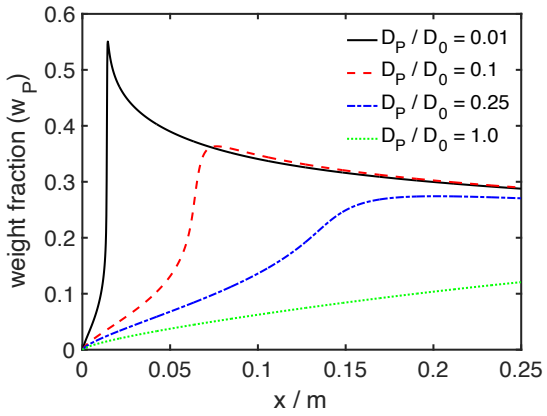

Figure 96. Polymer weight fraction w_P profiles in x-direction in the geometry shown in Figure 81 at the wall (green line in Figure 81) after 2400 s for different Stefan-Maxwell diffusion coefficient ratios $\mathfrak{D}_P/\mathfrak{D}_0$. All other parameters are those of the reference conditions described in Section 5.1 to Section 5.2.

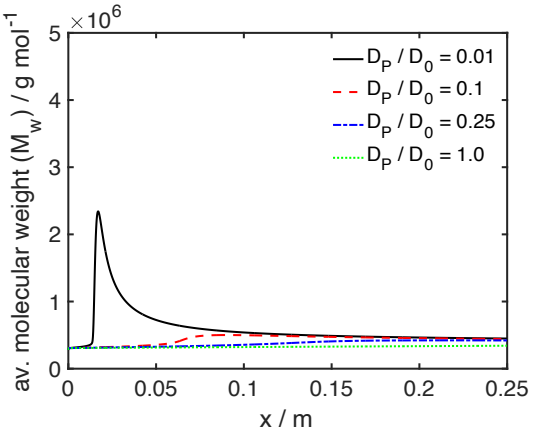

Figure 97. Weight average molecular weight $\overline{M_w}$ profiles in x-direction in the geometry shown in Figure 81 at the wall (green line in Figure 81) after 2400 s for different Stefan-Maxwell diffusion coefficient ratios $\mathfrak{D}_P/\mathfrak{D}_0$. All other parameters are those of the reference conditions described in Section 5.1 to Section 5.2.

Gelation also occurs for higher ratios $\mathfrak{D}_P/\mathfrak{D}_0$, but the timescale of gelation increases as shown in Figure 98. When the Maxwell-Stefan diffusion coefficient for polymers $\mathfrak{D}_P = \mathfrak{D}_0$ for low molecular species no distinctive wall layer is formed since the transport rate of polymer perpendicular to the wall layer is high enough. Neither does gelation occur under these conditions. To validate, that the wall layer is not formed at a position outside the

simulation domain, the reactor length was extended to $L_x = 2.5$ m for the simulation with $\mathfrak{D}_P = \mathfrak{D}_0$. In this case, monomer conversion close to unity at the reactor outlet is safely reached under plug flow conditions. In the larger domain, no gelation is observed for this case as well. The results are shown in Section A.2.7 of the appendix.

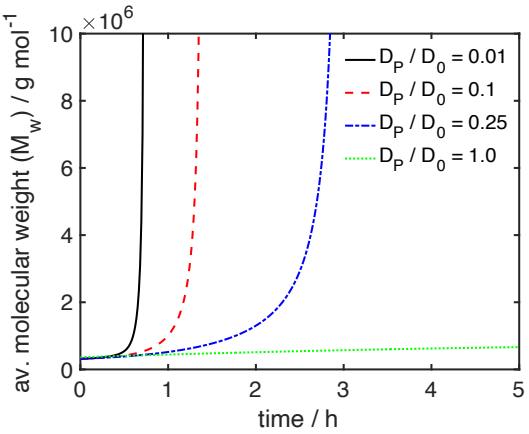

Figure 98. Evolution of the maximum value of the weight average molecular weight $\overline{M_w}$ in the geometry shown in Figure 81 for different Stefan-Maxwell diffusion coefficient ratios $\mathfrak{D}_P/\mathfrak{D}_0$. All other parameters are those of the reference conditions described in Section 5.1 to Section 5.2.

Another important factor, which affects the barycentric velocity field as well as diffusive mass transport, is the increase in viscosity with increasing polymer content. To illustrate this effect, the reference case conditions were compared to a simulation in which the viscosity was fixed to a constant value of $\eta = 1$ mPa s as illustrated in Figure 99 and Figure 100. Similar to the increased polymer diffusion coefficient in the previously discussed case with $\mathfrak{D}_P = \mathfrak{D}_0$, no gelation can be observed with a constant solution viscosity. Again, a larger simulation domain was used for validation purposes. To validate, that the wall layer is not formed at a position outside the simulation domain, the reactor length was extended to $L_x = 2.5$ m for the simulation with a constant viscosity. In the larger domain, no gelation is observed for this case as well. The results are shown in Section A.2.7 of the appendix.

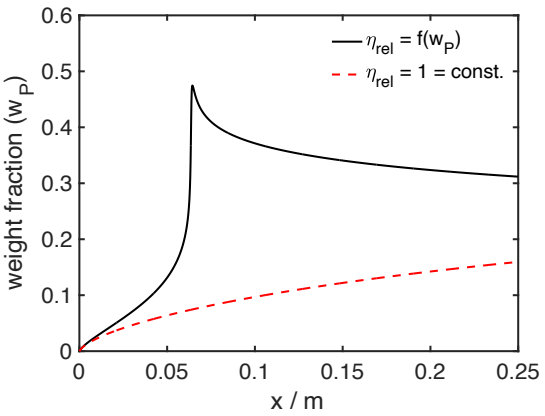

Figure 99. Polymer weight fraction w_P profiles in x-direction in the geometry shown in Figure 81 at the wall (green line in Figure 81) after 4500 s for a constant and variable relative viscosity. All other parameters are those of the reference conditions described in Section 5.1 to Section 5.2.

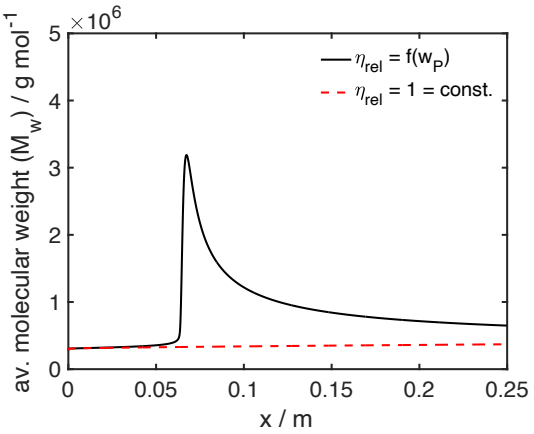

Figure 100. Weight average molecular weight $\overline{M_w}$ profiles in x-direction in the geometry shown in Figure 81 at the wall (green line in Figure 81) after 4500 s for a constant and variable relative viscosity. All other parameters are those of the reference conditions described in Section 5.1 to Section 5.2.

5.2.3 Residence time distributions under reactive conditions

The formation of viscous wall layers distorts the flow field and must, therefore, also affect the residence time distribution. In Section 3.3.2, residence times distributions under reactive conditions in experiments have been discussed and will be compared to results from simulations in this section. To do so, the geometry in Figure 81 was modified to match the geometry of the capillary reactor that has been described in Section 3.3.1. Besides changing the domain length to 3000 mm and the height to 0.88 mm, the symmetry plane was collapsed to form a symmetry line. The resulting geometry is a wedge with an angle of 5°, which is shown in Figure 101.

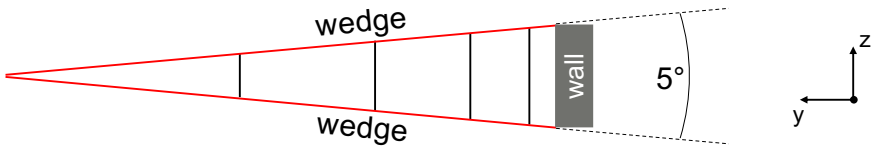

Figure 101. Modification of the geometry in Figure 81 for pipe flow cases: The x-axis and y-axis were scaled and the mesh was coarsened for visualization purposes. Details on the case setup are given in the text.

To measure the residence time distribution in simulations, a tracer species T was included in the simulations that are presented in this section. The tracer is assumed to be passive and, therefore, no interaction with other species or reaction were included in the transport equation

$$\frac{\partial c_T}{\partial t} = -\nabla \cdot \left(\boldsymbol{v}^m - \frac{1}{\rho} \sum_{i \neq T} MW_i \boldsymbol{J}_i^N \right) c_T - \nabla \cdot \boldsymbol{J}_T^N \tag{165}$$

with

$$\boldsymbol{J}_T^N = -D_T \cdot \left(\nabla c_T - c_T \frac{1}{c} \nabla c \right) \tag{166}$$

and the Fickian type diffusion coefficient D_T for the tracer species. Consequently, the effect of the tracer species on the overall concentration c was neglected as well.

To mimic the injection of the tracer by an HPLC switching valve, the Dirichlet boundary condition at the inlet for the tracer was modified to vary in time. The time dependent value at the inlet patch was chosen from a lookup table, which was generated using a measured inlet signal. This signal was generated by replacing the reactor with a direct connection between the HPLC valve and the conductivity flow cell. To ensure that the same amount of tracer as in the experiments was injected, the measured signal was normalized and scaled leading to the time-dependent inlet concentration

$$c_{T,in}^{sim} = N_T^0 \frac{i_{in}}{\int i_{in}\, dt}. \tag{167}$$

with the current i_{in} that was measured using the conductivity flow cell and the constant N_T^0, which was fixed by matching the amount of tracer that was injected in experiments. A detailed discussion of this inlet concentration signal is given in Section A.3.3 of the appendix. To mimic multiple injections, the modified signal was copied, shifted and added to the lookup table as illustrated in Figure 102.

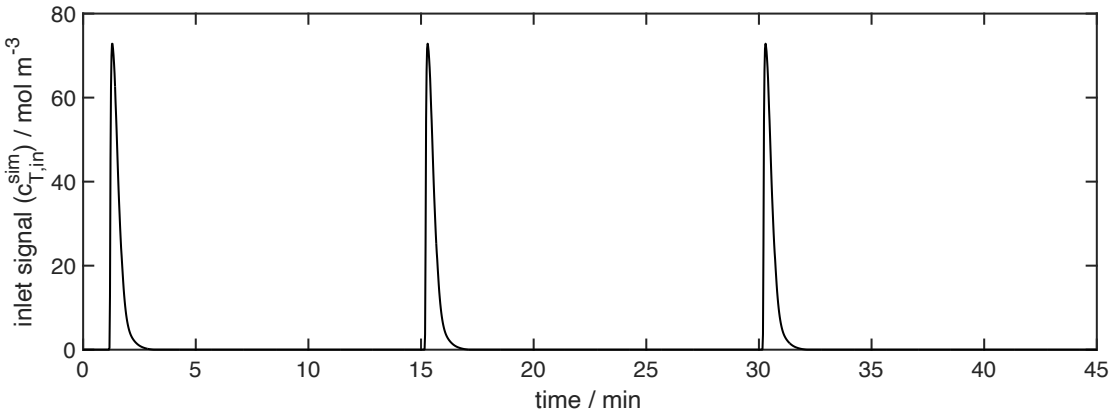

Figure 102. Tracer concentration inlet signal $c_{T,in}^{sim}$ (Eq. (299)) for the first 45 min of simulations as described in Section 5.2.3. Injection times are 1 min, 15 min and 30 min.

The outlet concentration signal was measured by calculating the patch average

$$c_{T,out} = \frac{\sum_{f_{out}} \left(c_{T,out}\right)_{f_{out}} \left|\boldsymbol{S}_{f_{out}}\right|}{\sum_{f_{out}} \left|\boldsymbol{S}_{f_{out}}\right|} \tag{168}$$

with the summation over all faces f_{out}, that were part of the outlet patch, their face area $\left|\boldsymbol{S}_{f_{out}}\right|$ and the tracer concentration at the faces $\left(c_{T,out}\right)_{f_{out}}$. A comparison of the outlet signals

$$E_{out} = \frac{c_{T,out}}{N_T^0} \tag{169}$$

in pure water that correspond to the inlet signal in Figure 103 for different tracer diffusion coefficients D_T is given in Figure 104. Additionally, two reference solutions are illustrated in Figure 104. A laminar reference without any dispersion by diffusion was calculated by convolution of the inlet signal from the lookup table

$$E_{in} = \frac{c_{T,in}^{sim}}{N_T^0} \tag{170}$$

and the residence time distribution of a Hagen Poiseuille flow pattern [59]

$$E_{lam} = \begin{cases} 0, & t < \dfrac{\tau}{2} \\ \dfrac{\tau^2}{2}\dfrac{1}{t^3}, & t \geq \dfrac{\tau}{2} \end{cases} . \tag{171}$$

The Taylor dispersion reference was calculated by convolution of the inlet signal and the solution of the Taylor dispersion problem in a circular tube with a laminar flow pattern [38]

$$E_{Taylor} = \sqrt{\frac{Pe_{Taylor}}{4\pi\tau_{PF}^2}} \exp\left(-\frac{(t-\tau_{PF})^2 Pe_{Taylor}}{4\tau_{PF}^2}\right). \tag{172}$$

In Equation (172),

$$\tau_{PF} = \frac{L_{reac}}{v^{mean}} \tag{173}$$

is the plug flow residence time and

$$Pe_{Taylor} = \frac{v^{mean} L_{reac}}{D_{Taylor}} \tag{174}$$

is the Peclet number for Taylor dispersion with the effective dispersion coefficient [60], [61]

$$D_{Taylor} = D_T \left(1 + \frac{1}{48}\left(\frac{v^{mean} R_{reac}}{D_T}\right)^2\right). \tag{175}$$

Due to radial diffusion and the non-uniform velocity distribution in the channel cross section, the effective axial dispersion decreases with increasing value of D_T [38]. A further discussion of the Taylor dispersion reference is given in Section A.3.3.1 of the appendix. As illustrated in Figure 104, the measured outlet signal approaches the Taylor dispersion reference for high values of D_T.

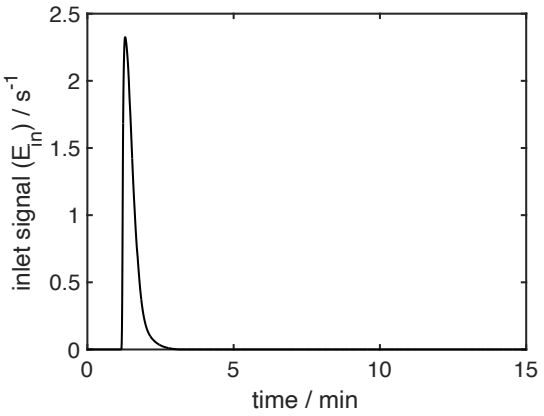

Figure 103. Normalized tracer inlet signal E_{in} for simulations as described in Section 5.2.3. The hypothetical injection time for this signal is 1 min.

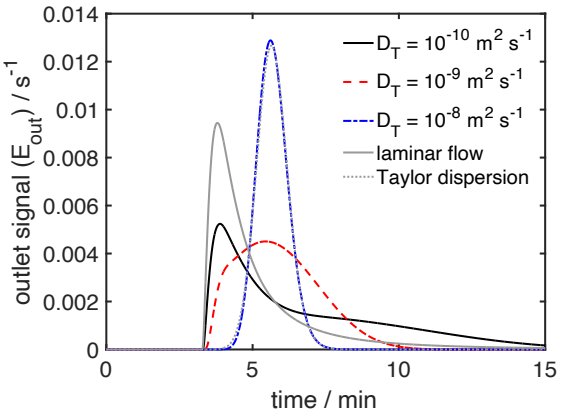

Figure 104. Output signals E_{out} of simulation in pure solvent for different tracer diffusion coefficients D_T that correspond to the inlet signal in Figure 103. The laminar and Taylor dispersion reference signals were generated as described in Section 5.2.3.

As discussed in Section A.3.3 of the appendix, a diffusion coefficient of $D_T = 5\ 10^{-9}\ m^2\ s^{-1}$ results in outlet signals that are in very good agreement with the experimental observation in pure water from Section 3.3.2 and will be used subsequently.

The measured outlet signals for different injection times are shown in Figure 106. The TDB propagation reaction was switched off by setting the TDB propagation rate coeffi-

cient $k_{p,TDB} = 0\ \mathrm{l\ mol^{-1}\ s^{-1}}$ to achieve longer operation times and the Maxwell-Stefan diffusion coefficient for low molecular species $\mathfrak{D}_0$ was set to $\mathfrak{D}_0 = D_T = 5\ 10^{-9}\ \mathrm{m^2\ s^{-1}}$. The ratio of the Maxwell-Stefan diffusion coefficient for polymers and low molecular species $\mathfrak{D}_P/\mathfrak{D}_0$ was set to 0.014, since this value is closer to the expected value for the average chain length of around $\mu^{1,0}/\mu^{0,0} \approx 1300$ according to Table 14. As discussed in Section 5.2.2, the effect of the side reaction on the layer formation is small and, therefore, does not affect the results significantly. For a better comparison to experimental results in Figure 105, the outlet signals are presented in a normalized form using the average residence time in the reactor system. A detailed discussion of this normalization procedure is given in Section A.3.3 of the appendix. The results from experiments and simulations are generally in good agreement, although tailing is less pronounced in simulations and the break-through is slightly earlier in experiments. This may be due to simplifications that had to be made in the transport model and the simple correlation for the increase in viscosity. The larger difference between signals from the injection after 1 min of operation

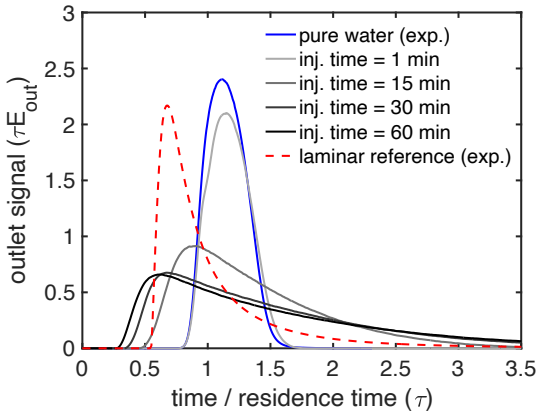

Figure 105. Normalized outlet signals for different injection times in experiments. The normalization procedure is explained in Section A.3.3 of the appendix.

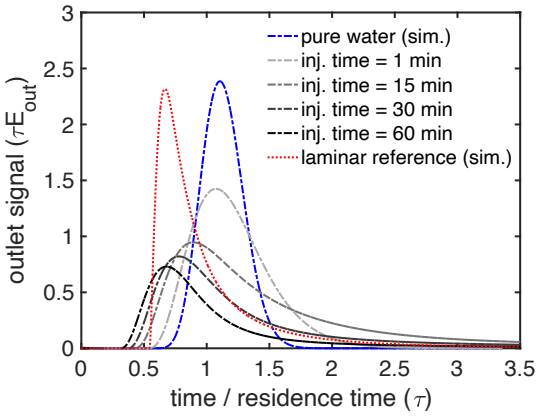

Figure 106. Normalized outlet signals for different injection times in simulations. The normalization procedure is explained in Section A.3.3 of the appendix.

is attributed to the different initial condition, which is pure water in experiments and a plug flow solution in simulations.

5.3 Tubular reactors with static mixer-like inserts

As a step towards static mixer reactors, which are of interest for the transfer of batch to continuous processes, further simulations in more complex but still two-dimensional geometries were carried out. The geometry that is illustrated in Figure 107 is motivated by the wall region of a Fluitec CSE/X® static mixer element and intended to capture the flow field in representative regions qualitatively. Again, a plug flow solution using the same inlet velocity was mapped onto the mesh as initial conditions. The boundary conditions are the same as for the channel flow case that has been discussed in Section 5.2. The inlet concentrations are the ones from Table 16 if not stated otherwise. The mixer geometry was generated using the *blockMesh* utility and cut out using the *snappyHexMesh* utility starting from a mesh of 192 cells in x-direction and 60 cells in y-direction. Regions that

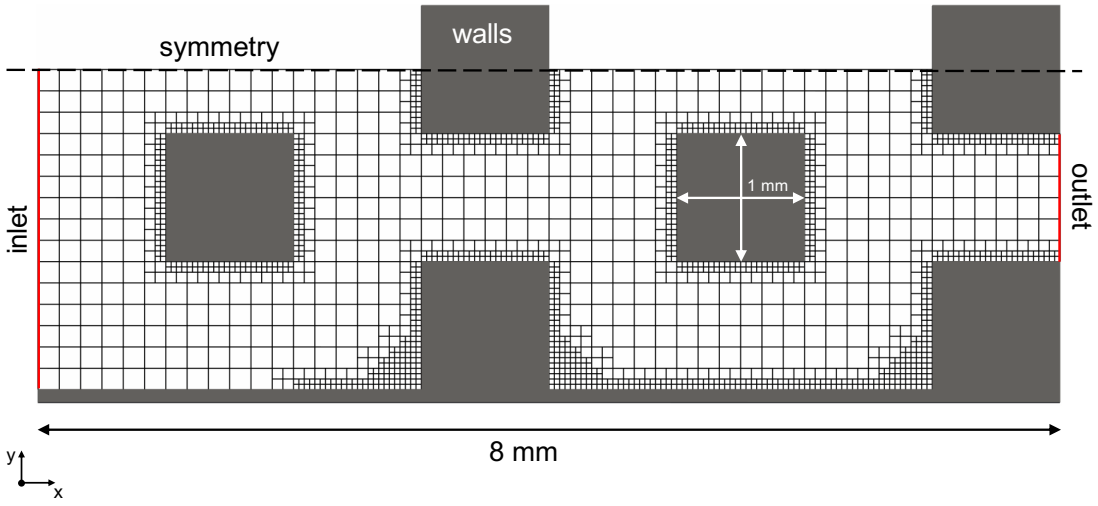

Figure 107. Geometry for the two-dimensional static mixer-like flow cases: The mesh was coarsened for visualization purposes. Details on the case setup are given in Section 5.3.

had proven critical in preliminary studies were refined twice by a factor of 0.5.

Since the effect of transport coefficients has been discussed extensively in the preceding section, the focus of this section will be on the effect of the reactor geometry, i.e alternating the flow pattern, and different initial conditions in the reactor. The model parameters in this section are those from Table 15 but the Maxwell-Stefan diffusion coefficient for low molecular species $\mathfrak{D}_0$ was set to $\mathfrak{D}_0 = D_T = 5\ 10^{-9}\ \mathrm{m^2\ s^{-1}}$ and the ratio of the Maxwell-Stefan diffusion coefficient for polymers and low molecular species $\mathfrak{D}_P/\mathfrak{D}_0$ was set to 0.014 for the same reasons as explained in Section 5.2.3.

5.3.1 Fouling in dead-water zones in static mixer-like geometries

The flow field in the geometry in Figure 107 is shown in Figure 108 for an inlet velocity of 1 mm $\mathrm{s^{-1}}$. In regions where mixer elements are in contact with walls, almost stagnant dead-water zones are formed, which lead to a highly increased local residence time. For

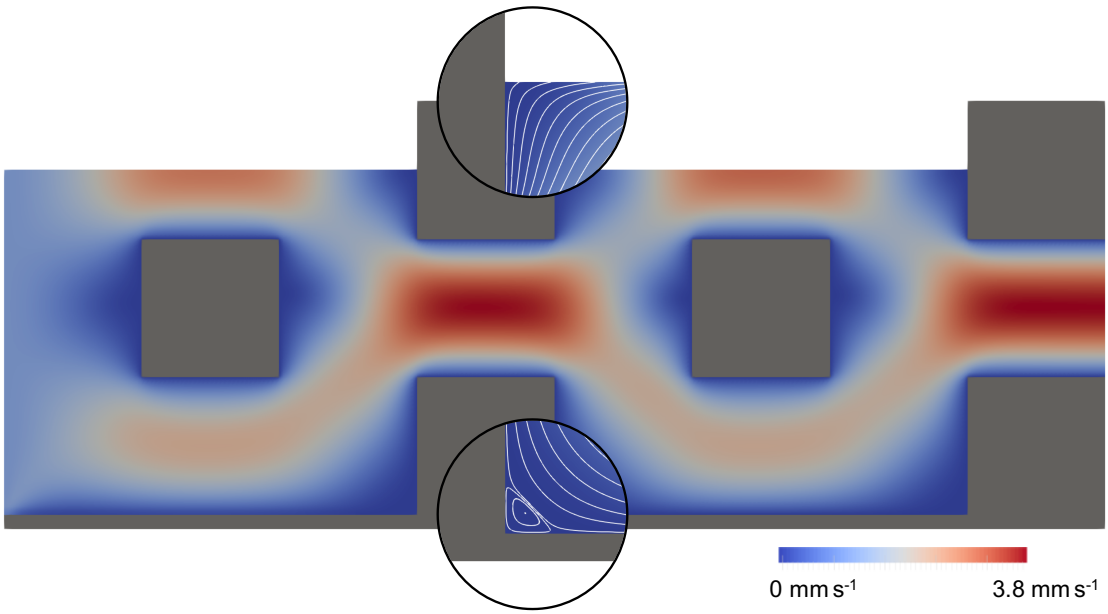

Figure 108. Steady state barycentric velocity field in the geometry shown in Figure 107. The inlet velocity in 1 mm $\mathrm{s^{-1}}$. All other parameters are those of the reference conditions described in Section 5.1 to Section 5.2. Vortices are formed upwind and downwind of all mixer element that are in contact with the reactor wall region but not at mixer elements that are fully immersed in fluid.

the geometry and conditions that are considered here, this effect only occurs in the wall regions upwind and downwind of all mixer element that are in contact with the lower reactor wall but not at mixer elements that are fully immersed in fluid. Similar to the formation of highly viscous wall layers in geometries without mixer elements, the polymer weight fraction w_P increases in these regions while the monomer weight fraction w_M decreases. As illustrated in Figure 109, the increase in the polymer weight fraction w_P is less pronounced than in an empty channel and a steady state is reached.

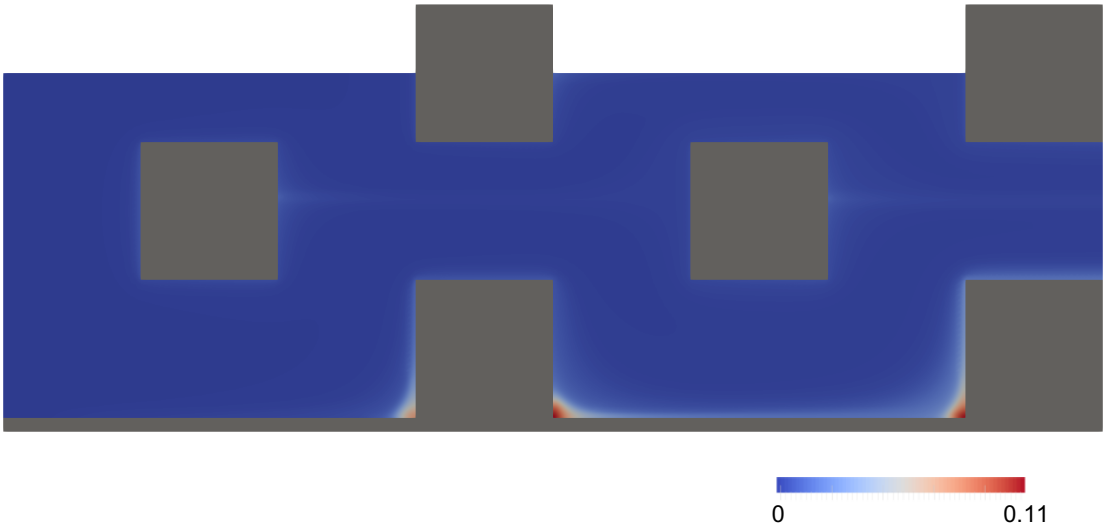

Figure 109. Steady state polymer weight fraction w_P field in the geometry shown in Figure 107. The inlet velocity is 1 mm s^{-1}. All other parameters are those of the reference conditions described in Section 5.1 to Section 5.2.

5.3.2 Influence of scale up on fouling in static mixer-like geometries

As discussed in the preceding section, static mixer-like geometries may lead to the formation of dead-water zones, with significantly different composition than the bulk phase. Although polymer accumulates in these regions, no gelation was observed in the simulation illustrated in Figure 109. Since the increase in the polymer weight fraction w_P is caused by diffusive mass transport limitations, the size of dead-water zones must also affect the

composition and, ultimately, the formation of deposits. To demonstrate this effect, the geometry was scaled by the same factor in the x- and y-direction while keeping the inlet velocity constant, which is equivalent to scaling the mass flow rate by the same factor. This choice is a trade-off between keeping the Reynolds number

$$Re_{mixer} = \frac{\rho^{in} v^{in} L_{mixer}}{\eta^{in}} \tag{176}$$

or average residence time

$$\tau_{mixer} = \frac{\epsilon_{mixer} L_x}{v^{in}} \tag{177}$$

constant. In this way, the form of the flow pattern as well as the magnitude of the velocity field remain similar and the average residence time at the position of the mixer elements does not change dramatically. On the other hand, the size of dead-water zones increases approximately with the scaling factor. See Section A.2.8 of the appendix for a more detailed discussion. In Equation (176) and Equation (177), ρ^{in} is the average density at the inlet, v^{in} the inlet velocity, η^{in} the viscosity at the inlet, ϵ_{mixer} the empty volume fraction in the geometry, L_{mixer} is the edge length of an immersed mixer element part and L_x the domain length in x direction. The size of the refinement regions was scaled by the geometric scaling factor as well and the number of cells in x- and y-direction was scaled accordingly for all geometries with a scaling factor larger than 1.15.

As can be understood from Figure 110 to Figure 112, the size of dead-water zones has a large impact on the composition and consequently on the formation of fouling deposits. Concentration gradients between the bulk phase and the dead-water zone increase with the size of the zone due to the limited mass transport perpendicular to the streamlines of

the barycentric velocity field. While mass transport is fast enough to prevent the accumulation of polymer to a critical level in small geometries, the polymer weight fraction w_P increases to very large values in larger geometries and leads to gelation.

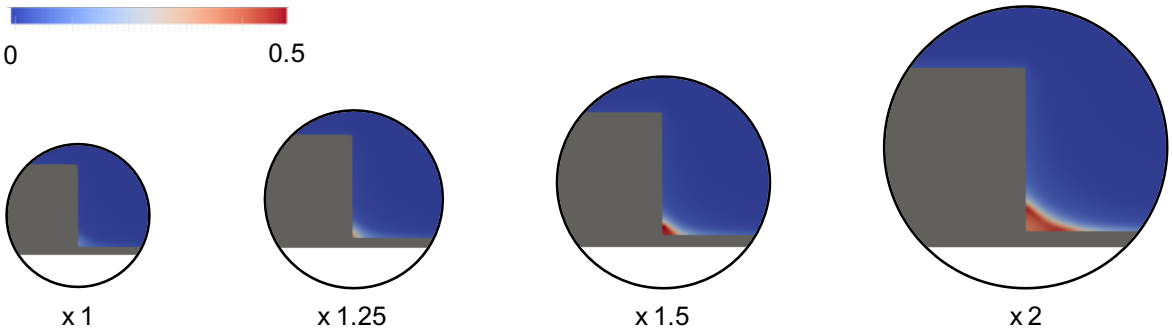

Figure 110. Magnification of the polymer weight fraction w_P field in the geometry shown in Figure 107 for different geometric scaling factors as described in Section 5.3.2 after 0.5 h of operation and an inlet velocity is 1 mm s^{-1}. The position of the magnified region corresponds the lower magnification circle in Figure 108. All other parameters are those of the reference conditions described in Section 5.1 to Section 5.2.

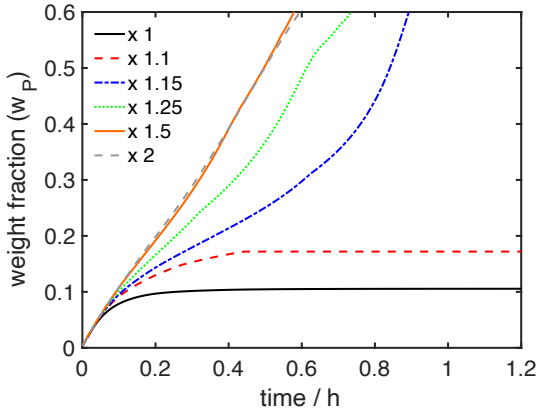

Figure 111. Evolution of the maximum value of the weight fraction w_P in the geometry shown in Figure 107 for different geometric scaling factors and an inlet velocity is 1 mm s^{-1}. All other parameters are those of the reference conditions described in Section 5.1 to Section 5.2.

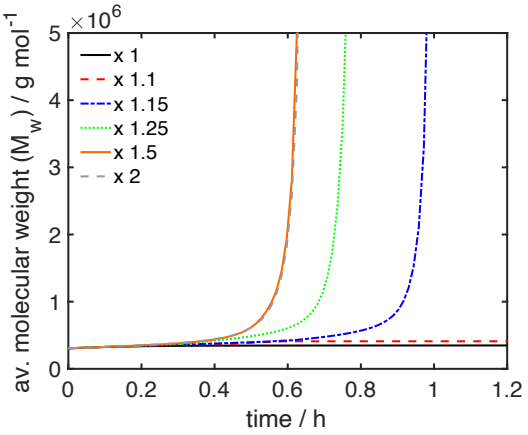

Figure 112. Evolution of the maximum value of the weight average molecular weight $\overline{M_w}$ in the geometry shown in Figure 107 for different geometric scaling factors and an inlet velocity is 1 mm s^{-1}. All other parameters are those of the reference conditions described in Section 5.1 to Section 5.2.

5.3.3 Fouling at different positions along the reactor central axis

So far, only effects in the first millimeters after the reactor inlet have been discussed using reference conditions that are summarized in Table 16 as inlet conditions. The composition of the bulk phase changes along the reactor central axis, which affects the possible magnitude of concentration gradients and viscosity differences between the bulk phase and dead-water zones. Two mimic this effect, plug flow solutions from positions further along the reactor central axis, i.e. longer residence times, were mapped onto the geometry as inlet and initial conditions. These positions correspond to those that have been discussed in Section 3.1.2.3. The initiator, monomer and polymer and weight fractions w_i^0 at the inlet for these simulations are given in Table 17. For these simulations, a geometry that was scaled by a factor of 1.5 was used to enhance fouling.

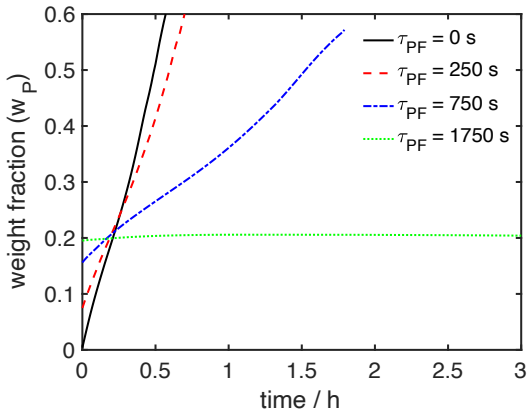

Figure 113. Evolution of the maximum value of the polymer weight fraction w_P in the geometry shown in Figure 107 for different inlet and initial conditions as defined in Table 17 and an inlet velocity is 1 mm s^{-1}. Geometry and number of cells were scaled by a factor of 1.5 as described in Section 5.3.3. All other parameters are those of the reference conditions described in Section 5.1 to Section 5.2.

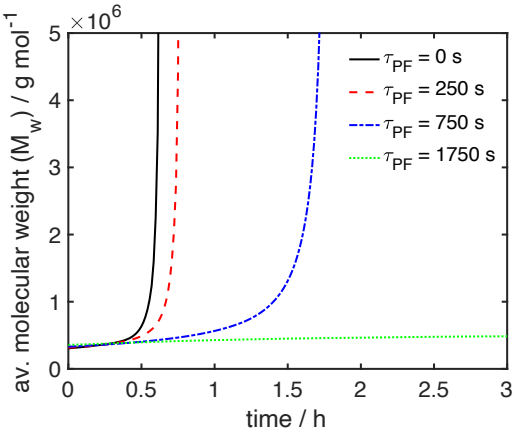

Figure 114. Evolution of the maximum value of the weight average molecular weight $\overline{M_w}$ in the geometry shown in Figure 107 for different inlet and initial conditions as defined in Table 17 and an inlet velocity is 1 mm s^{-1}. Geometry and number of cells were scaled by a factor of 1.5 as described in Section 5.3.3. All other parameters are those of the reference conditions described in Section 5.1 to Section 5.2.

Table 17. Inlet concentrations and weight fractions for the simulation cases that are discussed in Section 5.3.3.

Corresponding plug flow residence time τ_{PF} (inlet)	Component i	Inlet concentration c_i / mol l^{-1}	Inlet weight fraction w_i^0
0 s	I_2	$7.113 \cdot 10^{-4}$	$2 \cdot 10^{-4}$
	M	1.734	0.2
	P	0	0
250 s	I_2	$5.912 \cdot 10^{-4}$	$1.642 \cdot 10^{-4}$
	M	1.126	0.1281
	P	$4.471 \cdot 10^{-4}$	0.07188
750 s	I_2	$4.019 \cdot 10^{-4}$	$1.100 \cdot 10^{-4}$
	M	0.4022	0.04511
	P	$9.695 \cdot 10^{-4}$	0.15489
1750 s	I_2	$1.801 \cdot 10^{-4}$	$4.895 \cdot 10^{-5}$
	M	0.04407	0.004908
	P	$1.225 \cdot 10^{-3}$	0.1951

In Figure 113 and Figure 114, the effect of different inlet and initial conditions, i.e. lower monomer and higher polymer contents at the reactor inlet, is illustrated. The time scale on which gelation occurs decreases with increasing monomer conversion in the bulk phase, and a stationary state is reached, if a monomer conversion of around 97.5 percent is specified at the inlet of the simulation domain. The polymer accumulation under these conditions is less pronounced and, therefore, the viscosity difference between the bulk and the dead-water region is small. Additionally, the largest possible monomer gradient is small.

These results are in agreement with the observation that fouling deposits are initially formed close to the reactor inlet as discussed in Section 3.1.2.3.

5.4 Concluding remarks

The simple simulation cases that have been discussed in this section offer important insight into transport phenomena that are relevant for the formation of fouling deposits. Regions with locally increased residence time, e.g. regions close to reactor walls or dead-water zones, may cause strong concentration gradients, which induce mass transport between such regions and the bulk phase. Polymer molecules accumulate in these regions due to their lower diffusion coefficients in comparison to low molecular species, which increases the viscosity locally. Viscosity gradients distort the flow pattern and the size of regions with increased residence time grows. Besides an increased residence time, such regions are characterized by high polymer and low monomer contents, which promotes the formation of polymer gels by side reactions.

The simulation results that have been presented in this chapter are in agreement with reports in literature and experimental observation that have been discussed in Section 3.3. Highly viscous wall layers in tubular reactors without mixer elements have also been suggested to be an important factor in the formation of fouling deposits in other polymerization systems in [6], [16], [19], [21]. Residence time measurements in tubular reactors under reactive conditions have been discussed in Section 3.3.2 and point to the existence of such layers as well. Simulations of residence times distributions under similar conditions are in agreement with these experiments and substantiate the suggestion of the formation of highly viscous wall layers.

Dead-water zones in reactors including static mixer elements were suggested in [5] and Section 3.1 based on experimental observations and critical regions were identified in CFD

simulations in static mixer geometries in [6]. The results from Section 5.3 confirm the existence of dead-water zones upwind and downwind of mixer elements and their importance for the formation of fouling deposits. Since diffusive mass transport causes the accumulation of polymer, the size of such regions affects the magnitude of polymer accumulation. The effect is most pronounced in regions that are close to the reactor inlet where concentration and viscosity gradients are the highest. This observation is in agreement with experimental results in static mixer reactors, which have been discussed in Section 3.1.2.3.

6 Conclusion and Outlook

The goal of this thesis was to gain mechanistic insight into the underlying phenomena of the formation of fouling deposits in solution polymerization and to find a model-based description of these phenomena. As an exemplary system, the aqueous phase polymerization of NVP was studied since this system is prone to the formation of fouling deposits. Experimental results of fouling in different continuously operated reactors have been presented and a hypothesis on the fouling mechanism has been formulated based on these observations in Chapter 3. The essence of this hypothesis is that side reactions lead to the formation of insoluble polymers gels, which are highly adhesive and stick to the reactor walls. The formation of these polymer gels is most pronounced in regions with increased local residence times where side reactions are fostered in comparison to reactions that lead to linear, soluble polymer chains. To substantiate this hypothesis, kinetic models were developed and a CFD solver was modified to include a reduced version of these kinetic models as well as a model for diffusive mass transport. Using these models, the polymerization of NVP was studied in simulations of different reactor systems and the results were compared to experimental observations.

As had been proposed in [49] and confirmed in this thesis, the reaction mechanism includes side reaction, which lead to the formation and propagation of TDBs and produce high-molecular, branched polymers. The kinetic models, which were developed on the basis of this reaction mechanism, have been discussed in Chapter 4. They are capable of predicting microstructural property distributions, i.e. the distribution of chain lengths or the distribution of TDBs. Additionally, a computationally efficient version of these models, which

gives only average properties of the system, was derived. Experimental and simulated results show that very high molecular and branched chains are formed especially in reactors with very broad residence time distributions, e.g. CSTRs with long average residence times. The simulations also show that these polymer chains are still highly reactive since they carry a large number of unreacted TDBs and that the number of TDBs $p(n)$ increases with the chain length. If such polymer chains remain in the reactor system, either due to adhesion on surfaces or in zones with a locally increased residence time, they may grow up to form a polymer gel. Indeed, polymer gel deposits were found at the baffles of the CSTR but no gelation of the bulk phase was observed under the conditions studied in this thesis.

These observations emphasize the importance of the flow pattern and diffusive mass transport, which have been discussed in Chapter 5. CFD simulations including a model for diffusive mass transport, which includes the transport of statistical moments and is, therefore, consistent with the reaction kinetics model, were conducted in different geometries, which correspond to segments of tubular reactors with and without static mixer elements. The results confirm that polymers accumulate in regions with increased local residence time, i.e. regions close to the reactor walls or dead-water zones at static mixer elements. Local residence time differences cause concentration gradients, which induce mass transport and lead to the accumulation of polymer because of their lower diffusive mass transport coefficients compared to low molecular species. The increased polymer concentration causes large viscosity gradients between these regions and the bulk phase, which distort the flow pattern and increase the size of regions with increased local residence time even further. Since these regions are characterized by high local residence times, high polymer and low monomer content, side reactions are promoted and lead to the formation of polymer gels even if the composition in the bulk phase does not lead to gelation.

As has been discussed using experimental results in Section 3.1.2.1, PVP gels are highly adhesive to metal surfaces and cannot be removed completely by flushing with water. Polymer chains that are immobilized on surfaces are still reactive, since they carry a large number of TDBs and may grow by reaction with monomer and other polymer chains. Adsorbed polymer chains may act as seeds for the formation of fouling deposits in repeated experiments, if the reactor surfaces are not cleaned by degrading the polymer gel residue on reactor surfaces in advance.

In summary, these results support the hypothesis that has been formulated in Section 3.4. The reaction mechanism including side reactions that was proposed in [49] was confirmed by comparison of the newly developed kinetic models and CSTR experiments. The formation of viscous wall layers as well as the importance of dead-water regions and diffusive mass transport for the formation of polymer gels, were confirmed by CFD simulations and comparison to experimental results in tubular reactors with and without mixer elements. Additionally, the adsorption polymers on metal surfaces is certainly an important factor for the formation of fouling deposits and was demonstrated in experiments. Based on the mechanistic understanding that has been gained from the results in this thesis, some early conclusions how to reduce fouling deposits can be drawn. Since creation and propagation of TDBs is the reason for the formation of polymer gels, one approach may be to reduce the concentration of TBDs in polymer chains. This could be achieved by switching to organic solvents in which transfer reactions to solvent molecules are the dominating termination mechanism [41], for example. The downside of this approach is, of course, that product properties are altered significantly. As has been discussed in Section 5.2.2, the formation of highly viscous regions is an important factor for the formation of fouling deposits and highly sensitive to transport coefficients. Transport coefficients cannot be specified directly in a real-life scenario, but process parameters can be modified in order to steer the latter into a favourable direction. Since low viscosity differences and high

diffusivities are favourable, keeping the inlet monomer concentration and, consequently, the final polymer content in the bulk low might help. Since high polymer diffusivities relative to low molecular components seem to be favourable, low chain length or higher initiator to monomer ratios may lead to improvement, too. Again the disadvantage of this approach is that product properties are altered, the energy demand increases and space-time yield decrease. If the recipe is fixed, modifications on the reactor itself may be considered. Dead-water zones could be eliminated by additive manufacturing of mixer elements or the surface properties may be modified to prevent adsorption of polymers. Hydrophobic coatings were identified as a promising approach, but the stability of such coatings is limited. If fouling cannot be prevented but at least be delayed, cleaning intervals with an appropriate cleaning solution, e.g. NaClO solutions as discussed in Section 3.1.2.2, may enable production in continuously operated reactors. Future experimental work should focus on these suggestions. Future modelling work should focus on improving the predictive capabilities of the CFD solver by finding and improving correlations for transport coefficients. In this thesis, the transport coefficients were chosen on the basis of theoretical considerations or estimated from experiments, e.g. the reference diffusion coefficient $\mathfrak{D}_0 = D_T = 5\ 10^{-9}\ \mathrm{m^2\ s^{-1}}$. Improved correlations for diffusive mass transport coefficients and the solution viscosity would by beneficial, e.g. by considering the effect of the polymer chain length on the solution viscosity, which has not been done in this thesis. The adsorption of polymers on surfaces has also not been considered in simulations so far and the dependence of adsorption on factors as, for example, composition of the solution, the polymer microstructure or the hydrodynamic situation close to the wall is not fully understood. Further research in this area and development of models would improve the understanding how deposits are formed from polymer gels and, most importantly, how they can be prevented.

Literature

[1] A. M. Pritchard, "The Economics of Fouling," in *Fouling Science and Technology*, Dordrecht: Springer Netherlands, 1988, pp. 31–45.

[2] T. R. Bott, "General Fouling Problems," in *Fouling Science and Technology*, Dordrecht: Springer Netherlands, 1988, pp. 3–14.

[3] N. Epstein, "Thinking about Heat Transfer Fouling: A 5 × 5 Matrix," *Heat Transf. Eng.*, vol. 4, no. 1, pp. 43–56, 1983.

[4] M. Schoenitz, L. Grundemann, W. Augustin, and S. Scholl, "Fouling in microstructured devices: a review," *Chem. Commun.*, vol. 51, no. 39, pp. 8213–8228, Apr. 2015.

[5] D. Kohlmann *et al.*, "Modular, Flexible, and Continuous Plant for Radical Polymerization in Aqueous Solution," *Macromol. React. Eng.*, vol. 10, no. 4, pp. 339–353, 2016.

[6] M. Hellmund, "Kinetik und Modellierung der kontinuierlichen Polymerisation von N-Vinylpyrrolidon," Universität Stuttgart, 2020.

[7] J. W. Vanderhoff, "The Formation of Coagulum in Emulsion Polymerization," 1981, pp. 199–208.

[8] M. Kemmere, "Batch emulsion polymerization : a chemical engineering approach," 1999.

[9] J. Urrutia, "Fouling in Emulsion Polymerization Reactors," University of the Basque

Country, 2016.

[10] J. Urrutia, A. Peña, and J. M. Asua, "Reactor Fouling by Preformed Latexes," *Macromol. React. Eng.*, vol. 11, no. 1, pp. 1–14, 2017.

[11] M. Madani, "Belagsbildung in chemischen Reaktoren unter Berücksichtigung von Oberflächenaspekten," Universität Hamburg, 2017.

[12] C. S. Chern and Y. C. Chen, "Stability of the polymerizable surfactant stabilized latex particles during semibatch emulsion polymerization," *Colloid Polym. Sci.*, vol. 275, no. 2, pp. 124–130, 1997.

[13] C. Kiparissides, J. F. MacGregor, and A. E. Hamielec, "continuous emulsion polymerization of vinyl acetate Part II: parameter estimation and simulation studies," *Can. J. Chem. Eng.*, vol. 58, no. February, pp. 56–64, 1980.

[14] N. Gottschalk, J. C. Kuschnerow, H. Föste, W. Augustin, and S. Scholl, "Experimentelle Untersuchung zur Foulingneigung einer Polymerdispersion auf modifizierten Oberflächen," *Chemie-Ingenieur-Technik*, vol. 87, no. 5, pp. 600–608, 2015.

[15] M. Kroupa, M. Vonka, and J. Kosek, "Modeling the mechanism of coagulum formation in dispersions," *Langmuir*, vol. 30, no. 10, pp. 2693–2702, 2014.

[16] M. F. Cunningham, K. F. O'Driscoll, and H. K. Mahabadi, "Bulk polymerization in tubular reactors I. Experimental observations on fouling," *Can. J. Chem. Eng.*, vol. 69, no. 3, pp. 630–638, 1991.

[17] C. Bernstein, "Methoden zur Untersuchung der Belagsbildung in chemischen Reaktoren," Universität Hamburg, 2017.

[18] A. Buchelli, M. L. Call, A. L. Brown, A. Bird, S. Hearn, and J. Hannon, "Modeling Fouling Effects in LDPE Tubular Polymerization Reactors. 1. Fouling Thickness Determination," 2005.

[19] S. Fries, D. M. Castañeda-Zúñiga, J. Duchateau, P. Neuteboom, C. T. Porras, and M. Busch, "Fouling in the High Pressure LDPE Process: Experimental and Computational Investigation Approach," *Macromol. Symp.*, vol. 360, no. 1, pp. 78–86, 2016.

[20] S. Fries, "Modelling of Fouling Mechanisms in the LDPE Synthesis," Technische Universität Darmstadt, 2020.

[21] M. F. Cunningham, H. K. Mahabadi, and K. F. O´Driscol, "Bulk polymerization in tubular reactors iii. Modelling fouling behaviour," *Polym. React. Eng.*, vol. 1, no. 2, pp. 245–287, 1993.

[22] A. Buchelli, M. L. Call, A. L. Brown, A. Bird, S. Hearn, and J. Hannon, "Modeling Fouling Effects in LDPE Tubular Polymerization Reactors. 2. Heat Transfer, Computational Fluid Dynamics, and Phase Equilibria," 2005.

[23] G. F. M. Hoedemakers, "Continuous emulsion polymerization in a pulsed packed column," Technische Universiteit Eindhoven, 1990.

[24] F. G. Lueth, W. Pauer, and H. U. Moritz, "Properties of smart-scaled PTFE-tubular reactors for continuous emulsion polymerization reactions," *Macromol. Symp.*, vol. 333, no. 1, pp. 69–79, Nov. 2013.

[25] K. Rossow *et al.*, "Transfer of Emulsion Polymerization of Styrene and n -Butyl Acrylate from Semi-Batch to a Continuous Tubular Reactor," *Macromol. React. Eng.*, vol. 10, no. 4, pp. 324–338, Aug. 2016.

[26] T. Meyer and J. T. F. Keurentjes, *Handbook of Polymer Reaction Engineering*. Weinheim, Germany: Wiley-VCH Verlag GmbH, 2008.

[27] K.-D. Hungenberg and M. Wulkow, *Modeling and Simulation in Polymer Reaction Engineering*. Weinheim, Germany: Wiley-VCH Verlag GmbH & Co. KGaA, 2018.

[28] M. Rubinstein and R. H. Colby, *POLYMER PHYSICS*. Oxford University Press, 2003.

[29] B. H. Zimm and W. H. Stockmayer, "The dimensions of chain molecules containing branches and rings," *J. Chem. Phys.*, vol. 17, no. 12, pp. 1301–1314, Dec. 1949.

[30] C. Bustamante, Z. Bryant, and S. B. Smith, "Ten years of single molecule DNA mechanics," *Group*, vol. 421, no. January, 2003.

[31] A. Einstein, "Über die von der molekularkinetischen Theorie der Wärme geforderte Bewegung von in ruhenden Flüssigkeiten suspendierten Teilchen," *Ann. Phys.*, vol. 322, no. 8, pp. 549–560, 1905.

[32] S. Podzimek, *Light Scattering, Size Exclusion Chromatography and Asymmetric Flow Field Flow Fractionation: Powerful Tools for the Characterization of Polymers, Proteins and Nanoparticles*. Hoboken, NJ, USA: John Wiley & Sons, Inc., 2011.

[33] P. D. Iedema, S. Grcev, and H. C. J. Hoefsloot, "Molecular weight distribution modeling of radical polymerization in a CSTR with long chain branching through transfer to polymer and terminal double bond (TDB) propagation," *Macromolecules*, vol. 36, no. 2, pp. 458–476, 2003.

[34] M. Wulkow, "The simulation of molecular weight distributions in polyreaction kinetics by discrete Galerkin methods," *Macromol. Theory Simulations*, vol. 5, no.

3, pp. 393–416, May 1996.

[35] M. Wulkow, "Computer aided modeling of polymer reaction engineering-The status of predici, 1 - simulation," *Macromol. React. Eng.*, vol. 2, no. 6, pp. 461–494, Nov. 2008.

[36] P. D. Iedema, M. Wulkow, and H. C. J. Hoefsloot, "Modeling molecular weight and degree of branching distribution of low-density polyethylene," *Macromolecules*, vol. 33, no. 19, pp. 7173–7184, 2000.

[37] R. B. Bird, W. E. Stewart, and E. N. Lightfoot, *Transport phenomena*. 2007.

[38] W. M. Deen, *Analysis of transport phenomen*. Oxford university press New York, 1998.

[39] F. Moukalled, L. Mangani, and M. Darwish, *The Finite Volume Method in Computational Fluid Dynamics*. Springer, 2015.

[40] H. Jasak, "Error Analysis and Estimation for the finite volume method with applications to fluid flows," Imperial College, 1996.

[41] F. Haaf, A. Sanner, and F. Straub, "Polymers of N-Vinylpyrrolidone: Synthesis, Characterization and Uses," *Polym. J.*, vol. 17, no. 1, pp. 143–152, Jan. 1985.

[42] B. Pellegrin *et al.*, "Multi-scale analysis of hypochlorite induced PES/PVP ultrafiltration membranes degradation," *J. Memb. Sci.*, vol. 447, pp. 287–296, 2013.

[43] C. Causserand, S. Rouaix, J. P. Lafaille, and P. Aimar, "Ageing of polysulfone membranes in contact with bleach solution: Role of radical oxidation and of some dissolved metal ions," *Chem. Eng. Process. Process Intensif.*, vol. 47, no. 1, pp. 48–56, 2008.

[44] W. R. Dean, "Fluid motion in a curved channel," *Proc. R. Soc. London. Ser. A, Contain. Pap. a Math. Phys. Character*, vol. 121, no. 787, pp. 402–420, Nov. 1928.

[45] M. Stach *et al.*, "Propagation rate coefficient for radical polymerization of N-vinyl pyrrolidone in aqueous solution obtained by PLP-SEC," *Macromolecules*, vol. 41, no. 14, pp. 5174–5185, Jul. 2008.

[46] L. Uhelská, D. Chorvát, R. A. Hutchinson, S. Santanakrishnan, M. Buback, and I. Lacík, "Radical Propagation Kinetics of N -Vinylpyrrolidone in Organic Solvents Studied by Pulsed-Laser Polymerization-Size-Exclusion Chromatography (PLP-SEC)," *Macromol. Chem. Phys.*, vol. 215, no. 23, pp. 2327–2336, Dec. 2014.

[47] J. Schrooten, M. Buback, P. Hesse, R. A. Hutchinson, and I. Lacík, "Termination kinetics of 1-vinylpyrrolidin-2-one radical polymerization in aqueous solution," *Macromol. Chem. Phys.*, vol. 212, no. 13, pp. 1400–1409, Jul. 2011.

[48] S. Santanakrishnan *et al.*, "Kinetics and modeling of batch and semibatch aqueous-phase NVP free-radical polymerization," *Macromol. React. Eng.*, vol. 4, no. 8, pp. 499–509, Jun. 2010.

[49] P. Deglmann, M. Hellmund, K. Hungenberg, U. Nieken, C. Schwede, and C. Zander, "Side Reactions in Aqueous Phase Polymerization of N -Vinyl-Pyrrolidone as Possible Source for Fouling," *Macromol. React. Eng.*, p. 1900021, Aug. 2019.

[50] P. Pladis and C. Kiparissides, "A comprehensive model for the calculation of molecular weight–long-chain branching distribution in free-radical polymerizations," *Chem. Eng. Sci.*, vol. 53, no. 18, pp. 3315–3333, Sep. 1998.

[51] R. A. Hutchinson, "Modeling of Chain Length and Long-Chain Branching

Distributions in Free-Radical Polymerization," *Macromol. Theory Simulations*, vol. 10, no. 3, pp. 144–157, Mar. 2001.

[52] I. M. Neuhaus, "Modellierung der technischen LDPE-Synthese in industriellen Mehrzonenautoklaven," Technische Universität Darmstadt, 2014.

[53] D. Eckes, "Modellierung der industriellen LDPE-Synthese für die Tail-End Reaktortechnologie," Technischen Universität Darmstadt, 2017.

[54] S. Fries, "Modelling of Fouling Mechanisms in the LDPE Synthesis," Technische Universität Darmstadt, 2020.

[55] A. Donev *et al.*, "Low Mach Number Fluctuating Hydrodynamics of Multispecies Liquid Mixtures We develop a low Mach number formulation of the hydrodynamic equations describing transport of mass and momentum in a multispecies mixture of incompressible miscible liq-uids at spe," 241AD.

[56] A. Donev, A. Nonaka, Y. Sun, T. Fai, A. Garcia, and J. Bell, "Low Mach number fluctuating hydrodynamics of diffusively mixing fluids," *Commun. Appl. Math. Comput. Sci.*, vol. 9, no. 1, pp. 47–105, May 2014.

[57] W. Saeckel, "unpublished, in preparation," University of Stuttgart, 2021.

[58] M. Buback, "Free-radical polymerization up to high conversion. A general kinetic treatment," *Die Makromol. Chemie*, vol. 191, no. 7, pp. 1575–1587, 1990.

[59] J.-H. Ham and B. Platzer, "Semi-Empirical Equations for the Residence Time Distributions in Disperse Systems - Part 1: Continuous Phase," *Chem. Eng. Technol.*, vol. 27, no. 11, pp. 1172–1178, Nov. 2004.

[60] G. Taylor, "Dispersion of soluble matter in solvent flowing slowly through a tube,"

Proc. R. Soc. London. Ser. A. Math. Phys. Sci., vol. 219, no. 1137, pp. 186–203, Aug. 1953.

[61] R. Aris, "On the dispersion of a solute in a fluid flowing through a tube," *Proc. R. Soc. London. Ser. A. Math. Phys. Sci.*, vol. 235, no. 1200, pp. 67–77, Apr. 1956.

[62] H. M. Hulburt and S. Katz, "Some problems in particle technology. A statistical mechanical formulation," *Chem. Eng. Sci.*, vol. 19, no. 8, pp. 555–574, Aug. 1964.

[63] C. Zander, K. Hungenberg, T. Schall, C. Schwede, and U. Nieken, "Modeling Strategies for the Propagation of Terminal Double Bonds During the Polymerization of N-Vinylpyrrolidone and Experimental Validation," *Macromol. React. Eng.*, p. 2000009, May 2020.

[64] O. Levenspiel, *Chemical reaction engineering*. Wiley, 1999.

Appendix

A.1 Kinetic Models

A.1.1 Modeling workflow and summary of extractable microstructural polymer properties

In Figure 115, an illustration of modelling workflow that is described in detail in Chapter 4 is given. The most important microstructural polymer properties that can be extracted from the models in Figure 115 are summarized in Table 18 to Table 20.

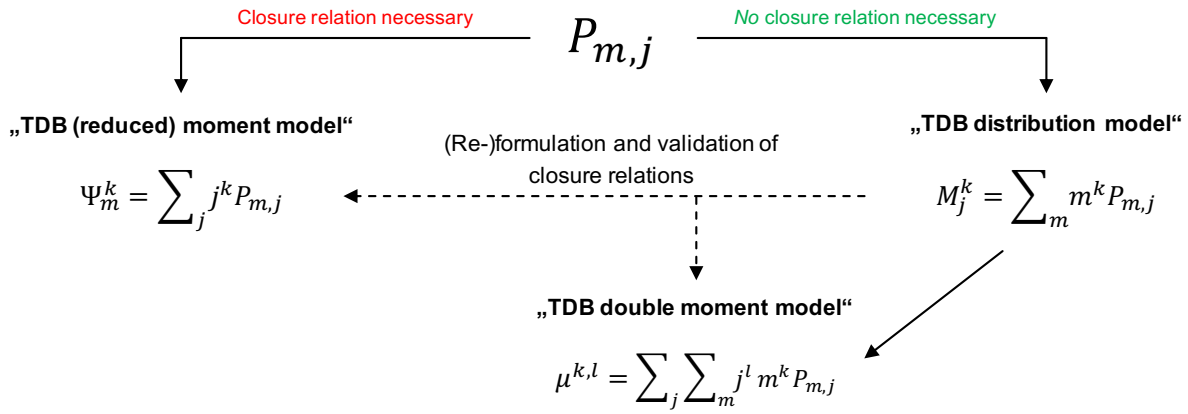

Figure 115. Simplified illustration of the modeling workflow in Chapter 4.

Table 18. Most important microstructural polymer properties that can be extracted from the TDB (reduced) moment model.

$P_n = \Psi_n^0$	Chain length distribution
$\overline{M_n} = \frac{\lambda_1^P}{\lambda_0^P} MW_M$	Number average molecular weight
$\overline{M_w} = \frac{\lambda_2^P}{\lambda_1^P} MW_M$	Weight average molecular weight
$p(n) = \frac{\Psi_n^1}{\Psi_n^0}$	Average number of TDBs per chain of length n (output of TDB moment model, input für TDB reduced moment model)
$\frac{H^{TDB}}{\lambda_0^P} = \frac{\sum_n \Psi_n^1}{\sum_n \Psi_n^0}$	Average number of TDBs per molecule
$\frac{H^B}{\lambda_0^P}$	Average number of branches per molecule
$\frac{H^B}{\lambda_1^P}$	Average number of branches per repeat unit

Table 19. Most important microstructural polymer properties that can be extracted from the TDB distribution model.

M_i^0	TDB distribution
$\overline{M_n} = \frac{\sum_{i=0}^{\infty} M_i^1}{\sum_{i=0}^{\infty} M_i^0} MW_M$	Number average molecular weight
$\overline{M_w} = \frac{\sum_{i=0}^{\infty} M_i^2}{\sum_{i=0}^{\infty} M_i^1} MW_M$	Weight average molecular weight

$\frac{H^{TDB}}{\lambda_0^P} = \frac{\sum_i i M_i^0}{\sum_i M_i^0}$	Average number of TDBs per molecule
$\frac{H^B}{\sum_i M_i^0}$	Average number of branches per molecule
$\frac{H^B}{\sum_i M_i^1}$	Average number of branches per repeat unit

Table 20. Most important microstructural polymer properties that can be extracted from the TDB double moment model.

$\overline{M_n} = \frac{\mu^{1,0}}{\mu^{0,0}} MW_M$	Number average molecular weight
$\overline{M_w} = \frac{\mu^{2,0}}{\mu^{1,0}} MW_M$	Weight average molecular weight
$\frac{H^{TDB}}{\lambda_0^P} = \frac{\mu^{0,1}}{\mu^{0,0}}$	Average number of TDBs per molecule
$\frac{H^B}{\mu^{0,0}}$	Average number of branches per molecule
$\frac{H^B}{\mu^{1,0}}$	Average number of branches per repeat unit
$A_2 = \frac{\mu^{1,1}\mu^{0,0} - \mu^{1,0}\mu^{0,1}}{\mu^{2,0}\mu^{0,0} - \mu^{1,0}\mu^{1,0}}$	Parameter of the TDB reduced moment model using the approximation p_2 (This parameter can be extracted from the TDB distribution model as well.)

A.1.2 Detailed discussion on the effect of *p(n)* in the TDB reduced moment model

The reaction scheme of the TDB propagation reaction

$$R_n + P_m \xrightarrow{p(m)\cdot k_{p,TDB}} R_{n+m} + H^B - H^{TDB} \tag{178}$$

does not influence the number of monomer units that are polymerized in R and P and since all living chains will terminate eventually the first chain length moment λ_1^P is not influenced significantly either as shown in Figure 117. The overall polymer concentration on the other hand changes in the reaction but does not depend on the choice of $p(n)$ if the coefficients are chosen as in Equation (96) and (98). The latter can be demonstrated by applying the moment operator on the contribution to the CODE of this reaction. The general expression of the contribution of the reaction scheme in Equation (178) in terms of chain length moments is

$$\begin{aligned}\sum_{n=1}^{\infty} n^k \frac{dR_n}{dt} \mathrel{+}= &\sum_{n=1}^{\infty} n^k \, k_{p,TDB} \left(-R_n \sum_{m=1}^{\infty} p(m) P_m \right) \\ &+ \sum_{m=1}^{\infty} k_{p,TDB} p(m) P_m \left(\sum_{o=1}^{\infty} (o+m)^k R_o \right)\end{aligned} \tag{179}$$

for the concentration of living chains and

$$\sum_{n=1}^{\infty} n^k \frac{dP_n}{dt} \mathrel{+}= \sum_{n=1}^{\infty} n^k k_{p,TDB} \left(-p(n) P_n \sum_{m=1}^{\infty} R_m \right) \tag{180}$$

for the concentration of dead chains. The consumption rate of TDBs by this reaction can be quantified by the contribution to the balance of the counter species H^{TDB}

$$\frac{dH^{TDB}}{dt} \mathrel{+}= \sum_{n=1}^{\infty} n^0 k_{p,TDB} \left(-p(n) P_n \sum_{m=1}^{\infty} R_m \right) . \tag{181}$$

Setting $k = 0$ leads to

$$\frac{d\lambda_0^R}{dt} += -k_{p,TDB}\lambda_0^R \frac{c^{TDB}}{\lambda_1^P}\lambda_1^P + k_{p,TDB}\lambda_0^R \frac{c^{TDB}}{\lambda_1^P}\lambda_1^P = 0 \ , \tag{182}$$

$$\frac{d\lambda_0^P}{dt} += -k_{p,TDB_{db}}\lambda_0^R c^{TDB} \tag{183}$$

if $p_1(n)$ is inserted and

$$\begin{aligned}\frac{d\lambda_0^R}{dt} += -k_{p,TDB}\lambda_0^R \left(A_2\lambda_1^P - A_2\frac{\lambda_1^P}{\lambda_0^P}\lambda_0^P + \frac{c^{TDB}}{\lambda_0^P}\lambda_0^P\right) \\ + k_{p,TDB}\lambda_0^R \left(A_2\lambda_1^P - A_2\frac{\lambda_1^P}{\lambda_0^P}\lambda_0^P + \frac{c^{TDB}}{\lambda_0^P}\lambda_0^P\right) = 0 \ ,\end{aligned} \tag{184}$$

$$\frac{d\lambda_0^P}{dt} += -k_{p,TDB}\lambda_0^R \left(A_2\lambda_1^P - A_2\frac{\lambda_1^P}{\lambda_0^P}\lambda_0^P + \frac{c^{TDB}}{\lambda_0^P}\lambda_0^P\right) = -k_{p,TDB_{db}}\lambda_0^R c^{TDB} \tag{185}$$

if $p_2(n)$ is inserted. It can easily be seen that the zeroth chain length moments, i.e. the polymer concentrations, are not influenced as proven in Figure 116. Since the contribution to the rate of consumption of H^{TDB} is the same as that for λ_0^P, the prior does not depend on the choice of $p(n)$ either. Consequently, the average concentration of the TDBs per molecule and the number average molecular weight $\overline{M_n}$ are not affected since the overall concentration of polymerized repeat units is not affected by the TDB propagation reaction, which can be proven by adding Equation (179) and (180) and setting $k = 1$. Inserting $p_1(n)$ leads to

$$\begin{aligned}\frac{d(\lambda_1^R+\lambda_1^P)}{dt} +&= \sum_{n=1}^{\infty} n^1\, k_{p,TDB}\left(-R_n \sum_{m=1}^{\infty}\frac{c^{TDB}}{\lambda_1^P} m P_m\right)\\ &+ \sum_{m=1}^{\infty} k_{p,TDB}\frac{c^{TDB}}{\lambda_1^P} m P_m\left(\sum_{o=1}^{\infty}(o+m)^1 R_o\right)\\ &+ \sum_{n=1}^{\infty} n^k k_{p,TDB}\left(-p(n)P_n \sum_{m=1}^{\infty} R_m\right)\\ &= k_{p,TDB}\left(-\lambda_1^R\frac{c^{TDB}}{\lambda_1^P}\lambda_1^P\right) + k_{p,TDB}\frac{c^{TDB}}{\lambda_1^P}\lambda_1^P\lambda_1^R\\ &+ k_{p,TDB}\frac{c^{TDB}}{\lambda_1^P}\lambda_2^P(\lambda_0^R) - k_{p,TDB}\frac{c^{TDB}}{\lambda_1^P}\lambda_2^P(\lambda_0^R)\\ &= k_{p,TDB}\lambda_0^R\frac{c^{TDB}}{\lambda_1^P}\lambda_2^P \; - k_{p,TDB}\lambda_0^R\frac{c^{TDB}}{\lambda_1^P}\lambda_2^P = 0\end{aligned} \tag{186}$$

and inserting $p_2(n)$ leads to

$$\begin{aligned}\frac{d(\lambda_1^R+\lambda_1^P)}{dt} +&= k_{p,TDB}\lambda_0^R\left(A_2\lambda_2^P - A_2\frac{\lambda_1^P}{\lambda_0^P}\lambda_1^P + \frac{c^{TDB}}{\lambda_0^P}\lambda_1^P\right)\\ &- k_{p,TDB}\lambda_0^R\left(A_2\lambda_2^P - A_2\frac{\lambda_1^P}{\lambda_0^P}\lambda_1^P + \frac{c^{TDB}}{\lambda_0^P}\lambda_1^P\right) = 0\,.\end{aligned} \tag{187}$$

Although the concentration of repeat units in living and dead chains respectively is affected, the overall concentration does not change. Since living chains will terminate eventually, the first chain length moments of dead chains for both approximations of $p(n)$ are indistinguishable by eye as illustrated in Figure 117. The weight average molecular weight $\overline{\overline{M_w}}$, on the other hand, does change, since the second chain length moment shown in Figure 118 depends on the choice of $p(n)$. This can be proven can by adding Equation (179) and (180) and setting $k = 2$ but will not be demonstrated here.

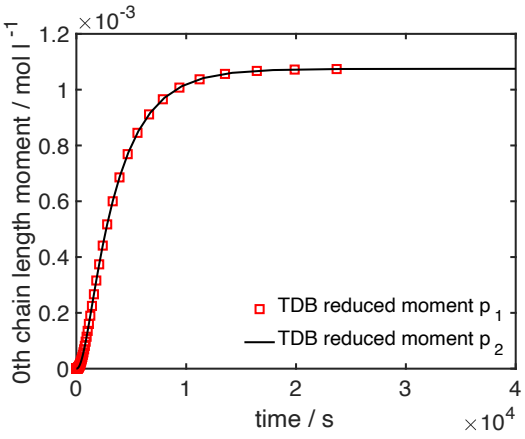

Figure 116. Comparison of the evolution of the zeroth chain length moments for the TDB reduced moment model with p_1 and p_2 ($A_2 = 9.49 \cdot 10^{-5}$) for the case of more than one TDB per chain and the reference case.

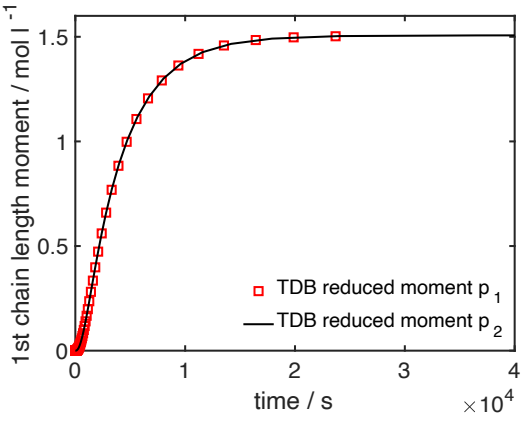

Figure 117. Comparison of the evolution of the first chain length moments for the TDB reduced moment model with p_1 and p_2 ($A_2 = 9.49 \cdot 10^{-5}$) for the case of more than one TDB per chain and the reference case.

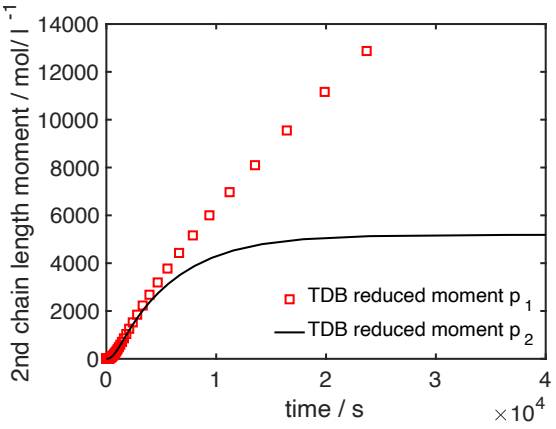

Figure 118. Comparison of the evolution of the second chain length moments for the TDB reduced moment model with p_1 and p_2 ($A_2 = 9.49 \cdot 10^{-5}$) for the case of more than one TDB per chain and the reference case.

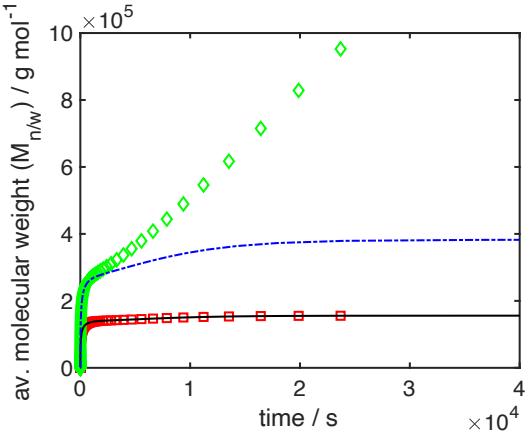

Figure 119. Comparison of the evolution of the molecular weight averages for the TDB reduced moment model with p_1 and p_2 ($A_2 = 9.49 \cdot 10^{-5}$) for the case of more than one TDB per chain and the reference case: red squares – number average molecular weight $\overline{M_n}$, p_1; black solid – $\overline{M_n}$, p_2; green diamonds – weight average molecular weight $\overline{M_w}$, p_1; blue dashed-dotted – $\overline{M_w}$, p_2.

A.1.3 The chain length moment version of the TDB reduced moment model

The reaction contribution to the balance equations for the chain length moment version of the TDB reduced moment model is given for completeness but was not used for any simulations in this thesis. The chain length moments are the those from Section A.1.2. The Hulburt-Katz closure relation [62] for the third chain length moment λ_3^P may be used, for example. This section has been published in the supplemental information of [63] before.

$$\frac{dI_2}{dt} += -k_d I_2 \tag{188}$$

$$\frac{dI}{dt} += -k_p MI + 2k_d f I_2 \tag{189}$$

$$\frac{dM}{dt} += -k_p MI - k_p M\lambda_0^R - k_{tr,m} M\lambda_0^R \tag{190}$$

$$\frac{dc^{TDB}}{dt} += -k_{p,TDB} c^{TDB} \lambda_0^R + k_{tr,m} M\lambda_0^R \tag{191}$$

$$\frac{dc^B}{dt} += k_{p,TDB} \lambda_0^R c^{TDB} \tag{192}$$

$$\frac{d\lambda_0^R}{dt} += k_p MI - k_{t,c} \lambda_0^R \lambda_0^R \tag{193}$$

$$\begin{aligned} \frac{d\lambda_1^R}{dt} += {} & k_p MI + k_p M\lambda_0^R - k_{t,c} \lambda_1^R \lambda_0^R - k_{tr,m} M(\lambda_1^R - \lambda_0^R) \\ & + k_{p,TDB} \lambda_0^R \left(A_2 \lambda_2^P - A_2 \frac{\lambda_1^P}{\lambda_0^P} \lambda_1^P + \frac{c^{TDB}}{\lambda_0^P} \lambda_1^P \right) \end{aligned} \tag{194}$$

$$\begin{aligned}\frac{d\lambda_2^R}{dt} \mathrel{+}= & \, k_p MI + k_p M(2\lambda_1^R + \lambda_0^R) - k_{t,c}\lambda_2^R\lambda_0^R - k_{tr,m}M(\lambda_2^R - \lambda_0^R) \\ & + 2k_{p,TDB}\lambda_1^R \left(A_2\lambda_2^P - A_2\frac{\lambda_1^P}{\lambda_0^P}\lambda_1^P + \frac{c^{TDB}}{\lambda_0^P}\lambda_1^P \right) \\ & + k_{p,TDB}\lambda_0^R \left(A_2\lambda_3^P - A_2\frac{\lambda_1^P}{\lambda_0^P}\lambda_2^P + \frac{c^{TDB}}{\lambda_0^P}\lambda_2^P \right)\end{aligned} \tag{195}$$

$$\frac{d\lambda_0^P}{dt} \mathrel{+}= \frac{1}{2}k_{t,c}\lambda_0^R\lambda_0^R + k_{tr,m}M\lambda_0^R - k_{p,TDB}c^{TDB}\lambda_0^R \tag{196}$$

$$\frac{d\lambda_1^P}{dt} \mathrel{+}= k_{t,c}\lambda_1^R\lambda_0^R + k_{tr,m}M\lambda_1^R - k_{p,TDB}\lambda_0^R \left(A_2\lambda_2^P - A_2\frac{\lambda_1^P}{\lambda_0^P}\lambda_1^P + \frac{c^{TDB}}{\lambda_0^P}\lambda_1^P \right) \tag{197}$$

$$\begin{aligned}\frac{d\lambda_2^P}{dt} \mathrel{+}= & \, k_{t,c}(\lambda_2^R\lambda_0^R + \lambda_1^R\lambda_1^R) + k_{tr,m}M\lambda_2^R \\ & - k_{p,TDB}\lambda_0^R \left(A_2\lambda_3^P - A_2\frac{\lambda_1^P}{\lambda_0^P}\lambda_2^P + \frac{c^{TDB}}{\lambda_0^P}\lambda_2^P \right)\end{aligned} \tag{198}$$

A.1.4 Full set of equations of the TDB distribution model

Only contributions from reactions are listed, no transport terms. This section has been published in the supplemental information of [63] before.

$$\frac{dI_2}{dt} \mathrel{+}= -k_d f I_2 \tag{199}$$

$$\frac{dI}{dt} \mathrel{+}= -k_p MI + 2k_d f I_2 \tag{200}$$

$$\frac{dM}{dt} \mathrel{+}= -k_p MI - k_p M\sum_{i=0}^{\infty}\Lambda_i^0 - k_{tr,m}M\sum_{i=0}^{\infty}\Lambda_i^0 \tag{201}$$

$$\frac{d\Lambda_0^{k=0,1,2}}{dt} \mathrel{+}= k_p MI \tag{202}$$

$$\frac{d\Lambda_1^{k=0,1,2}}{dt} += k_{tr,m} M \sum_{i=0}^{\infty} \Lambda_i^0 \tag{203}$$

$$\frac{d\Lambda_i^0}{dt} += -k_{t,c}\Lambda_i^0 \sum_{j=0}^{\infty} \Lambda_j^0 - k_{tr,m} M \Lambda_i^0 - k_{p,TDB} \left(\Lambda_i^0 \sum_{j=0}^{\infty} j M_j^0 - \sum_{j=0}^{i+1} j M_j^0 \Lambda_{i-j+1}^0 \right) \tag{204}$$

$$\begin{aligned} \frac{d\Lambda_i^1}{dt} += {} & k_p M \Lambda_i^0 - k_{t,c}\Lambda_i^1 \sum_{j=0}^{\infty} \Lambda_j^0 - k_{tr,m} M \Lambda_i^1 \\ & - k_{p,TDB} \left(\Lambda_i^1 \sum_{j=0}^{\infty} j M_j^0 - \sum_{j=0}^{i+1} j (M_j^0 \Lambda_{i-j+1}^1 + M_j^1 \Lambda_{i-j+1}^0) \right) \end{aligned} \tag{205}$$

$$\begin{aligned} \frac{d\Lambda_i^2}{dt} += {} & k_p M (2\Lambda_i^1 + \Lambda_i^0) - k_{t,c}\Lambda_i^2 \sum_{j=0}^{\infty} \Lambda_j^0 - k_{tr,m} M \Lambda_i^2 \\ & - k_{p,TDB} \left(\Lambda_i^2 \sum_{j=0}^{\infty} j M_j^0 \right. \\ & \left. - \sum_{j=0}^{i+1} j (M_j^0 \Lambda_{i-j+1}^2 + 2 M_j^1 \Lambda_{i-j+1}^1 + M_j^2 \Lambda_{i-j+1}^0) \right) \end{aligned} \tag{206}$$

$$\frac{dM_i^0}{dt} += \frac{1}{2} k_{t,c} \sum_{j=0}^{i} \Lambda_j^0 \Lambda_{i-j}^0 + k_{tr,m} M \Lambda_i^0 - k_{p,TDB} i M_i^0 \sum_{j=0}^{\infty} \Lambda_j^0 \tag{207}$$

$$\frac{dM_i^1}{dt} += k_{t,c} \sum_{j=0}^{i} \Lambda_j^1 \Lambda_{i-j}^0 + k_{tr,m} M \Lambda_i^1 - k_{p,TDB} i M_i^1 \sum_{j=0}^{\infty} \Lambda_j^0 \tag{208}$$

$$\frac{dM_i^2}{dt} += k_{t,c} \sum_{j=0}^{i} (\Lambda_j^2 \Lambda_{i-j}^0 + \Lambda_j^1 \Lambda_{i-j}^1) + k_{tr,m} M \Lambda_i^2 - k_{p,TDB} i M_i^2 \sum_{j=0}^{\infty} \Lambda_j^0 \tag{209}$$

A.1.5 Formulation of the TDB distribution model in terms of reaction modules

Some of the reaction modules listed below are only available in newer version of PREDICI®. This section has been published in the supplemental information of [63] before.

A.1.5.1 Initiation

$$
\begin{aligned}
I_2 &\overset{fk_d}{\rightarrow} 2I \\
I + M &\overset{k_p}{\rightarrow} \Lambda_0^0 \\
[I] + [M] &\overset{k_p}{\rightarrow} \Lambda_0^1 \\
[I] + [M] &\overset{k_p}{\rightarrow} \Lambda_0^2
\end{aligned}
\tag{210}
$$

A.1.5.2 Propagation

$$
\begin{aligned}
[\Lambda_i^0] + M &\overset{k_p}{\rightarrow} \Lambda_i^1 \\
[\Lambda_i^0] + [M] &\overset{k_p}{\rightarrow} \Lambda_i^2 \\
[\Lambda_i^1] + [M] &\overset{2k_p}{\rightarrow} \Lambda_i^2
\end{aligned}
\tag{211}
$$

A.1.5.3 Termination by combination

$$
\begin{aligned}
\Lambda_i^0 + \Lambda_j^0 &\overset{k_{t,c}}{\rightarrow} M_{i+j}^0 \\
\Lambda_i^1 + [\Lambda_j^0] &\overset{k_{t,c}}{\rightarrow} M_{i+j}^1 \\
\Lambda_i^2 + [\Lambda_j^0] &\overset{k_{t,c}}{\rightarrow} M_{i+j}^2
\end{aligned}
\tag{212}
$$

$$[\Lambda_j^1] + [\Lambda_j^1] \overset{k_{t,c}}{\rightarrow} M_{i+j}^2$$

A.1.5.4 Transfer to monomer

$$\begin{aligned}
\Lambda_j^0 + M &\xrightarrow{k_{tr,m}} \Lambda_1^0 + M_j^0 \\
\Lambda_j^1 + [M] &\xrightarrow{k_{tr,m}} M_j^1 \\
[\Lambda_j^0] + [M] &\xrightarrow{k_{tr,m}} \Lambda_1^1 \\
\Lambda_j^2 + [M] &\xrightarrow{k_{tr,m}} M_j^2 \\
[\Lambda_j^0] + [M] &\xrightarrow{k_{tr,m}} \Lambda_1^2
\end{aligned} \tag{213}$$

A.1.5.5 Propagation of TDBs

$$\begin{aligned}
\Lambda_i^0 + M_j^0 &\xrightarrow{j\, k_{p,TDB}} \Lambda_{i+j-1}^0 \\
\Lambda_i^1 + [M_j^0] &\xrightarrow{j\, k_{p,TDB}} \Lambda_{i+j-1}^1 \\
[\Lambda_i^0] + M_j^1 &\xrightarrow{j\, k_{p,TDB}} \Lambda_{i+j-1}^1 \\
\Lambda_i^2 + [M_j^0] &\xrightarrow{j\, k_{p,TDB}} \Lambda_{i+j-1}^2 \\
[\Lambda_i^0] + M_j^2 &\xrightarrow{j\, k_{p,TDB}} \Lambda_{i+j-1}^2 \\
[\Lambda_i^1] + [M_j^1] &\xrightarrow{2\, j\, k_{p,TDB}} \Lambda_{i+j-1}^2
\end{aligned} \tag{214}$$

A.1.6 Full set of equations of the TDB double moment model

Closure relations for $\mu^{k,3}$ with $k = 0,1,2$ such as the ones in Section 4.2.4 are needed. Only contributions from reactions are listed, no transport terms. This section has been published in the supplemental information of [63] before.

$$\frac{dI_2}{dt} += -k_d I_2 \tag{215}$$

$$\frac{dI}{dt} += -k_p M I + 2k_d f I_2 \tag{216}$$

$$\frac{dM}{dt} += -k_p M I - k_p M \lambda^{0,0} - k_{tr,m} M \lambda^{0,0} \tag{217}$$

A.1.6.1 Zeroth chain length moments

$$\frac{d\lambda^{0,0}}{dt} += k_p M I - k_{t,c} \lambda^{0,0} \lambda^{0,0} \tag{218}$$

$$\frac{d\lambda^{0,1}}{dt} += -k_{t,c} \lambda^{0,1} \lambda^{0,0} - k_{tr,m} M (\lambda^{0,1} - \lambda^{0,0}) + k_{p,TDB} (\lambda^{0,0} \mu^{0,2} - \lambda^{0,0} \mu^{0,1}) \tag{219}$$

$$\begin{aligned} \frac{d\lambda^{0,2}}{dt} += & -k_{t,c} \lambda^{0,2} \lambda^{0,0} - k_{tr,m} M (\lambda^{0,2} - \lambda^{0,0}) \\ & + k_{p,TDB} (2\lambda^{0,1} \mu^{0,2} - 2\lambda^{0,1} \mu^{0,1} + \lambda^{0,0} \mu^{0,3} - 2\lambda^{0,0} \mu^{0,2} + \lambda^{0,0} \mu^{0,1}) \end{aligned} \tag{220}$$

$$\frac{d\mu^{0,0}}{dt} += \frac{1}{2} k_{t,c} \lambda^{0,0} \lambda^{0,0} + k_{tr,m} M \lambda^{0,0} - k_{p,TDB} \lambda^{0,0} \mu^{0,1} \tag{221}$$

$$\frac{d\mu^{0,1}}{dt} += k_{t,c} \lambda^{0,1} \lambda^{0,0} + k_{tr,m} M \lambda^{0,1} - k_{p,TDB} \lambda^{0,0} \mu^{0,2} \tag{222}$$

$$\frac{d\mu^{0,2}}{dt} += k_{t,c} (\lambda^{0,0} \lambda^{0,2} + \lambda^{0,1} \lambda^{0,1}) + k_{tr,m} M \lambda^{0,2} - k_{p,TDB} \lambda^{0,0} \mu^{0,3} \tag{223}$$

A.1.6.2 First chain length moments

$$\frac{d\lambda^{1,0}}{dt} += k_p MI + k_p M\lambda^{0,0} - k_{t,c}\lambda^{1,0}\lambda^{0,0} - k_{tr,m}M(\lambda^{1,0} - \lambda^{0,0}) + k_{p,TDB}\lambda^{0,0}\mu^{1,1} \tag{224}$$

$$\begin{aligned}\frac{d\lambda^{1,1}}{dt} += {} & k_p M\lambda^{0,1} - k_{t,c}\lambda^{1,1}\lambda^{0,0} - k_{tr,m}M(\lambda^{1,1} - \lambda^{0,0}) \\ & + k_{p,TDB}(\lambda^{1,0}\mu^{0,2} - \lambda^{1,0}\mu^{0,1} + \lambda^{0,1}\mu^{1,1} + \lambda^{0,0}\mu^{1,2} - \lambda^{0,0}\mu^{1,1})\end{aligned} \tag{225}$$

$$\begin{aligned}\frac{d\lambda^{1,2}}{dt} += {} & k_p M\lambda^{0,2} - k_{t,c}\lambda^{1,2}\lambda^{0,0} - k_{tr,m}M(\lambda^{1,2} - \lambda^{0,0}) \\ & + k_{p,TDB}(2\lambda^{1,1}\mu^{0,2} - 2\lambda^{1,1}\mu^{0,1} + \lambda^{1,0}\mu^{0,3} - 2\lambda^{1,0}\mu^{0,2} + \lambda^{1,0}\mu^{0,1} \\ & + \lambda^{0,2}\mu^{1,1} + 2\lambda^{0,1}\mu^{1,2} - 2\lambda^{0,1}\mu^{1,1} + \lambda^{0,0}\mu^{1,3} - 2\lambda^{0,0}\mu^{1,2} \\ & + \lambda^{0,0}\mu^{1,1})\end{aligned} \tag{226}$$

$$\frac{d\mu^{1,0}}{dt} += k_{t,c}\lambda^{1,0}\lambda^{0,0} + k_{tr,m}M\lambda^{1,0} - k_{p,TDB}\lambda^{0,0}\mu^{1,1} \tag{227}$$

$$\frac{d\mu^{1,1}}{dt} += k_{t,c}(\lambda^{1,0}\lambda^{0,1} + \lambda^{1,1}\lambda^{0,0}) + k_{tr,m}M\lambda^{1,1} - k_{p,TDB}\lambda^{0,0}\mu^{1,2} \tag{228}$$

$$\frac{d\mu^{1,2}}{dt} += k_{t,c}(\lambda^{1,0}\lambda^{0,2} + 2\lambda^{1,1}\lambda^{0,1} + \lambda^{1,2}\lambda^{0,0}) + k_{tr,m}M\lambda^{1,2} - k_{p,TDB}\lambda^{0,0}\mu^{1,3} \tag{229}$$

A.1.6.3 Second chain length moments

$$\begin{aligned}\frac{d\lambda^{2,0}}{dt} += {} & k_p MI + k_p M(2\lambda^{1,0} + \lambda^{0,0}) - k_{t,c}\lambda^{2,0}\lambda^{0,0} - k_{tr,m}M(\lambda^{2,0} - \lambda^{0,0}) \\ & + k_{p,TDB}(2\lambda^{1,0}\mu^{1,1} + \lambda^{0,0}\mu^{2,1})\end{aligned} \tag{230}$$

$$\begin{aligned}\frac{d\lambda^{2,1}}{dt} \mathrel{+}= {} & k_p M(2\lambda^{1,1} + \lambda^{0,1}) - k_{t,c}\lambda^{2,1}\lambda^{0,0} - k_{tr,m}M(\lambda^{2,1} - \lambda^{0,0}) \\ & + k_{p,TDB}(\lambda^{2,0}\mu^{0,2} - \lambda^{2,0}\mu^{0,1} + 2(\lambda^{1,1}\mu^{1,1} + \lambda^{1,0}\mu^{1,2} - \lambda^{1,0}\mu^{1,1}) \\ & + \lambda^{0,1}\mu^{2,1} + \lambda^{0,0}\mu^{2,2} - \lambda^{0,0}\mu^{2,1})\end{aligned} \tag{231}$$

$$\begin{aligned}\frac{d\lambda^{2,2}}{dt} \mathrel{+}= {} & k_p M(2\lambda^{1,2} + \lambda^{0,2}) - k_{t,c}\lambda^{2,2}\lambda^{0,0} - k_{tr,m}M(\lambda^{2,2} - \lambda^{0,0}) \\ & + k_{p,TDB}(2\lambda^{2,1}\mu^{0,2} - 2\lambda^{2,1}\mu^{0,1} + \lambda^{2,0}\mu^{0,3} - 2\lambda^{2,0}\mu^{0,2} + \lambda^{2,0}\mu^{0,1} \\ & + 2(\lambda^{1,2}\mu^{1,1} + 2\lambda^{1,1}\mu^{1,2} - 2\lambda^{1,1}\mu^{1,1} + \lambda^{1,0}\mu^{1,3} - 2\lambda^{1,0}\mu^{1,2} \\ & + \lambda^{1,0}\mu^{1,1}) + \lambda^{0,2}\mu^{2,1} + 2\lambda^{0,1}\mu^{2,2} - 2\lambda^{0,1}\mu^{2,1} + \lambda^{0,0}\mu^{2,3} \\ & - 2\lambda^{0,0}\mu^{2,2} + \lambda^{0,0}\mu^{2,1})\end{aligned} \tag{232}$$

$$\frac{d\mu^{2,0}}{dt} \mathrel{+}= k_{t,c}(\lambda^{2,0}\lambda^{0,0} + \lambda^{1,0}\lambda^{1,0}) + k_{tr,m}M\lambda^{2,0} - k_{p,TDB}\lambda^{0,0}\mu^{2,1} \tag{233}$$

$$\frac{d\mu^{2,1}}{dt} \mathrel{+}= k_{t,c}(\lambda^{2,0}\lambda^{0,1} + 2\lambda^{1,0}\lambda^{1,1} + \lambda^{2,1}\lambda^{0,0}) + k_{tr,m}M\lambda^{2,1} - k_{p,TDB}\lambda^{0,0}\mu^{2,2} \tag{234}$$

$$\begin{aligned}\frac{d\mu^{2,2}}{dt} \mathrel{+}= {} & k_{t,c}(\lambda^{2,0}\lambda^{0,2} + 2\lambda^{2,1}\lambda^{0,1} + \lambda^{2,2}\lambda^{0,0} + \lambda^{1,0}\lambda^{1,2} + 2\lambda^{1,1}\lambda^{1,1} + \lambda^{1,2}\lambda^{1,0}) \\ & + k_{tr,m}M\lambda^{2,2} - k_{p,TDB}\lambda^{0,0}\mu^{2,3}\end{aligned} \tag{235}$$

A.1.7 Comparison of simulation results to batch experiments

In addition to CSTR experiments, a comparison to experiments in batch mode with different monomer weight fractions w_M^0 were carried out. The data of these experiments has been taken from [49]. The results in Figure 120 and Figure 121 show stronger deviations from simulations than CSTR experiments. As in CSTR experiments, the increase in the weight average molecular weight $\overline{M_w}$ is much more pronounced for higher initial monomer weight fractions w_M^0. The reason for the deviation between experiment and simulation for higher polymer contents, may also be the diffusion limitation of the TDB

propagation reaction, which was suggested in the context of CSTR experiments. Additionally, the initiator efficiency may decrease during the batch experiments.

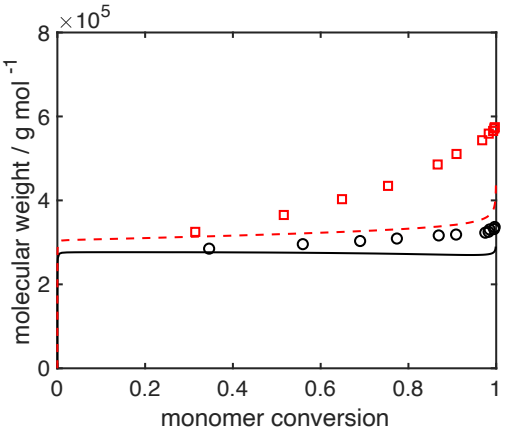

Figure 120. Comparison of the evolution of the weight average molecular weight $\overline{M_w}$ from experiments (markers) and simulations using the TDB distribution model (lines) for batch experiments with different monomer weight fractions w_M^0: black, solid – 10 wt.-%; red, dashed – 20 wt.-%. Experimental data from [49] was used.

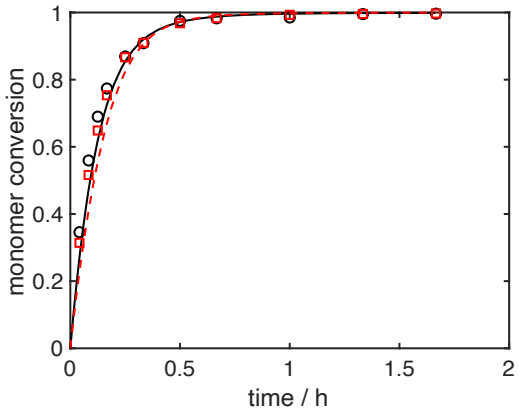

Figure 121. Comparison of the evolution of the monomer conversion from experiments (markers) and simulations using the TDB distribution model (lines) for batch experiments with different monomer weight fractions w_M^0: black, solid – 10 wt.-%; red, dashed – 20 wt.-%. Experimental data from [49] was used.

Table 21. Comparison of weight average molecular $\overline{M_w}$ weight data from experiments and model predictions for batch experiments. The parameters are listed in Table 10. Experimental data from [49] was used.

Initial monomer weight fraction w_M^0	$\overline{M_w}$ after 1.67 h / 10^3 g mol^{-1}		
	TDB distribution model	TDB reduced moment model	experiment
0.2	449	445 ($A_2 = 10^{-4}$)	574
0.1	290	286 ($A_2 = 7.7 \cdot 10^{-5}$)	337

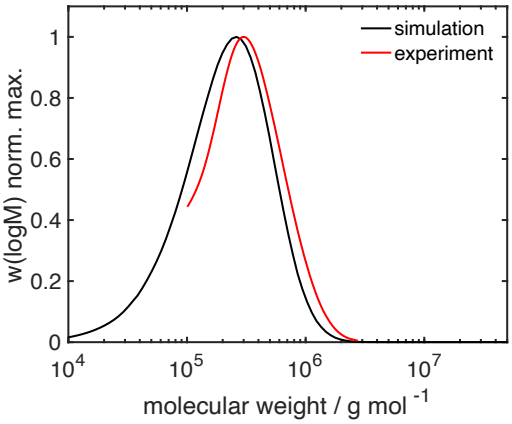

Figure 122. Comparison of the normalized GPC distribution from experiment and simulation after 1h of reaction time using the TDB reduced moment model with p_2 ($A_2 = 9.49 \cdot 10^{-5}$) for a batch experiment with a monomer weight fraction w_M^0 of 10%. Experimental data from [49] was used.

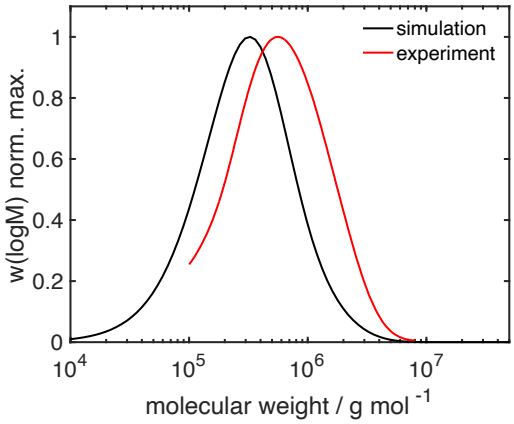

Figure 123. Comparison of the normalized GPC distribution from experiment and simulation after 1h of reaction time using the TDB reduced moment model with p_2 ($A_2 = 9.49 \cdot 10^{-5}$) for a batch experiment with a monomer weight fraction w_M^0 of 20%. Experimental data from [49] was used.

The molecular weight distributions at an operation time of 1.67 h are shown in Figure 122 and Figure 123. As expected from the previous discussion on the molecular weight averages, the results are in reasonable agreement for lower initial monomer weight fraction w_M^0, while higher deviations at higher initial monomer weight fractions w_M^0 are observed.

A.2 Flow pattern and diffusive mass transport

A.2.1 Connection between different frames of reference

Diffusive fluxes are often defined relative to the molar average velocity

$$\boldsymbol{v}^N = \sum_j x_j \boldsymbol{v}_j \tag{236}$$

in which $\boldsymbol{v}_j$ is the overall transport velocity of species j with molar fraction x_j and can, therefore, be applied in balance equations that are based on this reference frame, e.g. the molar component balance

$$\frac{\partial c_j}{\partial t} + \nabla \cdot \boldsymbol{v}^N c_j + \nabla \cdot \boldsymbol{J}_j^N = r_j^{total}. \tag{237}$$

In CFD simulations, the velocity field is calculated from the momentum balance and, therefore, in the barycentric frame of reference

$$\boldsymbol{v}^m = \sum_j \omega_j \boldsymbol{v}_j \,. \tag{238}$$

Therefore, a connection between the average velocities $\boldsymbol{v}^N$ and $\boldsymbol{v}^m$ has to be made in order to use Equation (237) in CFD simulations.

Multiplying Equation (237) with the molecular weight of species j and summing over all species

$$\sum_j \left(\frac{\partial MW_j c_j}{\partial t} + \nabla \cdot \boldsymbol{v}^N MW_j c_j + \nabla \cdot MW_j \boldsymbol{J}_j^N = MW_j r_j^{total} \right) \tag{239}$$

gives an alternative form of the continuity equation in a molar frame of reference

$$\frac{\partial \rho}{\partial t} + \nabla \cdot \boldsymbol{v}^N \rho + \nabla \cdot \sum_j MW_j \boldsymbol{J}_j^N = 0. \tag{240}$$

By comparison with the continuity equation in the barycentric frame

$$\frac{\partial \rho}{\partial t} + \nabla \cdot \boldsymbol{v}^m \rho = 0 \tag{241}$$

a relation of the average velocities

$$\boldsymbol{v}^N = \boldsymbol{v}^m - \frac{1}{\rho}\sum_j MW_j \boldsymbol{J}_j^N \tag{242}$$

can be found and the molar component balance equation may be rewritten as

$$\frac{\partial c_j}{\partial t} + \nabla \cdot \left(\boldsymbol{v}^m - \frac{1}{\rho}\sum_{i=1}^{N} MW_i \boldsymbol{J}_i^N \right) c_j + \nabla \cdot \boldsymbol{J}_j^N = r_j^{total} \ . \tag{243}$$

in which the barycentric velocity can be applied.

A.2.2 The divergence constraint for incompressible fluids with non-constant density

In an ideal mixture, the volume fractions can be calculated from the pure component densities

$$\frac{V_j}{V} = \frac{m_j/\rho_j^0}{V} = \frac{V\rho_j/\rho_j^0}{V} = \frac{\rho_j}{\rho_j^0} \tag{244}$$

and the sum these must be unity

$$\sum_j \frac{\rho_j}{\rho_j^0} = 1. \tag{245}$$

By taking the temporal derivative of Equation (245) and substituting the component balance equation (237)

$$\begin{aligned} 0 = \sum_j \frac{\partial}{\partial t}\frac{\rho_j}{\rho_j^0} = \sum_j \frac{1}{\rho_j^0}\frac{\partial \rho_j}{\partial t} = \sum_j \frac{MW_j}{\rho_j^0}\frac{\partial c_j}{\partial t} \\ = \sum_j \frac{MW_j}{\rho_j^0}\left(-\nabla \cdot \left(\boldsymbol{v}^m - \frac{1}{\rho}\sum_{i=1}^{N} MW_i \boldsymbol{J}_i^N \right) c_j - \nabla \cdot \boldsymbol{J}_j^N \right. \\ \left. + r_j^{total} \right) , \end{aligned} \tag{246}$$

the divergence of the barycentric velocity can be calculated to be [56]

$$\nabla \cdot \boldsymbol{v}^m = \nabla \cdot \frac{1}{\rho} \sum_{i=1}^{N} MW_i \boldsymbol{J}_i^N - \nabla \cdot \sum_j \frac{MW_j}{\rho_j^0} \boldsymbol{J}_j^N + \sum_j \frac{MW_j}{\rho_j^0} r_j^{total} \tag{247}$$

with

$$\begin{aligned} \nabla \cdot \frac{1}{\rho} \sum_j MW_j \boldsymbol{J}_j^N - \nabla \cdot \sum_j \frac{MW_j}{\rho_j^0} \boldsymbol{J}_j^N &= \nabla \cdot \sum_j MW_j \boldsymbol{J}_j^N \left(\frac{1}{\rho} - \frac{1}{\rho_j^0} \right) \\ &= \nabla \cdot \sum_j MW_j \boldsymbol{J}_j^N \frac{\rho_j^0 - \rho}{\rho \rho_j^0} \,. \end{aligned} \tag{248}$$

Therefore, the divergence of the barycentric velocity is

$$\nabla \cdot \boldsymbol{v}^m = \nabla \cdot \sum_j MW_j \boldsymbol{J}_j^N \frac{\rho_j^0 - \rho}{\rho \rho_j^0} + \sum_j \frac{MW_j}{\rho_j^0} r_j^{total} \tag{249}$$

and can only be equal to zero if $\rho_j^0 = \rho = const.$ as is usually assumed in the pressure correction equations in CFD simulations with a constant overall density.

A.2.3 Detailed discussion of the Stefan-Maxwell equations for systems containing polymers

The general Stefan-Maxwell equations for isothermal diffusion in J–component systems are

$$\boldsymbol{d}_i = -\frac{1}{RT} \nabla \mu_i = \sum_{j=1}^{J} \frac{x_j \boldsymbol{v}_i - x_j \boldsymbol{v}_j}{\mathfrak{D}_{ij}} \tag{250}$$

with the driving force $\boldsymbol{d}_i$ for species i, the ideal gas constant R, the temperature T, the chemical potential μ_i of species i, its molar fraction x_i, its overall transport velocity $\boldsymbol{v}_i$ and the Stefan–Maxwell diffusion coefficient $\mathfrak{D}_{ij}$ for interactions between species i and j. Their application can be demonstrated compactly at the example of a ternary mixture:

$$\boldsymbol{d}_1 = -\frac{1}{RT}\nabla\mu_1 = \sum_{j=1}^{3}\frac{x_j\boldsymbol{v}_1 - x_j\boldsymbol{v}_j}{\mathfrak{D}_{1j}} = \frac{x_2\boldsymbol{v}_1 - x_2\boldsymbol{v}_2}{\mathfrak{D}_{12}} + \frac{x_3\boldsymbol{v}_1 - x_3\boldsymbol{v}_3}{\mathfrak{D}_{13}}\,, \tag{251}$$

$$\boldsymbol{d}_2 = -\frac{1}{RT}\nabla\mu_2 = \sum_{j=1}^{3}\frac{x_j\boldsymbol{v}_2 - x_j\boldsymbol{v}_j}{\mathfrak{D}_{2j}} = \frac{x_1\boldsymbol{v}_2 - x_1\boldsymbol{v}_1}{\mathfrak{D}_{21}} + \frac{x_3\boldsymbol{v}_2 - x_3\boldsymbol{v}_3}{\mathfrak{D}_{23}}\,. \tag{252}$$

Redefining the component velocities relative to the molar average frame of reference $\boldsymbol{v}_i^N = \boldsymbol{v}_i - \boldsymbol{v}^N$ with the reference velocity $\boldsymbol{v}^N$, the velocity of the species with index 3 can be determined from

$$x_3\boldsymbol{v}_3^N = -x_1\boldsymbol{v}_1^N - x_2\boldsymbol{v}_2^N\,. \tag{253}$$

Inserting Equation (253) into Equation (251) and Equation (252) and changing the reference frame gives

$$\boldsymbol{d}_1 = \frac{x_2\boldsymbol{v}_1^N - x_2\boldsymbol{v}_2^N}{\mathfrak{D}_{12}} + \frac{x_3\boldsymbol{v}_1^N + x_1\boldsymbol{v}_1^N + x_2\boldsymbol{v}_2^N}{\mathfrak{D}_{13}}\,, \tag{254}$$

$$\boldsymbol{d}_2 = \frac{x_1\boldsymbol{v}_2^N - x_1\boldsymbol{v}_1^N}{\mathfrak{D}_{21}} + \frac{x_3\boldsymbol{v}_2^N + x_1\boldsymbol{v}_1^N + x_2\boldsymbol{v}_2^N}{\mathfrak{D}_{23}}\,, \tag{255}$$

which can be reformulated to

$$\boldsymbol{d}_1 = \left(\frac{x_2}{\mathfrak{D}_{12}} + \frac{x_1}{\mathfrak{D}_{13}} + \frac{x_3}{\mathfrak{D}_{13}}\right)\boldsymbol{v}_1^N + \left(\frac{-x_2}{\mathfrak{D}_{12}} + \frac{x_2}{\mathfrak{D}_{13}}\right)\boldsymbol{v}_2^N\,, \tag{256}$$

$$\boldsymbol{d}_2 = \left(\frac{-x_1}{\mathfrak{D}_{12}} + \frac{x_1}{\mathfrak{D}_{23}}\right)\boldsymbol{v}_1^N + \left(\frac{x_1}{\mathfrak{D}_{12}} + \frac{x_2}{\mathfrak{D}_{23}} + \frac{x_3}{\mathfrak{D}_{23}}\right)\boldsymbol{v}_2^N\,. \tag{257}$$

This example suggests the compact form

$$\boldsymbol{d}_i = \sum_{j=1}^{J-1} B_{ij}^v\,\boldsymbol{v}_j^N \tag{258}$$

to write the Maxwell-Stefan equations. For a general multicomponent system, the matrix entries are

$$B_{ij}^{v} = x_j \left(\frac{1}{\mathfrak{D}_{iJ}} - \frac{1}{\mathfrak{D}_{ij}} + \delta_{ij} \sum_{k=1}^{J} \frac{x_k}{x_j} \frac{1}{\mathfrak{D}_{jk}} \right) \tag{259}$$

with the Kronecker delta δ_{ij}. Usually, the molar fluxes

$$\boldsymbol{J}_j^N = c_j \boldsymbol{v}_j^N \tag{260}$$

are desired rather than the component velocities. This can be achieved by multiplying Equation (258) with the overall concentration c

$$-\frac{c}{RT} \nabla \mu_i = \sum_{j=1}^{J-1} c_j \left(\frac{1}{\mathfrak{D}_{iJ}} - \frac{1}{\mathfrak{D}_{ij}} + \delta_{ij} \sum_{k=1}^{J} \frac{x_k}{x_j} \frac{1}{\mathfrak{D}_{jk}} \right) \boldsymbol{v}_j^N = \sum_{j=1}^{J-1} B_{ij}^N \boldsymbol{J}_j^N \tag{261}$$

with

$$B_{ij}^N = \left(\frac{1}{\mathfrak{D}_{iJ}} - \frac{1}{\mathfrak{D}_{ij}} + \delta_{ij} \sum_{k=1}^{J} \frac{c_k}{c_j} \frac{1}{\mathfrak{D}_{jk}} \right) . \tag{262}$$

In the isothermal case

$$\begin{aligned} \nabla \mu_i &= \nabla \big(\mu_i^0 + RT \cdot ln(x_i \gamma_i) \big) = RT \nabla \big(ln(x_i) + ln(\gamma_i) \big) \\ &= RT \frac{1}{x_i} \nabla x_i \\ &+ RT \sum_{j=1}^{J} \frac{\partial ln(\gamma_i)}{\partial x_j} \nabla x_j = RT \frac{1}{x_i} \sum_{j=1}^{J} \left(\delta_{ij} + x_i \frac{\partial ln(\gamma_i)}{\partial x_j} \right) \nabla x_j \end{aligned} \tag{263}$$

with the chemical potential at a reference state μ_i^0 and the activity coefficient γ_i for species i. In case of an ideal mixture in which $\gamma_i = 1 = const.$

$$\nabla \mu_i = RT \frac{1}{x_i} \sum_{j=1}^{J} \delta_{ij} \nabla x_j = RT \frac{1}{x_i} \nabla x_i \ . \tag{264}$$

Therefore,

$$-\frac{c}{RT}RT\frac{1}{x_i}\nabla x_i = -\frac{1}{x_i}c\nabla x_i = \sum_{j=1}^{J-1} B_{ij}^N \boldsymbol{J}_j^N \tag{265}$$

or

$$-c\nabla x_i = -\nabla c x_i + x_i\nabla c = -\nabla c_i + \frac{c_i}{c}\nabla c = \sum_{j=1}^{J-1} x_i B_{ij}^N \boldsymbol{J}_j^N \ . \tag{266}$$

Redefining B_{ij}^N to

$$B_{ij} = \frac{c_i}{c}\left(\frac{1}{\mathfrak{D}_{iJ}} - \frac{1}{\mathfrak{D}_{ij}} + \delta_{ij}\sum_{k=1}^{J}\frac{c_k}{c_j}\frac{1}{\mathfrak{D}_{jk}}\right) \tag{267}$$

allows a formulation, which is explicit in the fluxes $\boldsymbol{J}_j^N$ and suitable for numerical simulation codes based on molar concentrations, by inverting the matrix $\boldsymbol{B}$ containing the elements B_{ij} as

$$J_j^N = \sum_{i=1}^{J-1} -(\boldsymbol{B}^{-1})_{ji}\left(\nabla c_i - c_i\frac{1}{c}\nabla c\right) = \sum_{i=1}^{J-1} -D_{ji}^F\left(\nabla c_i - c_i\frac{1}{c}\nabla c\right) \ . \tag{268}$$

The matrix $\boldsymbol{D}^F = \boldsymbol{B}^{-1}$ is a matrix of Fickian type diffusion coefficients. Since the fluxes $\boldsymbol{J}_j^N$ are defined relative to the molar average velocity $\boldsymbol{v}^N$

$$\boldsymbol{J}_J^N = -\sum_{j=1}^{J-1}\boldsymbol{J}_j^N \tag{269}$$

must hold.

Systems containing polymers are usually treated using the moments of the polymer property distributions and, therefore, a constitutive relation of the fluxes of these moments is needed. Such a relation can be derived from the Maxwell-Stefan equations for polymers of different chain lengths as proposed in [57]. A generalization to multi-dimensional property

distributions is straight forward. Starting from the equation for chains of length s and an additional property index l, e.g. the number of TDBs,

$$\boldsymbol{d}_{P_{s,l}} = \sum_{j=1}^{J-1} -\frac{c_{P_{s,l}}}{c}\left(\frac{1}{\mathfrak{D}_{P_{s,l}J}} - \frac{1}{\mathfrak{D}_{P_{s,l}j}} + \delta_{P_{s,l}j}\sum_{k=1}^{J}\frac{c_k}{c_j}\frac{1}{\mathfrak{D}_{jk}}\right)\boldsymbol{J}_j^N \tag{270}$$

in which J includes all low molecular species and polymers $P_{s,l}$ and splitting

$$\begin{aligned}\boldsymbol{d}_{P_{s,l}} = &\sum_{j=1}^{J_{low}-1} -\frac{c_{P_{s,l}}}{c}\left(\frac{1}{\mathfrak{D}_{P_{s,l}J}} - \frac{1}{\mathfrak{D}_{P_{s,l}j}} + \delta_{P_{s,l}j}\sum_{k=1}^{J}\frac{c_k}{c_j}\frac{1}{\mathfrak{D}_{jk}}\right)\boldsymbol{J}_j^N \\ &+ \sum_{r=1}^{\infty}\sum_{n=0}^{\infty} -\frac{c_{P_{s,l}}}{c}\left(\frac{1}{\mathfrak{D}_{P_{s,l}J}} - \frac{1}{\mathfrak{D}_{P_{s,l}P_{r,n}}}\right. \\ &\left. + \delta_{P_{s,l}P_{r,n}}\sum_{k=1}^{J}\frac{c_k}{c_{P_{r,n}}}\frac{1}{\mathfrak{D}_{P_{r,n}k}}\right)\boldsymbol{J}_{P_{r,n}}^N\end{aligned} \tag{271}$$

with the number of low molecular species J_{low}. The second sum is over all polymer chain lengths and additional distributed properties, which generally $\to \infty$. A simplification can be achieved if the Stefan-Maxwell diffusion coefficients for polymers are assumed to be $\mathfrak{D}_{P_{s,l}P_{r,n}} = \mathfrak{D}_{PP}$

$$\begin{aligned}\mathfrak{D}_{PP}\boldsymbol{d}_{P_{s,l}} = &\sum_{j=1}^{J_{low}-1} -\frac{c_{P_{s,l}}}{c}\left(\frac{\mathfrak{D}_{PP}}{\mathfrak{D}_{P_{s,l}J}} - \frac{\mathfrak{D}_{PP}}{\mathfrak{D}_{P_{s,l}j}} + \delta_{P_{s,l}j}\sum_{k=1}^{J}\frac{c_k}{c_j}\frac{\mathfrak{D}_{PP}}{\mathfrak{D}_{jk}}\right)\boldsymbol{J}_j^N \\ &+ \sum_{r=1}^{\infty}\sum_{n=0}^{\infty} -\frac{c_{P_{s,l}}}{c}\left(\frac{\mathfrak{D}_{PP}}{\mathfrak{D}_{P_{s,l}J}} - \frac{\mathfrak{D}_{PP}}{\mathfrak{D}_{P_{s,l}P_{r,n}}}\right. \\ &\left. + \delta_{P_{s,l}P_{r,n}}\sum_{k=1}^{J}\frac{c_k}{c_{P_{r,n}}}\frac{\mathfrak{D}_{PP}}{\mathfrak{D}_{P_{r,n}k}}\right)\boldsymbol{J}_{P_{r,n}}^N\ .\end{aligned} \tag{272}$$

The gray term in Equation (272) is never active, since the first sum is only over low molecular species. Further assuming that $\mathfrak{D}_{PP} \to 0$, which implies that all polymer are transported with the same diffusive velocity, it follows that

$$0 = \sum_{r=1}^{\infty}\sum_{n=0}^{\infty} -\frac{c_{P_{s,l}}}{c}\left(-1 + \delta_{P_{s,l}P_{r,n}}\sum_{k=1}^{J}\frac{c_k}{c_{P_{r,n}}}\frac{\mathfrak{D}_{PP}}{\mathfrak{D}_{P_{r,n}k}}\right)\boldsymbol{J}_{P_{r,n}}^{N} \ , \tag{273}$$

$$\sum_{r=1}^{\infty}\sum_{n=0}^{\infty}\frac{c_{P_{s,l}}}{c}\boldsymbol{J}_{P_{r,n}}^{N} = \sum_{r=1}^{\infty}\sum_{n=0}^{\infty}\frac{c_{P_{s,l}}}{c}\left(\delta_{P_{s,l}P_{r,n}}\sum_{k=1}^{J}\frac{c_k}{c_{P_{r,n}}}\frac{\mathfrak{D}_{PP}}{\mathfrak{D}_{P_{r,n}k}}\right)\boldsymbol{J}_{P_{r,n}}^{N} \ . \tag{274}$$

The summands on the right-hand side is only non-zero for polymers

$$\frac{c_{P_{s,l}}}{c}\sum_{r=1}^{\infty}\sum_{n=0}^{\infty}\boldsymbol{J}_{P_{r,n}}^{N} = \frac{1}{c}\left(\sum_{r=1}^{\infty}\sum_{n=0}^{\infty}c_{P_{r,n}}\right)\boldsymbol{J}_{P_{s,l}}^{N} \tag{275}$$

and, thereby, a relation for the flux of the polymer moments can be derived

$$c_{P_{s,l}}\sum_{r=1}^{\infty}\sum_{n=0}^{\infty}\boldsymbol{J}_{P_{r,n}}^{N} = \left(\sum_{r=1}^{\infty}\sum_{n=0}^{\infty}c_{P_{r,n}}\right)\boldsymbol{J}_{P_{s,l}}^{N} \ , \tag{276}$$

$$c_{P_{s,l}}\sum_{r=1}^{\infty}\sum_{n=0}^{\infty}\boldsymbol{J}_{P_{r,n}}^{N} = \mu^{0,0}\boldsymbol{J}_{P_{s,l}}^{N} \ , \tag{277}$$

$$\boldsymbol{J}_{P_{s,l}}^{N} = \frac{c_{P_{s,l}}}{\mu^{0,0}}\sum_{r=1}^{\infty}\sum_{n=0}^{\infty}\boldsymbol{J}_{P_{r,n}}^{N} = \frac{c_{P_{s,l}}}{\mu^{0,0}}\boldsymbol{J}_{P}^{N} \ , \tag{278}$$

$$\sum_{s=1}^{\infty}s^m\sum_{l=0}^{\infty}l^o\,\boldsymbol{J}_{P_{s,l}}^{N} = \frac{\sum_{s=1}^{\infty}s^m\sum_{l=0}^{\infty}l^o\,c_{P_{s,l}}}{\mu^{0,0}}\boldsymbol{J}_{P}^{N} \ , \tag{279}$$

$$\boldsymbol{J}_{\mu^{m,o}}^{N} = \frac{\mu^{m,o}}{\mu^{0,0}}\boldsymbol{J}_{P}^{N} \tag{280}$$

and

$$\boldsymbol{J}_{\mu^{0,0}}^{N} = \boldsymbol{J}_{P}^{N}. \tag{281}$$

Radical species usually have a very short lifetime and exist only in very small concentrations. Therefore, diffusive fluxes for these components were neglected as in [57] and the Maxwell-Stefan equations need to be solved only for I_2, M and P. The solvent S was considered as the J-th species which's flux does not need to be calculated explicitly. Assuming

that the Maxwell-Stefan diffusion coefficients involving only low molecular species to be $\mathfrak{D}_0 = const.$ and those involving polymer and low molecular species to be $\mathfrak{D}_P = const.$, the matrix $\boldsymbol{B}$ can be rewritten as

$$
\begin{aligned}
&c\boldsymbol{B} \\
&= \begin{pmatrix}
\frac{c_{I_2} + c_{LM}}{\mathfrak{D}_0} + \frac{c_M}{\mathfrak{D}_0} + \frac{c_P}{\mathfrak{D}_P} & \frac{c_{I_2}}{\mathfrak{D}_0} - \frac{c_{I_2}}{\mathfrak{D}_0} & \frac{c_{I_2}}{\mathfrak{D}_0} - \frac{c_{I_2}}{\mathfrak{D}_P} \\
\frac{c_M}{\mathfrak{D}_0} - \frac{c_M}{\mathfrak{D}_0} & \frac{c_M + c_{LM}}{\mathfrak{D}_0} + \frac{c_{I_2}}{\mathfrak{D}_0} + \frac{c_P}{\mathfrak{D}_P} & \frac{c_M}{\mathfrak{D}_0} - \frac{c_M}{\mathfrak{D}_P} \\
\frac{c_P}{\mathfrak{D}_P} - \frac{c_P}{\mathfrak{D}_P} & \frac{c_P}{\mathfrak{D}_P} - \frac{c_P}{\mathfrak{D}_P} & \frac{c_P + c_{LM}}{\mathfrak{D}_P} + \frac{c_{I_2}}{\mathfrak{D}_P} + \frac{c_M}{\mathfrak{D}_P}
\end{pmatrix}
\end{aligned}
\tag{282}
$$

and simplifies to

$$
\begin{aligned}
&c\boldsymbol{B} = \boldsymbol{B}^C \\
&= \begin{pmatrix}
\frac{c_{I_2} + c_M + c_{LM}}{\mathfrak{D}_0} + \frac{c_P}{\mathfrak{D}_P} & 0 & \frac{c_{I_2}}{\mathfrak{D}_0} - \frac{c_{I_2}}{\mathfrak{D}_P} \\
0 & \frac{c_M + c_{I_2} + c_{LM}}{\mathfrak{D}_0} + \frac{c_P}{\mathfrak{D}_P} & \frac{c_M}{\mathfrak{D}_0} - \frac{c_M}{\mathfrak{D}_P} \\
0 & 0 & \frac{c_P + c_{LM} + c_{I_2} + c_M}{\mathfrak{D}_P}
\end{pmatrix}.
\end{aligned}
\tag{283}
$$

The inverse of this matrix can be derived analytically to be

$$
(\boldsymbol{B}^C)^{-1} = \begin{pmatrix}
\frac{1}{B_a^C} & 0 & -\frac{B_c^C}{B_a^C B_i^C} \\
0 & \frac{1}{B_e^C} & -\frac{B_f^C}{B_e^C B_i^C} \\
0 & 0 & \frac{1}{B_i^C}
\end{pmatrix}
\tag{284}
$$

with

$$
\begin{aligned}
B_a^C = B_e^C &= \frac{c_{I_2} + c_M + c_{LM}}{\mathfrak{D}_0} + \frac{c_P}{\mathfrak{D}_P}\,, \\
B_c^C &= \frac{c_{I_2}}{D_0} - \frac{c_{I_2}}{D_P} = c_{I_2}\frac{\mathfrak{D}_P - \mathfrak{D}_0}{\mathfrak{D}_0\mathfrak{D}_P}\,, \\
B_f^C &= \frac{c_M}{\mathfrak{D}_0} - \frac{c_M}{\mathfrak{D}_P} = c_M\frac{\mathfrak{D}_P - \mathfrak{D}_0}{\mathfrak{D}_0\mathfrak{D}_P}\,, \\
B_i^C &= \frac{c_P + c_{LM} + c_{I_2} + c_M}{\mathfrak{D}_P}\,.
\end{aligned}
\tag{285}
$$

The resulting Fickian type diffusion coefficients are

$$
D_{I_2,I_2}^F = D_{M,M}^F = \frac{c}{B_a^C} = \frac{c}{B_e^C} = \frac{c\mathfrak{D}_0\mathfrak{D}_P}{(c_{I_2} + c_M + c_{LM})\mathfrak{D}_P + c_P\mathfrak{D}_0}\,, \tag{286}
$$

$$
\begin{aligned}
D_{I_2,P}^F &= -\frac{B_c^C}{B_a^C B_i^C}c \\
&= -c\frac{c_{I_2}(\mathfrak{D}_P - \mathfrak{D}_0)}{\mathfrak{D}_0\mathfrak{D}_P}\cdot\frac{\mathfrak{D}_0\mathfrak{D}_P}{(c_{I_2} + c_M + c_{LM})D_P + c_P D_0} \\
&\quad\cdot\frac{\mathfrak{D}_P}{c_P + c_{LM} + c_{I_2} + c_M}
\end{aligned}
\tag{287}
$$

$$
\begin{aligned}
D_{M,P}^F &= -\frac{B_f^C}{B_a^C B_i^C}c \\
&= -c\frac{c_M(\mathfrak{D}_P - \mathfrak{D}_0)}{\mathfrak{D}_0\mathfrak{D}_P}\cdot\frac{\mathfrak{D}_0\mathfrak{D}_P}{(c_{I_2} + c_M + c_{LM})\mathfrak{D}_P + c_P\mathfrak{D}_0} \\
&\quad\cdot\frac{\mathfrak{D}_P}{c_P + c_{LM} + c_{I_2} + c_M}
\end{aligned}
\tag{288}
$$

and

$$
D_{P,P}^F = \frac{c}{B_i^C} = c\left(\frac{c_P + c_{LM} + c_{I_2} + c_M}{\mathfrak{D}_P}\right)^{-1} = \frac{c\mathfrak{D}_P}{c_P + c_{LM} + c_{I_2} + c_M}. \tag{289}
$$

The diffusive fluxes

$$\boldsymbol{J}_j^N = \sum_{i=1}^{J-1} -D_{ji}^F \cdot \left(\nabla c_i - c_i \frac{1}{\mathrm{c}} \nabla c \right) \tag{290}$$

are given in Section 5.1.2.

A.2.4 Algorithm and numerical setup for the calculation of transient reactive flow

The model equations described in Section 5.1.2 were solved using an algorithm based on the pimpleFOAM solver for incompressible transient flow problems, which is included in the OpenFOAM® software package. Figure 124 shows the flow chart for one time step of the algorithm. After the mesh has been constructed, the initial and boundary conditions have been read and initial calculations of densities as well as transport and kinetic coefficients have been performed, an appropriate time step size Δt is chosen. Besides the common Courant number restriction

$$Co = \frac{|\boldsymbol{u}|}{L_c} \Delta t < 1 \tag{291}$$

with the cell size L_c, a second criterion based on the reaction rates was found to be crucial for the stability of the solver. Neglecting any transport of component i, the rate of change of concentration c_i in each cell is

$$\frac{\partial c_i}{\partial t} \approx \frac{c_i - c_i^0}{\Delta t} = r_i^{total} \tag{292}$$

with the concentration at a reference time step 0 and the overall reaction rate involving all reactions, which affect the concentration of component i. By defining the relative change of c_i per time step

$$\frac{c_i - c_i^0}{c_i^0} = C_{r_i} = \frac{1}{c_i^0} r_i^{total} \Delta t \ , \tag{293}$$

large changes of c_i can be prevented and the stability of the solution can be improved by choosing the time step size so

$$\max(C_{r_i}, Co) < f_{\Delta t} \tag{294}$$

for each cell, with i going over all species for which a component balance needs to be solved. The initial time step sizes was chosen to be 10^{-10} s to ensure convergence and the factor $f_{\Delta t}$ was chosen to be small for the initial time steps and then increased subsequently to values close to unity to keep the number of iterations within one time step in a specified range, usually between 10 and 30. After the time step size has been chosen, the time step iteration loop, which is highlighted by the gray box in Figure 124, is entered. First, the overall mass and molar densities, as well as the transport and kinetic coefficients are calculated. Afterwards the diffusive fluxes and the reaction rates are estimated using the old concentration fields to calculate the velocity correction from Equation (127) and the non-zero divergence contributions from Equation (132) are calculated subsequently. With this information, the momentum equation can be solved using the pressure field from the previous time step and the velocity field is corrected subsequently using the pressure correction method described in Section 2.4.2 but the non-zero divergence. The species equations are then solved sequentially using the corrected velocity field in the order listed in Figure 124. Since the species equations are coupled, the order of solution was chosen to calculate as many concentrations as possible before inserting them into other balance equations and to improve convergence. The procedure is then repeated until the convergence criteria for all equations are met, before the time t is incremented.

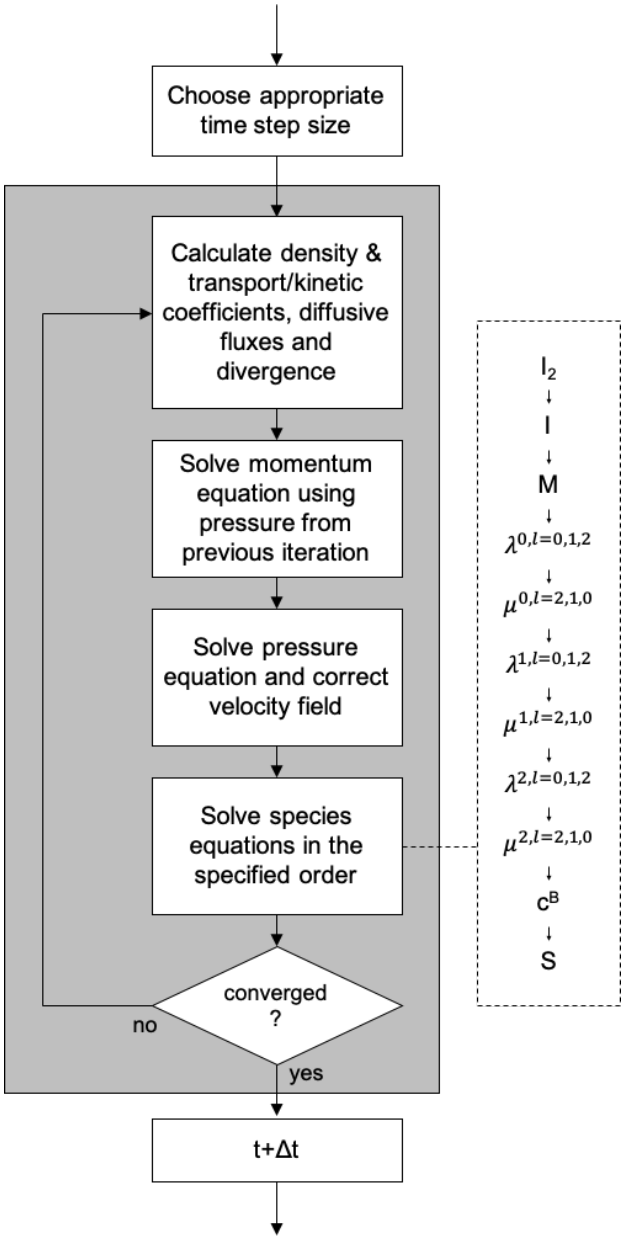

Figure 124. Illustration of the solution algorithm (based on the PIMPLE algorithm as part of OpenFOAM® 2.3.0).

The discretization schemes that were chosen for all simulations in this thesis are given in Table 22. All schemes are second order accurate and limiters were chosen for the divergence schemes to avoid oscillations of the solution. The *"backward"* time scheme is the one that

has been defined in Equation (52) and *"Gauss"* specifies the standard finite volume discretization using the gaussian theorem.

Table 22. Summary of the discretization schemes used in OpenFOAM®. Operator and discretization schemes are written in OpenFOAM® syntax.

Operator	Variable	Descretization scheme in OpenFOAM®
ddtSchemes $(\frac{\partial}{\partial t})$	default	*"backward"*
gradSchemes (∇)	default	*"Gauss linear"*
divSchemes $(\nabla \cdot)$	default	*"Gauss MUSCL"*
	$\rho \boldsymbol{u}\boldsymbol{u}$	*„Gauss linearUpwind grad(U)"*
laplacianSchemes $(\nabla \cdot \nabla)$	default	*"Gauss linear corrected"*
snGradSchemes	default	*"corrected"*

A.2.5 Demonstration of transport phenomena in reactive polymer solutions

To demonstrate the transport phenomena occurring in solution polymerization a one-dimensional system was initialized at rest with most other conditions based on the reference case in Table 10. Differences to these reference conditions will be highlighted in the text. The initiator concentration was initialized as a gaussian type function

$$c_{I_2}^0 = 0.712244 \exp\left(-\frac{x^2}{8}\right) + 0.00071224 \tag{295}$$

as illustrated in Figure 125. The weight fraction of initiator w_{I_2} decreases from 0.02 at x = 0 mm to 0.0002 at x = 10 mm.

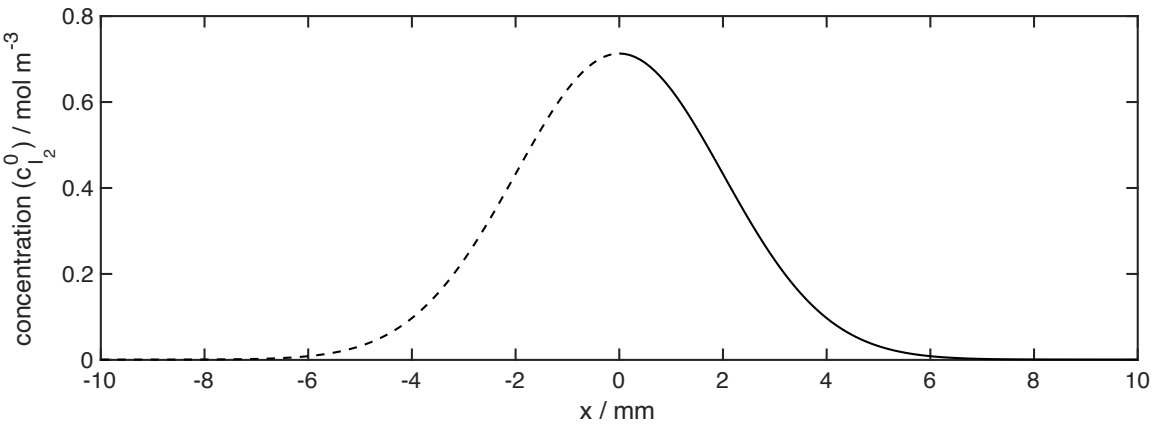

Figure 125. Initial initiator concentration profile in the one-dimensional example for the discussion of transport phenomena in reactive polymer solution systems.

Since the problem is symmetric, only the positive part of the x-axis was considered in the simulation and the barycentric velocity was fixed to zero at position $x = 0$ mm. For all concentrations, a zero gradient Neumann boundary condition was chosen at both $x = 0$ mm and $x = 10$ mm and the pressure was fixed to zero at $x = 10$ mm and zero gradient at $x = 0$ mm was assumed.

Starting from a system with a simplified diffusion model and a constant overall density, the complexity will be increased in multiple steps to discuss the effect of different transport phenomena included in the model. This can be achieved by changing the values of transport coefficients and pure component densities for different components as will be seen in the subsequent paragraphs.

By setting all pure component densities to the same constant value of 964.68 kg m^{-3}, the overall density will not change during the reaction and transport of mass induced by a non-zero divergence of the barycentric velocity field will, therefore, not occur. If, additionally, all Maxwell-Stefan diffusion coefficients are assumed to take the same constant value of $\mathfrak{D}_P = \mathfrak{D}_0 = 10^{-9}$ m^2 s^{-1}, all non-diagonal entries of the diffusion matrix vanish, and the

result is a simplified model for diffusion without any cross effects. This is a crude assumption, since polymers are typically much larger molecules than their solvents and the Maxwell-Stefan coefficient for diffusive transport of polymers in a solvent should be significantly lower than those for the transport of low molecular species in the same solvent. Therefore, a comparison of the simplified diffusion model that has been described above and a Maxwell-Stefan diffusion model with $\mathfrak{D}_P = 0.1\,\mathfrak{D}_0$ was made to illustrate the effect of different mass transport coefficients. In Figure 126 and Figure 128 the evolution of the weight fractions of polymers w_P and monomer molecules w_M are shown. Starting from an initial weight fraction w_M of 0.2, monomer is consumed at a faster rate on left-hand side of the simulation domain due to the higher initiator concentration and diffusive mass transport is induced by the gradient in molar fractions x_j. As illustrated in Figure 127, most of the initiator is consumed after around 8000 s and the concentration profile of monomer is leveled out by diffusive mass transport. While the transport model only has

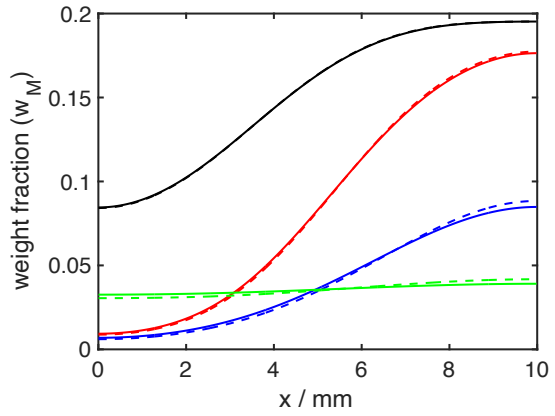

Figure 126. Evolution of the monomer weight fraction w_M profile for the simplified diffusion model with constant density (solid lines) and the Maxwell-Stefan diffusion model with constant density (dashed lines) for the simple 1D case discussed in Section A.2.5; Colors denote simulation times: black – 500 s, red – 2000 s, blue – 8000 s, green – 32000 s.

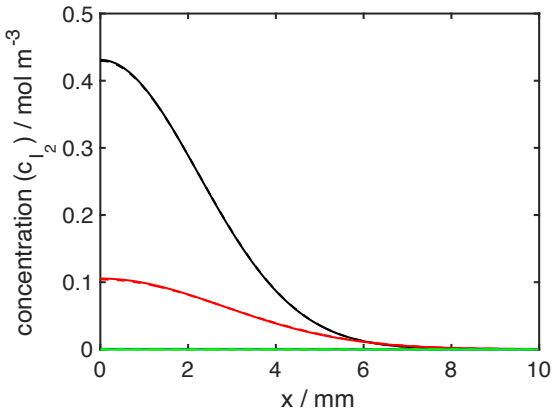

Figure 127. Evolution of the initiator concentration profile c_{I_2} for the simplified diffusion model with constant density (solid lines) and the Maxwell-Stefan diffusion model with constant density (dashed lines) for the simple 1D case discussed in Section A.2.5; Colors denote simulation times: black – 500 s, red – 2000 s, blue – 8000 s, green – 32000 s.

a minor effect on the profile of the monomer weight fraction w_M, a significant difference can be observed for the polymer weight fraction w_P. The latter increases up to values that are higher than 0.2, which would be expected in a batch experiment at full conversion.

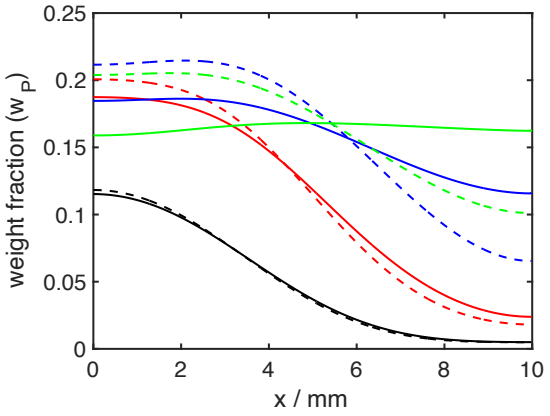

Figure 128. Evolution of the polymer weight fraction w_P profile for the simplified diffusion model with constant density (solid lines) and the Maxwell-Stefan diffusion model with constant density (dashed lines) for the simple 1D case discussed in Section A.2.5; Colors denote simulation times: black – 500 s, red – 2000 s, blue – 8000 s, green – 32000 s.

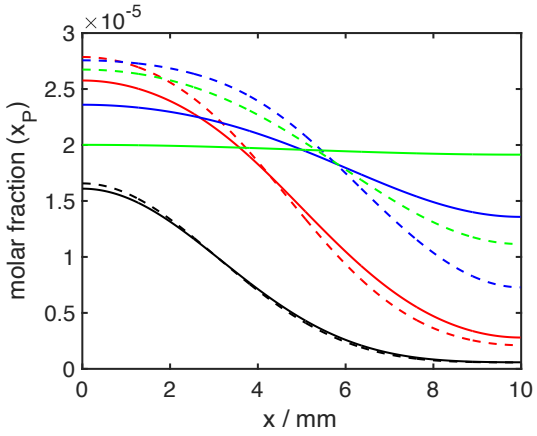

Figure 129. Evolution of the polymer molar fraction x_P profile for the simplified diffusion model with constant density (solid lines) and the Maxwell-Stefan diffusion model with constant density (dashed lines) for the simple 1D case discussed in Section A.2.5; Colors denote simulation times: black – 500 s, red – 2000 s, blue – 8000 s, green – 32000 s.

As can be understood from Figure 130, the diffusive transport velocity of polymers

$$\boldsymbol{v}_P^N = \frac{\boldsymbol{J}_{\mu^{0,0}}^N}{\mu^{0,0}} \tag{296}$$

is much lower in case of different Maxwell-Stefan diffusion coefficients and, therefore, polymer accumulates on the left-hand side of the simulation domain. For comparison, the monomer transport velocity is shown in Figure 131. Differences are small compared to the diffusive transport velocity of polymers. It should be noted, that the polymer weight fraction w_P is characterized by the first polymer chain length moment since

$$\rho_P = MW_M \mu^{1,0} \tag{297}$$

but the polymer transport velocity is determined by gradients of the molar fraction of polymers x_P, which is shown in Figure 129. This is the reason behind the peak in the polymer weight fraction w_P profile.

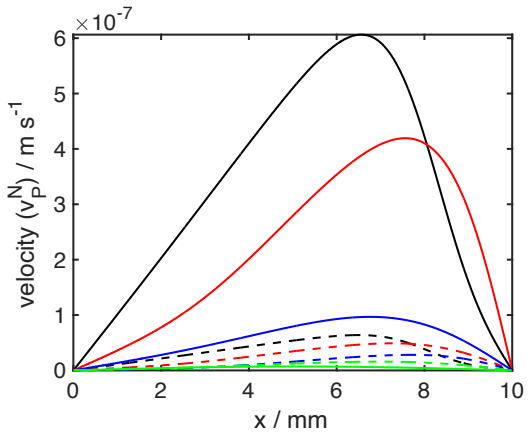

Figure 130. Evolution of the polymer diffusion velocity $\boldsymbol{v}_P^N$ profile for the simplified diffusion model with constant density (solid lines) and the Maxwell-Stefan diffusion model with constant density (dashed lines) for the simple 1D case discussed in Section A.2.5; Colors denote simulation times: black – 500 s, red – 2000 s, blue – 8000 s, green – 32000 s.

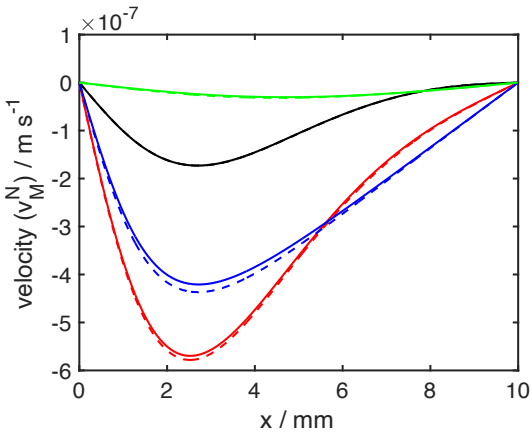

Figure 131. Evolution of the monomer diffusion velocity $\boldsymbol{v}_M^N$ profile for the simplified diffusion model with constant density (solid lines) and the Maxwell-Stefan diffusion model with constant density (dashed lines) for the simple 1D case discussed in Section A.2.5; Colors denote simulation times: black – 500 s, red – 2000 s, blue – 8000 s, green – 32000 s.

As illustrated in Figure 133, the weight average molecular weight $\overline{M_w}$ increases due to the higher polymer weight fraction w_P, which fosters the importance of the TDB propagation reaction. Since mass transport of all higher polymer moments is coupled to the transport velocity that is determined by the zeroth moment, the molecular weight averages and other properties move with the polymer transport velocity, e.g. the number of TDB per molecule c^{TDB}/λ_0^P, which is shown in Figure 132. As can be seen from Figure 132, almost every polymer chain on the right hand side of the simulation domain carries one TDB. The

reason for this observation is the low radical concentration. Under these conditions, transfer to monomer becomes the dominating termination mechanism.

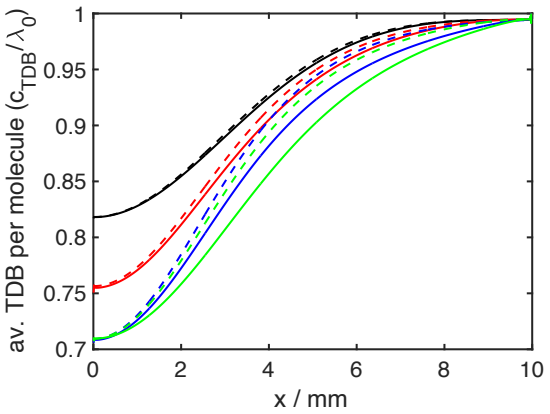

Figure 132. Evolution of the number TDB per molecule c^{TDB}/λ_0^P profile for the simplified diffusion model with constant density (solid lines) and the Maxwell-Stefan diffusion model with constant density (dashed lines) for the simple 1D case discussed in Section A.2.5; Colors denote simulation times: black – 500 s, red – 2000 s, blue – 8000 s, green – 32000 s.

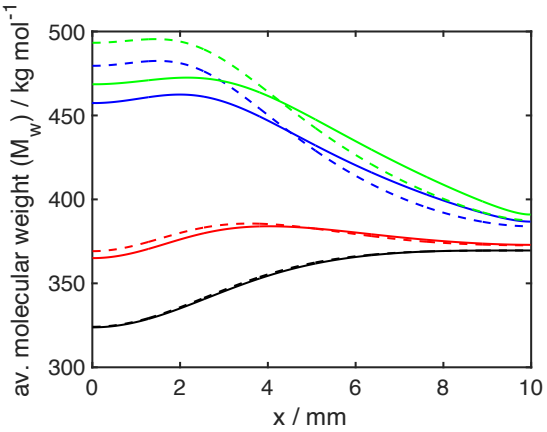

Figure 133. Evolution of the weight average molecular weight $\overline{M_w}$ profile for the simplified diffusion model with constant density (solid lines) and the Maxwell-Stefan diffusion model with constant density (dashed lines) for the simple 1D case discussed in Section A.2.5; Colors denote simulation times: black – 500 s, red – 2000 s, blue – 8000 s, green – 32000 s.

The pure component density of polymers is usually higher than those of the corresponding monomers and typical solvents. Therefore, the mass density ρ of the system increases during a polymerization reaction, which corresponds to shrinking of the bulk phase. In the model presented in Section 5.1, this effect is included through changes of the divergence of the barycentric velocity field as specified by Equation (132). Figure 135 illustrates the effect of increasing the polymer pure component density to 1200 kg m^{-3} compared to the model with Maxwell-Stefan diffusion coefficients and a constant mass density ρ, which was discussed before. The overall mass density ρ increases with the polymer weight fraction w_P shown in Figure 134 and Figure 135 as expected. The polymerization reaction creates a sink in the barycentric velocity field, which is manifested in a negative divergence as

shown in Figure 136 and induces mass transport from right to the left of the domain. The divergence is closely linked to the barycentric velocity profile since it determines its slope as can be seen from Figure 137. However, this effect is relatively small in comparison to different Maxwell-Stefan diffusion coefficients.

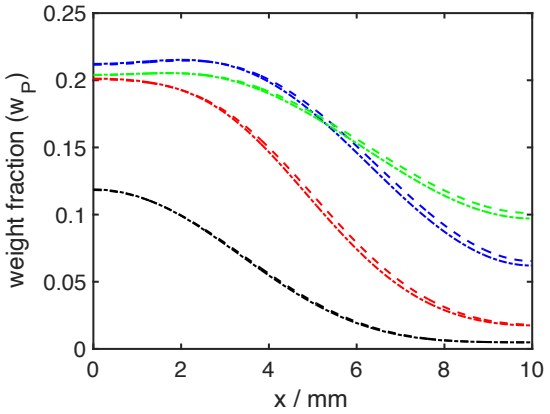

Figure 134. Evolution of the polymer weight fraction w_P profile for the Maxwell-Stefan diffusion model with constant density (dashed lines) and variable density (dashed-dotted lines) for the simple 1D case discussed in Section A.2.5; Colors denote simulation times: black – 500 s, red – 2000 s, blue – 8000 s, green – 32000 s.

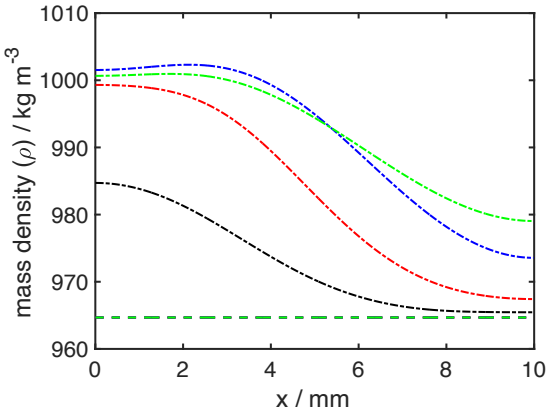

Figure 135. Evolution of the mass density ρ profile for the Maxwell-Stefan diffusion model with constant density (dashed lines) and variable density (dashed-dotted lines) for the simple 1D case discussed in Section A.2.5; Colors denote simulation times: black – 500 s, red – 2000 s, blue – 8000 s, green – 32000 s.

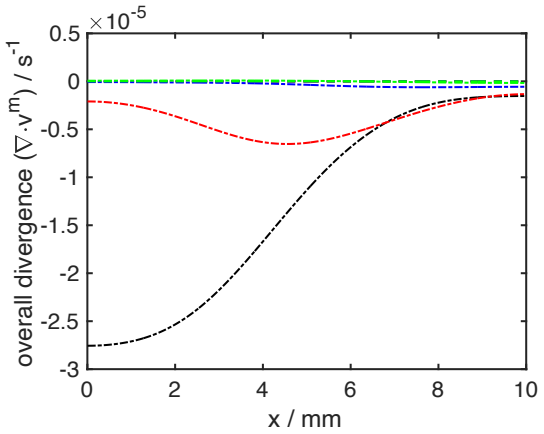

Figure 136. Evolution of the overall divergence profile for the Maxwell-Stefan diffusion model with constant density (dashed lines) and variable density (dashed-dotted lines) for the simple 1D case discussed in Section A.2.5; Colors denote simulation times: black – 500 s, red – 2000 s, blue – 8000 s, green – 32000 s.

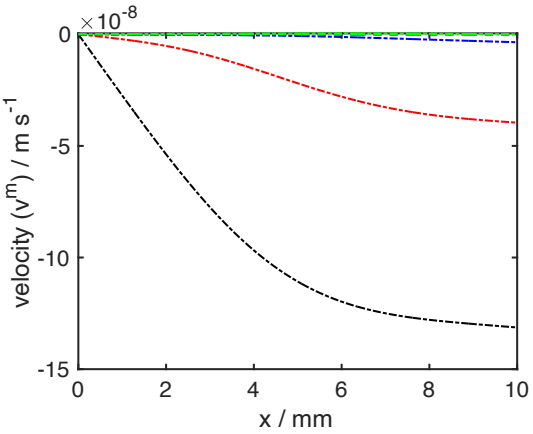

Figure 137. Evolution of the barycentric velocity profile for the Maxwell-Stefan diffusion model with constant density (dashed lines) and variable density (dashed-dotted lines) for the simple 1D case discussed in Section A.2.5; Colors denote simulation times: black – 500 s, red – 2000 s, blue – 8000 s, green – 32000 s.

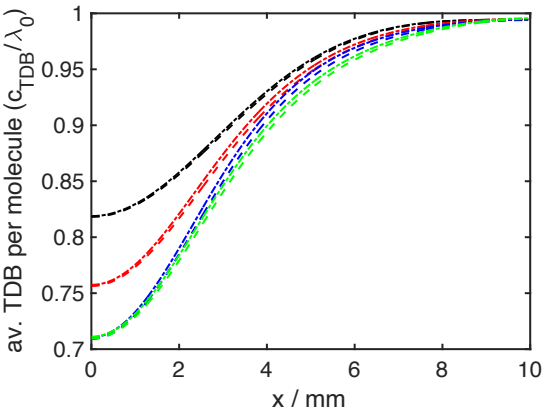

Figure 138. Evolution of the average number of TDB per molecule c^{TDB}/λ_0^P profile for the Maxwell-Stefan diffusion model with constant density (dashed lines) and variable density (dashed-dotted lines) for the simple 1D case discussed in Section A.2.5; Colors denote simulation times: black – 500 s, red – 2000 s, blue – 8000 s, green – 32000 s.

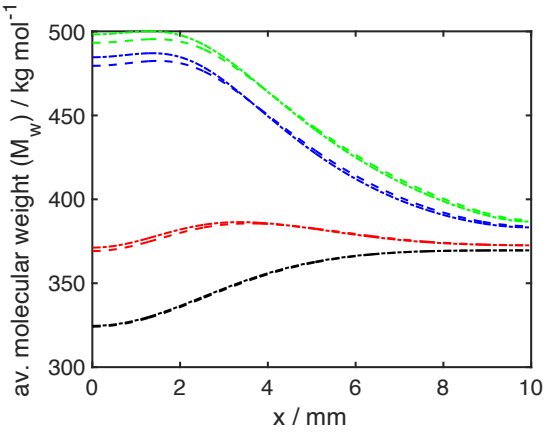

Figure 139. Evolution of the weight average molecular weight $\overline{M_w}$ profile for the Maxwell-Stefan diffusion model with constant density (dashed lines) and variable density (dashed-dotted lines) for the simple 1D case discussed in Section A.2.5; Colors denote simulation times: black – 500 s, red – 2000 s, blue – 8000 s, green – 32000 s.

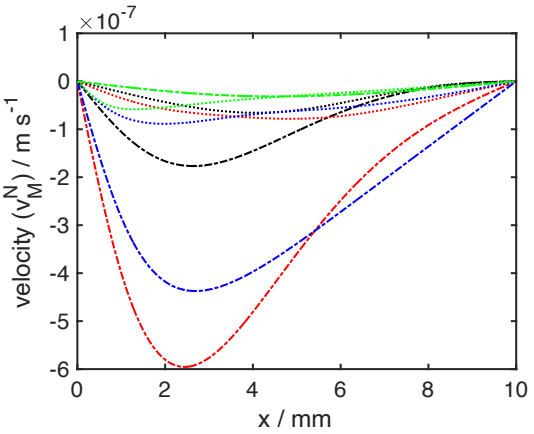

Figure 140. Evolution of the monomer diffusion velocity $\boldsymbol{v}_M^N$ profile for the Maxwell-Stefan diffusion model with variable density and constant viscosity (dashed-dotted lines) or variable density and variable viscosity (dotted lines) for the simple 1D case discussed in Section A.2.5; Colors denote simulation times: black – 500 s, red – 2000 s, blue – 8000 s, green – 32000 s.

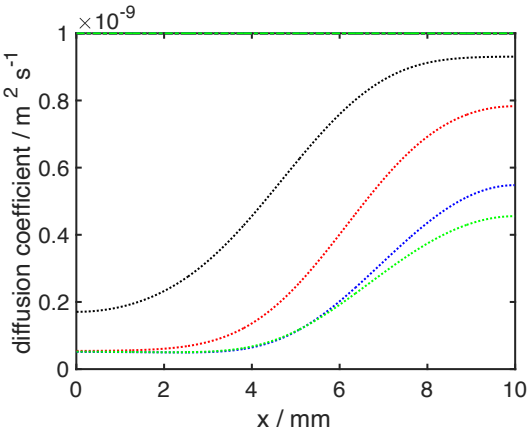

Figure 141. Evolution of the Maxwell-Stefan diffusion coefficient $\mathfrak{D}_0$ profile for the Maxwell-Stefan diffusion model with variable density and constant viscosity (dashed-dotted lines) or variable density and variable viscosity (dotted lines) for the simple 1D case discussed in Section A.2.5; Colors denote simulation times: black – 500 s, red – 2000 s, blue – 8000 s, green – 32000 s.

Another characteristic of a polymerization reaction is a significant increase of the shear viscosity with increasing polymer concentration and polymer chain length. While viscous dissipation by shearing is not relevant for the 1D problem studied here, the diffusion coefficient is linked to the viscosity by the Stokes-Einstein relation. So far, this effect has not been considered but may of course influence the results significantly. Using the viscosity correlation from Equation (148), the Maxwell-Stefan diffusion coefficients decrease as illustrated in Figure 141 and, thereby, the diffusive mass transport velocity also decreases as shown for the monomer transport velocity $\boldsymbol{v}_M^N$ in Figure 140. Since monomer is consumed at a faster rate than it is transported to the left, its concentration decreases to a value close to zero as shown in Figure 143. Consequently, the polymer weight fraction w_P reaches a lower final level as well as illustrated in Figure 142. Although the polymer weight fraction w_P is slightly lower, the weight average molecular weight $\overline{M_w}$ increases

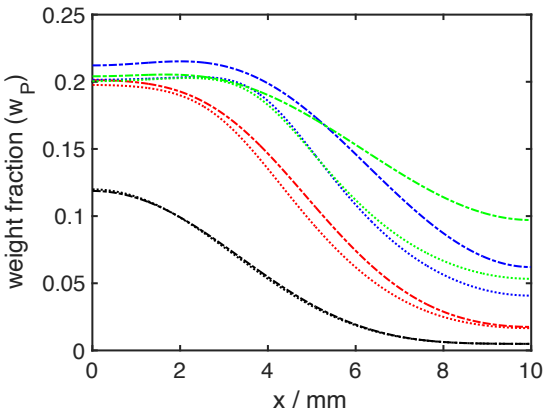

Figure 142. Evolution of the polymer weight fraction w_P profile for the Maxwell-Stefan diffusion model with variable density and constant viscosity (dashed-dotted lines) or variable density and variable viscosity (dotted lines) for the simple 1D case discussed in Section A.2.5; Colors denote simulation times: black – 500 s, red – 2000 s, blue – 8000 s, green – 32000 s.

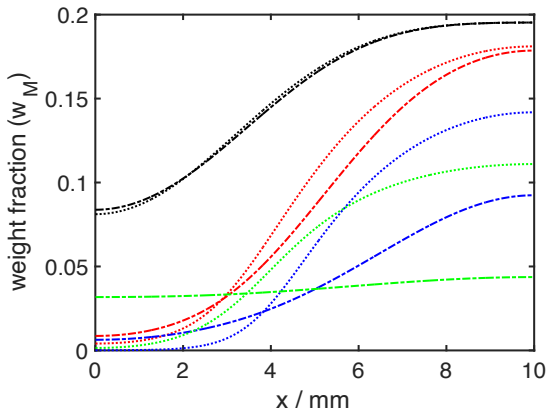

Figure 143. Evolution of the monomer weight fraction w_M profile for the Maxwell-Stefan diffusion model with variable density and constant viscosity (dashed-dotted lines) or variable density and variable viscosity (dotted lines) for the simple 1D case discussed in Section A.2.5; Colors denote simulation times: black – 500 s, red – 2000 s, blue – 8000 s, green – 32000 s.

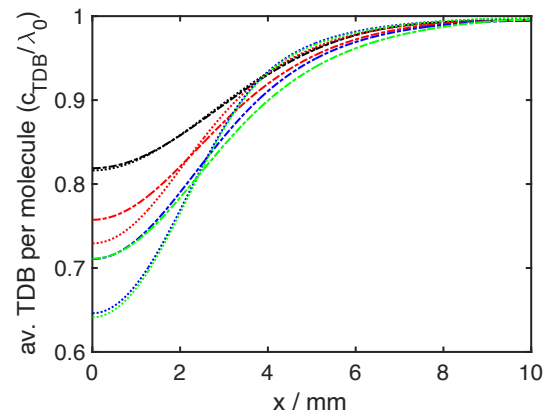

Figure 144. Evolution of the average number of TDB per molecule c^{TDB}/λ_0^P profile for the Maxwell-Stefan diffusion model with variable density and constant viscosity (dashed-dotted lines) or variable density and variable viscosity (dotted lines) for the simple 1D case discussed in Section A.2.5; Colors denote simulation times: black – 500 s, red – 2000 s, blue – 8000 s, green – 32000 s.

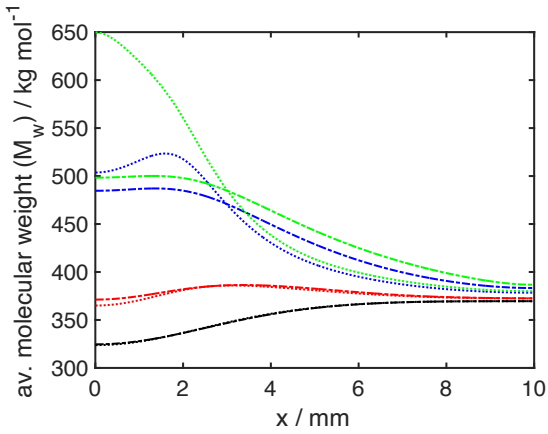

Figure 145. Evolution of the weight average molecular weight $\overline{M_w}$ profile for the Maxwell-Stefan diffusion model with variable density and constant viscosity (dashed-dotted lines) or variable density and variable viscosity (dotted lines) for the simple 1D case discussed in Section A.2.5; Colors denote simulation times: black – 500 s, red – 2000 s, blue – 8000 s, green – 32000 s.

even further since the consumption of TDB is enhanced under these conditions as shown in Figure 144 and Figure 145.

A.2.6 Concentrations of different species in the channel flow case

In Figure 147, the concentration fields of different species are shown for the channel flow case in Section 5.2.1

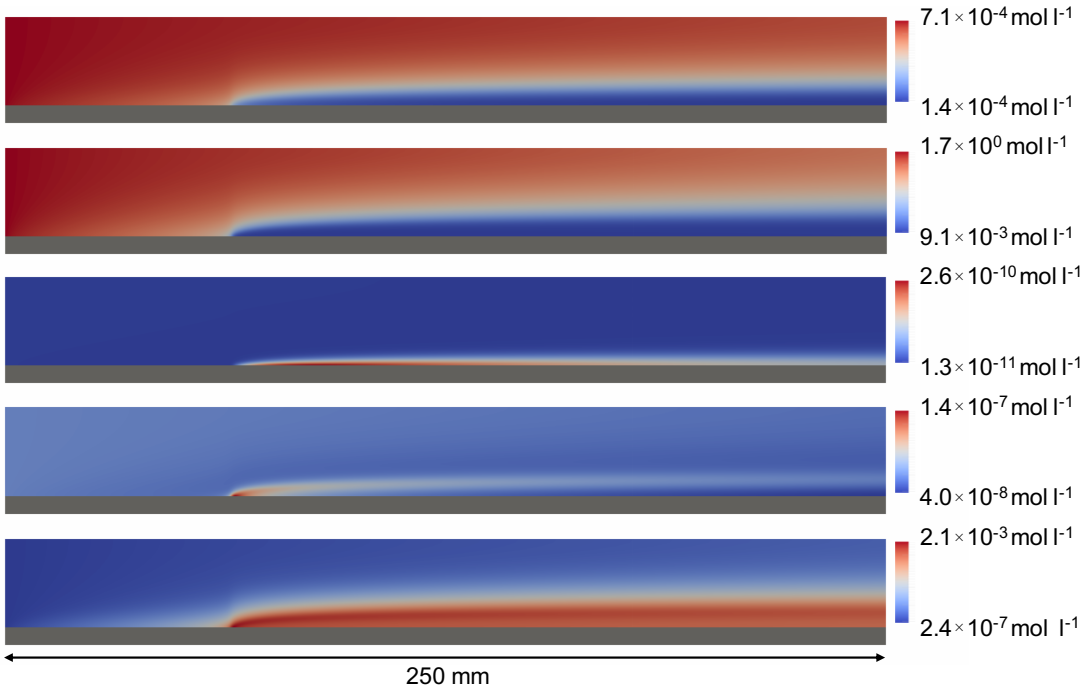

Figure 146. Concentration fields in the geometry shown in Figure 81 after 3600 s: undissociated initiator c_{I_2}, monomer c_M, initiator radical c_I, polymer radical $\lambda^{0,0}$, polymer $\mu^{0,0}$ (top to bottom). All parameters are those of the reference conditions described in Section 5.1 to Section 5.2.

A.2.7 Simulations in longer channels for validation purposes

As discussed in Section 5.2.2, simulations in longer channels have been carried out additionally for simulation cases without gelation to validate that gelation does not occur outside the simulation domain. The results for the case in which $\mathfrak{D}_P = \mathfrak{D}_0$ with a reactor

length of $L_x = 2.5$ m are shown in Figure 147. The polymer weight fraction w_P at the wall even decreases for very long simulation times. The molar fraction of polymer x_P reaches a stationary value as shown in Figure 148.

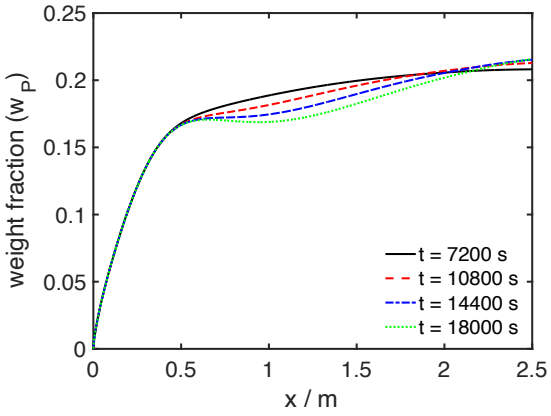

Figure 147. Polymer weight fraction w_P profiles in x-direction in a geometry similar to the one shown in Figure 81 at the wall (green line in Figure 81) for different times. The extension of the simulation domain in x direction was scaled by a factor of 10 and the corresponding number of cells was increased to 5000. All other parameters are those of the reference conditions described in Section 5.1 to Section 5.2 except $\mathfrak{D}_P = \mathfrak{D}_0$.

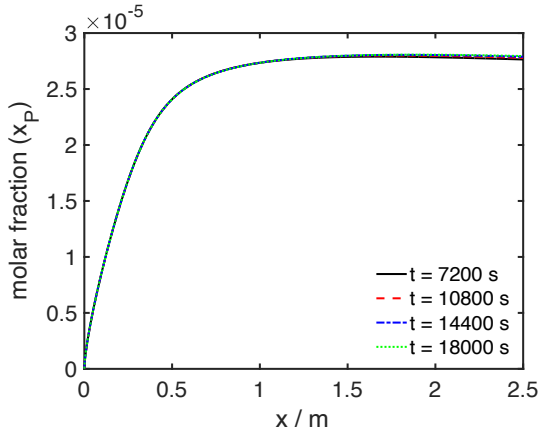

Figure 148. Polymer molar fraction x_P profiles in x-direction in a geometry similar to the one shown in Figure 81 at the wall (green line in Figure 81) for different times. The extension of the simulation domain in x direction was scaled by a factor of 10 and the corresponding number of cells was increased to 5000. All other parameters are those of the reference conditions described in Section 5.1 to Section 5.2 except $\mathfrak{D}_P = \mathfrak{D}_0$.

Figure 149 shows the polymer content at the wall for a simulation with a reactor length of $L_x = 2.5$ m for the case of a constant relative viscosity $\eta_{rel} = 1$. Since the polymer diffusion coefficient $\mathfrak{D}_P$ is an order of magnitude lower than $\mathfrak{D}_0$, the polymer weight fraction w_P also increases to values higher than 0.2 at a position further along the x-axis. The increase is less pronounced, since the Maxwell-Stefan diffusion coefficients do not decrease due to the constant viscosity. As illustrated in Figure 150, the weight average molecular is higher at positions where higher polymer weight fractions w_P exist, but the increase does not accelerate as in the previously discussed cases in which gelation occurred.

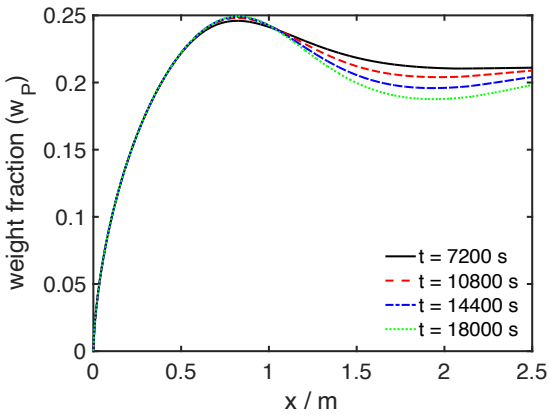

Figure 149. Polymer weight fraction w_P profiles in x-direction in a geometry similar to the one shown in Figure 81 at the wall (green line in Figure 81) for different times. The extension of the simulation domain in x direction was scaled by a factor of 10 and the corresponding number of cells was increased to 5000. All other parameters are those of the reference conditions described in Section 5.1 to Section 5.2 except $\eta_{rel} = 1 = \text{const}$.

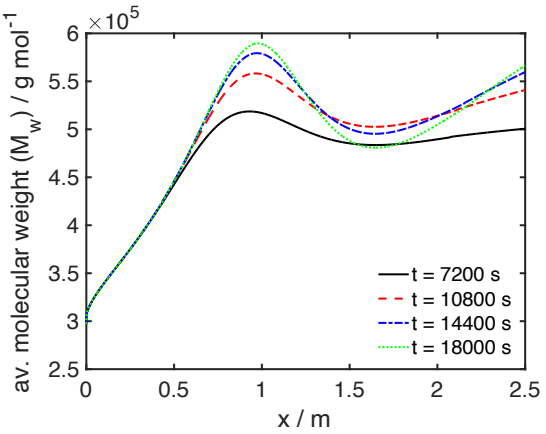

Figure 150. Weight average molecular weight $\overline{M_w}$ profiles in x-direction in a geometry similar to the one shown in Figure 81 at the wall (green line in Figure 81) for different times. The extension of the simulation domain in x direction was scaled by a factor of 10 and the corresponding number of cells was increased to 5000. All other parameters are those of the reference conditions described in Section 5.1 to Section 5.2 except $\eta_{rel} = 1 = \text{const}$.

A.2.8 Effect of different scale up criteria on the flow pattern in static mixer-like geometries

As discussed in Section 5.3.2, keeping the inlet velocity constant while scaling the geometry in x and y direction leads to a similar flow pattern and magnitude of the velocity field. The magnitude of the velocity field is illustrated in Figure 151 for two scaling factors and is indistinguishable by eye. As demonstrated in Figure 152, the flow pattern in the contact region of walls and mixer elements scales almost with the geometry scaling factor but its size increases by slightly larger factor. Keeping the Reynolds number from Equation (176) constant, i.e. decreasing the inlet velocity by the geometry scaling factor, leads to a flow pattern that is scaled by the same factor. Keeping the average residence time from Equation (177) constant, i.e. increasing the inlet velocity by the geometry scaling factor, the

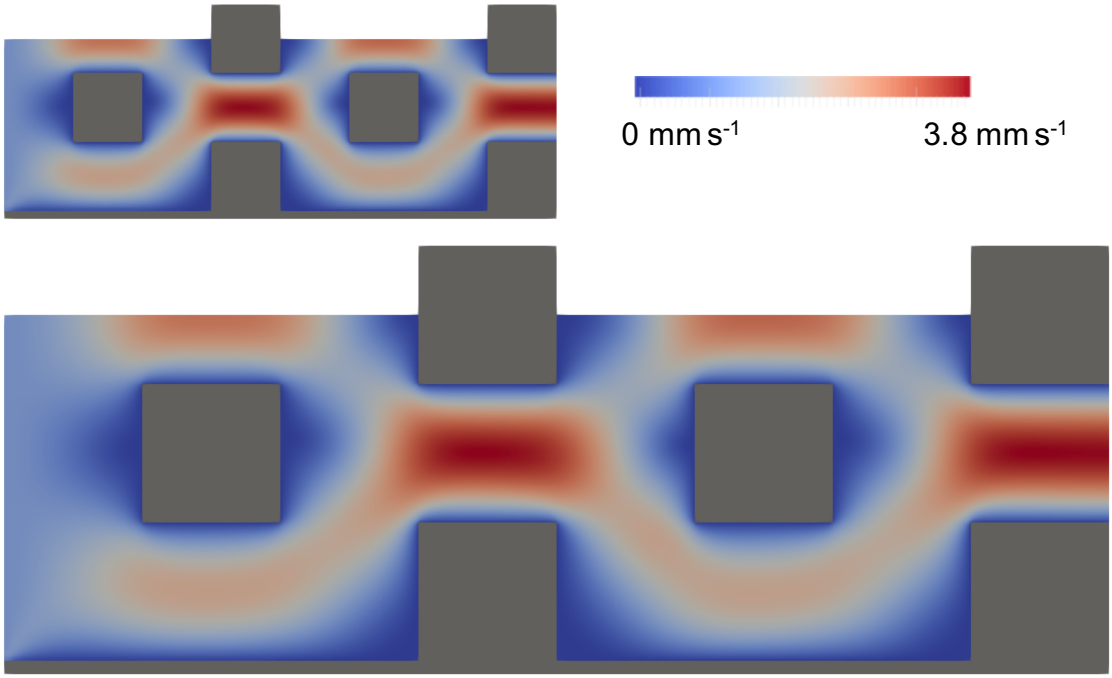

Figure 151. Magnitude of the barycentric velocity field for the reference case and an inlet velocity of 1 mm s^{-1}. Top – original geometry with scaling factor 1, bottom – geometry with a scaling factor of 2.

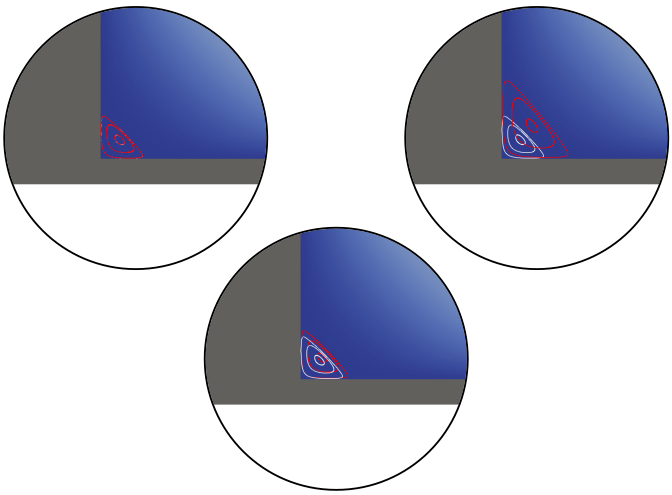

Figure 152. Comparison of the effect of different scale up criteria on the flow pattern in dead-water zones downwind of mixer elements. Only streamlines in the dead-water zones are shown. The white reference is the flow pattern of a simulation in the original geometry with a scale up factor of 1 (top of Figure 151), which was scaled by a factor of 2 in post processing. The red flow patterns were extracted from simulations in a geometry that was scaled by a factor of 2 (bottom of Figure 151). Top left – constant Reynolds number (Eq. (176)), top right – constant average residence time (Eq. (177)), bottom – const inlet velocity.

size of the dead-water zone increases by a factor that is much larger than the geometry scaling factor.

A.3 Experimental and analytical setups and conditions

A.3.1 Chemicals, preparation and sampling procedures

Monomer was supplied by BASF SE in 30 kg barrels that were stabilized with 0.5% NaOH and filled in bottles, which were stored in the freezer directly after delivery. The latter were unfrozen on demand and the monomer was distilled under vacuum at a temperature of 81-83°C in the column head to remove stabilizer and high-molecular components. If experiments were carried out on the next day the distillate was store in a fridge or frozen again if storage over a couple of days was necessary. The distillate was transparent and colorless while the column feed had a yellow color. The bottom fraction turned from yellow over a dark orange to brown and was removed when color was dark brown. Initiator, V-50, was obtained from WAKO chemicals and stored in a fridge and used as delivered. MEHQ was used as stopper and deionized water was used as solvent.

Feed containers were filled with specified mixtures of monomer and water or initiator and water and were degassed using a vacuum pump for 10-15 min at 80-100 mbar. For kinetic studies in tank reactors, the feed containers were put under argon atmosphere. Samples were diluted in aqueous MEHQ mixtures, which had been stored in the fridge to stop the reaction. A small amount was further diluted for HPLC measurements, the rest was dried in an exicator for 24 h at 0.001 mbar for storage and SEC analysis.

A.3.2 Equipment

Table 23. Specifications of the equipment and sensors that were included in the experimental setups.

Equipment	Short name in flowsheet	Specifications
HPLC piston pumps	P1 – P4	SmartLine 1050 piston pumps with 10 and 50 ml pump heads, Knauer Wissenschaftliche Geräte GmbH
Circulation pump	P5	Type TOE-CY-4281.0226, Speck Pumpen (up to 55 l min^{-1})
High press mixing tee	M1	Static mixing tee with 0.5 mm thru-holes and a 10 µm UHMWPE frit in the center port
Dynamic mixing chamber	M2	Dynamic Mixing Chamber, Knauer Wissenschaftliche Geräte GmbH
Heating circulator	T1	Haake temperature control module DC5 in oil bath (Baysilon M10)
Heating circulator	T2	VWR digital temperature controller in water bath
Heating circulator	T3	VWR digital temperature controller in oil bath (up to 250 °C)
Purge valve	V1 and V3	3 way valve (1/16“ and 1/8“), Swagelok
HPLC switching valve	V2	Two Position Microelectric Valve Actuator (8 ports), VICI Valco Instruments Co. Inc.

		• Sample loop: PEEK capillary, length: 125 mm, internal volume: 55 µl
Mass flow meter	FIRC	Bronckhorst miniCoriFlow
Rotameter	FIR	Rotameter (up to 24 l min^{-1}), Wagner
Pressure sensors	PIR	Omega/Wagner pressure sensors (0-70 bar / 0-100 bar)
Temperature sensors	TIR/TIRC	Type-K elements
Conductivity flow cell	EIR	ET908 Flow-Thru Conductivity Electrode (93 µl, 1/8" connectors), eDaq Pty Ltd.

Table 24. Specifications of the reactor system that were used in experiments.

Reactor	Specifications
Static mixer heat exchanger	Fluitec Contiplant static mixer heat exchanger: • 4 reactors in series connection • internal diameter: 12.3 mm • length: 500 mm • mixer elements: CSE/X8, CSE/X4, CSE/X4T • material (walls/mixer elements): 1.4571/1.4404 • jacket medium: water, circulated using P5 and heated using coiled pipe, which is placed in T3
Tank reactor	Juchheim stainless steel tank reactor: • internal volume: 650 ml

	• internal diameter: 88 mm • material (vessel): 1.4571 • baffle ring: 4 plates, 10 mm × 80 mm • plate stirrer: 45 mm × 45 mm, operated at 250 rpm • jacket medium: water, circulated and heated using T1
Capillary tubular reactor	Stainless steel tube: • placed in oil bath (Baysilone M10) with T2 • material: 1.4435 • length: 3000 mm • inner diameter: 1.76 mm • outer diameter: 3.18 mm • winding diameter: 250 mm

A.3.3 Residence time distribution measurements and comparison to simulations

Figure 153 shows residence time distributions, which were measured by placing the conductivity flow cell directly before the reactor inlet at room temperature. These signals correspond to the actual inlet signal that is injected into the reactor and deviate from an ideal Dirac delta function as described in Section 3.3.1. Nevertheless, the reproducibility is very good.

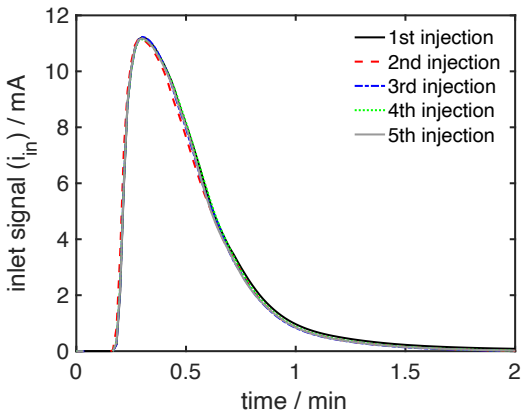

Figure 153. Inlet signals from multiple injections, which were measured at room temperature by placing the conductivity flow cell at the reactor inlet (colors), and the input signal that was used for simulations.

To generate a lookup table for simulations, the measured signal was normalized

$$E_{in} = \frac{i_{in}}{\int i_{in}\ dt} \tag{298}$$

and scaled

$$c_{T,in}^{sim} = N_T^0 E_{in} \tag{299}$$

with the current i_{in} that was measured using the conductivity flow. The constant N_T^0 was chosen to match the amount of tracer that was injected in experiments

$$n_{T,in}^{exp} = c_{T,in}^{exp} V_{loop} = 5.5\ 10^{-5}\ \text{mol}, \tag{300}$$

with the tracer concentration in the sample loop $c_{T,in}^{exp}$, which is 1 mol l^{-1} NaCl solution, and the volume of the sample loop V_{loop}. The normalization constant N_T^0 can be calculated as

$$n_{T,in}^{sim} = \int c_{T,in}^{sim} v^{in} A_{in} dt = n_{T,in}^{exp}, \tag{301}$$

$$\frac{n_{T,in}^{exp}}{v^{in} A_{in}} = \int c_{T,in}^{sim} dt = N_T^0 = 1.88\ 10^3 \text{ mol s m}^{-3} \tag{302}$$

As mentioned in Section 3.3.2 and illustrated in Figure 154, a baseline correction was performed to correct for the increased conductivity in presence of initiator in experiments. The baseline was approximated using piecewise cubic hermite interpolation on the measured data excluding the signal peaks.

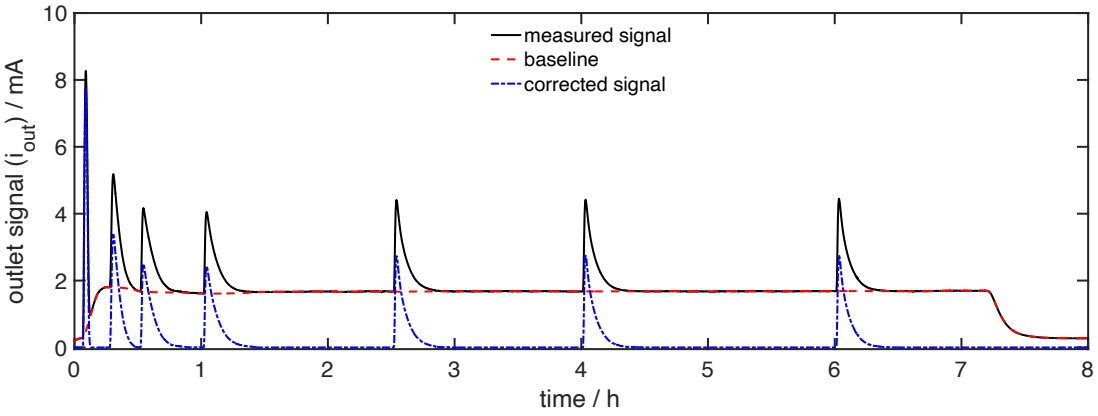

Figure 154. Illustration of the baseline correction method for residence time measurements using the conductivity flow cell. See Section A.3.3 for details.

To get a better estimate, the residence time distribution in pure water was measured for different tracer diffusion coefficients D_T. As illustrated in Figure 155, a diffusion coefficient of $D_T = 5\ 10^{-9}$ m^2 s^{-1} is a reasonable choice for the process parameters of the reference case. For better comparison, the dimensionless time t/τ and the outlet signal τE_{out} have been plotted in Figure 155. This was necessary to correct for uncertainties in the experimental residence time, due to reactor tolerances and possible density differences between the real system and simulations.

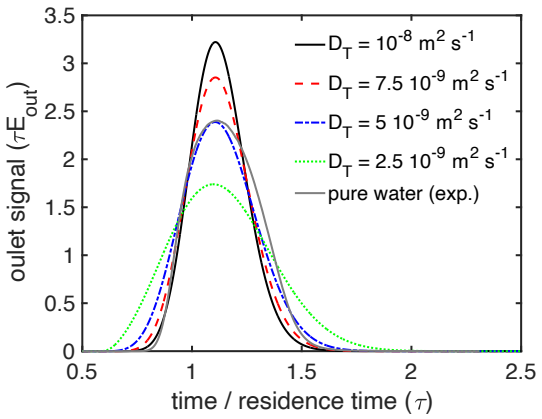

Figure 155. Comparison of the output signals τE_{out} in pure solvent of simulations for different tracer diffusion coefficients D_T and experiments.

The residence was estimated from

$$\tilde{\tau} = \int tE_{out}\ dt - \int tE_{in}\ dt \tag{303}$$

using the input signal from Equation (298) and the output signal in pure water. Doing so for simulations yields the expected value of $L_{reac}/v_{in} = 250$ s. For experiments, a slightly lower value of 229 s was determined. These values were used in Figure 155 as well as in Figure 105 and Figure 106 in Section 5.2.3. To generate the area normalized signal E_{out} for experiments, the area of pure water outlet signal was used all signals. This choice was made since tailing was low and the baseline was constant.

A.3.3.1 Residence time distribution for Taylor dispersion

The normalized distribution that describes spreading of a point source in 1D is [38]

$$\tilde{E}_{ps} = \frac{1}{\sqrt{4\pi D_{disp} t}} \exp\left(-\frac{x^2}{4\pi D_{disp} t}\right) \tag{304}$$

with the dispersion coefficient D_{disp}, the position in space in x and the time t. For a point source, which has been transported in a plug flow reactor with the constant velocity v_{av} for

$$\tau_{PF} = \frac{L_{reac}}{v_{av}} \tag{305}$$

over the reactor length L_{reac}, the distribution becomes

$$\tilde{E}_{ps} = \frac{1}{\sqrt{4\pi D_{disp}\tau_{PF}}} \exp\left(-\frac{(x - L_{reac})^2}{4\pi D_{disp}\tau_{PF}}\right). \tag{306}$$

If the flow pattern is not a plug flow but a Hagen-Poiseuille flow in a circular tube, the effective dispersion coefficient is [60], [61]

$$D_{disp} = D_{Taylor} = D_T \left(1 + \frac{1}{48}\left(\frac{v_{av} R_{reac}}{D_T}\right)^2\right) \tag{307}$$

with the pipe radius R_{reac}. This effective dispersion coefficient accounts for the fact that radial diffusion sharpens the distribution due to the non-uniform axial velocity profile, which is referred to as Taylor dispersion [38]. The transformation to $t = x/v_{av}$ leads to

$$E_{Taylor}(t) = \frac{v_{av}}{\sqrt{4\pi D_{Taylor}\tau_{PF}}} \exp\left(-\frac{(t v_{av} - L_{reac})^2}{4\pi D_{Taylor}\tau_{PF}}\right), \tag{308}$$

which can be reformulated to

$$E_{Taylor}(t) = \sqrt{\frac{Pe_{Taylor}}{4\pi\tau_{PF}^2}}\, exp\left(-\frac{(t - \tau_{PF})^2 Pe_{Taylor}}{4\tau_{PF}^2}\right) \tag{309}$$

with Peclet number

$$Pe_{Taylor} = \frac{v_{av} L_{reac}}{D_{Taylor}}. \tag{310}$$

Equation (309) is the solution of the dispersion model for low axial dispersion [64], i.e $Pe_{Taylor} \gg 1$.

A.3.4 Size exclusion chromatography

For SEC analysis, the dried polymer samples were dissolved in eluent at a concentration of 5 g l^{-1} and stirred at low speed for 24 h. The injection volume was 100 µl. The concentration is rather high but acceptable for broad MWDs. Elugrams for different concentration were checked and showed no artefacts due to too high concentrations.

Size exclusion chromatography was performed on a setup by PSS (polymer standard service, Mainz, Germany) using DMAc with 5 g l^{-1} LiBr as eluent at 0.8 ml min^{-1}. The injector, degasser, pumps etc. were from the Agilent 1260 series and columns from the PSS gram series were used for separation. A combination of one column with 100 Å and two 10000 Å pore size (GRAM combination ultrahigh colums set) was used. As a concentration sensitive detector, an RI detector from the Agilent 1260 series was included and the PSS SLD 7100 detector was used as a molar mass sensitive. Data was recorded using the WinGPC software, but processing of the detector raw data was done using a self-programmed Matlab tool since structural analysis could not be performed in WinGPC due to non-adjustable filters in the software. A validation of the Matlab tool for data processing is shown in Figure 156 using the conformational plot for a typical sample. While the radii of gyration are filtered in the WinGPC software and can therefore not be exported over

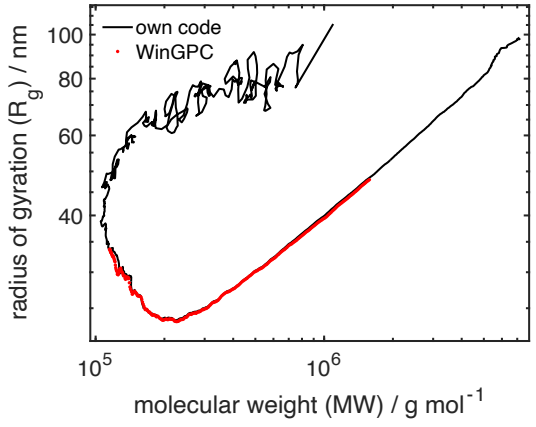

Figure 156. Comparison of the conformation plots obtained from commercial software and the own code: WinGPC uses a non-adjustable filter which does not allow the user to export the conformation plot over the full range of molecular weights. Slight differences are due to the different polynomial fit to the measured calibration in the WinGPC software.

the full range of molecular weight, the self-made software for data processing allows a characterization of the full range of molecular weights.

The workflow for the calculation of MWDs averages as well as conformation plots and the degree of branching is illustrated in Figure 157 to Figure 162. The Berry fit method using a linear fit proved appropriate for the range of molecular weights and sizes used in this thesis as demonstrated for a typical sample in Figure 158.

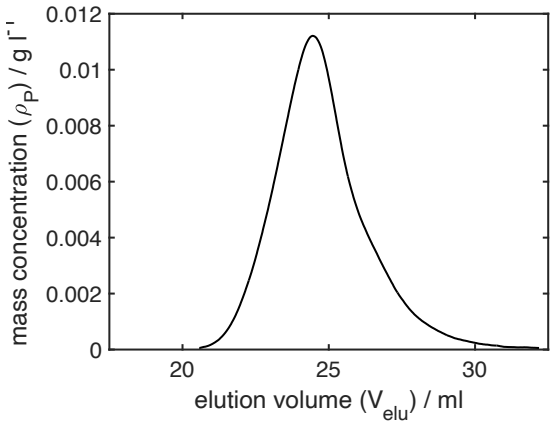

Figure 157. Concentration from RI detector elugram for a sample from a CSTR experiment.

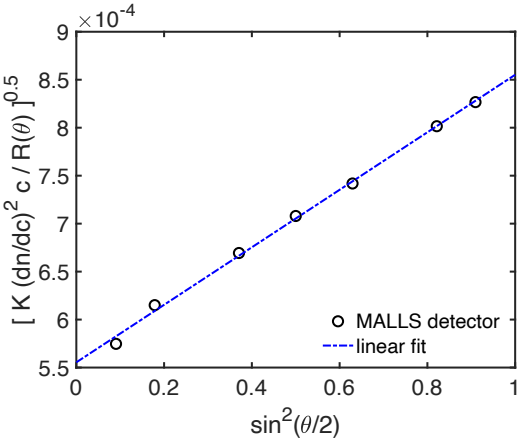

Figure 158. Berry plot at 21.6 ml elution volume for a sample from a CSTR experiment: The weight average molecular at this elution volume is around 3 10^6 g mol^{-1}

Plotting the molecular weight data from the Berry fit against the elution volume to obtain the calibration curve revealed a strong influence of the so-called anchoring effect [32]. The latter can be observed in SEC measurements of branched systems since branches may behave as low molecular molecules which enter smaller pores of the SEC columns causing the chain to elute with low molecular material at higher elution volumes. Since the MALS detector gives the weight average molecular weight $\overline{M_w}$ of a sample, the molecular weight obtained for these elution volumina is strongly affected by the presence of high-molecular chains even if their concentration is low. The effect is even more pronounced for the radius

of gyration since measurements using a MALS detector give the z-average of the latter. Examples for typical samples are shown in Figure 159 and Figure 160. As explained in Section 2.2, the overall weight average molecular weight $\overline{M_w}$ is not affected by this behavior and was calculated using data from the Berry fit after applying a spline filter to reduce noise as illustrated in Figure 159. The weight average molecular weight $\overline{M_w}$ is then

$$\overline{M_w} \approx \overline{M_w}^{spline} = \frac{\sum_i c_i M_i^{spline}}{\sum_i c_i} \tag{311}$$

in which M_i^{spline} is the molecular weight from the spline approximation and i goes over all elution volumina. Other molecular weight averages as well as the MWD and conformation plot are of course strongly affected by the anchoring effect.

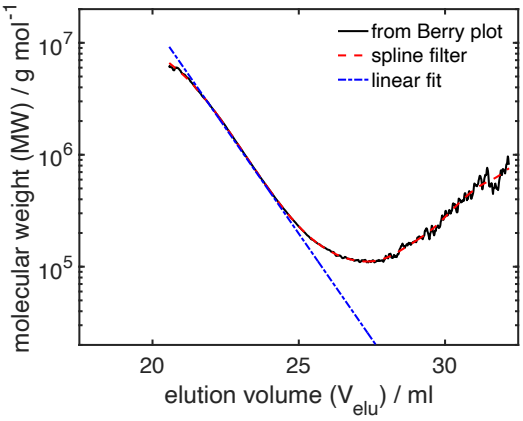

Figure 159. Measured calibration curve for a sample from a CSTR experiment: The increase at high elution volumes is due to the anchoring effect (see Section A.3.4). A linear approximation was used for calculation of the MWD and conformation plot and a spline filter for the calculation of molecular weight averages.

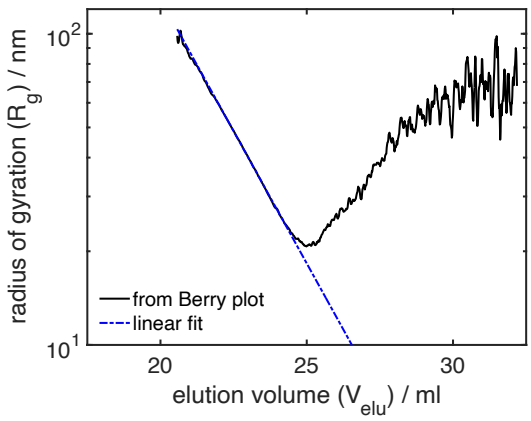

Figure 160. Radius of gyration as a function of elution volume for a sample from a CSTR experiment: The increase at high elution volumes is due to the anchoring effect (see Section A.3.4). A linear approximation was used for calculation of the conformation plot.

The most effective way to circumvent this problem would be to change the separation system to field flow fractionation in which molecules are separated due to their mobility in a cross flow. Since no porous column material is involved, linear calibration curves are

usually observed even for highly branched chains. If no such method is available, at least an approximation of the real calibration curve of the sample can be obtained by extrapolating a fit to the high-molecular regime, which should be less affected by the anchoring effect. The SEC columns used in this work show a linear elution behavior at high-molecular weights and, therefore, linear fits were used to estimate molecular weights and radii of gyration at high elution volumes. The MWD that is obtained using the fitted calibration curve is illustrated in Figure 161. The tailing at low molecular weights is due to the assumption of a linear elution behavior in this regime and has no physical background. Figure 162 shows the conformation plot using data from the Berry fit directly in comparison of with one that is obtained from linear fits shown in Figure 159 and Figure 160. The loop in the former appears since the anchoring effect disturbs the z-average of the radius of gyration more strongly than the weight average of the molecular weight. The approximation using linear fits is in very good agreement in the high-molecular regime and gives

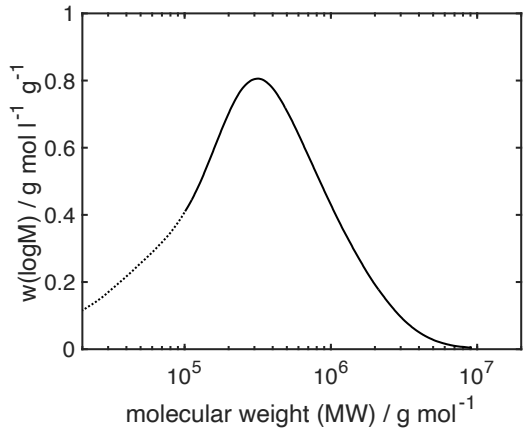

Figure 161. MWD for a sample from a CSTR experiment: A linear approximation for the calibration curve was used. The shoulder below 10^5 g mol^{-1} is due to the linear extrapolation has not been plotted in Section 4.3.2.

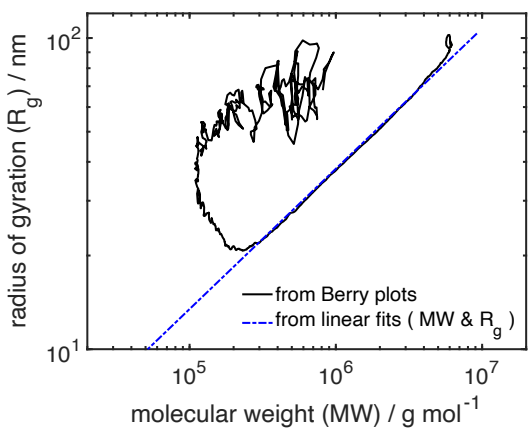

Figure 162. Comparison of the conformation plot using data from the Berry plot directly and from linear fits with extrapolation. The artificial increase of the radius if gyration at low molecular weight is due to the anchoring effect (see Section A.3.4).

a more realistic approximation in the low molecular regime. Therefore, the latter was used to estimate the degree of branching in Section 4.3.3.

A.3.5 High pressure liquid chromatography

High pressure liquid chromatography was performed on an Agilent 1260 series setup using a mixture of Water and Acetonitril (90:10) as an eluent at 0.5 ml min^{-1}. The injection volume was 3 µl. For separation a Poroshell 120EC-C18 column was used and the UV adsorption at 235 nm was measured. The results were averaged from three injections.